UNIVERSITY OF SOUTHAMPTON

A Chirped, Pulsed Laser System and Magneto-Optical Trap for Rubidium

by

Sunil Patel

A thesis submitted in partial fulfillment for the
degree of Doctor of Philosophy

in the
Faculty of Engineering, Science and Mathematics
School of Physics and Astronomy

March 2009

Declaration of Authorship

I, Sunil Patel, declare that this thesis titled, 'A Chirped, Pulsed Laser System and Magneto-Optical Trap for Rubidium' and the work presented in it are my own. I confirm that:

- This work was done wholly or mainly while in candidature for a research degree at this University
- Where any part of this thesis has previously been submitted for a degree or any other qualification at this University or any other institution, this has been clearly stated
- Where I have consulted the published work of others, this is always clearly attributed
- Where I have quoted from the work of others, the source is always given. With the exception of such quotations, this thesis is entirely my own work
- I have acknowledged all main sources of help
- Where the thesis is based on work done by myself jointly with others, I have made clear exactly what was done by others and what I have contributed myself

Signed: _____

Date: _____

"I finally got round to it,
in between doing the laundry, taking out the recycle-bin and hoovering the cat."

UNIVERSITY OF SOUTHAMPTON

Abstract

Faculty of Engineering, Science and Mathematics
School of Physics and Astronomy

Doctor of Philosophy

by Sunil Patel

This thesis covers the construction and characterisation of a magneto-optical trap (MOT) for ^{85}Rb from the very beginning. It details both the optical and mechanical aspects from laser diode assembly, tuning and stabilisation to the preparation and assembly of the vacuum system.

The MOT construction forms the first goal of the project, the second was to develop a laser system capable of producing custom programmable, amplitude modulated and frequency chirped pulses (on the tens of microseconds timescale) from a continuous wave source. This involved developing software and computer control for several arbitrary signal generators linked to drivers for acousto-optic and electro-optic modulators. This chirped, pulsed laser system will be used to perform state manipulations on the ^{85}Rb MOT cloud using two-photon Raman transitions in an adiabatic rapid passage regime.

The chirped pulse system was initially tested with a rubidium vapour cell in an attempt to perform atomic interferometry that would produce spatial interference fringes along the length of the cell. However, due to the beam power requirements, the beam diameter together with the large Doppler shift at room temperature meant these fringes were not seen and so the vapour cell was replaced with the cold atom cloud in the MOT.

Two-photon Λ experiments were attempted with the MOT cloud using the chirped pulse system, however despite greatly improved laser power and detection efficiency, the signal indicating ground state population transfer via a two-photon interaction was not seen. The results indicate that the hyperfine-ground state splitting frequency has been shifted due to the proximity of the ion pump magnet to the vacuum system. Presently, efforts are being directed towards searching for the correct frequency.

Acknowledgements

There are many people I would like to acknowledge and thank for their help and support during my time on this project. I would like to begin by thanking my supervisor, Dr. Tim Freegarde whose guidance, humour and frequent prodding kept me going in the right direction.

I would also like to thank the other three members of our group, 'Quantum Control', who worked with me in the lab, James Bateman, Matt Himsworth and Rich Murray. This project is a major group effort, where we all depended on each other to have the separate components of the MOT built and tested so we could confidently put them together towards the end. The crucial laser locking and feedback system was down to Matt's efforts and the maths worked through by James ensured we had a good theoretical basis for the chirped, pulsed system and vapour cell work.

I would like to thank Mark Bampton, who machined the vacuum chamber in the Mechanical Workshop. His expertise and professional skill turned Tim's designs and CAD drawings into quite possibly the most elegant and beautiful MOT vacuum chamber any atomic physics group has.

I would like to also mention Chad in the Electronics Workshop for his help in wiring together the new designed laser diodes. These were especially tricky to assemble and I am grateful for Chad's help in this; and also for not making me feel too stupid when I used to ask the most basic electronics questions, which were on par with 'DC transformers'.

There is a long list of crazy house mates and fellow post graduate students whom I would also like to thank for their help, time and advice; as well as their equipment, particularly Keith Wilcox and Matthew Markham.

On a more personal note, I am also very grateful to Pearl John, who introduced me to the world of Schools Outreach and especially the Light Express laser light shows. It put the fun back into physics and reminded me of why I wanted to study it in the first place and let me explore the creative side of my brain.

Finally I would like to thank my family and closest friends, who supported me through many of the more difficult times and were always there, urging me on and eagerly waiting for me to return back home to them, after such a long time away.

Contents

List of Figures

List of Tables

Abbreviations

AOM	**A**cousto-**O**ptic **M**odulator
ARP	**A**ddress **R**esolution **P**rotocol
ARP	**A**diabatic **R**apid **P**assage
AWG	**A**merican **W**ire **G**auge
BS	(optical) **B**eam **S**plitter
CCD	**C**harge **C**oupled **D**evice (video camera)
CPT	**C**oherent **P**opulation **T**rapping
CW	**C**ontinuous **W**ave
DAVLL	**D**ichroic **A**tomic **V**apour **L**aser **L**ock(ing)
DFFML	**D**oppler-**F**ree **F**requency **M**odulation **L**ock
ECDL	**E**xternal **C**avity **D**iode **L**aser
EIT	**E**lectromagnetically **I**nduced **T**ransparency
EOM	**E**lectro-**O**ptic **M**odulator
FOV	**F**ield **o**f **V**iew
FPS	**F**rames **p**er **S**econd
FSR	**F**ree **S**pectral **R**ange
FWHM	**F**ull **W**idth at **H**alf **M**aximum
GPIB	**G**eneral **P**urpose **I**nterface **B**us
HV	**H**igh **V**acuum
HP	**H**igh **P**ass (frequency filter)
LIAD	**L**ight-**I**nduced **A**tomic **D**esorption
LP	**L**ow **P**ass (frequency filter)
MOT	**M**agneto-**O**ptical **T**rap
ND	**N**eutral **D**ensity (filter)
NIST	**N**ational **I**nstitute of **S**tandards and **T**echnology

NPL	the UK **N**ational **P**hysical **L**aboratory
Op-amp	**O**peration **Amp**lifier
OSA	**O**ptical **S**pectrum **A**nalyser
PBS	**P**olarising **B**eam **S**plitter (cube)
PC	**P**ersonal **C**omputer
PCB	**P**rinted **C**ircuit **B**oard
PID	**P**roportional **I**ntegral **D**erivative
QED	**Q**uantum **E**lectro **D**ynamics
RF	**R**adio **F**requency
ROI	**R**egion **o**f **I**nterest
SAS	(Doppler-free) **S**aturated **A**bsorption **S**pectroscopy
SCPI	**S**tandard **C**ommands for **P**rogrammable **I**nstruments
STIRAP	**STI**mulated **R**aman **A**diabatic **P**assage
SWG	**S**tandard **W**ire **G**auge
TCP/IP	**T**ransmission **C**ontrol **P**rotocol / **I**nternet **P**rotocol
TTL	**T**ransistor-**T**ransistor **L**ogic
UDP	**U**ser **D**atagram **P**rotocol
UHV	**U**ltra **H**igh **V**acuum
VCO	**V**oltage **C**ontrolled **O**scillator
VSWR	**V**oltage **S**tanding **W**ave **R**atio
WP	**W**ave **P**late (multi-order)

Physical Constants

Speed of Light	c	=	$2.997\ 924\ 58 \times 10^{8}\ \mathrm{ms}^{-\mathrm{S}}$ (exact)
Permeability of Free Space	μ_0	=	$4\pi \times 10^{-7}\ \mathrm{NA}^{-1}$ (exact)
Permittivity of Free Space	ϵ_0	=	$\mu_0 c^2 = 8.854\ 187\ 817 \times 10^{-12}\ \mathrm{Fm}^{-1}$
Planck Constant	h	=	$6.626\ 0693\,(11) \times 10^{-34}$ Js
Bohr Magneton	μ_B	=	$927.400\ 949\,(80) \times 10^{-26}\ \mathrm{JT}^{-1}$
Bohr Radius	a_0	=	$0.529\ 177\ 2108\,(18) \times 10^{-10}$ m
Elementary Charge	e^-	=	$1.602\ 176\ 53\,(14) \times 10^{-19}$ C
Coulomb	C	=	$6.241\ 509\ 629\ 152\ 65 \times 10^{18}$ electrons
Electron Mass	m_e	=	$9.109\ 3826\,(16) \times 10^{-31}$ kg
Proton Mass	m_p	=	$1.672\ 621\ 71\,(29) \times 10^{-27}$ kg
Neutron Mass	m_n	=	$1.674\ 927\ 28\,(29) \times 10^{-27}$ kg
Atomic Mass Unit	m_u	=	$1.660\ 538\ 86\,(28) \times 10^{-27}$ kg
Avogadro's Constant	N_A	=	$6.022\ 1415\,(10) \times 10^{23}\ \mathrm{mol}^{-1}$
Boltzmann's Constant	k_B	=	$1.380\ 6505\,(24) \times 10^{-23}\ \mathrm{JK}^{-1}$
Molar Gas Constant	R	=	$8.314\ 472\,(15)\ \mathrm{Jmol}^{-1}\mathrm{K}^{-1}$
Standard Atmosphere	atm	=	$101,325$ Pa (exact)
Stefan-Boltzmann Constant	σ	=	$5.670\ 400\,(40) \times 10^{-8}\ \mathrm{Wm}^{-2}\mathrm{K}^{-4}$
Wien Displacement Law	b	=	$2.897\ 7685\,(51) \times 10^{-3}$ mK

Number in brackets is the standard deviation in the last two digits of the given value[1]

Symbols

a	anti-Helmholtz coil radius	m
a, $\mathbf{a}$	acceleration (scalar, vector)	ms^{-2}
a_0	atomic radius	m
A	cross sectional area	m^2
A_{hfs}	hyperfine magnetic dipole constant	MHz
b	half the distance between the anti-Helmholtz coils	m
$\mathbf{B}$	magnetic field	T
B_{hfs}	hyperfine electric quadrupole moment	MHz
B_z	magnetic field along the z axis	T
$\lvert c_1\rvert^2$	ground state occupation probability	
$\lvert c_2\rvert^2$	excited state occupation probability	
C_{ge}	Clebsch-Gordan coefficient between the ground and excited state	
$\hat{\mathbf{e}}_{(x,y,z)}$	electric field polarisation vector (in x, y, z)	
d_l	MOT to imaging-lens distance	m
E	energy	J
$\mathbf{E}$	electric field (of the laser)	Vm^{-1}
E_0	electric field magnitude	Vm^{-1}
ΔE_g	ground state energy light shift	
$(\Delta)E_{\mathrm{hfs}}$	hyperfine level energy splitting	J
f	frequency (generic)	Hz
F, $\mathbf{F}$	force (generic), force (vector)	N
F_{MOT}	force of the magneto-optical trap	N
F_{OM}	force of Optical Molasses (Doppler force)	N
F	total angular momentum quantum number, $= I + J$	
F_g, F_e	ground and excited state F number	

$\mathbf{F}_s$	scattering force	N
g_F	total angular momentum g-factor	
g_I	nuclear g-factor	
g_J	fine-structure Landé g factor	
g_L	electron orbital angular momentum g-factor	
g_S	electron spin g-factor	
I	nuclear spin magnetic moment quantum number	
I	electric current	A
I	light intensity	cd
I_0	saturation intensity	cd
J	total electron angular momentum, $= L + S$	
J_g, J_e	ground and excited state J number	
k	wave-vector, $k = 2\pi/\lambda$	m^{-1}
l	length	m
L	orbital angular momentum	
m	mass (generic)	kg
m_F	magnetic sublevels of the F hyperfine level	
m_{Rb}	mass of rubidium	kg
n	principal quantum number	
N	neutron number of an atomic nucleus	
N	number/quantity (e.g. of photons, collisions etc...)	
N_s	number of scattered photons	
p, $\langle p \rangle$	momentum (generic), momentum (time averaged)	kgms^{-1}
p_{Rb}	momentum of rubidium	kgms^{-1}
p_λ	momentum of the photon	kgms^{-1}
q	electric charge	C
P	power	W (Js^{-1})
r_l	lens radius	m
R	resistance	Ω
s	distance	m
s	off-resonance saturation parameter	
s_0	saturation parameter, I/I_0	
$\mathbf{S}$	Poynting Vector	$\mathrm{Jm}^{-2}\mathrm{s}^{-1}$

t	time	s
T	temperature (generic)	K
T_0	"temperature depth" of the MOT	K
T_D	Doppler temperature	K
T_r	recoil temperature	K
u	energy density of the electromagnetic field	Jm^{-3}
$\mathbf{u}, u$	atomic velocity, atomic speed	ms^{-1}
v	velocity (generic)	ms^{-1}
v_c	MOT capture velocity	ms^{-1}
v_Rb	velocity of rubidium	ms^{-1}
V	voltage	V
V	volume	m^3
z'	laser beam diameter	m
Z	proton number of an atomic nucleus	
α	constant of proportionality	
β	Doppler force damping parameter	kgs^{-1}
Γ	line-width, $\simeq 1/\tau$	
δ	Doppler (angular) frequency shift	(rads^{-1}), Hz
δ	laser detuning, $\omega_L - \omega_0$ (angular) frequency	rads^{-1}
δ_q	quantum defect parameter for hydrogen-like atoms	
ε	effective field vector	
η_e	geometrical detection efficiency	
ϑ	solid angle	sr
λ	wavelength (generic)	m
μ_L	electron orbital magnetic moment	
μ_S	electron spin magnetic moment	
ξ	measured photodiode fluorescence	
ρ	resistivity	$\Omega\mathrm{m}$
ρ	density	kgm^{-3}
ρ_Cu	density of Copper	kgm^{-3}
σ	absorption cross-section	m^2
τ	excited state lifetime	s

ψ	electronic state vector	
ω	angular frequency	rads^{-1}
ω_L	laser light angular frequency	rads^{-1}
ω'_L	Doppler shifted laser angular frequency	rads^{-1}
ω_0	atomic transition or resonant angular frequency	rads^{-1}
Ω	Rabi frequency	rads^{-1}
$\mathrm{d}B/\mathrm{d}z$, $\partial B/\partial z$	magnetic field gradient	Tm^{-1}

To my extended family, including the felines

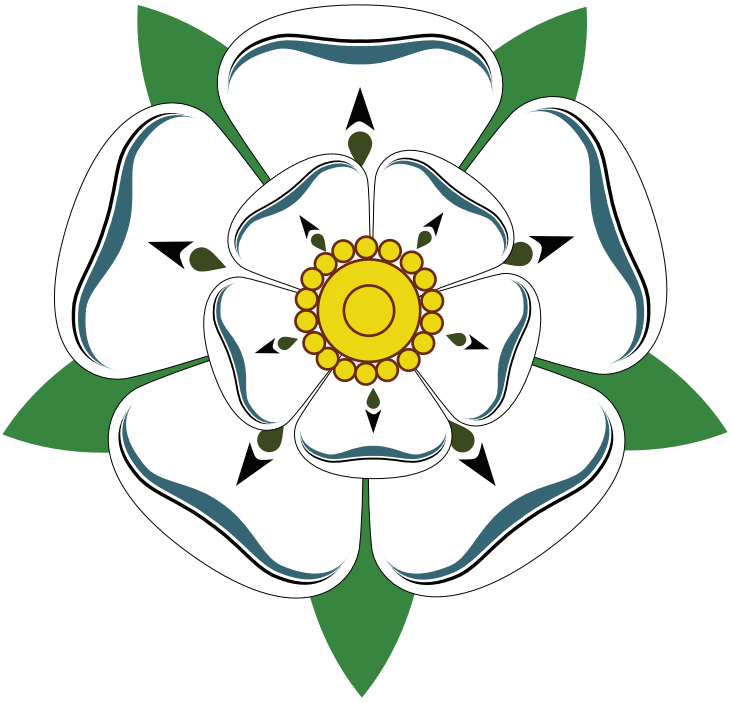

Chapter 1

Introduction

Making precise and subtle observations of tiny objects moving randomly at high speed is very difficult. In this thesis, these objects are atoms and they move with speeds of hundreds of metres per second at room temperature. As the best way to study atoms is by keeping them still, a way must be found to reduce their speed by cooling them down and confining them in one place for study – an atomic trap is required.

Our aim is to study novel optical cooling and trapping schemes that may be useful in extending the low temperature domain to other atoms and molecules. This thesis describes the construction and characterisation of the two components needed for such studies: a magneto-optical trap for rubidium, to provide the test species; and a chirped, pulsed laser system, to implement and explore the new schemes.

1.1 Atomic Traps

Atomic traps have been available for nearly two decades. There are many different types, each with their own variants. Traps exist that are optimised for ions or neutral atoms either using lasers, electric or magnetic fields (which can be static or time varying) or a combination of both. They have become standard equipment for any experimental cold atoms research group.

Of the multitude of traps available, the Magneto-Optical Trap (MOT) – which uses a combination of lasers and static magnetic fields – has become the standard tool for cooling and trapping, neutral atoms. MOTs have become so common because they form the first step for further cold atom experiments. For example, the production of a Bose-Einstein Condensate (BEC) begins with a MOT cloud, which is then transferred to a

magnetic trap and then evaporatively cooled. Slow light experiments can be performed on these BEC clouds [2, 3] as well as investigations into other highly non-linear light-matter interactions such as Electromagnetically-Induced Transparency (EIT) [4–6].

MOTs themselves exist in various manifestations: there are mirror-MOTs, pyramidal MOTs [7, 8] and dual-species MOTs. Though MOTs have become very common, and their construction well developed, they are not trivial to construct. The huge range of customisations and options available when planning a MOT system mean they are generally not available to buy 'off-the-shelf' from commercial suppliers.

1.2 Cold Atoms

The ability to cool and confine atoms has revolutionised the field of atomic physics as it allows atoms to be studied carefully in exquisite detail. Atomic spectroscopy has benefited hugely, the Doppler broadening – which at room temperature smothered all but the strongest spectral features – has now been drastically reduced with cold atoms and has allowed rich hyperfine structure to be revealed, boosting the development of atomic theory and QED [9].

Cold atoms have allowed new experiments and theory to drive each other, for example in determining constants such as magnetic moments, the Rydberg constant and g-factors to higher and higher precision [10–12]. Whole new areas of physics based on cold atoms such as cold collisions, cold chemistry and atomic coherence can now be explored. The cold trapped atomic cloud was the first step that allowed the Bose-Einstein Condensate to be achieved – an entirely new state of matter to investigate experimentally and theoretically. More recently, trapped atoms and ions have become potential candidates for quantum computing schemes because of their long coherence times, simple state preparation and addressability [13–15].

Cold atoms are no longer confined to research labs. Developments in trap technology have made it easier to produce cold atoms resulting in real-world applications. Arguably the most important of these are the atomic fountain clocks that have reached time-keeping accuracies of 10^{-15} in the frequency uncertainty [16] and are now used to define the second[1].

[1]The current (January 2006), primary standard is the caesium (^{133}Cs) microwave frequency standard at NIST. The secondary standard is ^{87}Rb, from NPL [17, 18]. Current efforts are pushing the frequency standard towards visible/optical frequencies [19].

1.3 Molecular Manipulation

The manipulation of molecules however, remains a much sought-after goal. There has been some success in producing cold molecules from photo-association [20], cold atomic collisions and Feshbach resonances [21–24] however in many cases, only short-lived unstable molecules in high energy or Rydberg states are produced and further manipulation is not possible.

The chirped pulse method described in the next chapter is a robust, adiabatic method for electronic state manipulation. It is a relatively new field in coherent manipulation and there have been some initial experimental investigations into using chirped pulses, which this project hopes to contribute to with the vapour cell and MOT experiments.

Though the initial work presented is with atoms, the long-term goal is to develop the techniques of the chirped pulse system on atoms and then transfer them across to work with molecules and in particular for the cooling and confining of molecules. Molecules have very different structures, energy levels and requirements, which means the vast majority of techniques used successfully to cool and trap atoms do not work with them.

1.4 Future Directions of Atom Traps

The MOT will continue to be a standard piece of equipment for atom trapping groups for some time, yet atomic traps are continually evolving. One of the principle directions of research is to miniaturise traps towards the goal of having, 'cold atoms on a chip' or even, 'BECs on a chip' [25–27].

New developments bring advances in nano-structuring, self-assembly and nano-templating together with developments in the miniaturisation of lasers and optics (e.g. integrated optics and quantum dot lasers). Though at present there is no 'mini-MOT' at the micro-scale, a portable MOT that can be taken out to labs and schools has been successfully demonstrated [28].

Quantum computing has also become a strong driving factor for the miniaturisation of atomic traps because it addresses the problem of 'scalability', where atom traps have been historically weak while other schemes (such as semiconductor quantum computers) have not.

1.5 Thesis Scope

Having a cloud of cooled and confined atoms makes it possible to perform manipulation experiments on them, for example: selectively changing their internal state, velocity or momentum distributions, looking at the atomic coherence times, even performing atomic interferometry [29, 30]. The first part of the research project is the construction, assembly and characterisation of the magneto-optical trap system. The second part involves developing software and constructing a set of apparatus for producing sequences of arbitrarily programmable laser pulses that can be frequency chirped (over MHz) and amplitude modulated from a continuous wave source. This 'chirped pulse system' will be used for manipulating the electronic state population and momentum distribution of the MOT cloud.

Success in being able to manipulate coherently the MOT cloud with the chirped pulse source will open the way to transferring those same experiments over to rubidium molecules (Rb_2). Being able to capture and confine molecules to study them may recreate the same explosion of interest and advancement in understanding that occurred with atomic trapping and manipulation. High-resolution spectroscopy of molecules will allow the ro-vibrational bands of molecules to be observed in exquisite detail, with the results being used to further the theory of molecular bonds and forces. The field of cold collisions would be greatly enriched by being able to use molecules instead of just atoms. Observing genuinely cold molecules – whose electrons are not in highly excited states – interacting together or reacting with other cold molecular species would greatly enrich the field of cold molecular chemistry. Finally, the molecule itself as a large quantum system (and perhaps quantum computer) can be investigated with experiments supplementing the theory.

It is the prospect of enabling these exciting possibilities that is behind the construction of the MOT and chirped pulse system, and the development of the coherent manipulation experiments.

This thesis describes the construction of a MOT system for ^{85}Rb. The three main components – the lasers, optics and stabilisation system, the anti-Helmholtz magnetic field coils and the vacuum chamber and pumping system – are covered in detail. The operating MOT is demonstrated and the MOT cloud characterised.

The development and testing of the chirped, pulse system is also presented and includes initial results from testing the system with a rubidium vapour cell. The difficulties of working with room temperature cells are outlined as well as how this system will be used with the MOT cloud.

Finally, an interesting 'induced transparency' effect in the vapour cell is described. This unusual phenomenon of a weaker, frequency shifted probe beam controlling the absorption of a resonant pump beam in a V-type system is investigated and initial spectroscopic results shown. The effect is reproducible though it does not appear to be described in current literature for the case presented here. The results obtained closely match those of other groups who used different experimental conditions [31]. The discovery of this effect for our experimental setup is surprising, requires further investigation and is an interesting side-line into coherent optical effects.

Chapter 2

Laser Cooling

2.1 The Two-level Atom

A common reference point throughout this thesis will be the simplest picture of an atom as a two-level system at rest, where an incoming photon of energy, $E = \hbar k$ – equal to the energy difference between the ground and excited states – is absorbed by a lone, outer atomic electron and excited to its upper state. The absorption gives a momentum kick of $\hbar k$ in the travelling direction of the absorbed photon[1].

After a short period of time, the atom spontaneously emits a photon (of energy equal to the energy gap between the levels) in a random direction. This is accompanied by a second momentum kick in the direction *opposite* to the emitted photon. The electron drops down to the ground state and is ready to absorb again [33, 34].

In this cycle the atom receives two units of $\hbar k$ of momentum, one in a defined direction (determined by the direction of the incoming photon) and the second in a random direction from spontaneous emission. If this cycle is repeated many times, it is intuitive to see there will be a particular direction of travel for the atom from the momentum obtained from absorption. The momentum from spontaneous emission makes the atom deviate from a direct path into a random walk, but the net effect summed over all directions for this averages to zero [35].

[1]The fact that light carries momentum has been known for a long time [32].

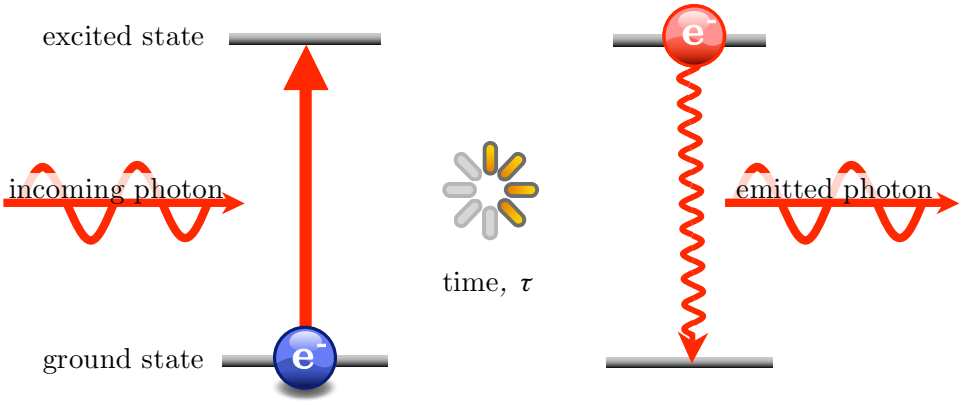

FIGURE 2.1: Absorption and emission in a two-level atom: The atom first receives a momentum kick in the direction of the incoming photon from absorption and later, receives a second kick in the direction *opposite* to the spontaneously emitted photon. Momentum from spontaneous emission events average to zero leaving just the momentum imparted by the incoming photons.

2.2 Doppler Cooling

Unfortunately atoms at room temperature are not at rest but have speeds of hundreds of metres per second. Equating their kinetic energy to their thermal (or internal) energy[2] gives

$$\frac{1}{2}mv^2 = \frac{3}{2}k_BT \tag{2.1}$$

$$v_{\mathrm{Rb}} = \sqrt{\frac{3k_BT}{m_{\mathrm{Rb}}}} \qquad \text{where } m_{\mathrm{Rb}} = \text{mass of rubidium}$$

$$v_{\mathrm{Rb}} = \sqrt{\frac{3 \times 1.38 \times 10^{-23} \times 298}{85 \times 1.67 \times 10^{-27}}}$$

$$v_{\mathrm{Rb}} \sim 300 \text{ ms}^{-1} \tag{2.2}$$

An atom at rest and one that is moving see very different light frequencies because of Doppler shift. An atom moving towards a stationary light source will see the frequency of that source shifted towards the blue (higher frequency/energy), whereas an atom moving in the opposite direction will experience the reverse and see the light red-shifted (lower frequency/energy).

The change in frequency, Δf can be significant and is given by

$$\Delta f = \frac{f_0 v_{\mathrm{Rb}}}{c} \tag{2.3}$$

[2]From the Equipartition of Energy theorem [36, 37].

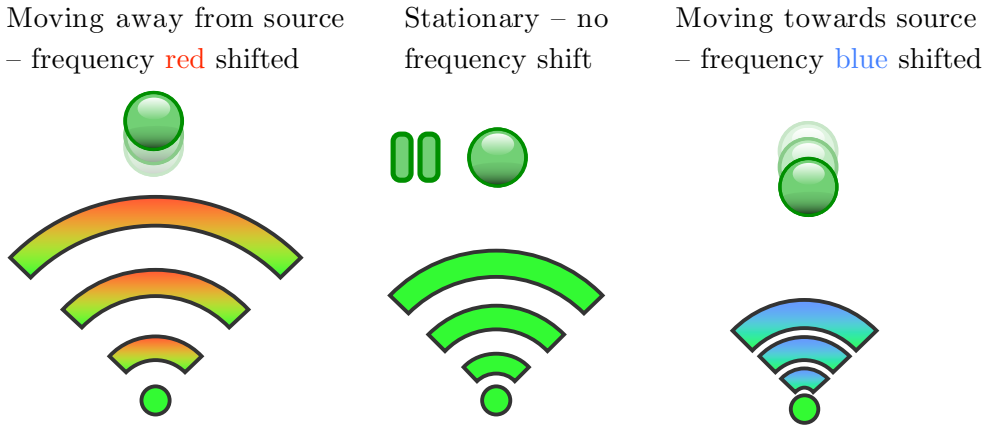

FIGURE 2.2: From the Doppler effect, atoms see different frequencies from the same source or identical sources depending on their motion relative to that source.

where f_0 is the original, unshifted frequency, v_{Rb} is the speed of the rubidium atoms and c is the speed of light. With room temperature atoms moving at hundreds of ms^{-1}, this causes a change in the MHz range of the original optical frequency.

The technique of Doppler cooling takes advantage of this effect to provide a velocity dependent force, which slows the motion of atoms. If a laser beam is slightly red-detuned with respect to an electronic transition, an atom at rest is unlikely to absorb since the photons do not have enough energy to excite. An atom moving away from the beam source is even less likely to absorb, as it will see the beam red detuned even further away from resonance. However an atom moving towards the laser beam will see the light blue shifted up to the correct frequency for excitation and will therefore absorb it. The momentum from absorption will act to oppose the motion of the atom [38].

For an atom moving towards the laser beam, its momentum is reduced by $\hbar k$ per photon absorption. The momentum of a single photon, p_λ is calculated by

$$p_\lambda = \hbar k \quad (\text{with } k = 2\pi/\lambda) \quad = h/\lambda \tag{2.4}$$

$$p_\lambda = 6.63 \times 10^{-34}/\,[780\text{ nm}] \quad \mathrm{kgms}^{-1} \text{ (for a red photon)}$$

$$p_\lambda \sim 1 \times 10^{-27}\ \mathrm{kgms}^{-1} \tag{2.5}$$

This is a very small amount compared with the momentum, p_{Rb} of the atom:

$$p_{\mathrm{Rb}} = m_{\mathrm{Rb}} v_{\mathrm{Rb}} \tag{2.6}$$

$$p_{\mathrm{Rb}} = 85 \times 1.67 \times 10^{-27} \times 300 \quad \mathrm{kgms}^{-1} \text{ using values for rubidium}$$

$$p_{\mathrm{Rb}} \sim 1 \times 10^{-23}\ \mathrm{kgms}^{-1} \tag{2.7}$$

If one absorption and emission cycle takes a few nanoseconds, however the atom can absorb many units of momentum per second and this becomes significant enough to reduce its speed from thermal speeds of hundred of metres per second to just metres per second or slower over a short time scale:

$$\begin{aligned} p_{\mathrm{Rb}}/p_{\lambda} &= 1 \times 10^4 \text{ absorptions} && (2.8) \\ t &= 1 \times 10^4 \times \tau_{\mathrm{Rb}} \text{ (upper level lifetime)} \\ t &= 1 \times 10^4 \times 23 \text{ ns} \\ t &\sim 0.2 \text{ ms} && (2.9) \end{aligned}$$

These simple calculations ignore many physical effects, but are useful as 'back of the envelope sums' to appreciate the order of magnitude of the variables and time scales involved.

2.2.1 Varying Doppler Shift

There is an added complication that as the atoms slow, they fall out of resonance with the laser light as it becomes less and less blue shifted until eventually the absorption stops. This needs to be compensated for to keep the atoms in tune with the light and can be done in two ways. The first is to *chirp* (sweep) the frequency of the laser light to reduce the amount of red detuning as the atoms slow down as demonstrated in [39]. This compensates for the reduction in blue shift as the atomic velocity decreases.

The second method keeps the laser frequency fixed but uses spatially varying magnetic field that causes a Zeeman shift in the excited level such that the frequency required for absorption is reduced. This means that even though the blue shift is reduced as the atoms slow down, the transition frequency is reduced to compensate.

These two techniques have been used to decelerate atomic beams by pointing the laser light directly into the face of an oncoming beam of atoms [40–42]. The second method of using a varying magnetic field is commonly used and the field itself is created by a tapered solenoid (conically shaped) where the optical and atomic beams travel along its axis. This is called a Zeeman Slower and is usually a metre or two in length depending on the initial velocity of the atoms.

2.3 Optical Molasses

From a single laser beam, the picture can be extended to having counter-propagating laser beams along a common axis (say vertical, z). This causes slowing of the atomic motion along this direction as no matter which way the atom moves (up or down), it preferentially absorbs from the beam it is moving towards hence its motion is always opposed.

Adding two further pairs of counter-propagating beams in the x and y axes so that all six beams intersect produces a system where the atoms are slowed in all directions at the centre. This is known as *Optical Molasses* (OM)[43–47] and is shown schematically in figure 2.3. Now, no matter which direction the atom moves in, its motion is likely to be opposed.

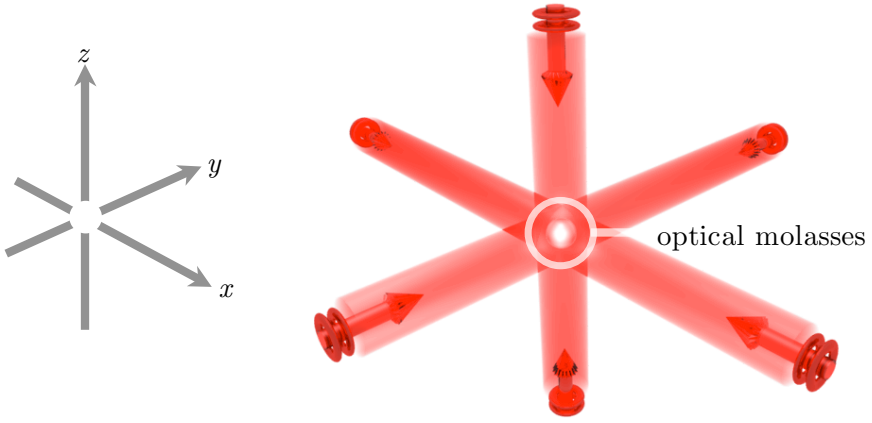

FIGURE 2.3: How to arrange three pairs of orthogonal, counter-propagating beams to produce Optical molasses that slows atoms down in all directions at the centre (overlap).

Doppler cooling is *velocity dependent* as only atoms moving within a certain velocity band will absorb from the laser beam and be slowed. It is important to note that Optical Molasses by itself does not constitute a trap; atoms are slowed considerably from thermal velocities but are not confined, even in the region where the beams overlap. There is an *optical* Earnshaw Theorem [48], which states that it is impossible to trap atoms or small particles at a stable equilibrium point using only the scattering force or conservative fields; this is discussed further in section 3.5. Turning the Molasses into a trap requires the addition of a *position dependent* force from a magnetic field and is discussed in section 2.5.

2.4 Limits of Doppler Cooling

2.4.1 Limit of Trappable Species

Though Doppler cooling has been demonstrated for many atomic species, these have been generally limited to the Group I and II alkali metals[3]. Figure 2.4 shows which of these Group I and II elements have been successfully trapped or Bose-Einstein condensed (as of August 2008)[4].

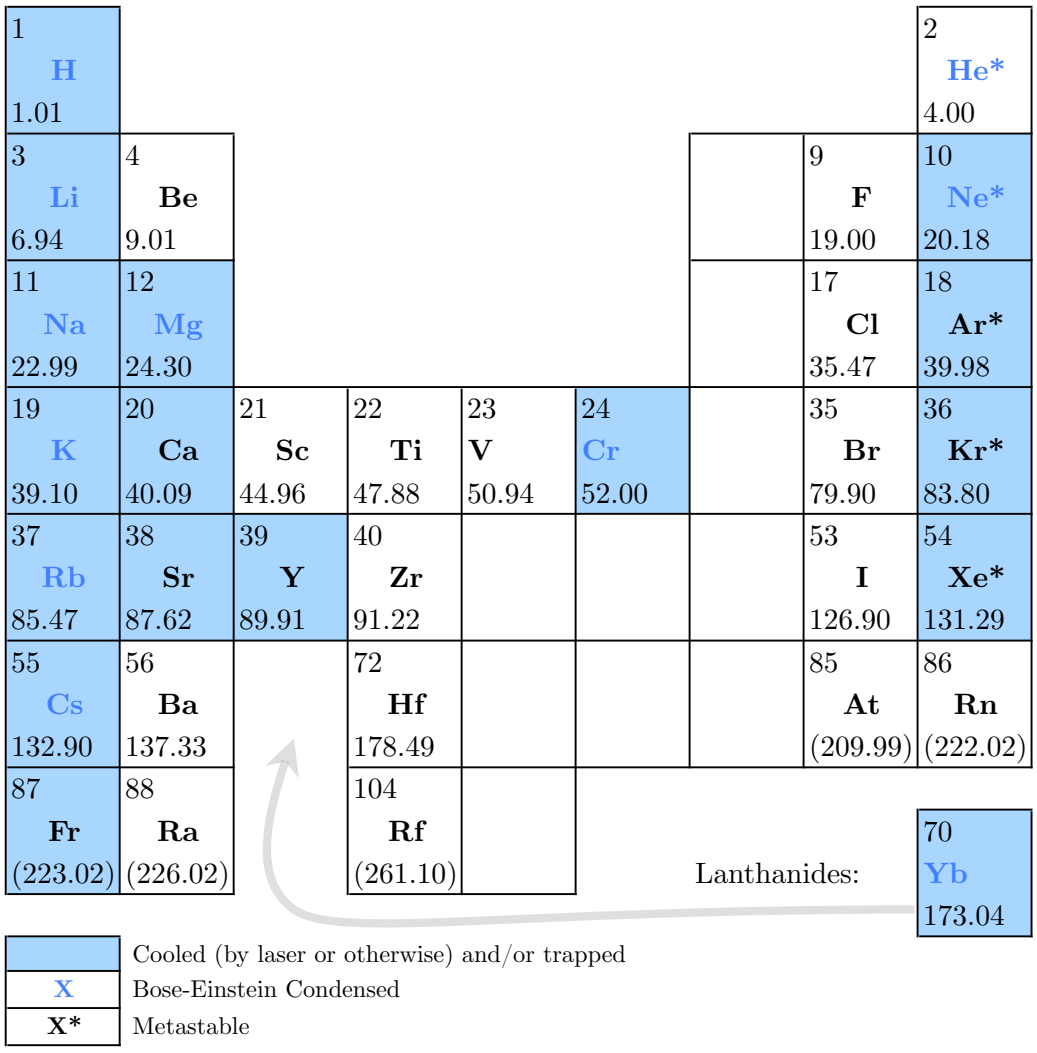

FIGURE 2.4: The Periodic table showing elements that have been successfully cooled or trapped or Bose-Einstein condensed. This is based on a list maintained by the University of Innsbruck, Atomic Physics and Cold Atoms group.

[3]The Group VIII elements are usually trapped as ions in Penning, Ioffe-Pritchard and Paul traps.

[4]Sourced from 'Atom Traps Worldwide' from the University of Innsbruck, present web site at: http://www.uibk.ac.at/exphys/ultracold/atomtraps.html

The restriction to Group I and II elements is because these have an electronic energy level structure that can be approximated by a two-level atom. A more physical picture of the energy level structure contains three or four levels where there is a ground and excited state and further states into which an atom can decay with a finite probability (see figure 2.5). There may be other ground states or 'metastable' states where a further transition back to the ground state is forbidden because of selection rules. In either case, the atom can fall out of the cooling scheme because the electron decays to a level that is not resonant with the Doppler cooling beam.

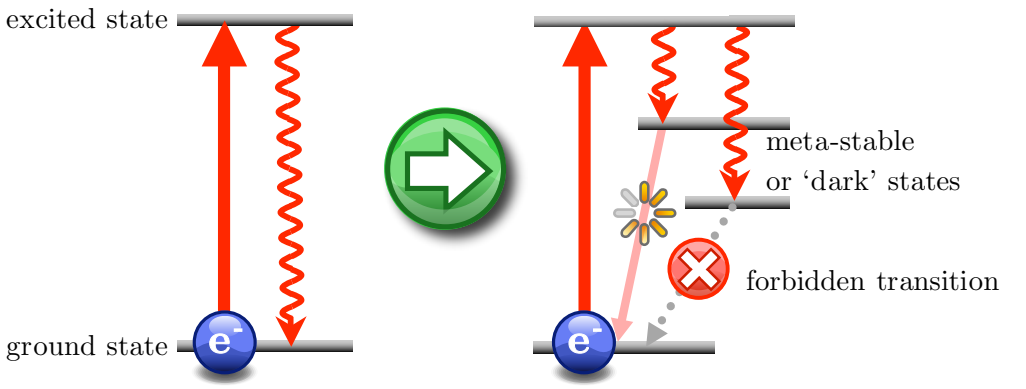

FIGURE 2.5: A more realistic picture of the energy levels of an atom where the electron can decay to other stable ground states or levels where the transition back to the ground state is very weak or forbidden.

The presence of additional states require 'repump' lasers resonant with these states and the excited state so should an electron decay to these levels, it is pumped back out again and can re-join the cooling scheme. As the energy level structure becomes more complicated with an increasing number of states, the addition of more and more repump lasers quickly becomes technically unfeasible. This is the main reason that Doppler cooling has had limited success with the rest of the periodic table outside the Group I, II elements.

The requirement of a simple energy level structure means that even the simplest diatomic molecules cannot be Doppler cooled. Molecules have a much richer structure where energy levels turn into bands because of the presence of rotational and vibrational degrees of freedom, which an individual atom does not have.

In order to be able to cool molecules, the reliance upon the spontaneous emission process to cycle the molecule must be drastically reduced. One method of achieving this is by using a technique called *amplified* Doppler cooling and is discussed in section 2.10. Amplified cooling changes the cooling transition used to one with a much longer lifetime

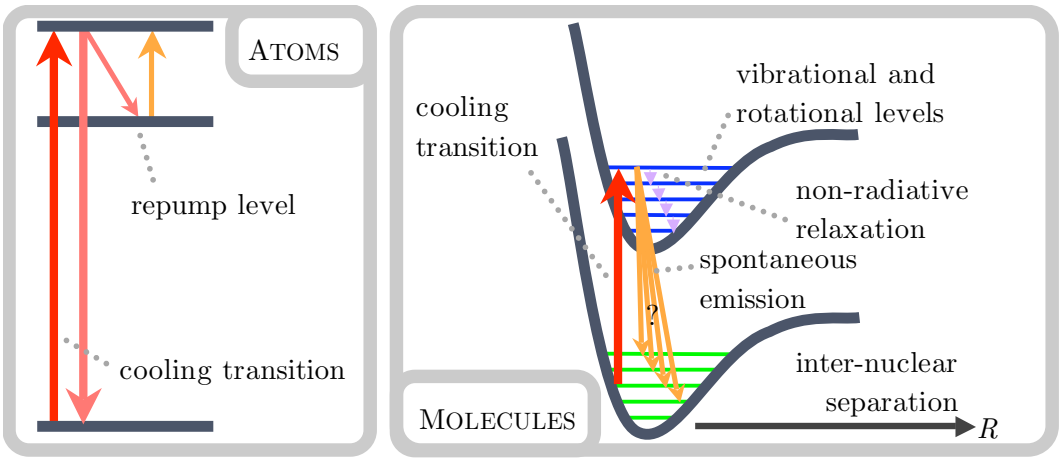

FIGURE 2.6: A comparison of the energy levels of atoms and molecules. Molecules have a much richer structure with additional vibrational and rotational energy bands which means they cannot be currently Doppler Cooled.

and allows the cycle to be driven using stimulated absorption and stimulated emission (a controllable, coherent process) instead of waiting for spontaneous emission.

2.4.2 Temperature Limit

In addition to the restrictions of species that can be used, there is also a limit to how low a temperature can be reached via Doppler cooling. The Doppler temperature limit, T_{D} is the lowest temperature attainable by simple Doppler cooling as described above and is typically in the hundreds of milli-Kelvin range[5]. At the Doppler limit, the laser cooling from optical molasses balances the heating arising from the spontaneous emission of the group of atoms. The T_{D} for ^{85}Rb is calculated by [35, 49]

$$k_B T_{\mathrm{D}} = \frac{\hbar\Gamma}{2} \tag{2.10}$$

$$\begin{aligned} T_{\mathrm{D}} &= \frac{\hbar\Gamma}{2k_B} \\ &= \frac{1.054 \times 10^{-34}\ [\mathrm{Js}] \times 1/26\ [\mathrm{ns}]}{2 \times 1.381 \times 10^{-23}\ [\mathrm{JK}^{-1}]} \\ &\simeq 150\ \mu\mathrm{K} \end{aligned} \tag{2.11}$$

Figure 2.7 shows a temperature scale of cooling techniques and their limits [35, 49]. From the figure, it can be seen that laser cooling itself is able to go beyond the Doppler limit by a further two orders of magnitude to reach a point called the *Recoil limit*. The temperature at this point is associated with individual photon momenta. To reach

[5]The Doppler temperature limit is derived and described in more detail in section 3.3.

colder temperatures – towards the Bose-Einstein Condensate (BEC) regime – requires evaporative or radio-frequency (RF) cooling techniques, which eject the hotter atoms from the trap[6] leaving the cooler ones behind.

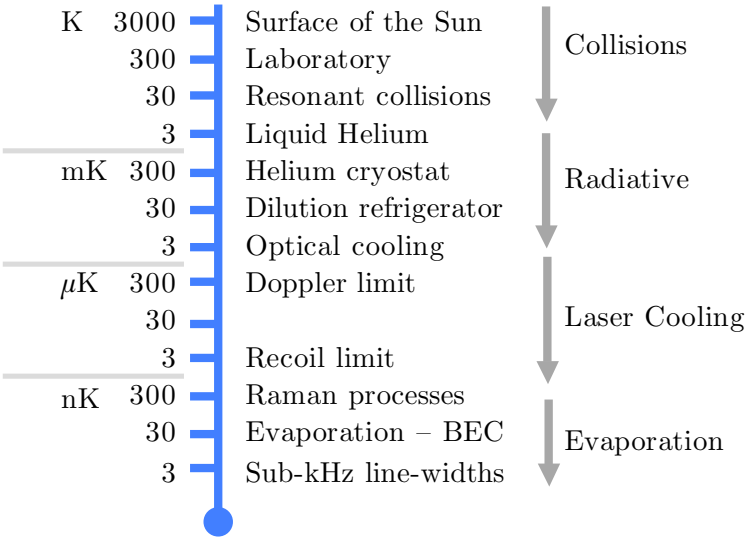

FIGURE 2.7: A temperature scale of cooling techniques and their limits. Laser cooling can reach micro-Kelvin temperatures but to go further requires evaporative process that involve discarding a large fraction of the atoms.

MOTs can achieve temperatures of several micro-Kelvin, close to the recoil limit. A description of how temperatures exceeding the Doppler limit and approaching the recoil limit can be reached (using the technique of polarisation gradient cooling) is given in section 3.4. Evaporative cooling and RF cooling was not used with the MOT system and is therefore not discussed in this thesis.

2.5 Position Dependent Cooling: the Magneto-Optical Trap

As mentioned above, the velocity dependent force from Doppler cooling must also be accompanied by a position dependent force to form a trap for neutral atoms. This is typically achieved by the addition of a temporally static but spatially non-uniform magnetic field so that the field varies in space and is zero at the trap centre, where the field *gradient* is at a maximum. The combination of optical molasses with a spatially dependent magnetic field is commonly known as the Magneto-Optical Trap (MOT). MOTs are now well developed as a standard tool for routinely producing clouds of cooled and trapped atoms that can be used for further experiments.

[6]Evaporative cooling chops the high energy tail of the Boltzmann distribution and allows the remaining atoms to re-thermalise at a lower average temperature.

The presence of an external magnetic field causes Zeeman splitting of the energy levels and lifts the degeneracy of the fine-structure sub-states, shifting them in energy depending on the strength of the field and the magnetic sub-level number. This can be seen in figure 2.8, where ω_L is the frequency of the laser beam and is red-detuned by an amount, δ. From the selection rules, a circularly polarised, $\sigma^{\pm}$ beam causes transitions from the $m_{Je} = 0$ to the $m_{Je} = \pm 1$ state only. The magnetic field B has the form $B = B_0 z$ ie. +ve for $z > 0$ and $-$ve for $z < 0$. The $m_{Je} = +1$ level increases in energy with increasing **B**. For an atom at position z', the magnetic field causes the $m_{Je} = -1$ sub-level to be closer to the laser frequency than the $m_{Je} = +1$ level and so the atom scatters preferentially from the σ^- beam as it is closer to resonance. The recoil from absorption pushes the atom towards the centre of the trap. The opposite is true if the atom were at position, $-z'$, here the magnetic field Zeeman shifts the energy levels in the opposite sense (because the field has switched direction) and now the atom preferentially scatters from the σ^+ beam instead, again pushing it towards the centre of the trap [35]. The atom will scatter from the σ^+ or σ^- beam depending on its position relative to the trap centre, hence a force whose direction is dependent upon the position.

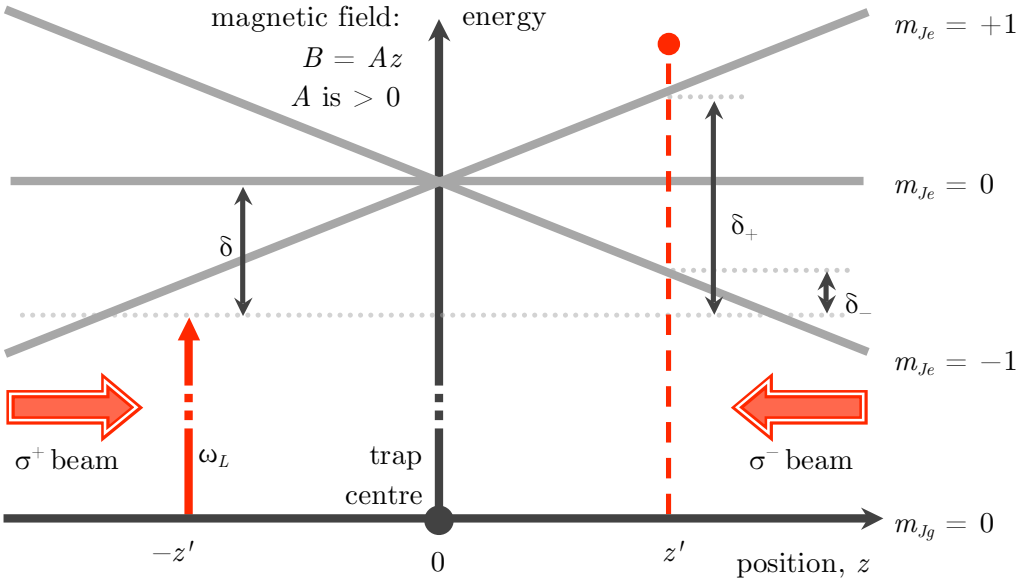

FIGURE 2.8: A one-dimensional MOT where the dotted line is the laser frequency, ω_L as seen by an atom at rest. Since the magnetic field causes position dependent Zeeman shifts, atoms at $z = z'$ are closer to resonance with the σ^- beam than the σ^+ beam and are therefore driven towards the centre of the trap.

Detailed calculations of the Zeeman shift in weak, medium and strong magnetic field regimes are determined in the next chapter.

Sodium was the first element demonstrated to be cooled and trapped with a MOT [50].

Though in the early days, trap lifetimes were fractions of a second[7] it was enough to perform temperature measurements to prove that indeed the atom cloud observed was cooled and confined.

2.6 Rabi Oscillations and Pi-Pulses

The solution to the time dependent Schrödinger equation of a two level atom in a resonant laser field gives the surprising result that the atom oscillates between the ground and excited states sinusoidally in time [51, 52]. The frequency of oscillation is known as the *Rabi frequency*, Ω and depends upon the intensity, I of the laser field, the detuning, δ from resonance and the coupling strength of the transition. Appendix A gives a description and derivation of the Rabi frequency.

If the Rabi frequency is known, atoms can be transferred from the ground to the excited state with 100% probability by firing a laser pulse whose duration is exactly half a Rabi cycle as shown in figure 2.9. For atoms initially in the excited state, conversely, the same pulse will transfer the whole population down to the ground state. This type of pulse is called a π-pulse and has the effect of inverting the occupation of the ground or excited states.

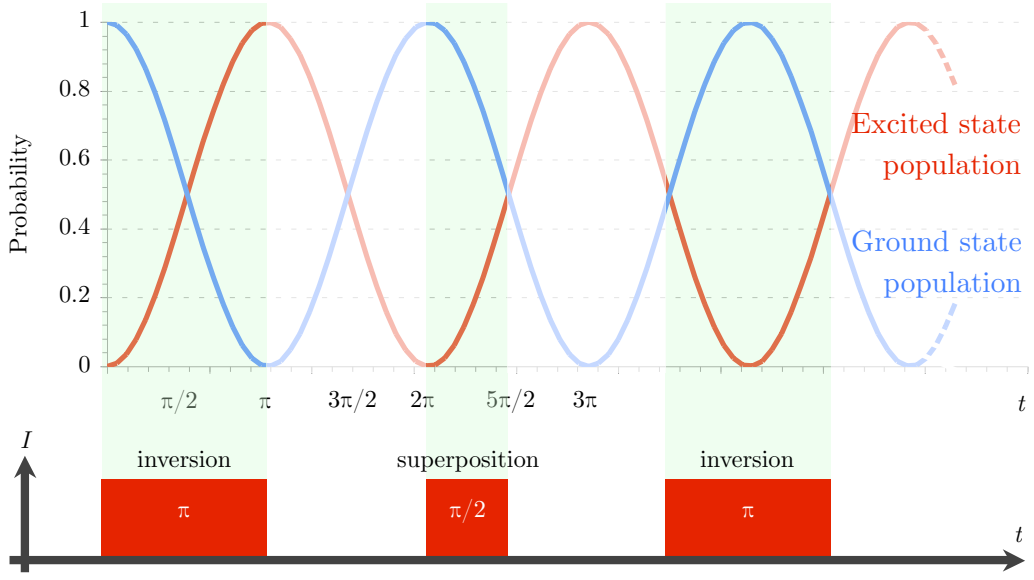

FIGURE 2.9: π- and $\pi/2$-pulses take advantage of the Rabi oscillation to invert a population or put it into a superposition of two states.

Additionally, a pulse can be fired at a population of ground state atoms whose duration lasts until only 50% of them have transferred to the excited state. This means that upon

[7] One of the reasons for this was the poor quality of the vacuum.

examining the state occupation of individual atoms at random, there is a 50% chance – for each one – of finding the atom in the excited state. Quantum mechanically, this means the whole ensemble of atoms is now in an equal superposition of the ground and excited states. This type of pulse is able to create a superposition from atoms that begin in a single state, or it can perform the reverse: collapsing an equal superposition into ground and excited states. This type of pulse is called a $\pi/2$-pulse.

Sequences of π- and $\pi/2$-pulses can be mixed together to manipulate a population of atoms. For example, a sequence of $\pi/2$-, $2 \times \pi$- and $\pi/2$-pulses applied to a group of atoms in the ground state first creates an equal superposition, which is then inverted twice by the $2 \times \pi$-pulses and the final $\pi/2$-pulse collapses the superposition. This forms the basis for an atomic interferometer scheme, which is described in more detail in section 2.9.

2.6.1 The Rabi Frequency and the Limitations of Pi-Pulses

The Rabi frequency must be known accurately in order to set the length of the π-pulse correctly. This can be difficult because it depends not only on the atomic species and the transition being used, but also on the laser amplitude and detuning from resonance. Experimentally, the technique of separated oscillatory fields – developed by Norman F. Ramsey – can be used to temporally map out and find Ω. Details of the experiment can be found in [53, 54] and the references therein.

Theoretical and experimental investigations of π-pulses have demonstrated that they can be successfully used to manipulate the electronic state population and momentum of groups of atoms [55–58]. Experimentally, however π-pulses are not generally used for inverting populations or creating superpositions of states. This is because it is difficult to 'chop' accurately a pulse to the length required for a π-pulse application. In addition, the pulse must have a top-hat intensity profile in time and across the face of the beam (as Ω is a function of intensity). The combination of these two difficulties results in a large uncertainty in the final π-pulse and provides an incentive to find another method for electronic state manipulation.

2.7 Chirped Adiabatic Passage

An alternative, more robust method – that produces similar results to the π-pulse method, but is easier to implement – uses frequency chirped pulses. The amplitude profile is not restricted to a top-hat function, but can be gently modulated. Small deviations from the ideal final pulse do not result in loss of population coherence to the

extent of imperfect π-pulses as it is the *area* under the pulse envelope and not its length that matters [59].

The chirped pulse works by a process called *Adiabatic Rapid Passage* (ARP) [60, 61] and can be visualised by referring the Bloch sphere picture described in Appendix B. Referring to figure 2.10, an ARP pulse begins far off-resonant with the transition and so the effective field vector, ε is at a high zenith angle (as this angle represents detuning) and the state vector, ψ precesses around it with a small solid angle, ϑ (a). As the pulse progresses, the frequency chirp continues towards the resonant frequency, this draws ε towards the x, y plane and the state vector follows, maintaining ϑ (b). Towards the end of the pulse, the frequency passes through resonance and becomes off-resonant again, ε continues to rotate towards the excited state, $|e\rangle$ with ψ still following, as shown in (c). At the end of the pulse, ψ has been 'deposited' at $|e\rangle$.

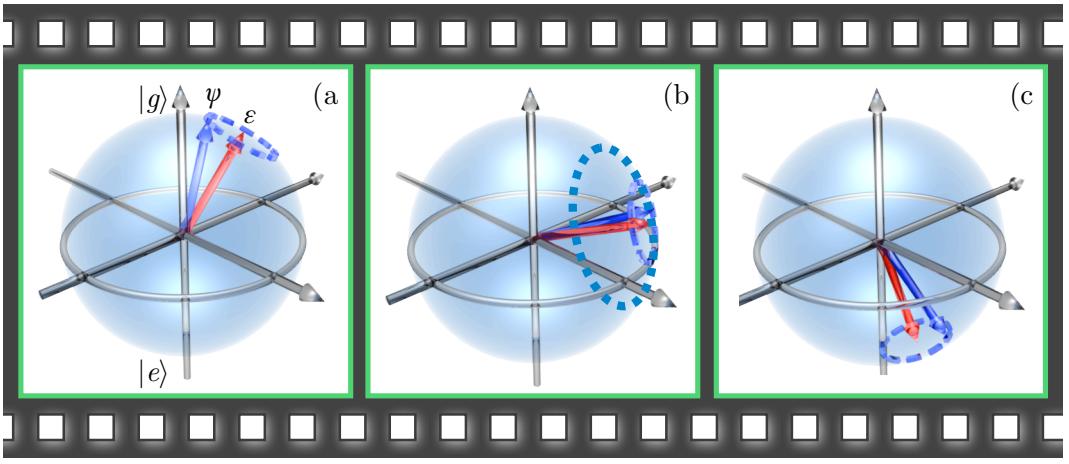

FIGURE 2.10: A 'film strip' picture of Adiabatic Rapid Passage (ARP) shown on the Bloch sphere. The state vector, ψ precesses around the effective field vector, ε maintaining a constant solid angle, ϑ as ε sweeps from $|g\rangle$ through to $|e\rangle$ and leaves ψ at $|e\rangle$.

ARP is extensively used in Nuclear Magnetic Resonance (NMR) [62, 63] and is very effective at causing complete inversion of the population in a two-level system [64, 65]. Though 'adiabatic' and 'rapid' appear together and seem to conflict, the adiabacity refers to keeping ε moving slowly enough for ψ to keep following and precessing around it with a constant ϑ and at the same time this is 'rapid' because the whole process must be completed within the lifetime of the states involved.

There have been many theoretical investigations into the optimum pulse parameters such as pulse length, amplitude profile and frequency-chirp profile [66–69]. The chirped pulse apparatus built in this project is capable of producing arbitrarily programmable frequency sweeps.

2.8 Two-photon Raman Transitions

When referring to the ground and excited states in a two level system, usually the excited state is coupled to the ground by a strong electric dipole transition with a lifetime of nanoseconds. This means the chirped pulse system for ARP cannot be used in this situation, as the time scales are too short. Fortunately the rubidium ground state is split by the hyperfine interaction into two ground states, both of which are coupled strongly to the excited state. The difference between the ground states is ~ 3.036 GHz and the coupling is via a magnetic dipole transition (a spin flip), which is intrinsically weak.

This three level system can be treated as a quasi-two-level one by causing excitation from the *lower* ground hyperfine state to the excited state and then a stimulated emission down to the *upper* ground state so that the electron is transferred between the ground states via the excited state. Experimentally, the lasers are tuned to a *virtual level*[8], which is detuned by an amount, δ from the excited state and the ground hyperfine states are coupled via this level[9]. Coupling the ground hyperfine states via a virtual level in this way is called a two-photon Λ (Lambda) or *Raman* transition, and the two laser beams required are called the Raman beams. The transition rate is enhanced by the detuning of the virtual state from the excited state[10] (known as *resonant enhancement*) and is shown in figure 2.11.

Implementing ARP with this scheme means replacing the single, chirped pulse with a pulse pair, one to 'excite' and the second to 'stimulate'. If the pulses are simultaneous, imagining the two-photon process as an excitation and subsequent stimulation is not strictly correct and is open to interpretation.

If the pulses are overlapping and counter-propagating, the absorption and subsequent stimulated emission can be visualised and the result can be seen as a photon from pulse 1 being scattered into pulse 2 via the atom. The atom acts as the medium for the photon exchange and absorbs the energy difference, which in this case means the atomic momentum change from the absorption of the first photon, followed by the recoil from stimulated emission into the second pulse. Both of these atomic momentum changes are in the same direction, since the pulses are counter-propagating.

The result is that the electron is transferred between ground hyperfine states – which are separated by microwave frequencies – by exchanging two photons at optical frequencies.

[8] The term 'virtual level' is used as defined in [70].

[9] Coupling directly to the excited state results in the absorption and uncontrolled stimulated emission picture described previously due to the short life time of the excited state.

[10] The closer the virtual level is to the real excited state, the stronger the two-photon process, but this increases the chance for atoms to be excited to the real excited state.

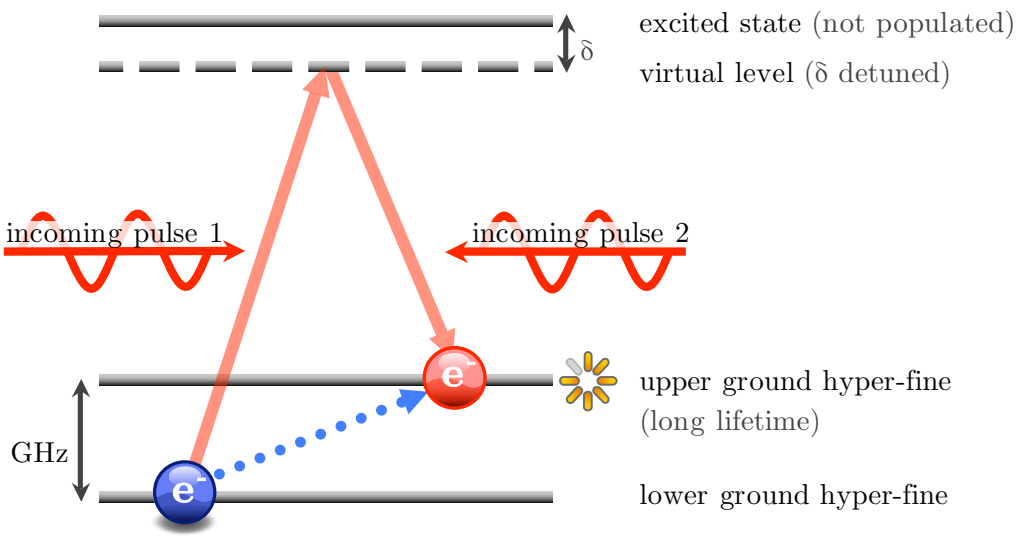

FIGURE 2.11: A two-photon Λ or Raman transition of an electron between two hyper-fine ground states with long lifetimes via a virtual excited state. The *effective* photon is shown by the dotted arrow.

Spontaneous emission has been avoided by using virtual levels and ground states with very long lifetimes. The *effective* photon coupling the ground hyperfine states has a momentum that is the sum of the two, real optical photons, but a frequency in the microwave region corresponding to their difference. This becomes the keystone of the amplified Doppler cooling scheme outlined in section 2.10.

Though spontaneous emission has been avoided by using a two-photon scheme, the energy difference between the ground hyperfine states is small enough for collisions to cause an atom to jump readily between the two. The collisions can be inter-atomic or between the atom and the container walls.

For the case of a room temperature rubidium vapour cell, the decoherence time depends on the density of the rubidium vapour (for atom-atom collisions) and the size of the cell (for collisions with the cell walls). A single collision with either the cell wall or an atom is sufficient to cause decoherence and so a *mean free time* can be calculated and is the average time that passes before an atom collides. It is calculated in detail in Appendix C and for a long cylindrical cell with a 2.5 cm diameter, the mean free time is $\simeq 40$ μs. This is also examined experimentally in section 7.1 and is discovered that atoms entering and leaving the laser beam volume contribute the most to the decrease in the coherence time.

The chirped pulsed system is able to perform pulse operations within the vapour cell coherence time scale. A system where this time is longer (and hence longer time for

more pulse operations) is the cold atom cloud inside the MOT.

2.9 Atomic Interferometry

First considered by M. Weitz and T. Hänsch and termed *frequency independent cooling* [71], the authors imagined an interferometric scheme where the absorption of the photon depends upon momentum of the atom but *not* the detuning of the laser from resonance as in Doppler cooling [29, 72, 73]. The scheme takes advantage of the quantum mechanical phase accrued by an atom depending on whether it is in the ground or excited state (as the phase evolution is state dependent).

An atomic analogue of the Mach-Zehnder interferometer can be set up with the chirped pulse system. Beginning with a group of atoms all prepared to be in the lower ground state, a $\pi/2$-pulse puts the population into an equal superposition. A π-pulse then separates the superposition further in momentum space (see figure 2.12). A second π-pulse inverts the population so that all the atoms spend equal amounts of time in both the ground and excited states, and reverses the extra separation introduced by the first. There is a final $\pi/2$-pulse that recombines the superposition so the final population distribution can be determined with a probe and fluorescence measurement.

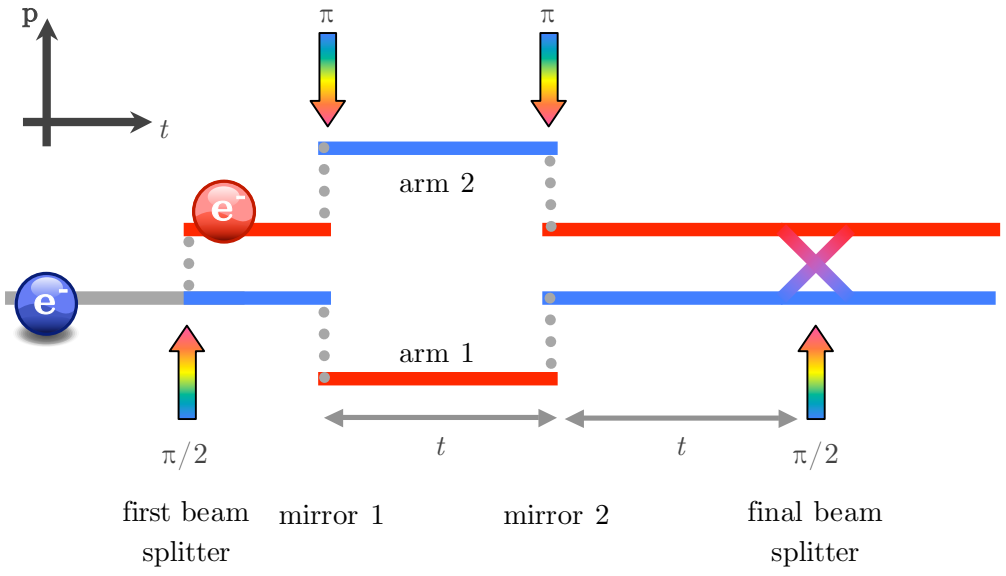

FIGURE 2.12: An atomic interferometer using a sequence of π- and $\pi/2$-pulses for the mirrors and beam-splitters respectively. Based on the scheme investigated by M. Weitz and T. Hänsch [71].

In this scheme the $\pi/2$-pulses behave as the beam splitter in the optical analogy and the π-pulses are the mirrors. Note that in figure 2.12 the axes are momentum and

time (as opposed to spatial position and time). It is a shorthand to refer to π- and $\pi/2$-pulses for the frequency chirped and amplitude modulated pulses used. The fact that all atoms spend an equal amount of time in both the ground and excited states is important and means that the phase evolution for a stationary atom along both paths of the interferometer is equal and independent of the laser frequency. In general, this can depend upon the local magnetic or electric field and the interferometer can be used to measure such properties; in the Weitz and Hänsch scheme, the only remaining energy contribution comes from the kinetic energy of the state, rendering the interferometer sensitive to the initial atomic momentum.

2.9.1 The Vapour Cell Interferometer

We have proposed an interferometry scheme with a vapour cell and counter-propagating chirped pulses. In this scheme the position of any particular rubidium atom along the length of the cell determines the time delay between pulses – due to the pulse propagation time – and so this causes a position dependent phase shift along the length of the cell.

Beginning with a state preparation pulse to place the atoms into the lower ground state, two sequential, counter-propagating $\pi/2$-pulses are fired. The first $\pi/2$ pulse puts the population into a superposition and causes the atoms to begin accruing phase, how much depends upon the atom's position along the vapour cell. Atoms that see the pulse first (i.e. at the near end of the vapour cell) will have more time to accrue phase than atoms at the far end. A second $\pi/2$ pulse from the opposite direction is now fired as soon as the first one has passed, this pulse now collapses the superposition. Atoms at the far end of the cell will have had very little time to accrue phase as the delay between the first and second pulses would ideally be zero, however atoms towards the near end of the cell will have had longer to evolve.

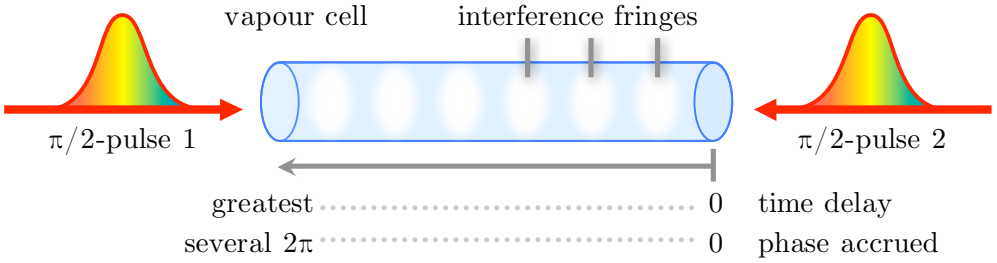

FIGURE 2.13: A vapour cell interferometer scheme using chirped pulses and ARP. The length along the vapour cell corresponds to the time an atom at that position has to phase-evolve.

Referring to the intuitive picture of the phase evolution on the Bloch sphere (described in Appendix B, it is possible that atoms towards the near end of the cell pass through several 2π cycles, which means when the superposition is collapsed, there will be atoms alternatively placed into the upper and lower ground states along the length of the vapour cell. Using a probe pulse that couples the upper ground hyperfine level to the excited levels, the fluorescence pattern should reveal dark and light fringes akin to an interference pattern, with bright areas where the phase accrued was an integer multiple of 2π, so that the second $\pi/2$ pulse finished transferring the atom from the lower ground to upper ground hyperfine state, and dark regions where the phase accrued was an odd multiple of π and so the second $\pi/2$ pulse transferred the atom back to the lower ground state again. The fringe spacing is an indication of how quickly the atomic phase evolves, with a higher number of fringes meaning a faster evolution of phase. The fringe contrast is an indication of the efficiency of the chirped pulses ($\pi/2$-pulses) to create and collapse the superposition state.

This scheme of spatially displaying the atomic coherence in an interference pattern is also a method of *spatially* mapping the Rabi frequency, in contrast to Ramsey's method of oscillatory fields – which is a *temporal* method – where each experiment plots one point of the Rabi cycle. Preliminary experimental studies are described in chapter 7.

2.10 Amplified Cooling

Whereas normal Doppler cooling relies on a closed level scheme and exploits spontaneous emission to cycle the atom, the use of an excited state with a long lifetime allows the atoms to undergo controlled stimulated emission processes before spontaneous emission occurs. This can be achieved, for example, using two-photon transitions in a quasi-two-level system, as the excited state is now a second ground state and transitions occur via a virtual level. In this scenario, an atom is driven up *and* down and this can be used to give an amplified cooling effect with a decreased reliance on spontaneous emission.

Figure 2.14 shows the momentum distribution in a cloud of atoms. An initial velocity selective pulse can be fired that excites all atoms moving in a particular direction (say left, see [74]). This splits the distribution into two: the 'excited' half and 'ground' half Next, π-pulses are fired from the right, then left then right etc... and this causes the two populations (excited and ground) to invert with each pulse. The effect on the momentum is to slide the two distributions in opposite directions over each other until there is a point of maximum overlap between the two.

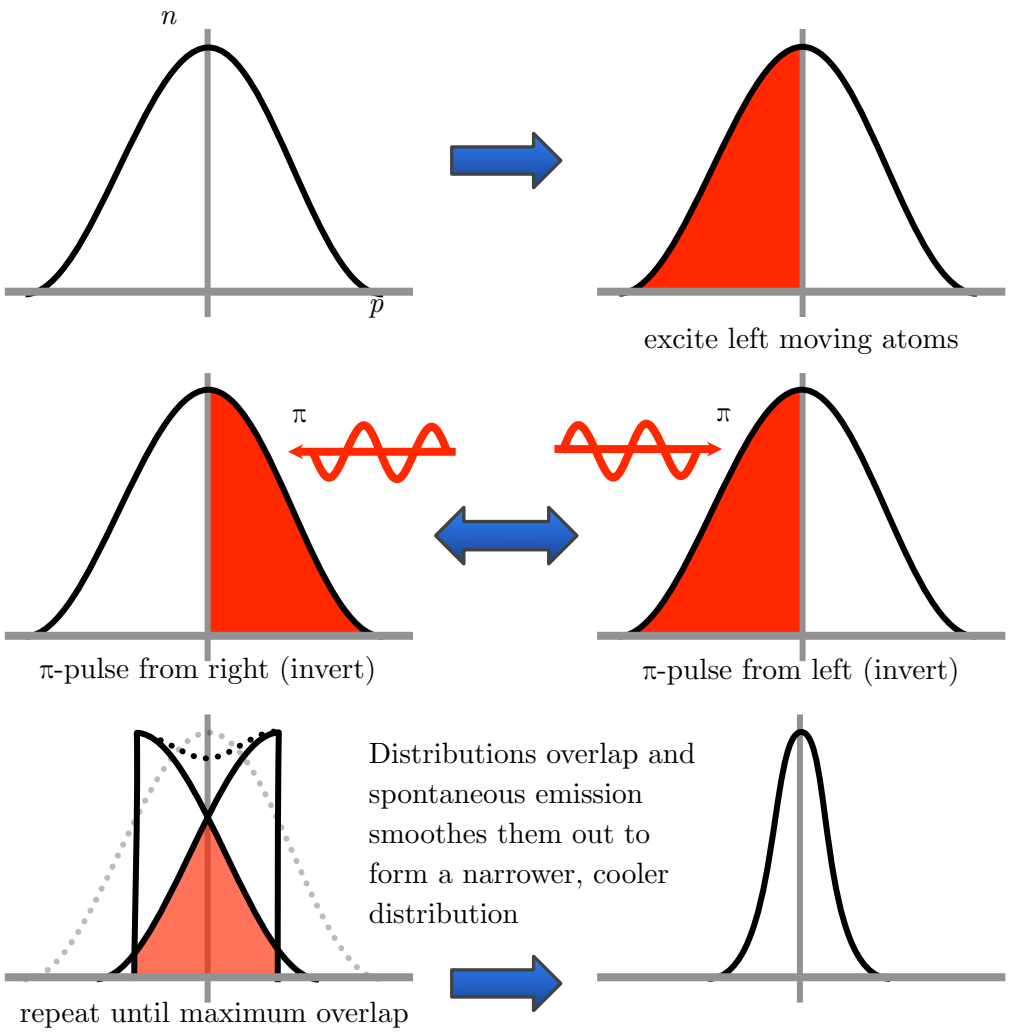

FIGURE 2.14: Amplified cooling scheme showing how beginning by exciting a specific velocity class of atoms and following through with π-pulses from alternating directions causes a 'folding' and narrowing of the momentum distribution by almost a half in just a single spontaneous emission event.

At this point, a final spontaneous emission process is allowed to occur so that both distributions are combined in the ground state and the overall result is a narrower – hence cooler – distribution shown in the final diagram [75]. In contrast to the traditional Doppler cooling method of *herding* the atoms towards a lower momentum from the tail ends, this process is more of a *folding* of the momentum distribution where the width can be almost halved per spontaneous emission event [76, 77].

Figure 2.15 shows how the momentum distribution of the cloud splits and separates as the π-pulses are fired from alternate directions.

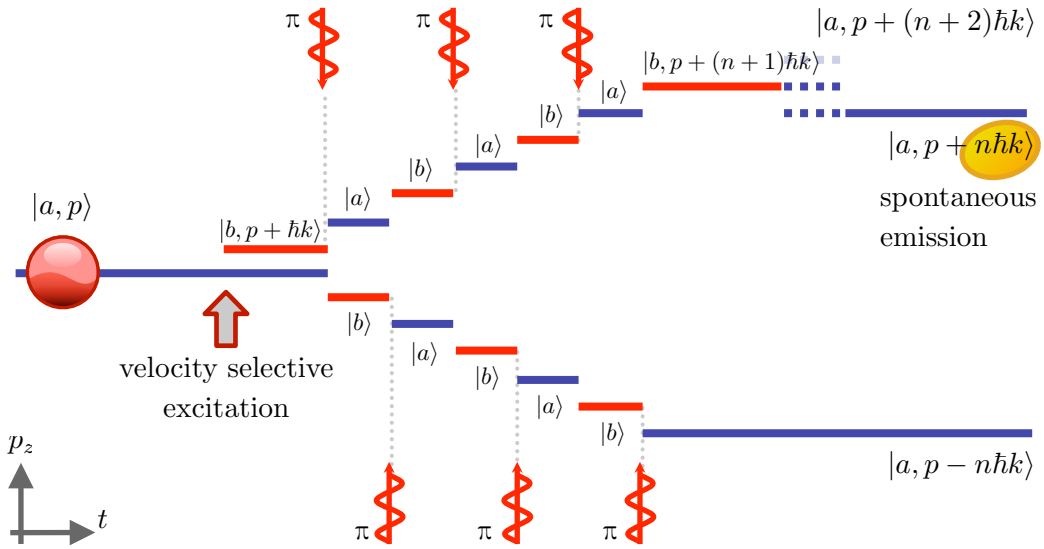

FIGURE 2.15: Amplified cooling scheme showing how beginning with a velocity selective excitation and following through with π-pulses from alternating directions causes a 'folding' of the momentum distribution by almost a half in just a single spontaneous emission event.

2.10.1 Focusing and Trapping

A final pulsed manipulation scheme – that results in a focusing and trapping effect – can be achieved by irradiating an atomic sample with simultaneous counter propagating π-pulses along an axis. The pulses overlap at a plane of coincidence as shown in figure 2.16 and this is the 'trap' centre. Atoms displaced from this position will see the near side (closer) pulse first before interacting with the far side pulse. The first pulse excites the atom and gives a momentum kick towards the centre and the second pulse will stimulate emission hence also give the atom an impulse towards the centre.

The effect is that each pulse pair leaves the atom in its original state while giving it a momentum of $2\hbar k$ in the direction of the centre. The region where the pulses overlap is less well defined and interference between the two pulses causes a deviation from the π-pulse ideal, causing spontaneous emission and atomic diffraction resulting from the standing wave. The overlap region hence can cause heating of the atomic sample without other cooling methods present [56]. This scheme may be particularly suited to narrowing the width of atomic beams.

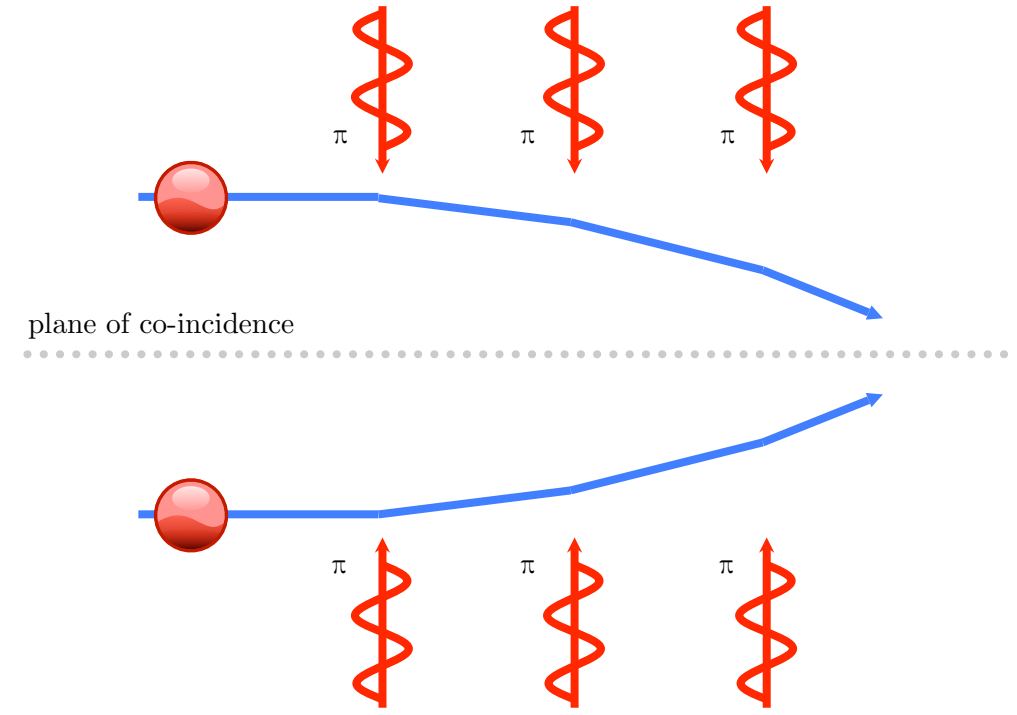

FIGURE 2.16: Scheme whereby simultaneous counter-propagating π-pulses can focus an atomic beam or cloud towards a plane of coincidence where the pulses overlap.

Chapter 3

Spectroscopic Properties of Atomic Rubidium

3.1 Rubidium Energy Levels

This thesis is concerned with atomic rubidium, which is favoured by its ready availability, convenient room temperature vapour pressure, optical transitions that are accessible to economical semiconductor lasers, and convenient spectroscopic characteristics.

The element exists as two naturally occurring isotopes, ^{85}Rb and ^{87}Rb, whose nuclear characteristics are summarised in table 3.1. Although identical in most of their material characteristics, the two isotopes differ in their nuclear spin, which is manifest spectroscopically in a difference in hyperfine splitting, degeneracy and Zeeman effect.

	85-Rb	87-Rb
Z (proton number)	37	37
N (neutron number)	48	50
Half-life	*stable*	4.88×10^{10} years
Abundance	72.165%	27.835%
Nuclear Spin (I)	5/2	3/2

TABLE 3.1: The principal differences between the two isotopes of Rubidium.

The rubidium atom has a single unpaired electron outside an optically inactive closed shell, and thus to a first approximation shows an energy level structure resembling that of atomic hydrogen. Different angular momentum states of the ground $n = 1$ level penetrate to different extents into the closed shell, however, resulting in a strong variation in their energies. The two lowest lying states – the 5S and 5P – are thus separated by ~ 1.59 eV, corresponding to a convenient optical wavelength a little below

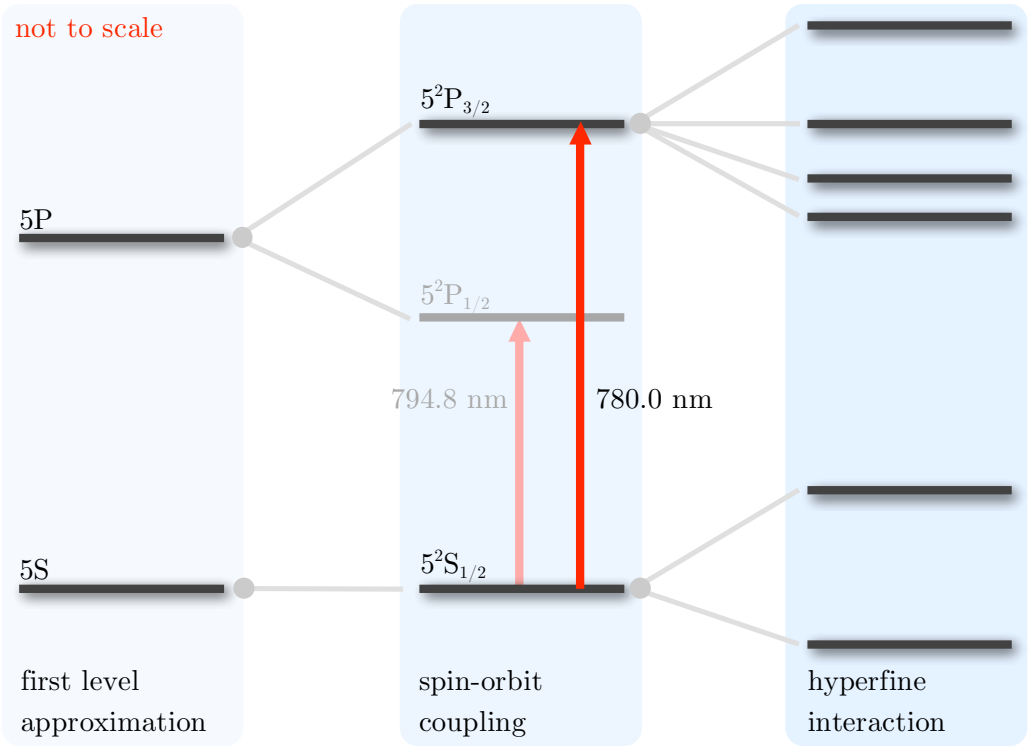

FIGURE 3.1: Energy levels of both ^{85}Rb and ^{87}Rb split from the 'two level atom' picture when the spin-orbit and hyperfine interactions are included. Only the 780 nm transition is of interest in this project.

800 nm, and for the purposes of this thesis may be regarded as an approximation to a two-level atom, shown in the first column of figure 3.1. The middle column shows the fine-structure that appears when the coupling between the orbital angular momentum of the electron, L, and its spin, S, is considered. The fine structure splits the $L = 1$ state into a doublet, described by $J = 1/2, 3/2$, where $J = L + S$ is a good quantum number in this regime and takes integer values in the range [51, 78]

$$|L - S| \leq J \leq L + S \tag{3.1}$$

The $5P_{3/2}$ excited state is used in our experiments for the MOT while the lower $5P_{1/2}$ level is over 14 nm away (at 794 nm) and beyond the tuning range of our diode lasers.

The interaction of the total angular momentum of the electron ($J = L + S$) with the total nuclear angular momentum I results in a further splitting of the levels, shown to the right in figure 3.1, producing the hyperfine structure. Here, the total angular momentum F, now given by $F = I + J$, takes values in the range [51, 78]

$$|J - I| \leq F \leq J + I \tag{3.2}$$

The different nuclear spins I thus result in different F numbers and hyperfine level splittings for the two isotopes, as shown later in figures 3.3 and 3.4. One of the main reasons for working with ^{85}Rb rather than ^{87}Rb in our experiments is that the ground hyperfine splitting is around 3 GHz rather than 6.8 GHz; the lower frequency also falls close to common commercial and communications frequencies and, for both reasons, electronic components such as amplifiers and electro-optic modulators are substantially less expensive for the lighter isotope. Figure 3.2 shows the quantum numbers for the two isotopes of rubidium for the states of interest.

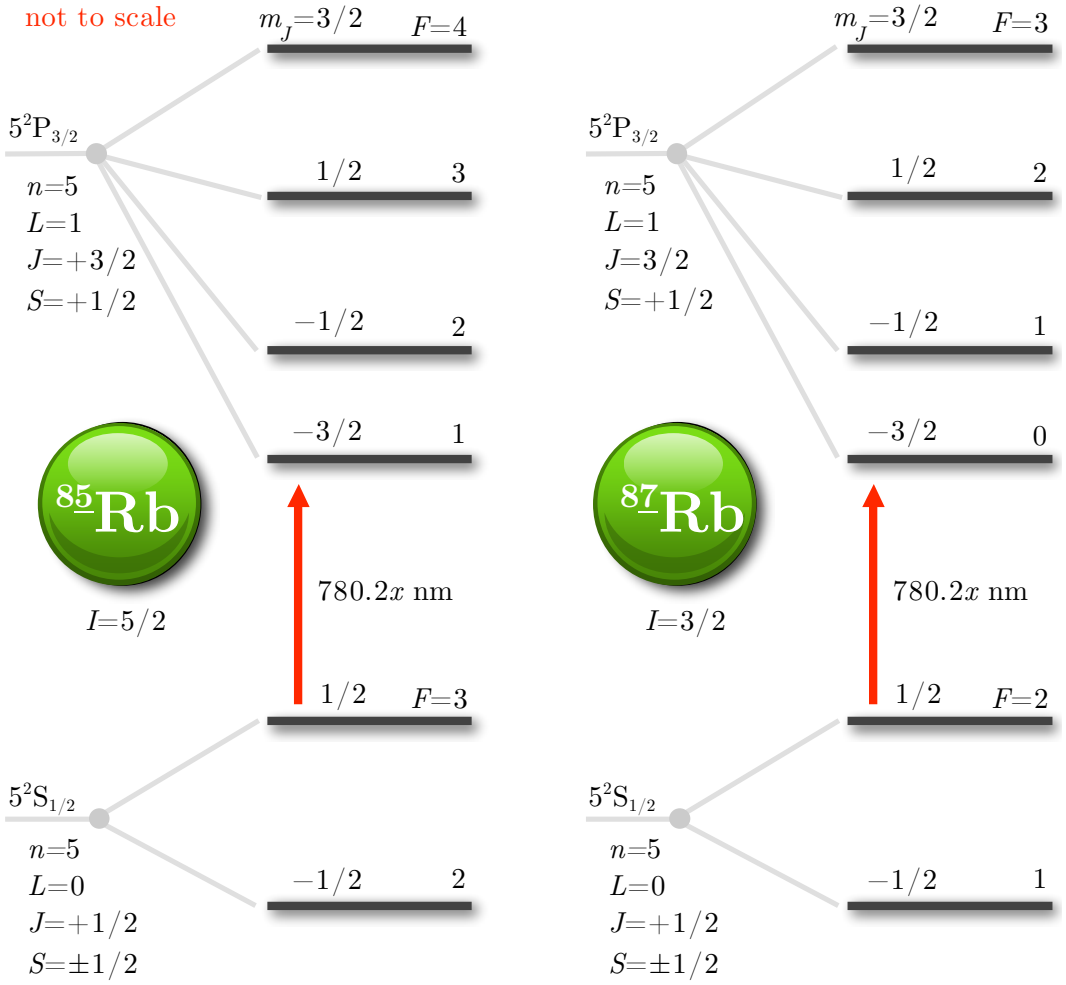

FIGURE 3.2: Differences in quantum numbers of the Rubidium hyperfine levels between ^{85}Rb and ^{87}Rb.

Measured values of the hyperfine splittings taken from experimental work by Rapol *et al* [79] are shown in figures 3.3 and 3.4. These frequencies can be calculated numerically, but to do this from first principles is involved and beyond the scope of this thesis. A

simpler method is to use a semi-empirical formula that requires two experimental values to be measured first, in order to calculate the level splittings: [35, 80]

$$\Delta E_{\text{hfs}} = \frac{1}{2} h A_{\text{hfs}} K + h B_{\text{hfs}} \frac{3/2K(K+1) - 2I(I+1)J(J+1)}{2I(2I-1)2J(J-1)} \tag{3.3}$$

where K is defined as

$$K = F(F+1) - I(I+1) - J(J+1) \tag{3.4}$$

ΔE is the shift of the hyperfine level from the fine-structure level, F, I and J are the usual quantum numbers and the constants, A_{hfs} and B_{hfs} need to be determined from experiment. This has been done by others in [9, 79, 81] and the values are quoted in table 3.2. F_g and F_e are the F numbers of the ground and excited state levels respectively. A_{hfs} is the magnetic dipole constant and B_{hfs} is the electric quadrupole moment. There is no electric quadrupole value for the ground state levels (S states, where $L = 0$ as these are spherically symmetric).

	I	F_g ($J_g = 1/2$)	A_{hfs} (MHz)	F_e ($J_e = 3/2$)	A_{hfs} (MHz)	B_{hfs} (MHz)
^{85}Rb	5/2	2, 3	1011.910	1, 2, 3, 4	25.009	25.88
^{87}Rb	3/2	1, 2	3417.341	0, 1, 2, 3	84.845	12.52

TABLE 3.2: Experimentally measured values of the A_{hfs} (magnetic dipole constant) and B_{hfs} (electric quadrupole moment) coefficients for ^{85}Rb and ^{87}Rb for both the ground (F_g) and excited (F_e) states, as taken from [79].

One can find the splitting between adjacent levels (F and $F+1$) by using equation 3.3 and taking the difference

$$\Delta E_{\text{hfs}}(F) - \Delta E_{\text{hfs}}(F-1) = h A_{\text{hfs}} F + 2 h B_{\text{hfs}} F \frac{F^2 - I(I+1) - J(J+1) + 1/2}{2I(2I-1)J(J-1)} \tag{3.5}$$

Using equations 3.3 and 3.4 or 3.5 together with the coefficients in table 3.2, the hyperfine splittings and differences can be calculated and are shown along side the experimentally measured values in figure 3.3 for ^{85}Rb and figure 3.4 for ^{87}Rb. ^{87}Rb shows a wider spread of excited state hyperfine levels of ~ 500 MHz between the top and bottom F' levels, on the scale of the Doppler broadening at room temperature, compared with a difference of only ~ 200 MHz for ^{85}Rb. The larger ground state splitting of ^{87}Rb means that the ^{85}Rb $F = 2, 3 \rightarrow F'$ transitions lie between the ^{87}Rb $F = 2, 1 \rightarrow F'$ profiles, as will be shown experimentally in the next chapter.

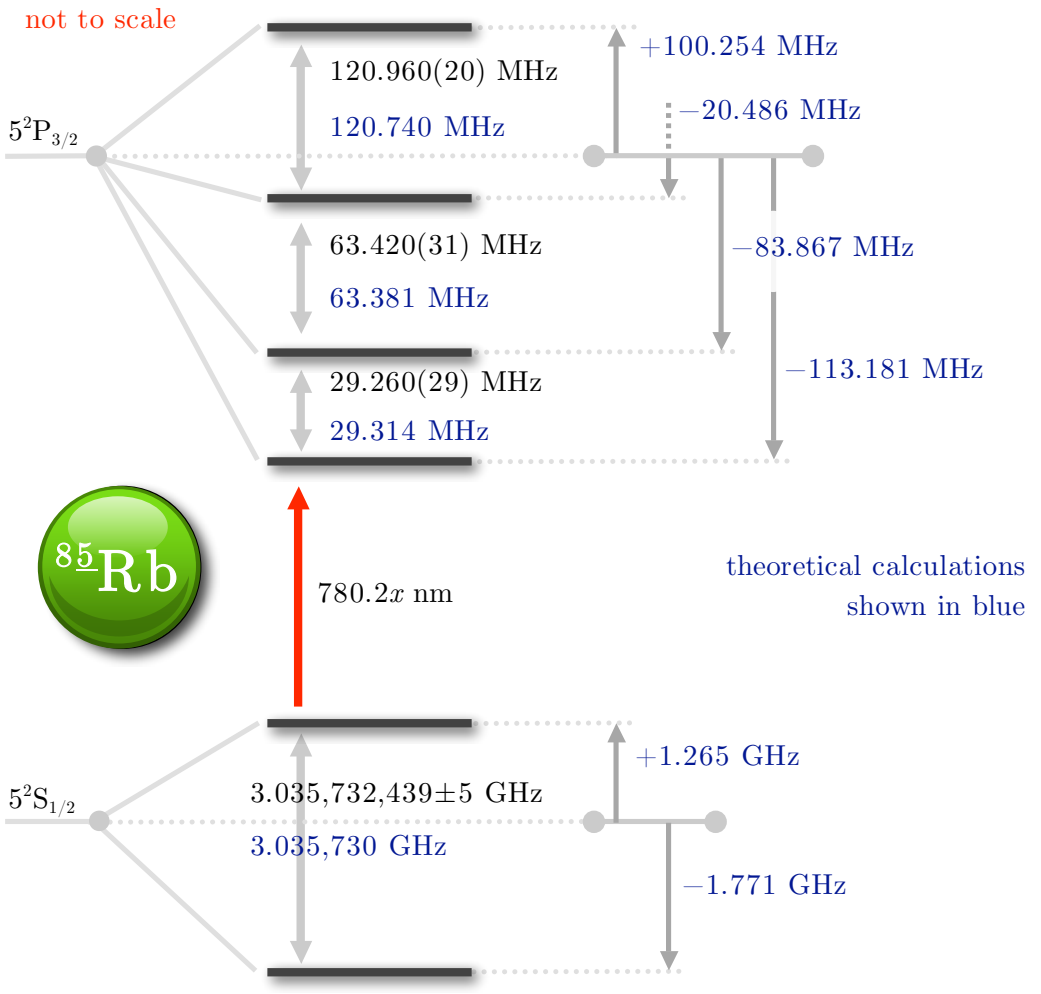

FIGURE 3.3: The hyperfine level splittings (experimentally measured in and taken from [79]) for ^{85}Rb from which the A_{hfs} and B_{hfs} values can be determined to calculate the hyperfine level shift from the fine-structure model. The numbers in brackets denote the standard deviation.

3.1.1 Zeeman Effect in an External Magnetic Field

With the addition of an externally applied magnetic field, each of the hyperfine levels is split again, a level with total angular momentum F being split into $2F + 1$ individual components. The energy splitting of these levels depends on the strength of the applied magnetic field and can result in an increase or decrease of energy. The Hamiltonian used to describe the interaction of the atom and the magnetic field is [35, 80]

$$H_B = \frac{\mu_B}{\hbar}(g_S\mathbf{S} + g_L\mathbf{L} + g_I\mathbf{I}) \cdot \mathbf{B} \tag{3.6}$$

where μ_B is the Bohr magneton ($e\hbar/2m_e = 9.274\ 009\ 49(80) \times 10^{-24}$ JT^{-1}) [1]. The

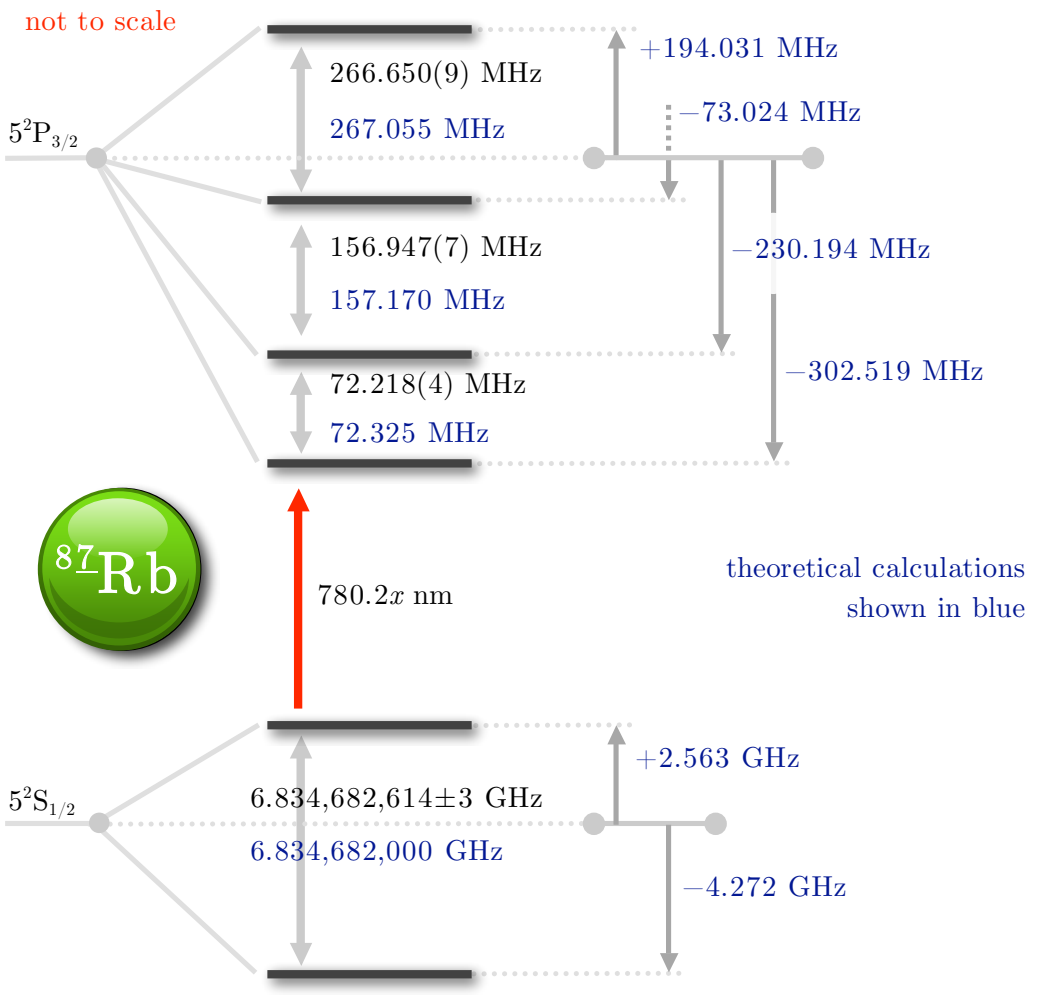

FIGURE 3.4: The hyperfine level splittings (experimentally measured in and taken from [79]) for ^{87}Rb from which the A_{hfs} and B_{hfs} values can be determined to calculate the hyperfine level shift from the fine-structure model. The numbers in brackets denote the standard deviation.

g-factors g_S, g_L and g_I describe the extent to which the spin, orbital angular momentum and nuclear angular momentum respectively interact with the external field.

The electron spin g-factor g_S, defined by $\mu_S = -g_S(\mu_B/\hbar)S$ (where μ_S is the spin magnetic moment of the electron, S the spin, and μ_B the Bohr magneton introduced above), can be calculated using quantum electrodynamics (QED) to be 2.002 319 304 3718(75) – slightly greater than the value of 2 obtained using Dirac's relativistic electron theory, itself twice the value of unity suggested by a non-relativistic semiclassical approach [52, 82]. The next g-factor in the Hamiltonian is g_L, the electron orbital angular momentum g-factor. This is approximately equal to one, but to account for the finite nuclear

mass is often quoted as [78, 80]

$$g_L = 1 - \frac{m_e}{m_{nuc}} \tag{3.7}$$

where m_e and m_{nuc} are the masses of the electron and nucleus respectively, giving $g_L = 0.999\ 993\ 598$ for ^{85}Rb. g_L can also be defined in a similar manner to g_S by [80]

$$\mu_L = -g_L \left(\frac{\mu_B}{\hbar}\right) L \tag{3.8}$$

Finally, there is g_I, which incorporates all the effects of the nucleus and hence is very difficult to calculate with any precision. In this case, the g_I constant is different for different nuclei and so experimental values are used: [35, 79, 81]

$$\text{Rb-85} \quad g_I = -0.000\ 293\ 640\ 0(2) \tag{3.9}$$

$$\text{Rb-87} \quad g_I = -0.000\ 995\ 141\ 4(1) \tag{3.10}$$

The Weak Field Regime

When calculating the effect of an external magnetic field there are three different regimes to consider. The first is the weak field or *anomalous Zeeman* case and has separate limits depending on the atomic energy level model being used (from figure 3.1). When considering only the fine structure, the weak field case applies as long as the spin-orbit interaction dominates over the effect of the external magnetic field and L and S cannot be considered independently. It can be used for fields of several hundred Gauss before a different approach is required, though this depends on the strength of the LS coupling. When considering the hyperfine model, the weak field regime applies only to the point before the external magnetic field begins to dominate over the interaction of the nuclear angular momentum, I with the total angular momentum of the electron, J. In this case, the weak field limit is much lower and for rubidium, is only a few tens of Gauss.

In the vector model picture of J, L and S, the total angular momentum vector, J precesses around the **B** field as shown in figure 3.5 [51]. This means J is well defined and so the Hamiltonian for the external magnetic field becomes [35, 80]

$$H_B = \frac{\mu_B}{\hbar} \left(g_J J_z + g_I I_z\right) B_z \tag{3.11}$$

where $J = L + S$. Unfortunately, $g_J \neq g_L + g_S$; g_J is known as the fine-structure *Landé g-factor* and confusingly can be given the symbol, g_L. The notation in this thesis is that g_L remains the g-factor for the orbital angular momentum and g_J is the fine-structure

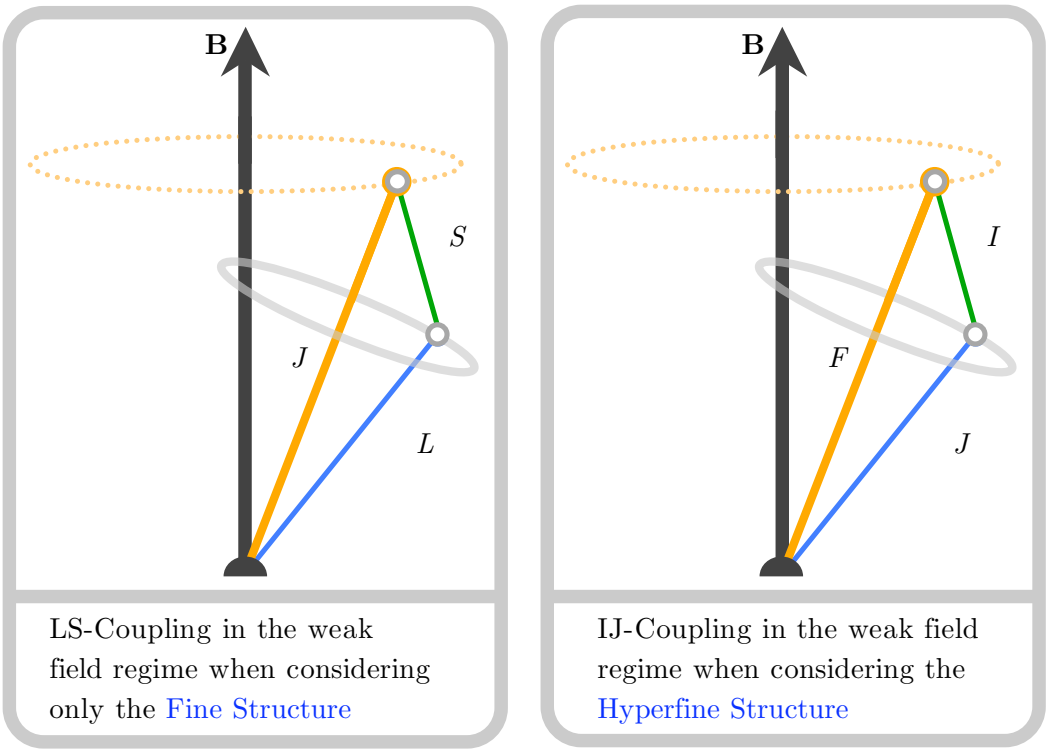

FIGURE 3.5: Vector coupling picture in a weak external magnetic field when considering the fine structure (left) or hyperfine interaction (right).

Landé g-factor. The fine-structure Landé g-factor depends on the particular energy level and is calculated by [51, 80]

$$g_J = g_L \frac{J(J+1) - S(S+1) + L(L+1)}{2J(J+1)} + g_S \frac{J(J+1) + S(S+1) - L(L+1)}{2J(J+1)} \tag{3.12}$$

Using the approximations, $g_S \simeq 2$ and $g_L \simeq 1$, equation 3.12 can be reduced to

$$g_J \simeq 1 + \frac{J(J+1) + S(S+1) - L(L+1)}{2J(J+1)} \tag{3.13}$$

Note that these equations (3.12 and 3.13) do not include multi-electron corrections or QED effects and can be used for rubidium because it is a Hydrogen-like element, having only one electron in the outer shell and the rest of the electrons shielding all but one unit of positive nuclear charge. The effects of the extra electrons and imperfections in the screening of the nucleus can be described by an experimentally determined 'quantum defect', δ_q. Table 3.3 shows the values of g_J calculated using equation 3.12 for the $5S_{1/2}$, $5P_{1/2}$ and $5P_{3/2}$ levels.

		L	S	J	Calculated g_J
^{85}Rb	$5S_{1/2}$	0	$\pm 1/2$	$\pm 1/2$	2.002 319 304
	$5P_{1/2}$	1	$-1/2$	$1/2$	-0.002 331 814
	$5P_{3/2}$	1	$+1/2$	$3/2$	1.334 102 265
^{87}Rb	$5S_{1/2}$	0	$\pm 1/2$	$\pm 1/2$	2.002 319 304
	$5P_{1/2}$	1	$-1/2$	$1/2$	-0.002 332 211
	$5P_{3/2}$	1	$+1/2$	$3/2$	1.334 102 167

TABLE 3.3: Calculated fine-structure Landé g factors (g_J) for ^{85}Rb and ^{87}Rb. Although L, S and J are the same for both isotopes, g_J is slightly different for the equivalent levels because of the different isotope masses.

The interaction Hamiltonian in equation 3.11 can be simplified by incorporating the J and I components to produce [80, 82]

$$H_B = \mu_B g_F F_z B_z \tag{3.14}$$

As previously, although $F = J + I$ but $g_F \neq g_J + g_I$, it can be calculated by

$$g_F = g_J \frac{F(F+1) - I(I+1) + J(J+1)}{2F(F+1)} + g_I \frac{F(F+1) + I(I+1) - J(J+1)}{2F(F+1)} \tag{3.15}$$

g_I is very small ($\sim 1 \times 10^{-3}$) so the second term can be neglected giving

$$g_F = g_J \frac{F(F+1) - I(I+1) + J(J+1)}{2F(F+1)} \tag{3.16}$$

For weak fields where the IJ-coupling (hyperfine interaction) is greater than the effect of the external field, the levels split and shift according to [35, 80]

$$\Delta E_{(F,m_F)} = \mu_B g_F m_F B \tag{3.17}$$

where m_F denotes the Zeeman level and takes integer values between $-F$ and $+F$. The total energy shift from the fine-structure is (to first order)

$$\Delta E_{(F,m_F)} = 1/2 A_{\text{hfs}} K + \mu_B g_F m_F B \tag{3.18}$$

where the coefficient A_{hfs} can be obtained from table 3.2 and K is defined in equation 3.4. The m_F levels shift in opposite directions depending on whether F is even or odd. The shift is shown as a function of magnetic field for the $5S_{1/2}$ ground state and $5P_{3/2}$ state for ^{85}Rb in figures 3.6 and 3.7. Zeeman sub-states from one F level begin to cross those of another above ~ 20 G.

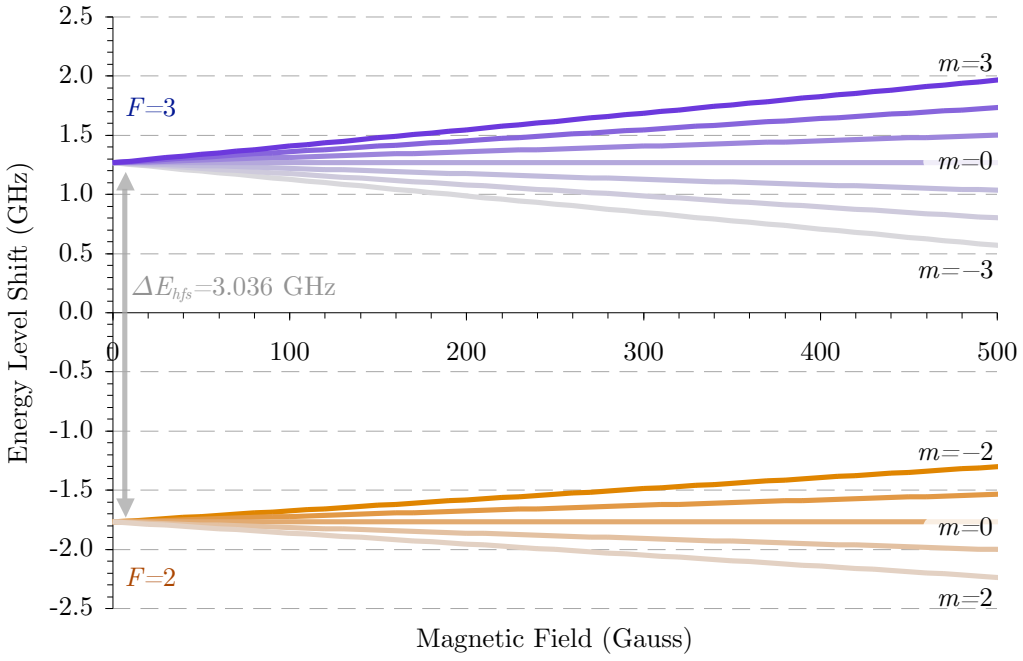

FIGURE 3.6: Zeeman level divergence in a weak magnetic field (anomalous Zeeman) case for the $5S_{1/2}$ ground states of ^{85}Rb.

The Strong Field Regime

The strong field regime – when considering only the fine structure only – occurs when the external magnetic field becomes dominant over the spin-orbit interaction and L and S precess around it independently as shown in figure 3.8, so that J is no longer defined. This is called the *Paschen-Back* effect. When considering the hyperfine interaction, the strong field regime occurs when the external magnetic field dominates over the interaction of the nuclear angular momentum, I with the total angular momentum of the electron, J.

The external magnetic field dominates over the hyperfine interaction and the energy level shift can be calculated by [35, 80]

$$E = A_{\text{hfs}} m_J m_I + B_{\text{hfs}} \frac{3\left(m_J m_I\right)^2 + 3/2 m_J m_I - I(I+1)J(J+1)}{2J(2J-1)I(2I-1)} + \mu_B \left(g_J m_J + g_I m_I\right) B \tag{3.19}$$

This is plotted for the $5S_{1/2}$ ground states of ^{85}Rb in figure 3.9.

The weak and the strong field energy levels can be linked together by following the rule that levels with the same $m = m_F = m_I + m_J$ never cross. This gives a rough schematic of what occurs between the two regimes, a more accurate treatment is described after the following section.

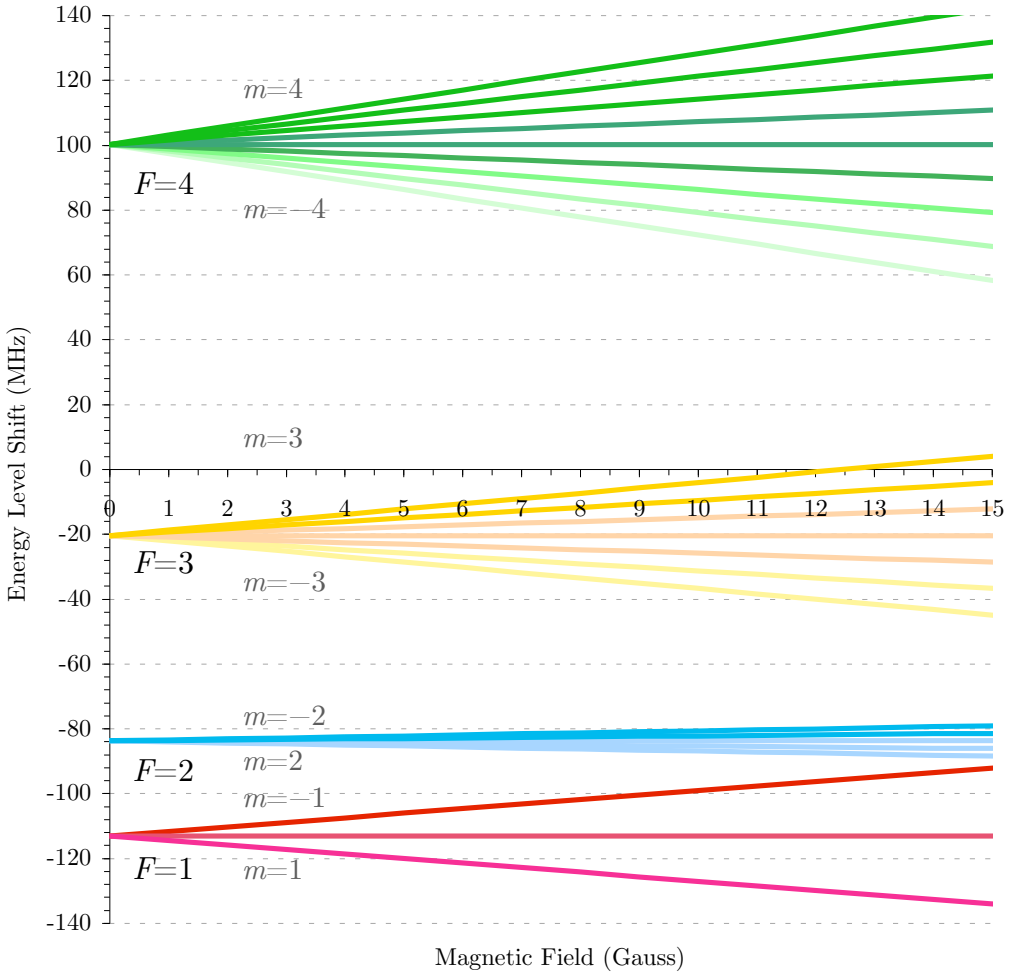

FIGURE 3.7: Zeeman level divergence in a weak magnetic field (anomalous Zeeman) regime for the $5P_{3/2}$ excited hyperfine states of ^{85}Rb.

Quadratic Zeeman Effect

At very high magnetic fields – typically $>\sim 100$ T – second order terms in the magnetic interaction Hamiltonian result in a quadratic shift of the Zeeman levels with magnetic field. This quadratic Zeeman effect is ignored in this thesis.

The Breit-Rabi Equation

There is a large region between the anomalous Zeeman shift (weak field case) and the Paschen-Back regime that needs to be studied. This is more difficult than the weak and strong field treatments, however for special cases where $L = 0$ (S states), it is possible

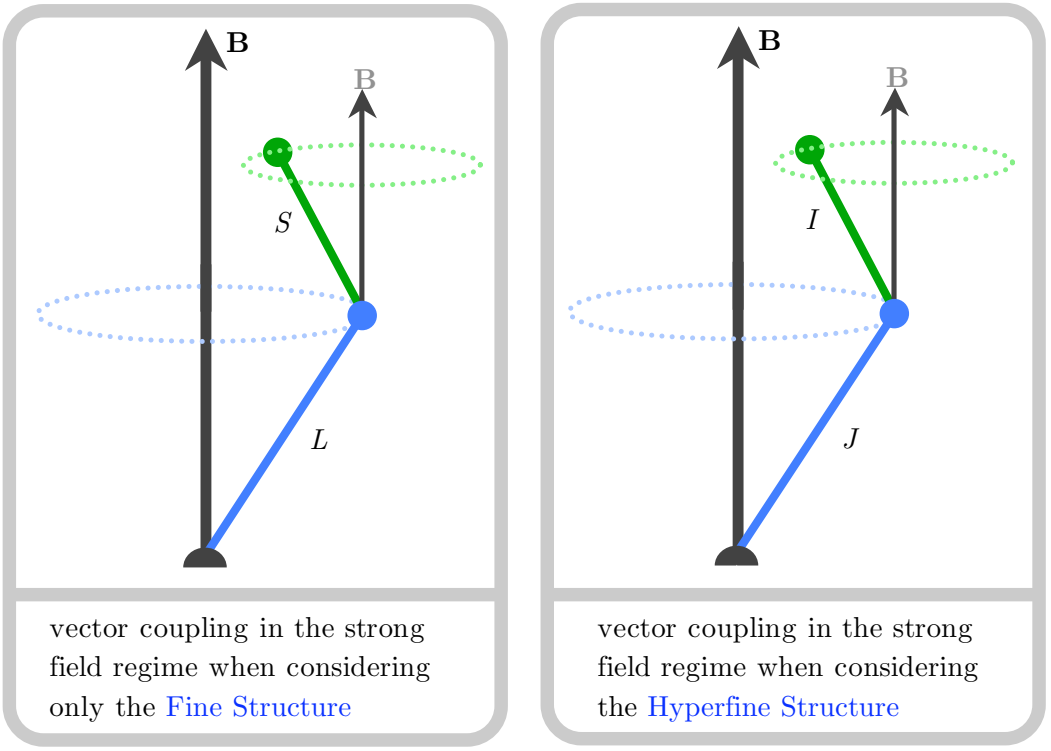

FIGURE 3.8: Vector coupling picture in a strong external magnetic field when considering the fine structure (left) or hyperfine interaction (right).

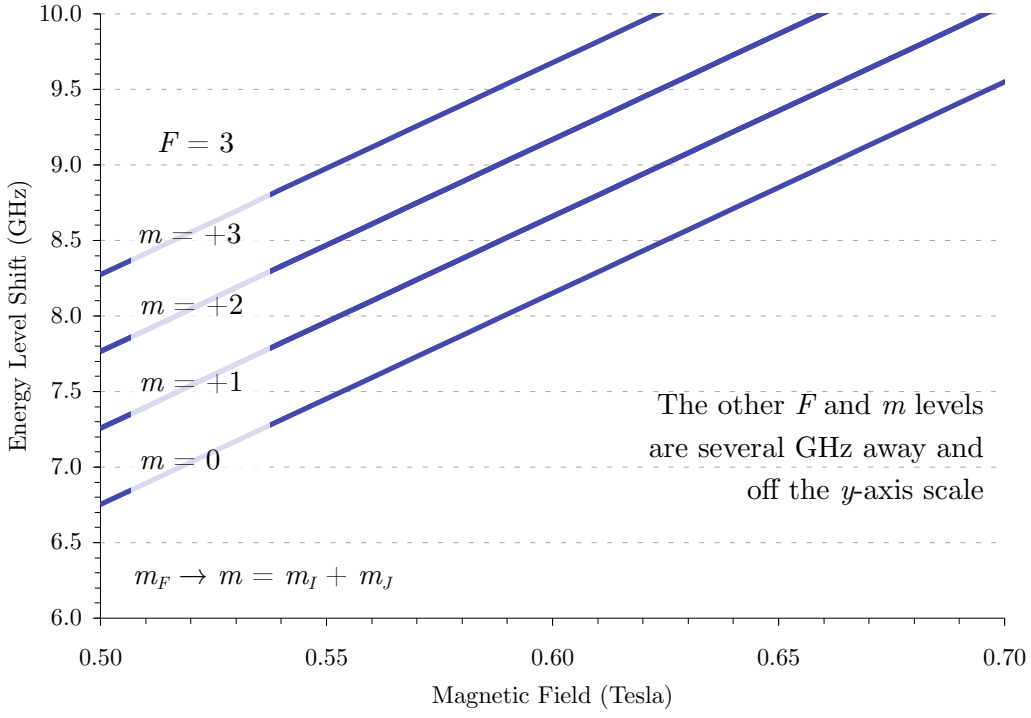

FIGURE 3.9: Zeeman shift for a small selection of the $F = 3, m_F$ levels of the $5S_{1/2}$ ground states of ^{85}Rb in the strong field (Paschen-Back regime).

to use the Breit-Rabi equation to find the energy level shift [80, 83]

$$E = -\frac{\Delta E_{\text{hfs}}}{2(2I+1)} + g_I \mu_B m_F B \pm \frac{\Delta E_{\text{hfs}}}{2}\left(1 + \frac{4mx}{2I+1} + x^2\right)^{1/2} \tag{3.20}$$

where

$$\Delta E_{\text{hfs}} = A_{\text{hfs}}(I + 1/2) \tag{3.21}$$

A_{hfs} is the quadrupole magnetic moment shown in table 3.2, m_F denotes the Zeeman level, and x is

$$x = \frac{(g_J - g_I)\mu_B B}{\Delta E_{\text{hfs}}} \tag{3.22}$$

The positive sign in equation 3.20 is taken for the higher number F level and the negative for the lower. Figure 3.10 plots the Breit-Rabi equation for the ground hyperfine states of ^{85}Rb. For weak fields, the levels are grouped together by their F number in the anomalous Zeeman regime, but at strong field (Paschen-Back regime) they become grouped by their m_J number ($\pm 1/2$). The Breit-Rabi equation can only be used for cases where $J = 1/2$ and so cannot be applied to the $5P_{3/2}$ excited state levels. To solve these requires a thorough working through the interaction Hamiltonian and calculation of all the m sub-matrices, which is beyond the scope of this thesis.

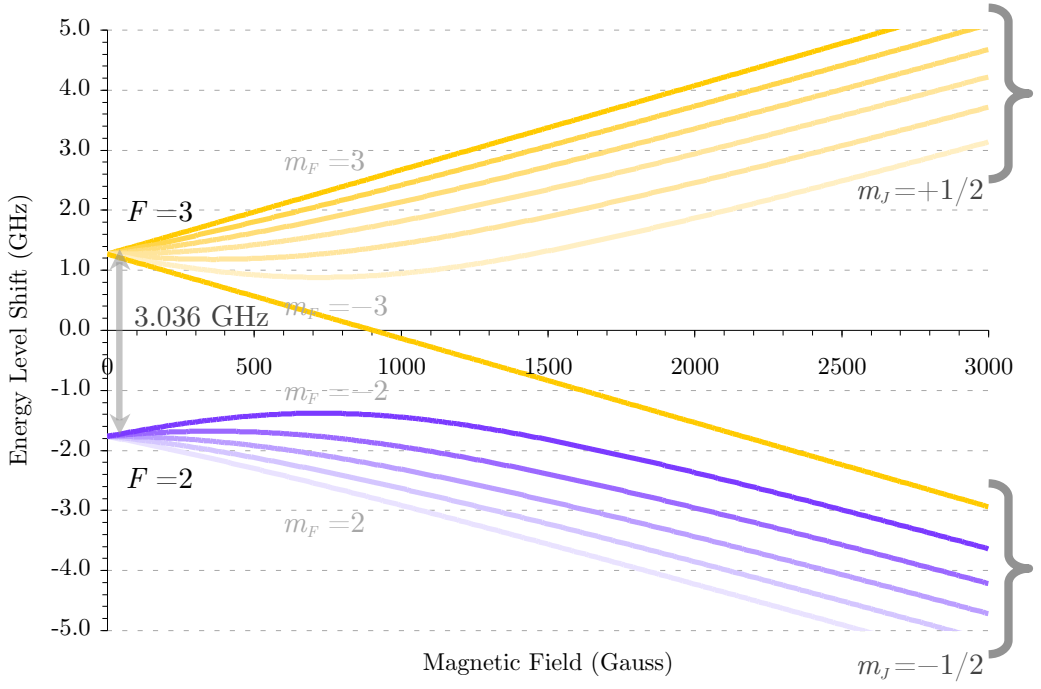

FIGURE 3.10: Energy level shifts in an external magnetic field for the $5S_{1/2}$, $F = 2$ and $F = 3$ ground hyperfine states of ^{85}Rb, according to the Breit-Rabi equation.

3.2 Doppler Cooling

The spectroscopic properties of the rubidium atom determine both the wavelengths needed by, and the performance of, the laser cooling processes upon which the magneto-optical trap depends.

3.2.1 Photon Recoil

As described in section 2.2, an atom moving in a laser field will see the frequency of light shifted according to its direction of motion. For an atom travelling at a velocity $\mathbf{u}$ in a laser beam towards the source whose frequency, ω_L is red-detuned from an atomic resonance, ω_0 (so $\omega_L < \omega_0$), the frequency seen by the atom is given by [33, 35]

$$\omega_L' = \omega_L - \mathbf{k}.\mathbf{u} \tag{3.23}$$

where k is the wavevector ($|k| = 2\pi/\lambda$). The result is that the atom sees the frequency shifted to the blue of the resonance, ω_0 as, when the atom travels towards the laser, $\mathbf{k}.\mathbf{u}$ is negative.

The average momentum gained after several absorption and emission cycles is, $\langle p \rangle = N_s \hbar k$, where N_s is the number of photons absorbed (i.e. scattered)[1]. There is no factor for the momentum of the emitted photons since the contribution from these spontaneous emission events average to zero.

The average force on the atom from photon scattering then becomes

$$\langle F_s \rangle = \hbar k \frac{\mathrm{d}}{\mathrm{d}t} N_s \tag{3.24}$$

where $\frac{\mathrm{d}}{\mathrm{d}t} N_s$ is the number of photons scattered per unit time. Taking into account the total force exerted on the atom for this process is given by [49]

$$\mathbf{F}_\pm = m\mathbf{a} = \pm \frac{\hbar k \Gamma}{2} \cdot \frac{s_0}{1 + s_0 + (2\delta/\Gamma)^2} \tag{3.25}$$

Though $\mathbf{u}$ is a vector, future equations are generally in one dimension and $\mathbf{u}$ becomes a simple scalar speed, u to give

$$F_\pm = \pm \frac{\hbar k \Gamma}{2} \cdot \frac{s_0}{1 + s_0 + (2(\delta \mp ku)/\Gamma)^2} \tag{3.26}$$

[1] Where $\langle p \rangle$ denotes the *time average* value of the momentum, p.

where δ is the detuning $(\omega_L - \omega_0)$ of the laser from resonance, Γ is the linewidth of the excited state (assuming two-levels atoms); $\Gamma = 1/\tau$, where τ is the lifetime of the excited state. Finally, s_0 is the saturation parameter at resonance and is defined by [35, 84]

$$s_0 = \frac{2|\Omega|^2}{\Gamma^2} = \frac{I}{I_S} \tag{3.27}$$

Ω is the Rabi frequency, I is the laser intensity and I_S is the saturation intensity at resonance given by $I_S = \hbar\omega/2\tau\sigma$, where σ is the cross section of absorption given by $\sigma = 3\lambda^2/2\pi$.

The δ factor in the Doppler Force equation (3.25) needs to be modified as it is currently an approximation. Taking into account the Doppler shift (equation 3.23) modifies the detuning, δ seen by the atoms to

$$\delta \rightarrow \delta - k.\mathbf{u} \tag{3.28}$$

A further modification to δ has to be applied when an external magnetic field is present. This is important because the MOT uses an inhomogeneous field (as described in section 2.5. The expression for δ becomes [80]

$$\delta - k.\mathbf{u} \rightarrow \delta_{\sigma^\pm} \mp k.\mathbf{u} \pm \mu_B g_J B(z)/\hbar \tag{3.29}$$

This is more complicated because the sign of the magnetic field factor depends on whether the laser light is σ^+ polarised or σ^- polarised (note that it is opposite to the sign of the Doppler shift term, $k.\mathbf{u}$). For the region close to the trap centre, $B(z)$ is linear and can be replaced by Az, where A is the gradient of the field [35].

The magnetic field adds a force analogous to a spring constant, κ and modifies the Doppler force by shunting it along the velocity axis depending on the strength of the field. This is described in more detail in section F.3 of Appendix F.

As a rough calculation, a maximum deceleration of an atom from the Doppler effect can be calculated to illustrate the numbers involved. For large laser intensities where $I \gg I_S$, so that $s_0 \gg 1$, equation 3.25 reduces to

$$F_{\max} = \hbar k\Gamma/2 \tag{3.30}$$

$$a_{\max} = \hbar k\Gamma/2m \tag{3.31}$$

Using common values for rubidium ($\lambda = 780$ nm, $m_{\mathrm{Rb}} = 1.4 \times 10^{-25}$ kg and $\Gamma = 1/[26\text{ ns}]$) gives a value of $a_{\max} = 1.15 \times 10^5$ ms^{-2}, which is a considerable deceleration, enabling typical thermal velocities to be eliminated on a millisecond timescale.

3.2.2 Force in Optical Molasses

From equation 3.25 the sum of the force exerted by the laser field on the atom can be calculated by taking the difference, $F_{\mathrm{OM}} = F_+ - F_-$ (for one dimension), which gives

$$F_{\mathrm{OM}} = \frac{\hbar k \Gamma s_0}{2} \left[\frac{1}{1 + s_0 + \left(\frac{2(\delta - ku)}{\Gamma}\right)^2} - \frac{1}{1 + s_0 + \left(\frac{2(\delta + ku)}{\Gamma}\right)^2} \right] \tag{3.32}$$

The result of this is plotted in figure 3.11 for typical values of rubidium.

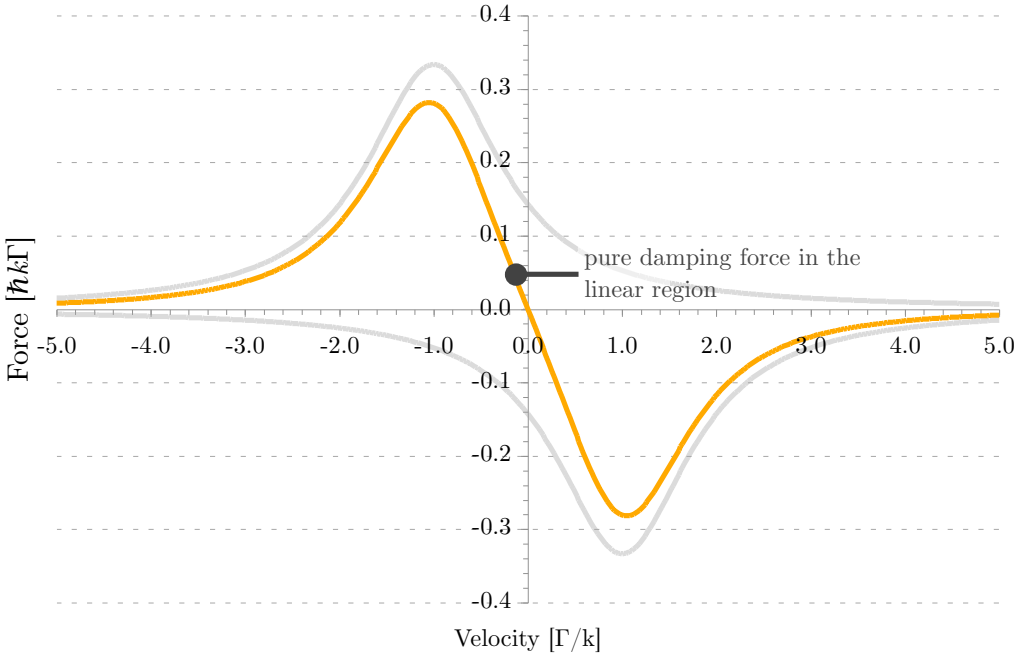

FIGURE 3.11: The velocity-dependent force for Optical Molasses (for one dimension). The lighter lines show the force from the individual beams while the orange line is the sum. For this graph, the detuning, $\delta = -\Gamma$.

Referring to figure 3.11, close to $u = 0$ the Doppler force can be approximated by a linear gradient, which demonstrates that it can be thought of as a linear, velocity dependent damping force, $F_{\mathrm{OM}} = \beta \dot{x}$. This is discussed in more detail in Appendix F, where the damping parameter, β is derived, plotted and is found to depend on the detuning, δ and the saturation parameter, s_0, the point where $\delta = -\Gamma/2$ and $s_0 = 2$ gives the maximum value of β.

The Doppler force is also a function of the detuning, δ and the 3D graph in figure 3.12 shows how its profile changes as the detuning is varied from zero upwards.

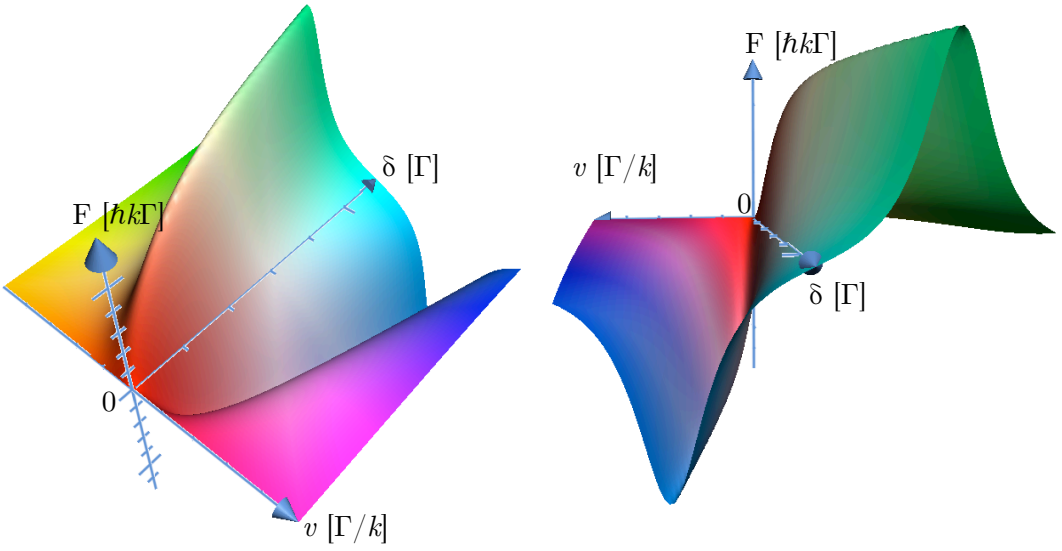

FIGURE 3.12: Two views of the same 3D graph showing how the Doppler force varies with the detuning, δ. For typical rubidium MOT operation, δ is kept roughly in the range $-0.5\Gamma \leq \delta \leq -3\Gamma$.

3.3 Doppler Temperature Limit

The Doppler temperature limit occurs when the laser cooling in optical molasses balances heating caused by spontaneous emission. As the atom undergoes many absorption and emission cycles, it drifts in momentum space (with the deviations originating from spontaneous emission). While the average momentum, $\langle p \rangle = 0$ from spontaneous emission, the square of the average momentum, $\langle p^2 \rangle \neq 0$ and this corresponds to an increase in the average kinetic energy of the atoms. The expression for $\langle p^2 \rangle$ is

$$\langle p^2 \rangle = 2\hbar^2 k^2 N_s \quad \text{for } N_s \text{ absorption and emission cycles} \tag{3.33}$$

The average kinetic energy, $\langle E_k \rangle$ is given by $\langle p^2 \rangle / 2m$, this gives the expression for the increase in energy due to heating to be [43, 48]

$$\left[\frac{\mathrm{d}E}{\mathrm{d}t}\right]_{\text{heat}} = \frac{2\hbar^2 k^2 \Gamma}{2m} \frac{s_0}{1 + s_0 + (2\delta/\Gamma)^2} \tag{3.34}$$

Competing against this is the Doppler cooling given by equation 3.25: [43, 48]

$$\left[\frac{\mathrm{d}E}{\mathrm{d}t}\right]_{\text{cool}} = Fv \tag{3.35}$$

The equilibrium point is found by setting the rate of change of energy due to heating equal to the rate of change of energy due to cooling

$$\left[\frac{\mathrm{d}E}{\mathrm{d}t}\right]_{\mathrm{heat}} = \left[\frac{\mathrm{d}E}{\mathrm{d}t}\right]_{\mathrm{cool}} \tag{3.36}$$

By substituting equations 3.34 and 3.35 into equation 3.36 and working through, the following expression is obtained:

$$mv^2 = \frac{\hbar\Gamma}{4}\frac{1+(2\delta/\Gamma)^2}{2|\delta|/\Gamma} \tag{3.37}$$

Working in one dimension, there is only one degree of freedom so the Equipartition of Energy theorem gives the internal energy for a 1-D gas to be $k_BT/2$. Setting this equal to the kinetic energy, $mv^2/2$, the expression for the Doppler temperature limit, T_{D} becomes

$$k_BT_{\mathrm{D}} = \frac{\hbar\Gamma}{4}\frac{1+(2\delta/\Gamma)^2}{2|\delta|/\Gamma} \tag{3.38}$$

So the minimum temperature reached depends on the detuning, δ. The optimum value for δ in terms of the linewidth, Γ can be found by minimising equation 3.38, resulting in the condition that $\delta = -\Gamma/2$ and hence, upon applying the Equipartition of Energy for a 1-D gas gives [35]

$$T_{\mathrm{D}} = \frac{\hbar\Gamma}{2k_B} \tag{3.39}$$

The excited state lifetime, τ ($\Gamma = 1/\tau$) is about 26 ns for rubidium and this corresponds to a minimum Doppler temperature of about 150 μK when $\delta = -\Gamma/2$. The velocity of the rubidium atoms at this temperature is ~ 20 cms^{-1}.

3.4 Beyond the Doppler Limit

When Paul Lett *et al* performed the first laser cooling experiments on Sodium [43, 46, 85], it was with great surprise that they discovered the temperature of the atoms to be far lower than the theoretical limit imposed by Doppler cooling. They measured ~ 40 μK for their cold Sodium cloud as opposed to the theoretically predicted minimum of ~ 240 μK. Though in the paper no explanation was given as to how the atoms could be so much colder than the theory predicted, it was noted that there was a significant temperature change when the linear polarisers of the Optical Molasses setup were rotated, hinting that the polarisation of the trapping beams has an important role to play.

Shortly after, Jean Dalibard and Claude Cohen-Tannoudji presented two theoretical descriptions – both involving the polarisation of the cooling beams – to explain the 'Sub-Doppler' temperatures reached by Lett's team. Termed *polarisation gradient cooling*, both theories take advantage of the way the polarisation of light causes the fine-structure sub-levels to shift in energy, which in turn causes selective absorption and spontaneous emission, resulting in an unbalanced force that has a cooling effect [86].

3.4.1 Linear ⊥ Linear Polarisation Gradient Cooling

For the first explanation, Dalibard and Cohen-Tannoudji considered a 1-D optical molasses where the polarisations of the laser beams were linear but orthogonal to each other. In this method, the atoms are optically pumped to the lower energy shifted level where, as they move in the strong polarisation gradient, they are forced to climb a potential as the sum polarisation changes. When they reach the top, they are optically pumped back into the lower energy level to begin climbing the potential once again. The atoms absorb photons of a lower energy than they spontaneously emit and so the kinetic energy of the atoms is carried away in the photon energy difference.

The scheme is described in detail in Appendix G. The polarisation gradients are derived and the energy level shifts shown to vary with them. The optical pumping process is shown to remove kinetic energy from the atoms. This sub-Doppler cooling scheme is known as *Sisyphus cooling*.

3.4.2 $\sigma^+ - \sigma^-$ Polarisation Gradient Cooling

The second theory of sub-Doppler cooling presented by Dalibard and Tannoudji uses counter-propagating, oppositely circular polarised beams and now takes into account the hyperfine levels [87]. By working through the electric field equations, one finds that unlike the linear ⊥ linear case, there is no phase difference between the x and y polarisation directions at any point along z. In this case, the sum polarisation vector, $\hat{\mathbf{e}}$ remains fixed in time but rotates in a complete cycle (2π), spatially with a period of λ, which means $\hat{\mathbf{e}}$ flips from linear vertical, to linear horizontal in a distance of only $\lambda/4$. As there are no σ^+, σ^- sum polarisations, only $\Delta m = 0$ transitions are allowed.

In this case, the Sisyphus cooling (see Appendix G) cannot apply, as there are no spatially varying light shifts from the polarisation gradient (the light shift remains constant). If a group of atoms were stationary in this field, optical pumping would tend to collect them into the $m_J = 0$ state. However, if the atoms are moving, the rotating polarisation vector, $\hat{\mathbf{e}}$ defines an axis about which the atoms rotate. In order to follow this rotation,

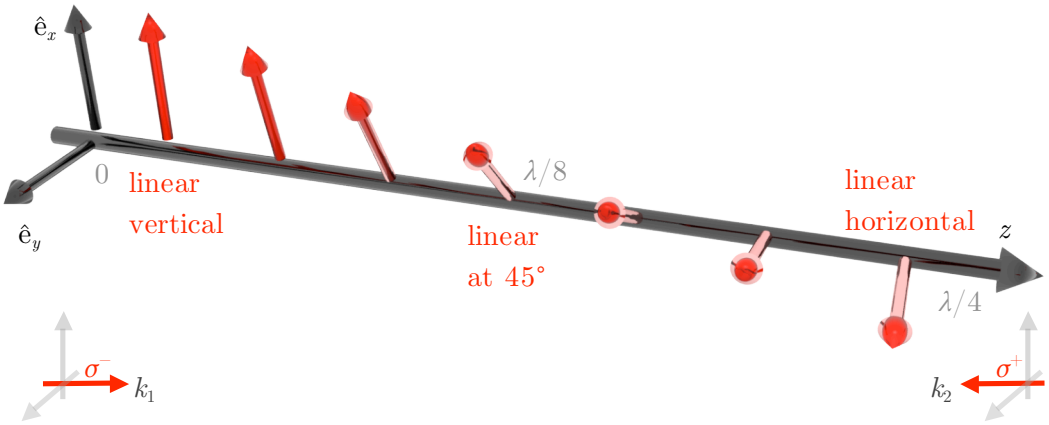

FIGURE 3.13: The sum polarisation seen by an atom in a 1-D optical molasses with oppositely circular polarised beams.

the atoms need to be optically pumped into the correct m_J states and this process is non-adiabatic and as a result, always lags behind the present direction of $\hat{\mathbf{e}}$.

It has been shown that atoms travelling towards a σ^+ laser beam source will want to absorb from it and scatter into the $|1,+1\rangle$ state more than the $|1,-1\rangle$ state. This is because the Clebsch-Gordan coefficient for remaining in the $|1,+1\rangle$ state is six times the coefficient for transferring across to the $|1,-1\rangle$ state (and hence beginning absorption from the σ^- beam). This means there is a large recoil against atoms travelling toward the σ^+ laser beam source.

Similarly, atoms travelling towards the σ^- laser beam source will see the polarisation vector, $\hat{\mathbf{e}}$ rotate in the opposite sense and so the opposite for the σ^+ case becomes true and atoms will now scatter into the $|1,-1\rangle$ state and the recoil will be in the opposite direction and again, oppose the motion of atoms travelling towards the σ^- laser beam source.

The result is a non-equal scattering force that depends upon the direction in which the atoms are travelling[2], combined with a magnetic field (for position dependent cooling). This results in the atoms being 'herded' towards the centre of the trap and cooling to a temperature approaching the recoil limit.

[2]Note that this is not the same as Doppler scattering, which relies upon the unequal frequency shifts of the opposing beams as seen by the atom, producing a non-equal scattering force that depends upon the direction the atom is travelling in.

3.4.3 The Recoil Limit

Polarisation gradient cooling (whether lin $\perp$ lin or $\sigma^+ - \sigma^-$) is able to bring the temperature of a cloud of atoms close to recoil limit, T_r, which corresponds directly to the momentum kick delivered to the atom when it spontaneously emits the last photon before it does not have enough kinetic energy to fully climb to the next potential hill in the Sisyphus scheme (see Appendix G) and is thus taken to be the temperature of an ensemble of atoms with momenta equal to a single photon recoil:

$$k_B T_r = \frac{p^2}{2m} = \frac{(\hbar k)^2}{2m}$$

and hence

$$T_r = \frac{(\hbar k)^2}{2k_B m} \tag{3.40}$$

Although this works out to be $T_r \simeq 0.1$ μK for rubidium, the temperature reached experimentally is on the order of a few micro-Kelvin ($3\ \mu K < T_r < 5\ \mu K$). The limit for Sisyphus cooling may be alternatively expressed as occurring when the de Broglie wavelength of the atom, $\lambda_{\mathrm{dB}} = h/p$, has grown to around half the wavelength of the laser light: as the atom is slowed, its momentum decreases, increasing λ_{dB} until it is large enough that the atom can no longer tell distinctly whether the light field is σ^+ or σ^- polarised, so that Sisyphus cooling no longer works.

The same argument holds for σ^+ – σ^- polarisation gradient cooling, and thus both schemes have similar temperature limits of a few T_r. rubidium atoms cooled in a MOT using a polarisation gradient cooling scheme are slowed down to speeds of a few centimetres per second.

3.5 The Earnshaw Theorem

The Earnshaw theorem is for electrostatic charges and states that it is not possible to create a stable trap (or confinement region) for a charged particle using any combination of fixed point electric charges alone. For the particle to be stable, all field lines surrounding the particle must point inwards to the equilibrium point so that if a particle at equilibrium is perturbed in any direction, it will return to its original position.

This can be seen by referring to figure 3.14 and noting that for a stable trap, field lines from the blue charges must all point inwards at the surface of the closed green sphere. This means that the divergence of the electric field integrated over the closed surface of the sphere is non-zero. Gauss's law tells us that this can only be possible if a charged

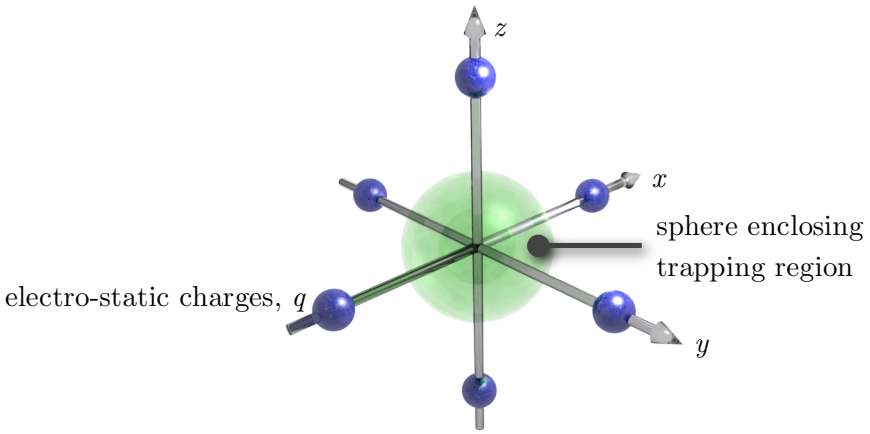

FIGURE 3.14: The Earnshaw theorem states that a stable trap cannot be made from any combination of electrostatic charges, only unstable saddle points can exist.

particle is situated at the trap centre; without this, there is no point in space for which all the field lines point inward from all directions. With no local maxima or minima in space, only unstable saddle points exist and that means there will always be a path for the particle to escape the 'trap'.

3.5.1 The Optical Earnshaw Theorem

There is an optical equivalent of the Earnshaw theorem that applies to Optical Molasses. It states that the light scattering force has zero divergence, $\nabla.\mathbf{F}_s = 0$, like Gauss's Law. To see this, Poynting's theorem for electrodynamics is required because it states that

$$\frac{\partial u}{\partial t} + \nabla.\mathbf{S} = 0 \tag{3.41}$$

Here, u is the energy density of the electromagnetic field and $\mathbf{S}$ is the Poynting vector, which represents the direction of the flow of electromagnetic energy. For Optical Molasses, u does not change in time since the laser beam intensity remains constant. This means $\nabla.\mathbf{S} = 0$, and if the light scattering force, $\mathbf{F}_s$ is proportional to the Poynting vector, it follows that $\nabla.\mathbf{F}_s = 0$ too, and this brings us back to the argument discussed about Gauss's Law.

This means Optical Molasses is inadequate for a trap, just as with static electric charges, there exists no stable equilibrium point and an atom 'caught' in the Molasses will escape it eventually. Either additional methods of confinement are required or work-arounds need to be found. For the MOT, the additional confinement comes from an inhomogeneous magnetic field, which adds a position dependent force.

Chapter 4

Lasers and Optics

Two lasers are required for the magneto-optical trap: the trapping laser, which is used to perform the Doppler cooling, and the repump laser, which is used to cycle atoms that have relaxed into a state different from the ground state of the cooling transition. The repump laser thus stimulates atoms in this state back up to the excited level where they have a chance to rejoin the cooling cycle.

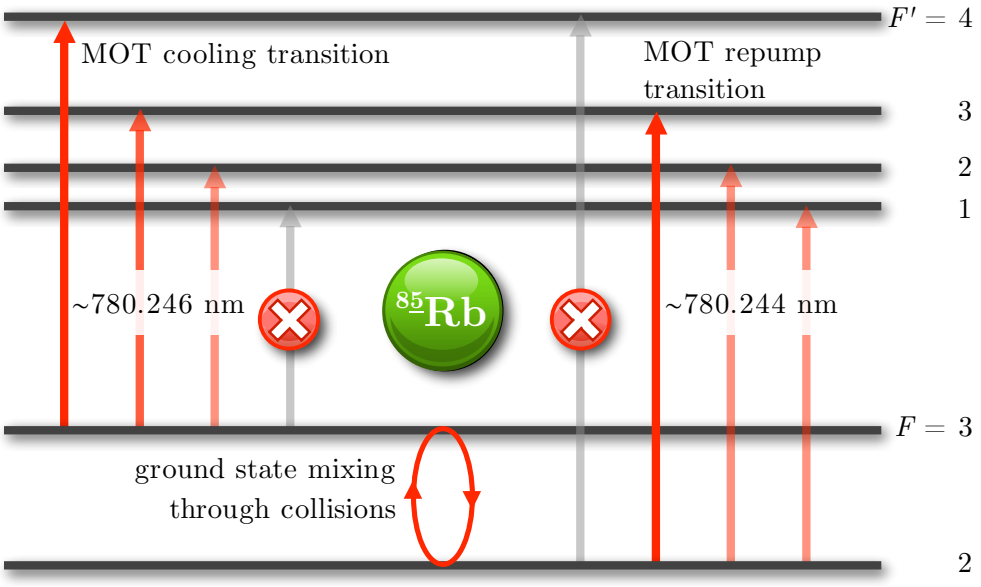

FIGURE 4.1: The cooling and repump transitions for a ^{85}Rb MOT and approximate wavelengths. Collisions allow the atoms to flip between the two hyperfine ground states requiring the repump transition to close the cooling cycle.

As shown in figure 4.1, the cooling transition for ^{85}Rb is from the upper ground, $F = 3$ to the excited hyperfine, $F' = 4$ level. The repump transition addresses the lower ground, $F = 2$ to the excited hyperfine, $F' = 3$ transition.

Both the trapping and repump transitions are conveniently accessible using semiconductor diode lasers. Indeed, moderately reliable commercial systems based upon diode lasers are now available with output powers up to 1 W, allowing their use for rapid atomic state manipulation as well as providing the weaker sources required for a magneto-optical trap. The experiments described in this thesis were therefore entirely based around semiconductor diode lasers, with home-made systems used for the MOT beams and a tunable high power commercial system at the heart of the manipulation source.

This chapter describes the diode laser external cavities, characterisation, control and stabilisation of the 'in house' built diode lasers for the MOT system as well as the assembly and testing of the commercial chirped pulse laser system.

4.1 Diode Lasers and External Cavities

Diode lasers are an established technology and widely used in atomic physics [88] because of their low cost, tunability and high performance. This has allowed some atomic physics experiments to be done in Undergraduate teaching laboratory [89, 90].

Diode lasers typically comprise a semiconductor gain region, bounded by two edges or 'facets', one of which is coated to form a high reflector while the other is differently coated or uncoated to act as a partially-reflecting output coupler.

External Cavity (semiconductor) Diode Lasers[1] (ECDLs) are used with rubidium atoms because laser diodes are readily available at the 780 nm wavelength required[2]. In our experiments, Sanyo DL7140-201 diodes were first used and these come in a 5.6 mm, three-pin package[3], have a centre wavelength of 785 nm with a maximum output power of 80 mW, CW. A higher power (120 mW, CW) diode from Sharp (GH0781JA2C) with a centre wavelength of 784 nm later became available and these were also used. The wiring for these diodes is simpler than for the Sanyo diodes because the photodiode anode pin is not connected (see figure 4.2).

The lasers were built to our own modification of the design of Malcolm Boshier *et al* [92] from the University of Sussex, the design, assembly and alignment is described in Appendix J.

[1] These are the common edge emitting diodes as opposed to vertical surface emitting (VCSEL/VECSEL) or front face emitting semiconductors.

[2] This is because these same diodes are used in computer CD-ROM/RW drives.

[3] The 5.6 mm and 9.0 mm dimensions are industry standard diode package sizes.

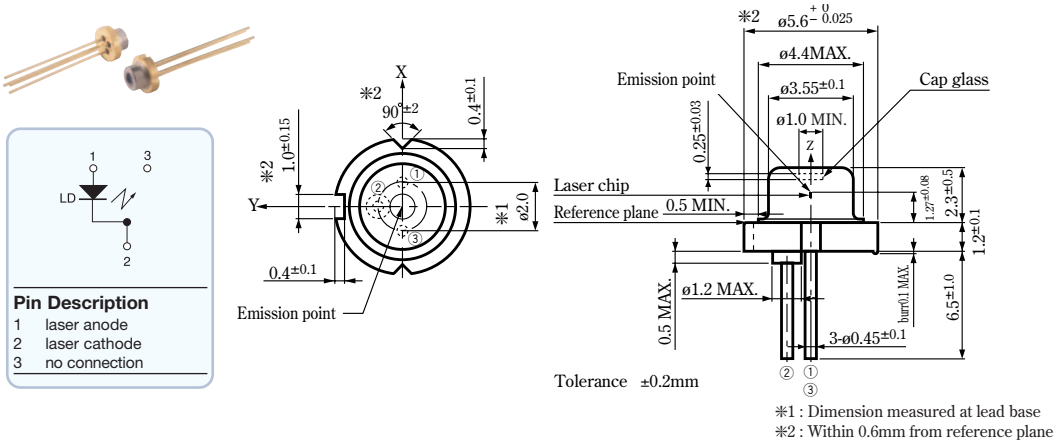

FIGURE 4.2: Technical drawings for the Sharp diodes, showing pin connections, package dimensions and tolerances; sourced from [91]

Diodes lasers typically have a large gain bandwidth of several nanometres around their centre frequency[4] [93]. This means that a 'free-running' diode is likely to be multi-mode, emitting several wavelengths that are likely to change over time, both slowly (continuous drift) and transiently (often called a discontinuous 'mode-hop').

Due to the narrow wave-guiding region inside the diodes, their output beam is highly elliptical and divergent, as shown in figure 4.3. The vertical direction, z is more confined than the horizontal and so the diffraction along z is greater. Typical values can be $\sim 10°$ horizontally and $\sim 30°$ vertically so aspheric lenses or anamorphic prism pairs are required to collimate the beam [94].

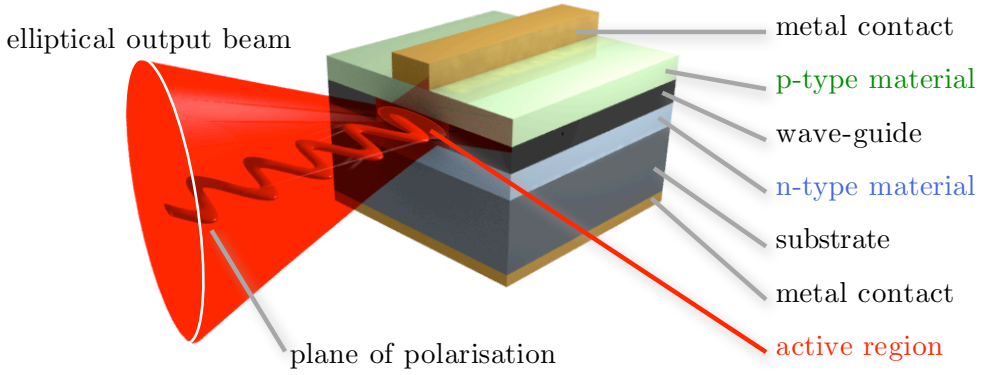

FIGURE 4.3: The various semiconductor layers in a laser diode. The tight confinement in the vertical direction leads to the highly elliptical output beam.

[4]This is dependent on the diode wavelength as diodes towards the blue end of the visible spectrum have a much smaller gain bandwidth of only one or two nm. This is likely to increase as the manufacturing process and technology for shorter wavelength diodes develops.

4.1.1 Feedback and Tuning

The emission wavelength of a free-running diode laser depends upon a number of parameters that influence the length of the optical cavity between the front and back facets, the refractive index of the gain region between them, and the wavelength dependence of the gain. For example, to increase the output power one generally increases the drive current, but this increases the electron density in the diode, which in turn changes the refractive index of the semiconductor and hence affects the optical cavity length, which changes the output wavelength. Simultaneously the increase in current causes an increase in temperature from resistive heating, this causes thermal expansion of the diode, changing the cavity length, which in turn changes the output wavelength. As semiconductors have high refractive indices, (typically > 3) small changes in cavity length are significant to cause the output to drift or become unstable and abruptly change (mode-hop).

The output wavelength of a diode laser can be controlled either by careful adjustment of the operating current and temperature in response to an external measurement of the running wavelength (electronic feedback), by injecting light at the required wavelength that swamps the optical field fed back from the output coupler (injection locking), or by feeding back a frequency- or phase-controlled fraction of the emission from an external optical system so that the 'internal' cavity formed by the two laser facets is replaced or dominated by an 'external' cavity comprising the back facet and the external optics [95]. The lasers used to provide our MOT beams use a combination of techniques, with an external cavity formed by the addition of a collimator and diffraction grating[5], and electronic feedback control of the grating and the laser current.

4.1.2 Wavelength Tuning via the External Cavity

A diode laser tends to lase at the wavelength of the light being fed back into it from the diffraction grating (from a diffracted order), provided it is an allowed cavity mode. In this case, the optical feedback will cause strong gain for this particular wavelength and strong suppression of all other modes (see figure 4.4). The linewidth of the output is also greatly reduced [96].

Though external optical feedback is a strong effect and sufficient to tune a diode laser to the desired wavelength, it is still necessary to tune the diode using the drive-current and temperature so the optical feedback and cavity modes overlap. This means scanning the parameter space, searching for 'sweet spots' where the diode output is single mode, stable and does not mode-hop.

[5]The diffraction grating used is a holographic grating with 1800 lines per mm as in [92].

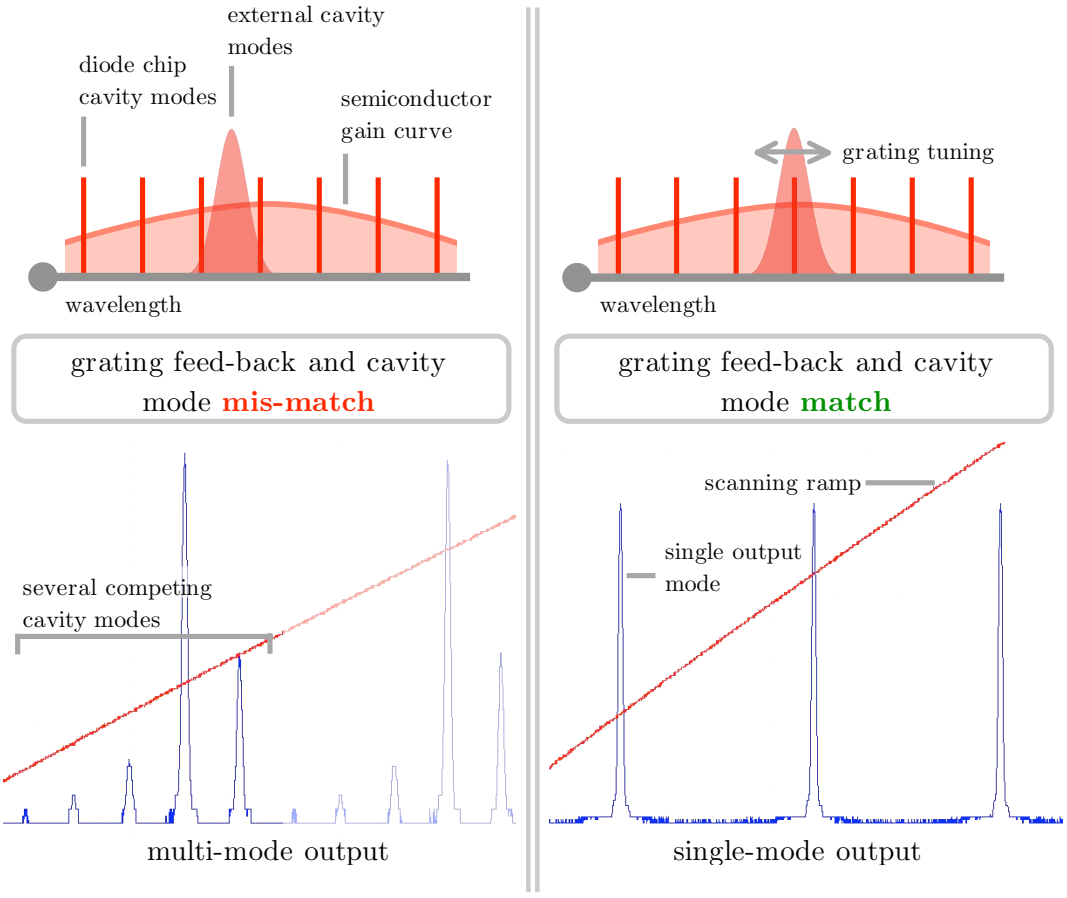

FIGURE 4.4: Mode-hopping and multi-mode output occurs when externally applied, optical feedback from a diffraction grating does not match any internal cavity modes. Single mode output is achieved by tuning the grating and cavity modes (through drive-current and temperature) so they overlap. The Optical Spectrum Analyser (lower images) shows the differences between single and multi-mode output for a laser based on the Sanyo diode.

There are two main cavity configurations possible when using a diffraction grating: Littman/Metcalf and Littrow. Both involve returning a fraction of the output beam back into the diode to provide the optical feedback.

Referring to figure 4.5, the Littman/Metcalf configuration involves the diode output (1) hitting the diffraction grating. The zeroth order becomes the final output beam (5) while the first order is directed to a tuning mirror (2). The mirror retro-reflects the first order back to the grating (3), which then directs it back into the laser diode (4). Light in the zeroth order from this second diffraction is lost. The wavelength can be tuned by rotating the tuning mirror (about a common pivot point with the grating and diode). Rotating the mirror changes the angle of the first order beam that is reflected back onto the grating, which changes the wavelength selected to go back into the diode [93, 97, 98].

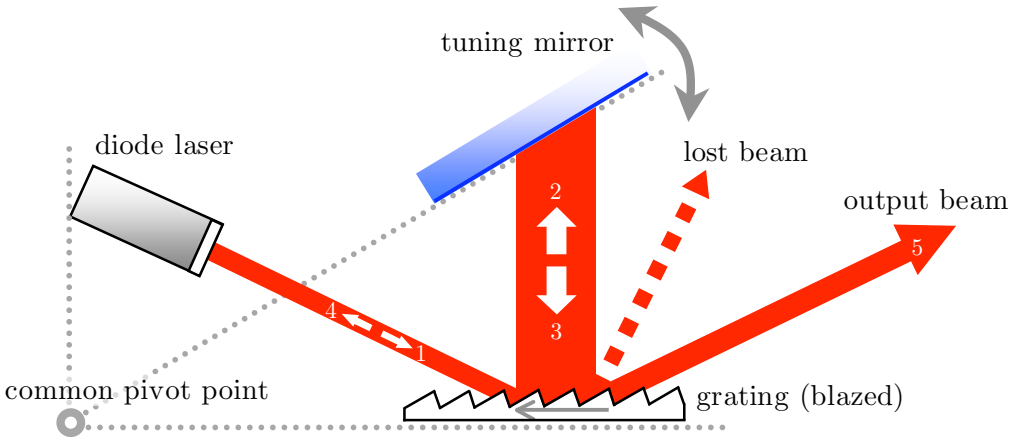

FIGURE 4.5: The external cavity layout for the Littman/Metcalf configuration ECDL

The principal aim of the Littman/Metcalf geometry was to achieve synchronous tuning of the grating angle and cavity length, so as to allow a broad tuning range without hopping between longitudinal modes. A further advantage of this configuration is the final output beam direction does not change with the rotation of the tuning mirror and the laser linewidth can be significantly reduced, from tens of MHz to hundreds of kHz. However the optical feedback is weaker as only the first order of the first order is returned back to the laser diode and the zeroth order beam from the second diffraction is lost. This means the final output beam can be as little as 30% of the total laser diode power.

The Littrow configuration (shown in figure 4.6) is simpler as there is no second diffraction process. The diode output (1) hits the diffraction grating and the first order beam is directed back to the laser diode (2) to provide the optical feedback while the zeroth order becomes the output (3). The wavelength is tuned by changing the angle of the diffraction grating.

The disadvantages of this configuration are the non-synchronous tuning – and hence tendency to mode-hop when tuned – and the change in output beam direction as the grating is rotated[6]; the reduction in linewidth is also not as great as for a Littman/Metcalf configuration. Advantages are the feedback is much stronger and so is the final output power [88, 93, 100, 101].

The Littrow configuration is commonly used for diode lasers when the higher output power is required. The strength of optical feedback can be increased, if necessary, by

[6]Recently there have been modified Littrow designs, which with the addition of a mirror about a common pivot point (similar to Littman/Metcalf) means the angle of the output beam direction no longer changes with tuning the diffraction grating [7, 99].

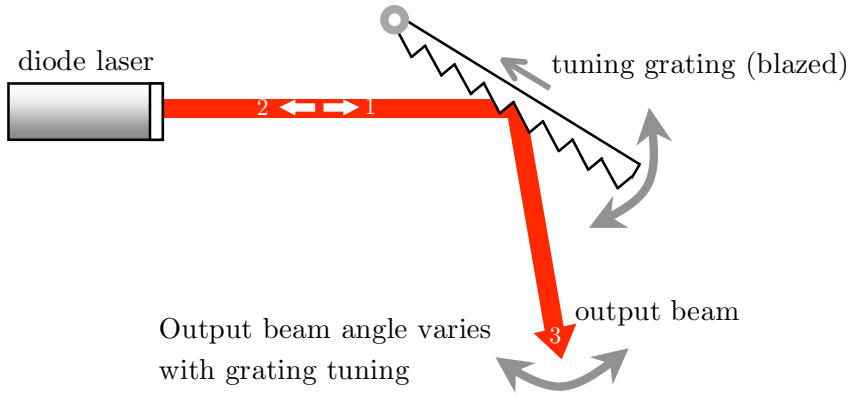

FIGURE 4.6: The external cavity layout for the Littrow configuration ECDL. This is the layout used for the diode lasers.

using a blazed diffraction grating[7].

4.2 Laser Characterisation

The external cavity diode lasers were built and their properties – such as output power, wavelength dependence upon temperature and mode structure – characterised to understand their operation. Two types of diode lasers were built. The first directly followed the design described in [92] and used the Sanyo diodes (and named Beryl). Subsequent lasers were built upon our own modified version of this design and uses the more powerful Sharp diodes (Nora and Ethel, see Appendix J).

4.2.1 Threshold Current and Output Power

A quick test was to check the linearity of the laser output power with the drive current. This was done for *Nora* (one of the lasers using the Sharp diode) and the expected result: a linear slope that begins at the lasing threshold current; was obtained and is shown in figure 4.7.

[7]A blazed grating has a 'saw tooth' profile, which means a larger fraction of the diffracted beam goes into the first order. The direction of the blaze (indicated by an arrow, marked by the manufacturer) indicates the direction of the more powerful, first order beam.

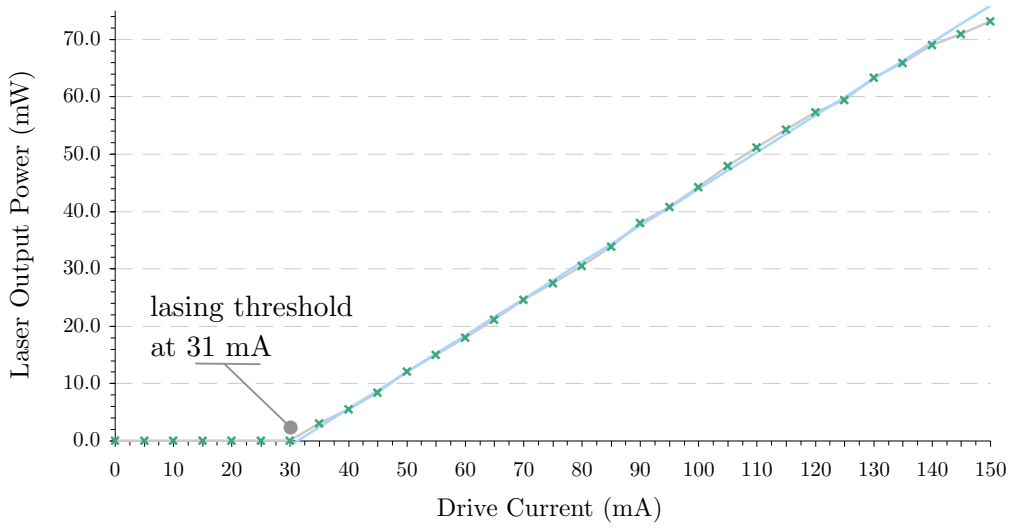

FIGURE 4.7: The linear relationship between the laser output power and the drive current. Lasing occurs once the threshold current is passed (31 mA for the above diode).

4.2.2 Wavelength Variation upon Drive Current

The dependence of the free-running output wavelength upon drive current was also studied, at a fixed laser mount temperature of 20 °C with *no* external cavity, grating feedback. The results are shown in figure 4.8 for the Sanyo diode, *Nora*.

The general trend – indicated by the broad blue band – indicates the current (hence associated carrier density and junction temperature) dependence of the peak gain wavelength, which varies by about 0.025 nm mA^{-1}. Structure within this band shows the individual diode chip longitudinal modes, and their own rather weaker dependence upon current. A hysteresis effect is also apparent, in the different behaviour of increasing and decreasing currents.

The graph in figure 4.9 was obtained by recording the output wavelength at each drive current over a long period of time, thereby recording mode hops and instabilities. The constant wavelength-spacing between the modes is a genuine result and not from resolution limited measurement[8].

In figure 4.9, the modes of the diode laser chip can clearly be seen. The trend to longer wavelength with drive current is from the increased drive current changing the refractive index and hence lengthening the optical path inside the diode laser chip. The average gradient is $3.37 \pm 0.33 \times 10^{-3}$ nm mA^{-1}, hence each milli-Amp increase decreases the

[8] A wavelength meter based on an interferometer was used to measure the wavelength and has a resolution of 0.001 nm.

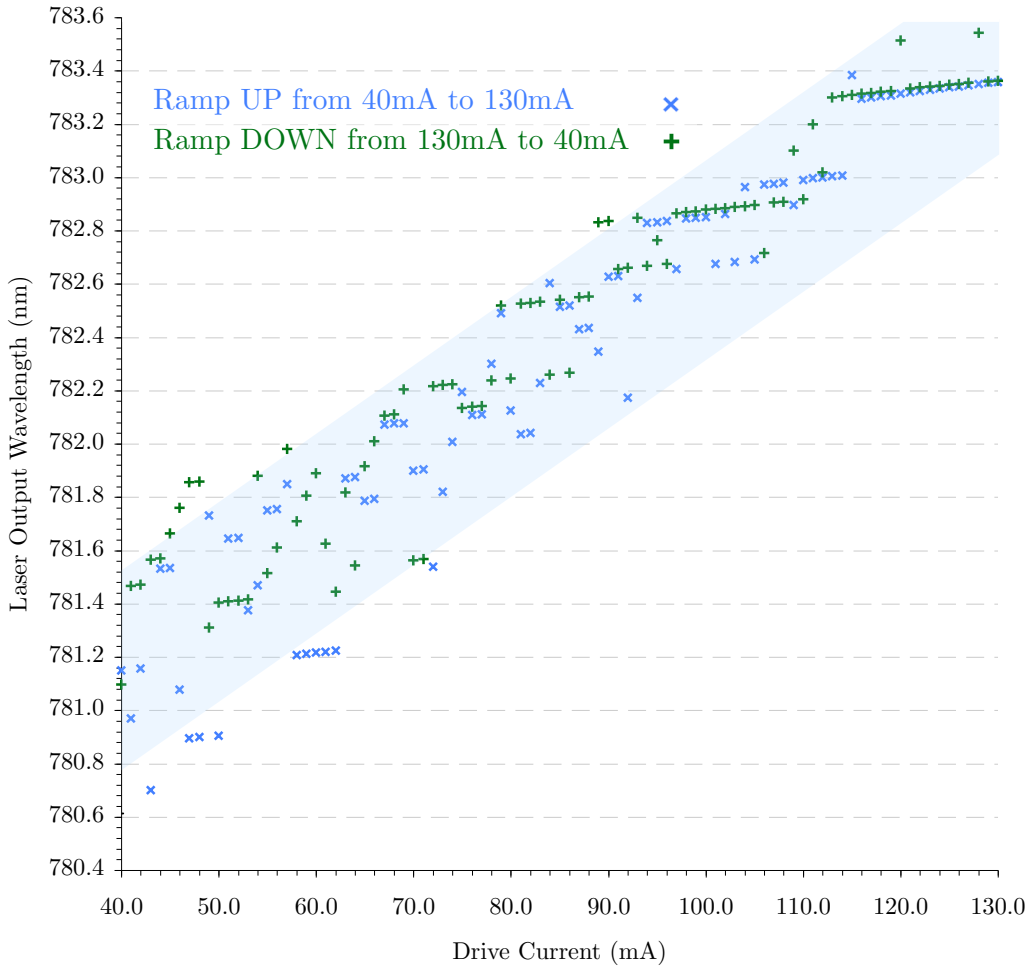

FIGURE 4.8: The laser wavelength variation with change in drive current for the Sanyo diode. Note the hysteresis from ramping up and down from the laser drifting due to environmental changes such as the air pressure and ambient temperature.

laser frequency by ∼1 GHz. This appears to be an excellent way to coarse tune the laser to the required wavelength, however too much change will cause the laser to mode-hop. The mode spacing was found to be an average of 0.10 ± 0.03 nm and translates to an optical path length of ∼3 mm. Adding the semiconductor diode refractive index of ∼3 gives a physical length of ∼1 mm and indicates that these modes are the internal modes of the diode chip.

The experiment was repeated with a wider current range using another diode laser, *Beryl*, but this time with the external cavity in place and reveals a stepped, triangular saw tooth pattern shown in figure 4.10.

The 'steps' of the sawtooth are ∼0.01 nm in height and this corresponds to a cavity length of ∼3 cm, which indicates that these are the external cavity modes. As the drive current is increased, the laser output mode-hops to the next stable 'step' at a longer

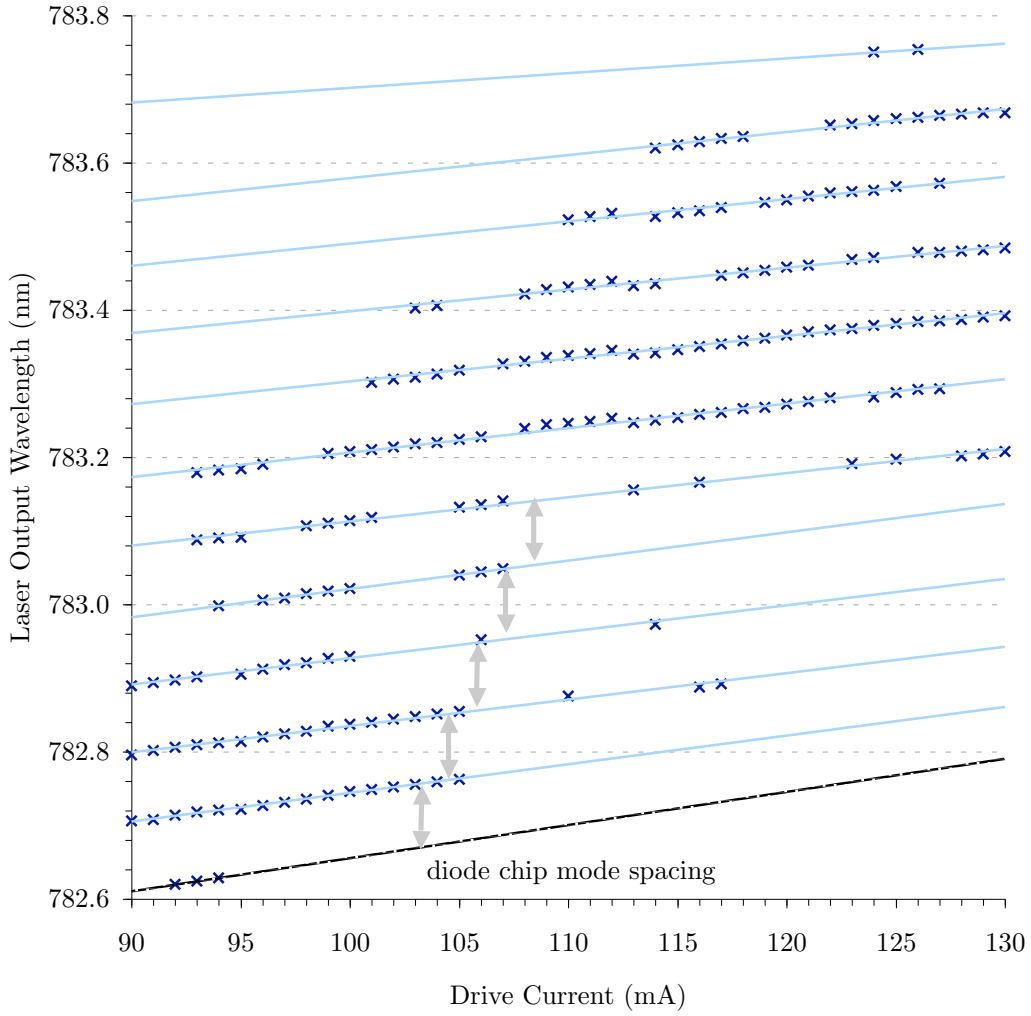

FIGURE 4.9: Details of the free-running diode chip mode structure and spacing with the increase in drive current. As the drive current is increased, modes at longer wavelength become preferred.

wavelength. It does not increase indefinitely but at ∼780.270 nm becomes unstable as the diode chip cavity mode becomes dominant and causes the output wavelength to 'reset'. This behaviour is remarkably consistent over the three scans shown in the graph.

4.2.3 Wavelength Dependence upon Temperature

So far the laser characterisation has been at fixed temperature. It is useful to repeat some of the previous scans at different temperatures to see the effect it has upon the mode structure.

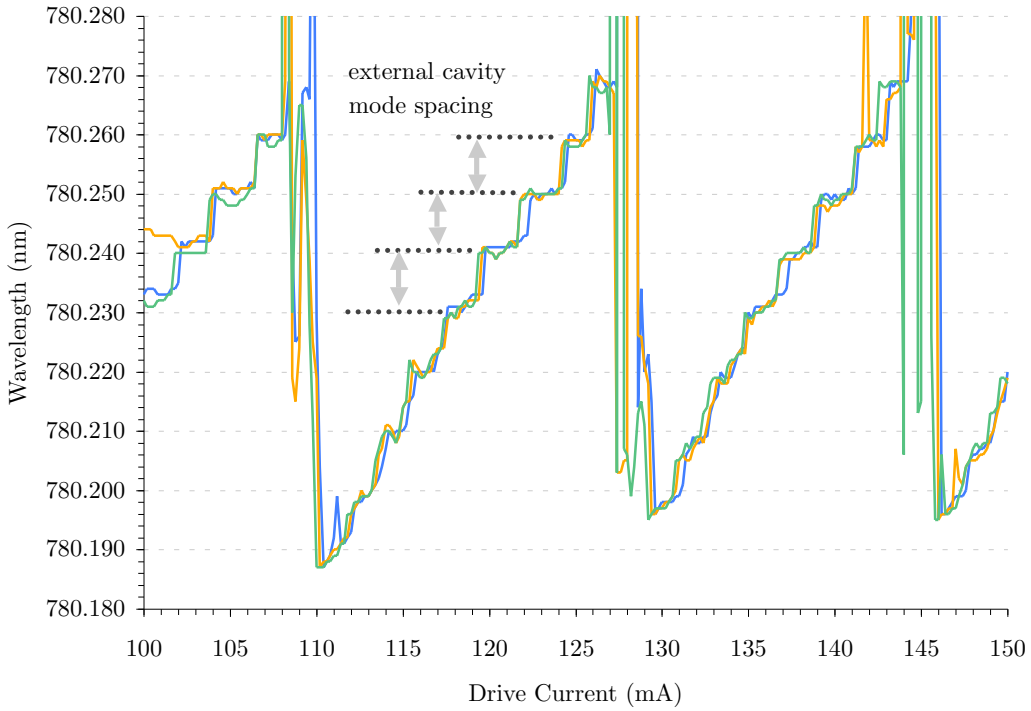

FIGURE 4.10: The external cavity modes of the laser (sawtooth 'steps') in the presence of the diode chip modes that 'reset' the wavelength when it becomes too long. This gives the triangular 'saw tooth' appearance of the graph.

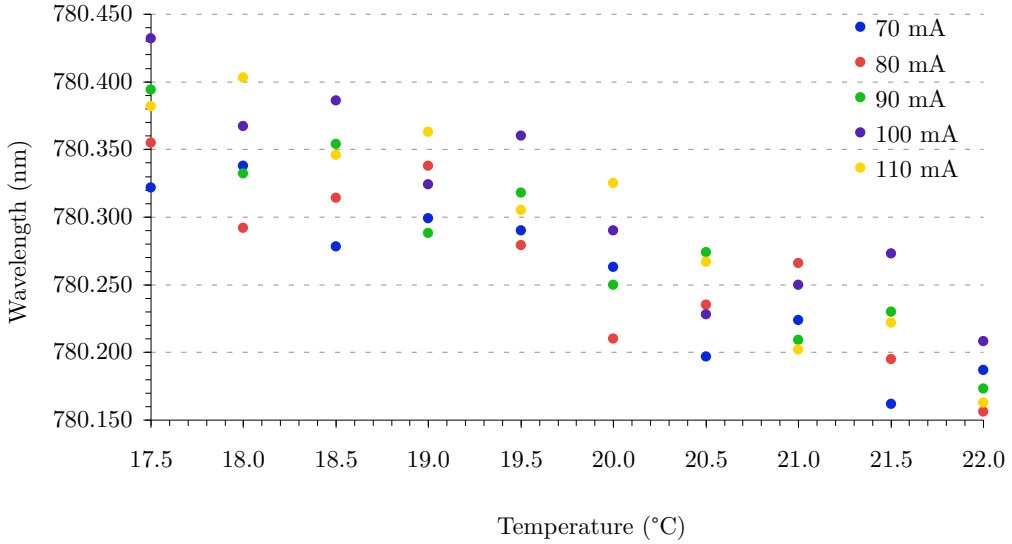

FIGURE 4.11: The laser output wavelength change with increasing temperature. There is a general trend for the output to move to shorter wavelengths with increasing temperature.

Figure 4.11 shows that the laser output shifts to shorter wavelengths as the temperature increases. The average gradient is -0.042 ± 0.006 nmK^{-1} and so is a far coarser wavelength tuning method than changing drive current, in practice, it is also more unstable with respect to mode-hops.

4.3 Rubidium Spectroscopy and Laser Stabilisation

The diode lasers are used to drive the trapping and repump transitions in ^{85}Rb and so need to be locked to specific transition lines. An initial spectrum[9] of both ^{85}Rb and ^{87}Rb across the D_2 lines (involving both hyperfine ground states) was conducted using a rubidium vapour cell and photodiode with the laser wavelength read by an interferometer-based wavelength meter[10] having a resolution of ~ 500 MHz.

The laser was tuned using the feedback grating[11] from 780.230 nm up to 780.250 nm to cover all four Doppler peaks for both hyperfine ground states and both isotopes of rubidium and the results can be seen in figure 4.12.

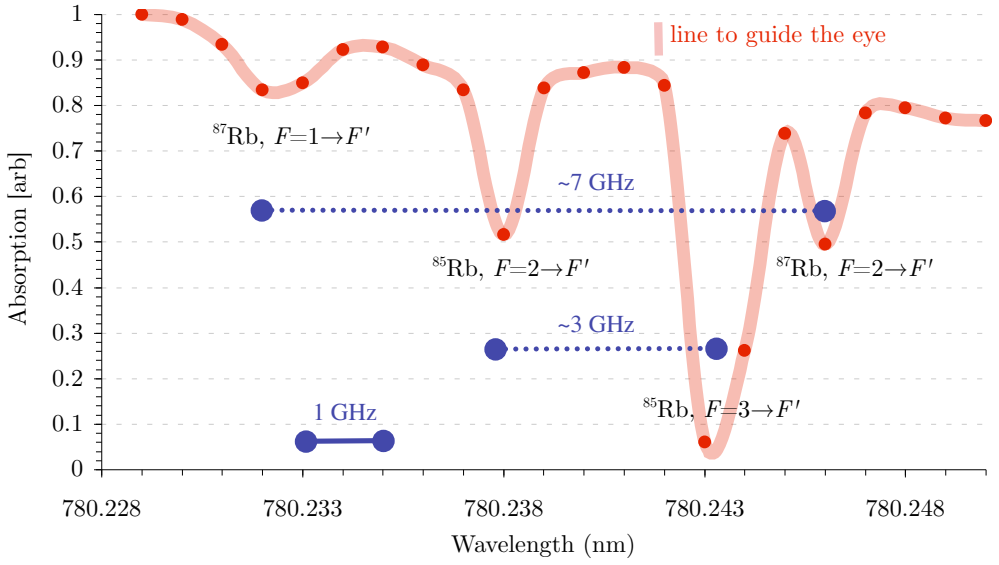

FIGURE 4.12: Room-temperature absorption spectrum for both ^{85}Rb and ^{87}Rb across the D_2 lines (both hyperfine ground states). Despite the low resolution of the wavelength meter, all four Doppler peaks are apparent and can be recognised and indentified. **Note:** the line drawn through the data points is to help guide the eye.

[9] A much more detailed spectrum, using the Doppler-free 'pump probe' method was performed in later experiments.

[10] The wavelength meter is interferometer-based with an internal, calibrated Helium-Neon (HeNe) reference laser source at 632 nm.

[11] Current control of the wavelength could *not* be used as this would change the laser output power and affect the absorption signal.

All four Doppler peaks in figure 4.12 are clearly apparent and the height of the peaks indicates the isotope (^{85}Rb is approximately three times more abundant than ^{87}Rb and so has the larger Doppler peaks). The smaller ground state hyperfine splitting of ^{85}Rb of ~ 3.0 GHz means that its peaks are enclosed by those of ^{87}Rb, which has a ground state splitting of ~ 6.8 GHz.

4.3.1 Laser Locking

Both trapping and repump lasers need to be actively locked to the transition frequency required. There are several methods to do this for example, by using the Pound-Drever-Hall method [102–105], a Dichroic Atomic Vapour Laser Lock (DAVLL) [106–108], polarisation lock [84, 109, 110], or injection lock [111, 112]. For our case the *Doppler-Free Frequency Modulation Lock* (DFFML) method was implemented [113, 114].

The DFFML lock monitors absorption of a laser beam by a hyperfine transition line and keeps it maximised. A decrease in absorption means the laser wavelength is drifting away from the transition line and so feedback electronics is used to add or subtract a quantity of drive current to bring the laser wavelength back onto the line-centre again.

A small amount of beam power (typically a few mW) is required for DFFML. Beam absorption is monitored using spectroscopy in a rubidium vapour cell. At room temperature the Doppler broadening from thermal velocities smothers the hyperfine structure with a single broad absorption peak hundreds of MHz wide and is unsuitable to use as the locking line. Instead, a technique known as 'pump-probe spectroscopy' or 'saturated absorption spectroscopy' (SAS) [115, 116] must be used to obtain the hyperfine spectrum.

Pump-Probe Spectroscopy

Pump Probe spectroscopy circumvents the Doppler broadening and allows the hyperfine structure to be resolved, even at room temperature. It works by splitting a single beam unequally into two, usually with a thin microscope slide. Using grating feedback, the laser can be tuned to within the room temperature Doppler profile of the hyperfine transitions. The stronger (pump) beam is passed through the rubidium cell and saturates the atoms[12] while the weaker (probe) beam is steered to overlap and counter-propagate the pump beam through the cell as shown in figure 4.13. The absorption of the probe beam is measured by a photo-detector.

[12]Saturating the transition does not require much optical power, the saturation value for ^{85}Rb is only 1.6 mWcm^{-2}.

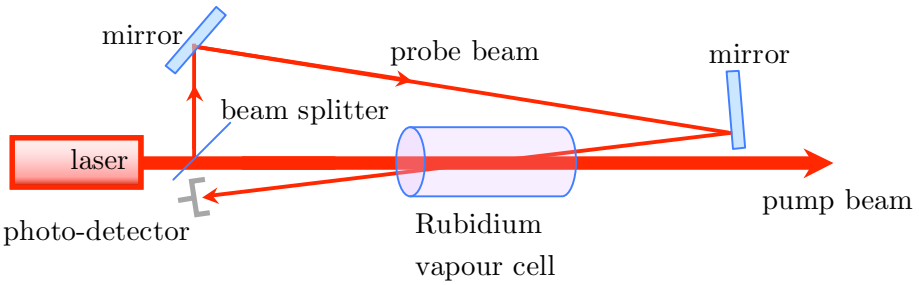

FIGURE 4.13: The optical layout for pump-probe spectroscopy. Maximum overlap of the pump and probe beam gives the best signal and full overlap can be obtained using linear polarisation optics.

The Doppler effect ensures that only atoms with no velocity component along the laser beam propagation axis see the frequencies of both pump and probe beams as equal. When the laser frequency approaches a transition these atoms begin to absorb from both beams, however the much stronger pump beam quickly saturates the transition line and the probe beam is unable to be absorbed. At this point the photo-detector measures a sharp increase in the probe power transmitted (i.e. a sharp decrease in absorption). When the probe absorption is at a minimum, the laser wavelength is on an atomic transition frequency of one of the hyperfine levels.

4.3.2 Pump-Probe Rubidium Spectra

Experimentally, if the photodiode measures the optical power of the probe beam as the laser is scanned across the entire Doppler width – covering all the hyperfine levels – the graph would show the typical room temperature Doppler broadened profile but at each hyperfine transition there would be a sharp peak in transmitted probe power. This can be seen in figure 4.14.

Now that the rubidium hyperfine structure can be resolved using pump-probe spectroscopy, the final step in the DFFML scheme is to take the derivative of the pump-probe spectrum (in figure 4.14) and this produces the signal that is used as the 'locking spectrum' and is shown in figures 4.21 and 4.22. These 'spectra' can now be used to lock the repump and trapping lasers. The point along the spectra that one decides to lock the lasers to depends upon the red-detuning desired.

Cross-Over Resonances

The hyperfine structure for ^{85}Rb and ^{87}Rb has four levels each, but up to six peaks can be seen in figure 4.14 for each spectrum. The extra peaks are called *cross-over resonances*

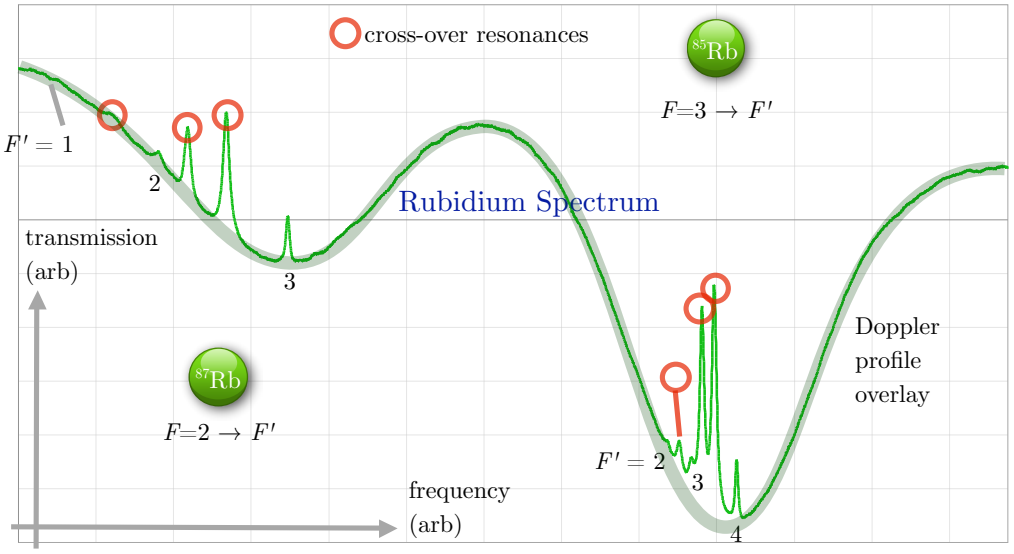

FIGURE 4.14: A pump-probe spectrum for both ^{85}Rb and ^{87}Rb showing the upper ground state to hyperfine (F') levels. The size of the cross-over resonances are significant.

but do *not* imply further atomic structure. These resonances occur at the mid-point between two 'real' hyperfine transitions. Cross-over resonances can be explained by referring to figure 4.15; atoms moving along the laser beam propagation axis see the pump and probe beams Doppler shifted by the *same magnitude*, δ but *opposite sign*. When the laser is at ω' – the mid-point between two transitions – atoms travelling at a particular velocity, v_x see a Doppler frequency shift enough to cause absorption from both beams. This occurs because atoms travelling at v_x along $+x$ see the probe blue-shifted to the higher energy hyperfine transition, ω_2 and simultaneously see the pump beam red-shifted to the lower energy hyperfine transition, ω_1. Since the pump beam is stronger, it saturates this class of atoms and the probe beam cannot be absorbed and so the photodiode records a peak in transmitted intensity. A similar case occurs if the atom were travelling at v_x along $-x$.

Pump-probe spectroscopy circumvents the room-temperature Doppler broadening, allowing the hyperfine structure to be resolved and so is suitable for the DFFML method. Unfortunately, simply feeding in the photo diode signal is not sufficient. This is because there is still the overall Doppler profile present in the spectrum and it needs to be subtracted from the photodiode signal. This can be done by using another weak 'control' beam (created by using another microscope slide) and passing it through the rubidium cell (with no overlap of the pump and probe beams) this is sent to another photo-detector. The signal of the probe beam is subtracted from the control beam. As

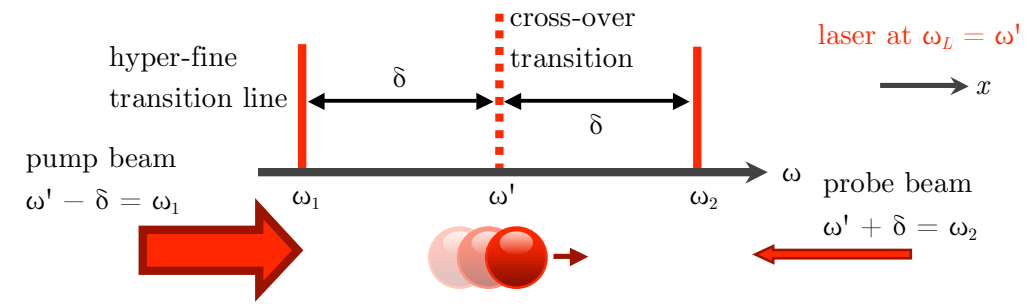

FIGURE 4.15: Cross-over resonances occur at the mid-points between two real hyperfine transitions because – for a particular velocity class of atoms – the Doppler shifts are such that the frequency of the laser beam, ω_L is blue-shifted to ω_2 or red-shifted to ω_1 and visa-versa for atoms travelling in the opposite direction.

separate photo-detectors have different gains, it is advisable to use a *balanced* photo-detector, which has two photodiodes of equal gain and outputs the result of one signal minus the other.

The control beam enables the wide Doppler profile to be removed from the spectrum and hence this type of setup is called *Doppler-free saturated absorption spectroscopy* [117–120].

4.3.3 Feedback Electronics

The photo detector signal from a SAS setup is used for the DFFML. The electronics used to take the signal and convert it into a current fed back into the laser drive current for correction is involved and is not covered in this thesis. Instead, the author recommends the thesis written by Matthew Himsworth[13], which describes in depth the correction signal requirements and the development of our own custom circuits for the feedback electronics. Not only does the feedback loop control the laser drive current, but there is also an output to the tuning grating (via the piezo) to control low frequency drifts in the laser wavelength.

A high-level schematic of the feedback electronics is shown in figure 4.16. The VCO adds an RF modulation on top of the drive current and this adds side-bands to the laser[14]. The result is a beam with a central carrier and a higher and lower side-bands. For ideal Frequency Modulation (FM) spectroscopy, only two side-bands are required (as opposed to additional, higher orders). In order to obtain this, a parameter known

[13] Quantum Control Group, School of Physics and Astronomy, University of Southampton, UK.

[14] The frequency of the VCO is set to around 20 MHz (changeable) as this is greater than the linewidth of the absorption feature, $\Gamma = 6$ MHz.

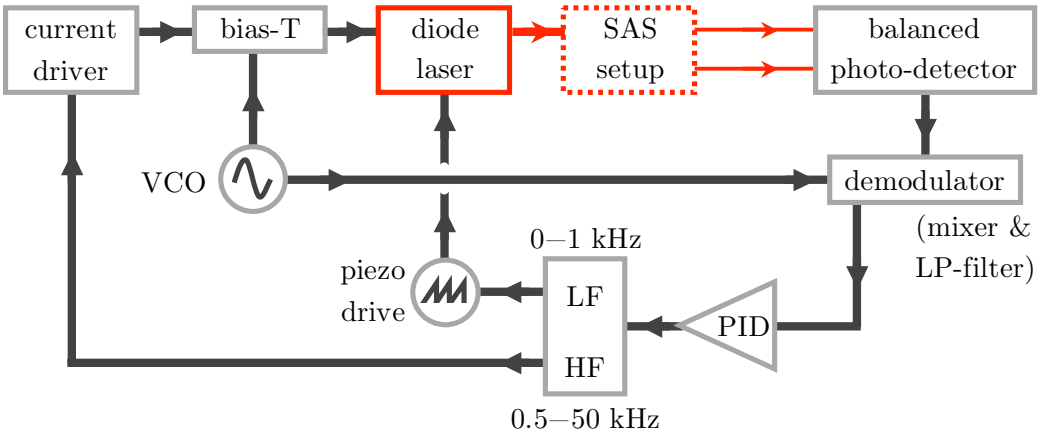

FIGURE 4.16: Electronic schematic for the Doppler-Free Frequency Modulation Lock (DFFML). The feedback system allows both active drive current and tuning grating control to cover a large frequency response range.

as the Modulation Index, $\beta \ll 1$,

$$\beta = \frac{\Delta f}{f_m} \tag{4.1}$$

where Δf is the frequency deviation of the sidebands and f_m is the modulation frequency.

The modulation frequency needs to be larger than the feature of interest meaning the sidebands are far apart enough in frequency so that only one sideband interacts with the atomic absorption feature at a time.

The Voltage Controlled Oscillator (VCO) supplies the modulation frequency to the diode laser and after a fraction of the beam passes through the SAS set up, the signal from the balanced photo detector is demodulated to obtain the error signal. The demodulation occurs by mixing the photo detector signal with the VCO frequency[15]. This produces an AC signal at twice the modulation frequency with an added DC offset. The AC term can be removed using a low-pass filter and the DC term remains. This DC signal is proportional to the change in absorption of the probe beam.

As a FM technique is being used, there is also extra information in the form of phase information between the side-bands. The phase difference between the two side-bands is π when there is no absorption in either side-band. When one of the side-bands encounters an absorption line, this phase difference and the difference in magnitude between the side-bands is seen in the error signal.

The error signal from the demodulator cannot simply be sent back to the diode laser current driver but first needs to be sent to a PID servo that conditions the error signal

[15]This is very much like using a lock-in detection technique with a known local oscillator frequency to improve the signal-to-noise ratio of a weak signal.

so that it is suitable as a correction signal. The output from the PID servo is then split into high and low frequency components. The low frequency components are sent to the piezo, which moves the tuning grating and the high frequency components are sent to the external modulation input of the current driver and added to the laser drive current.

4.3.4 Detuning for Optical Molasses

The DFFML method as described so far is able to lock the laser to an atomic hyperfine transition. However, for Optical Molasses, the laser needs to be red-detuned by a few linewidths. One method is to use an Acousto-Optic Modulator (AOM) to shift the frequency of the beam. Unfortunately this means a significant fraction of the beam power is lost due to AOM deflection inefficiency ($> 20\%$ lost). A second disadvantage is that the frequency shifts required are small – between 10 and 20 MHz (corresponding to between $2\Gamma - 3\Gamma$ where $\Gamma = 6$ MHz for rubidium) – while AOMs are designed to shift several tens of MHz (> 50 MHz) in frequency. An AOM's bandwidth is typically 10% of the centre frequency so an AOM that shifts a beam by only $20 - 30$ MHz is greatly inflexible should the detuning need to be scanned over a large range[16].

Fortunately, an alternative is to take advantage of the Zeeman effect; by surrounding the rubidium vapour cell with a Helmholtz coil pair, a uniform magnetic field can be applied that shifts the energy levels and hence shifts the actual lock position. The full optical layout for the trapping laser including the Helmholtz coil is shown in figure 4.17.

Investigations into the rubidium energy levels in the first part of Chapter 3 and calculations of the field and coils in Appendices D and I respectively mean that the field strength required to obtain a particular frequency shift is now known. For Optical Molasses, a typical detuning, δ would be one to four linewidths, Γ to the red. If $\Gamma \simeq 6$ MHz, this means a $15 - 20$ MHz Zeeman shift is needed and referring to the graph in figure 4.18 – which shows the zoomed in section for the weak-field Zeeman shift for rubidium[17] – this corresponds to a magnetic field of $\simeq 10$ G.

4.3.5 Repump Laser Setup

The repump laser is a second ECDL, which is identical to the trapping laser except that it is tuned from the lower ground hyperfine level ($F = 2$) to the $F' = 3$ excited state of ^{85}Rb. The stabilisation setup of the repump laser is much simpler than that for

[16] In addition, a smaller frequency shift means a smaller deflection angle. For frequency shifts of a few tens of MHz, the deflection angle can be 1° or less, requiring a large propagation distance to separate the deflected and undeflected beams.

[17] The original graph is shown in figure 3.7.

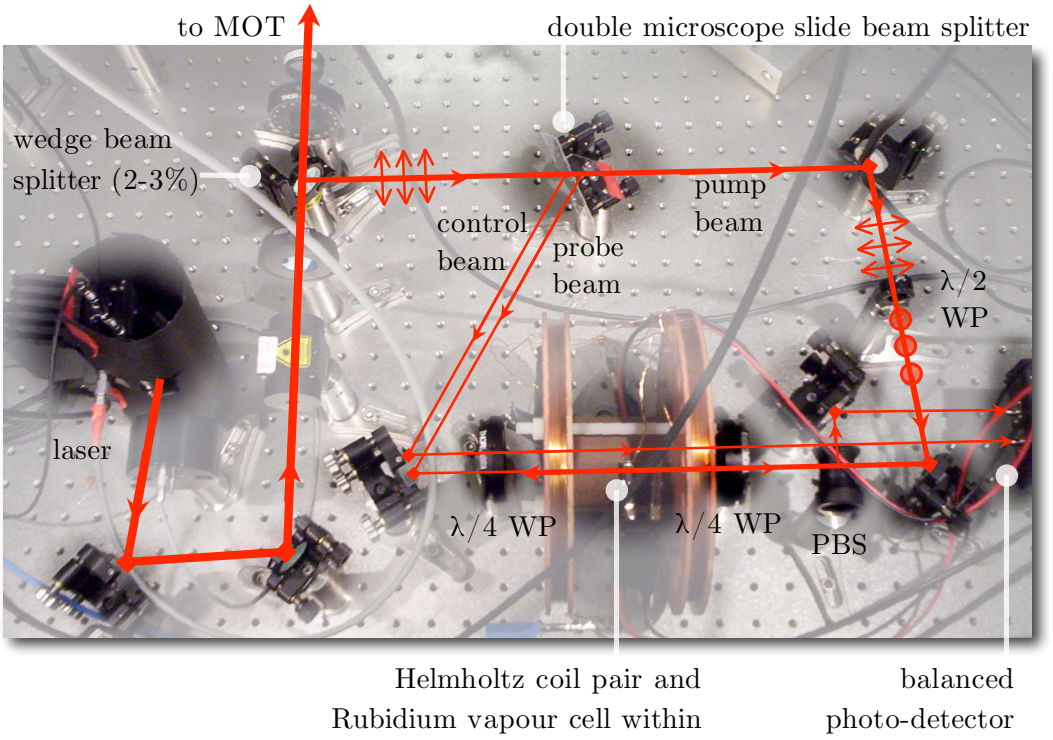

FIGURE 4.17: Optical layout for the trapping laser showing the full Doppler-free SAS setup with both pump-probe and control beams (for subtracting the Doppler profile). Note the Helmholtz coil pair for red-detuning the laser frequency.

the trapping laser in two ways. Firstly, there is no magnetic detuning apparatus as the exact transition frequency is required. Secondly, the Doppler background does not have to be subtracted from the Doppler-free saturated absorption spectrum as the lock point is to the side of the Doppler profile[18] and hence is much more useful for it to be present rather than removed.

A more streamlined optical setup is used in which only a single photodiode detector is required and is shown in figure 4.19.

Most of the laser output – after passing through the optical isolator – passes directly through the wedge beam splitter and on towards the MOT. The small fraction $(2-3\,\%)$ reflected by the beam splitter goes to a streamlined pump-probe spectroscopy setup. The beam passes through the rubidium vapour cell as the 'pump' beam and then through an ND filter. It is then retro-reflected back onto itself, passing though the ND filter again (thus becoming a much weaker, 'probe' beam) and the fraction that passes through the beam splitter is directed towards the photo-detector. The presence of the quarter waveplate is to rotate the polarisation of the probe beam (from vertical to horizontal)

[18]The setup could be simpler still since Doppler-free saturated absorption spectroscopy is not strictly required for the repump setup though is present to allow us to quickly distinguish between other Doppler profiles when tuning the laser (e.g. the ^{87}Rb profiles).

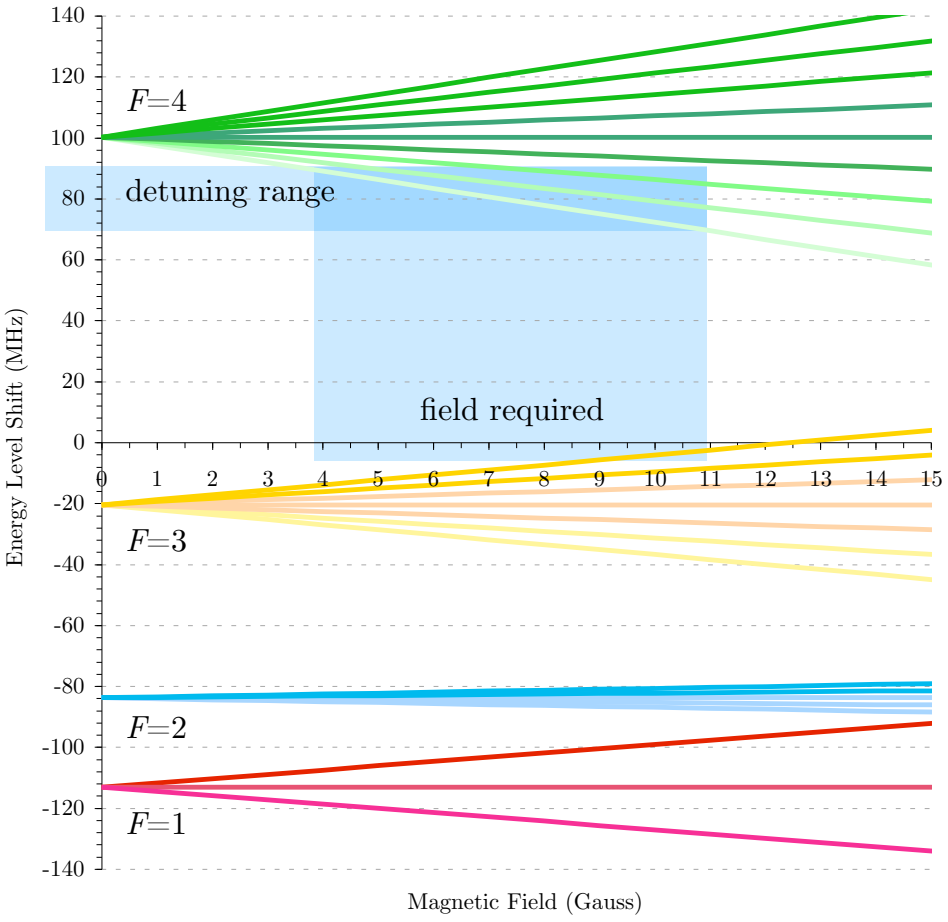

FIGURE 4.18: The weak field Zeeman shift for the excited $5P_{3/2}$ levels for ^{85}Rb. The detuning, δ for Optical Molasses is a few linewidths, Γ and so requires a field between 5 and 10 G.

so that more of the probe beam passes through the beam splitter and on to the photo-detector[19].

The alignment of the repump beam into the MOT is less critical than for the trapping laser, it is sufficient to have the repump beam pass through the MOT cloud once (as opposed to the three orthogonal directions). This greatly eases the optical alignment of the MOT system.

Before entering the MOT, both the trapping and repump beams are combined using half waveplates and polarising beam splitter cubes, their resulting orthogonal polarisations is not important.

[19]The wedge beam splitter is not strictly a polarising beam splitter but the reflected/transmitted beam ratio is still weakly affected by the incoming polarisation.

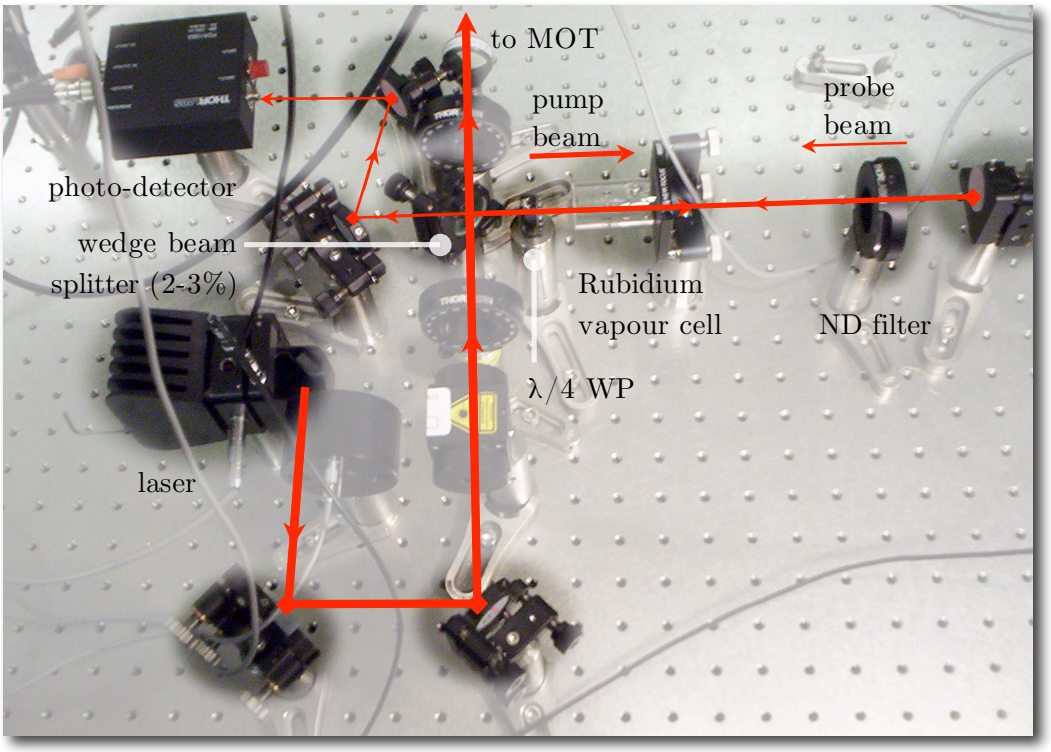

FIGURE 4.19: The optical layout for the repump laser. There is no detuning required so there is no Helmholtz coil pair and only one photodiode detector is required. These simple requirements mean that the optics can be greatly streamlined.

4.4 Laser Beam Steering and Control

Measuring the MOT cloud characteristics (in Chapter 4) requires control of the trapping and repump lasers. This is done by passing each beam though an AOM (at 110 MHz). The frequency shifted *down* diffracted orders are used for optical molasses. Using the AOMs means the optical molasses beams are 110 MHz less in frequency than required for the MOT transitions. This is compensated for by changing the position of the lock-point in the DFFML setup. Though a double-AOM-pass can be used to cancel the AOM frequency shift, this would have left too little power remaining in the trapping beam for the optical molasses.

The diffraction efficiencies are controlled by an arbitrary signal generator connected to the analogue modulation inputs of the AOM drivers. The signal generator in turn is computer controlled and allows the laser beams to be switched on or off independently in a pre-programmed sequence. Additionally the signal generator can trigger the oscilloscope to begin recording data at the time required. This arrangement is shown in figure 4.20.

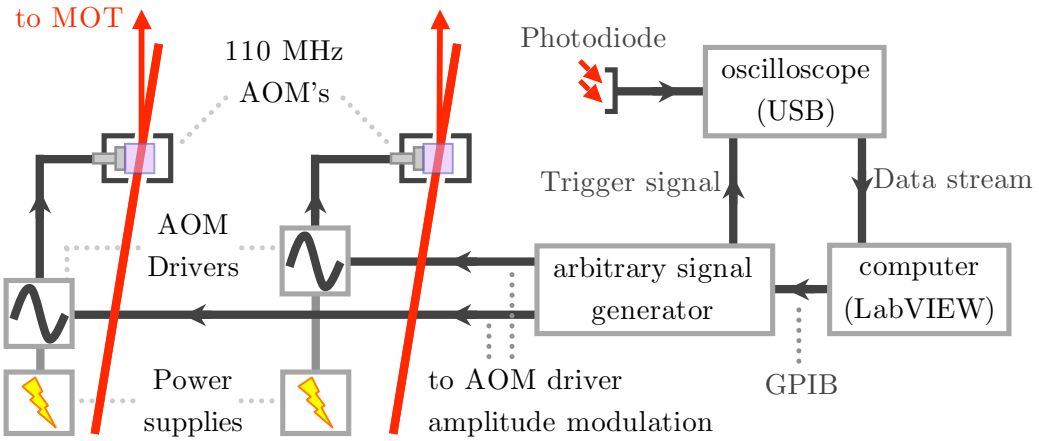

FIGURE 4.20: Schematic of how the optical molasses beams are controlled through AOMs connected to an arbitrary signal generator allowing computer control of the beam intensities, which is required for the MOT cloud characterisation experiments.

The 110 MHz shift means the position of the locking point on the DFFML spectrum needs to be compensated for. Figure 4.21 shows how the locking point for the repump laser – which would normally be on line centre with the $F = 2 \rightarrow F' = 3$ transition – has been shifted to the side of the Doppler profile.

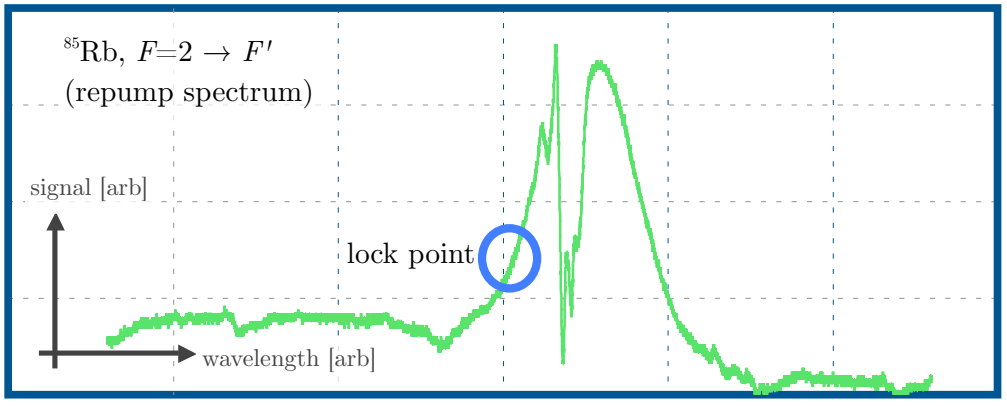

FIGURE 4.21: The derivative spectrum for the repump transition, $F = 2 \rightarrow F'(= 3)$ with the lock-point marked to be on the side of the Doppler profile instead of line-centre to compensate for the -110 MHz frequency shift of the AOM.

For the trapping lock point, the ~ -20 MHz detuning minus the -110 MHz shift means the $F = 3 \rightarrow F'$ must be shifted by $+90$ MHz and this requires a field of ~ 135 G from the Helmholtz coils surrounding the vapour cell. In addition, σ^+ polarised light is used so that the atoms are optically pumped into the $F = 3, m_F = 3 \rightarrow F' = 4, m_F = 4$ line. This almost eliminates all other spectral features and leaves a single sharp line to lock to as shown in figure 4.22.

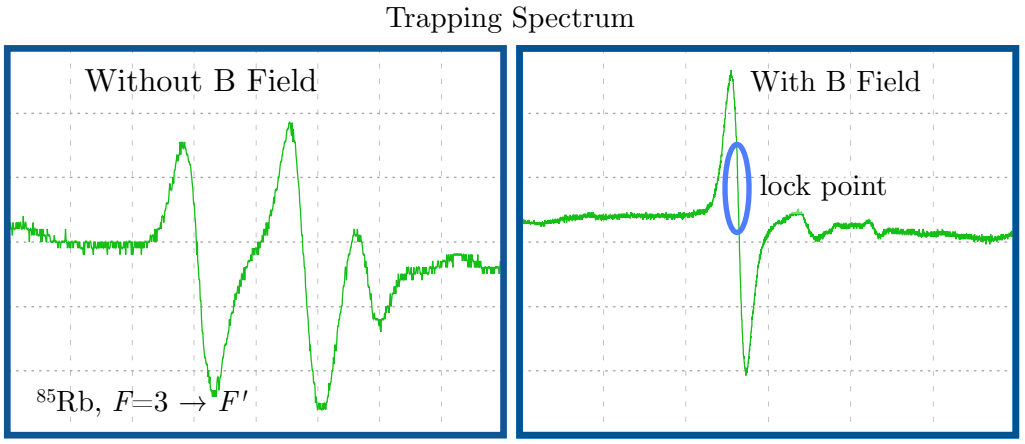

FIGURE 4.22: The left spectrum shows the Doppler-subtracted and differentiated $F = 3 \rightarrow F'$ spectrum without the B-field. Switching on the B-field and using σ^+ polarised light gives the spectrum on the right with the lock-point marked.

Note that for the trapping laser, the Doppler background has been subtracted from the pump-probe spectrum (of the ^{85}Rb, $F = 3 \rightarrow F'$ lines) and then the derivative taken to obtain the DFFML locking spectrum shown in figure 4.22. This increased the stability of the trapping laser lock point. For the repump laser, the simple pump-probe spectroscopy setup was sufficient, as the lock point is to the side of the Doppler profile. This means that the full Doppler-free SAS (as for the trapping laser setup) was not used for the repump laser.

4.4.1 Optical Layout for Optical Molasses

There are a few variations of the optical layout when setting up Optical Molasses. Three pairs of counter-propagating beams in the orthogonal directions (x, y, z) as shown in section 2.3 was used for our MOT system, though tetrahedral and pyramidal variations do exist. Any combination between six individual lasers (one for each beam) to one laser, split into six beams can be used.

Separate lasers mean greater power in each beam, allowing a large trapping beam diameter and a large MOT cloud with more atoms. The disadvantage is each laser has to have its own frequency stabilisation setup: six sets of vapour cells, detuning coils, balanced photo-detectors and electronics. For most cases – including ours – this is unfeasible.

The saturation intensity of the cooling transition for ^{85}Rb is 1.6 mWcm^{-2}. This low value means that a single diode laser of modest output power ($\simeq$ 100 mW) is sufficient for splitting into three retro-reflected trapping beams[20].

[20]The beam power required for the frequency stabilisation setup (described in section 4.3.1) is only a few mW and is negligible in comparison.

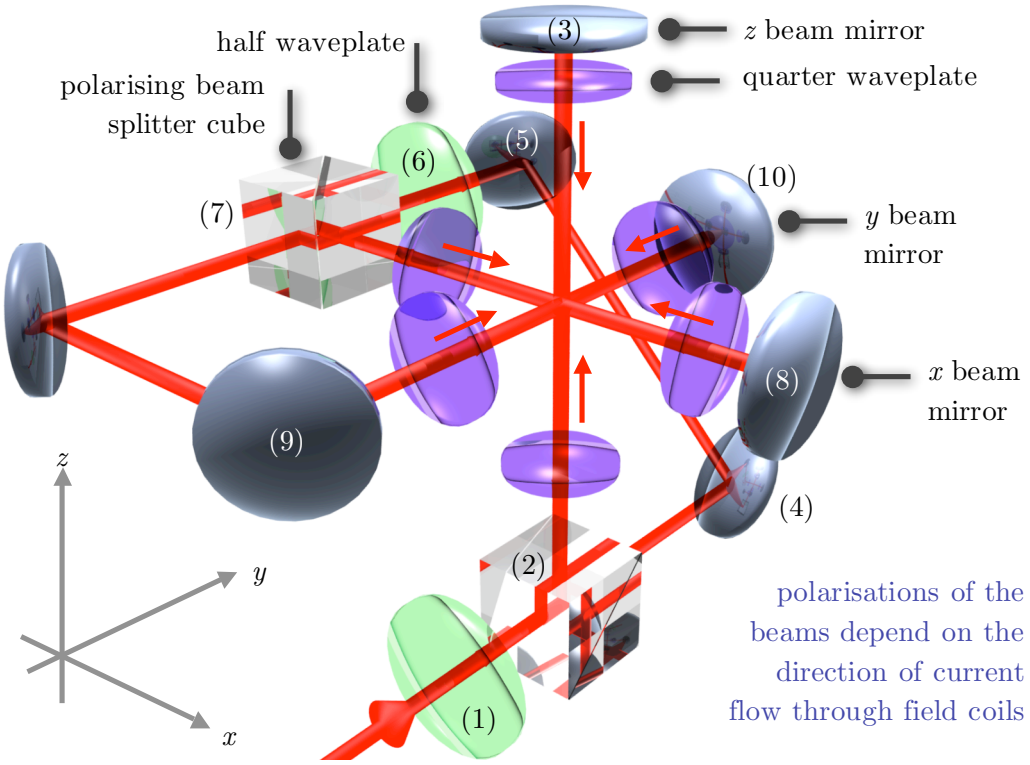

FIGURE 4.23: The optical layout for Optical Molasses where a single diode laser is split into three orthogonally directed beams, which are then retro-reflected.

Referring to figure 4.23, the laser beam passes though a half waveplate (1) and encounters a polarising beam-splitter cube (2). This first waveplate is rotated so that one third of the optical power is reflected vertically upwards, passes through the MOT chamber and is retro-reflected back down again (3); this forms the z pair of beams.

The remaining 2/3 power is reflected (4) up to the main chamber platform and levelled horizontally (5) so that it lies in the x, y plane where it passes through another half waveplate (6) and polarising beam-splitter cube (7). This waveplate is rotated so that half the power is reflected by the cube (now $1/3^{\text{rd}}$ of the total power) and the rest is transmitted (the remaining $1/3^{\text{rd}}$). The reflected beam passes through the MOT chamber and is retro-reflected back, forming the x pair of beams (8). The transmitted beam is reflected round by 90° (9) and then passed through the chamber and retro-reflected back to form the y pair of beams (10). The powers in each pair of beams can be varied by rotating the half waveplates.

Quarter waveplates are set outside every window into which the laser beams enter. They are for the position dependent force of the MOT and $\sigma^+ - \sigma^-$ polarisation gradient cooling. Setting the correct orientation of these waveplates and hence obtaining the correct circular handedness of the beams is very important for a working MOT. Information about quarter waveplates and how to orient their axes is given in Appendix H.

4.5 Chirped, Pulse System

The chirped, pulsed laser system is the system used to perform the electronic and momentum state manipulations on the rubidium in the vapour cell and MOT cloud. The laser itself is CW and through using a combination of AOMs and EOMs linked to (computer programmable) arbitrary signal generators, the continuous wave laser beam can be chopped into microsecond pulses that can be also be frequency chirped using the EOM.

4.5.1 Laser

The manipulation laser is a commercial system: a Sacher Diode Laser, 'Tiger' in a modified Littrow configuration. It has a maximum output power of 1 W and a wavelength ~780 nm (free running). The cavity design has been modified so that the output beam does not change direction with grating tuning. This is achieved by placing the tuning grating at the back facet of the diode (the back of the diode slab has no reflecting mirror or coating). Light escaping out of the back of the diode is coupled back in by the grating. An aspheric lens at the front collimates the beam. The high diode power means that the linewidth of the laser is quoted as being 1 MHz over 1 ms and that the beam quality is not optimal, with an M^2 value of 1.7.

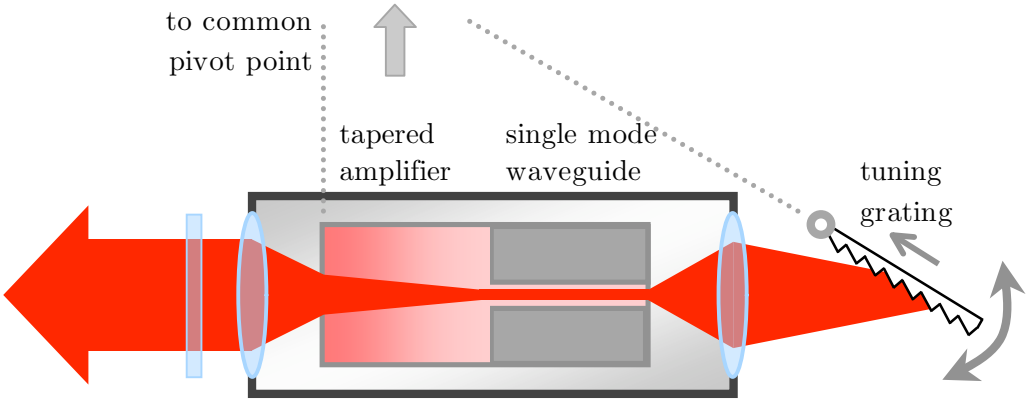

FIGURE 4.24: The 'Tiger' laser schematic with the modified Littrow configuration that keeps the output beam angle independent of the grating angle. The tapered amplifier allows a single diode to reach output powers of > 1 W.

4.5.2 Optical Layout

A simple schematic of the optical layout for the chirped pulse system is shown in figure 4.25. The laser has a built-in Faraday Optical Isolator and so the output polarisation is returned to linear vertical, using a half waveplate. Next, a telescope (pair of plano-convex lenses) is used to focus the beam through the first 110 MHz amplitude modulation AOM. The diffracted beam continues onto the experiment while the undiffracted beam is directed to a wavelength meter and other beam diagnostic apparatus.

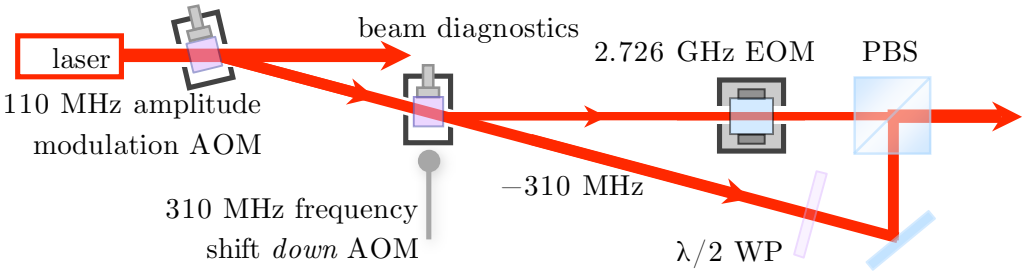

FIGURE 4.25: An overview of the chirped pulse system. The first AOM is able to amplitude modulate the CW into arbitrary shaped pulses and the 310 MHz AOM and 2.726 GHz EOM combine to produce the 3.036 GHz separated Raman beams.

After the 110 MHz AOM, another lens is used to narrow the beam to pass through a 310 MHz AOM. Both beams are used this time; the -1 order (frequency shifted *down*) beam continues on towards the vapour cell while the undiffracted beam is focussed through an EOM. The EOM has a small aperture of 0.5×1.0 mm and produces the 2.726 GHz frequency sidebands in the beam.

Together, the -310 MHz frequency down-shift of the second AOM with the 2.726 GHz upper sideband from the EOM equals the 3.036 GHz hyperfine ground state splitting for ^{85}Rb. This is tunable with the EOM over a small frequency range (tens of MHz).

4.5.3 Amplitude Modulation

The amplitude modulation is done by the 110 MHz AOM via the AOM driver (shown in figure 4.26), whose RF drive power (and hence diffraction efficiency) can be modulated using an analogue input that varies from 0 V (no drive power) to 1 V (maximum drive power). The input comes from an arbitrary signal generator, pre-programmed by computer with the laser amplitude profile desired for the pulse sequence (square wave, ramp or Gaussian etc.).

The AOM centre frequency is 110 MHz and the deflection angle, 1°. The low frequency allows a larger aperture (1.5×2.0 mm^2) and higher diffraction efficiency ($\sim 85\%$). The

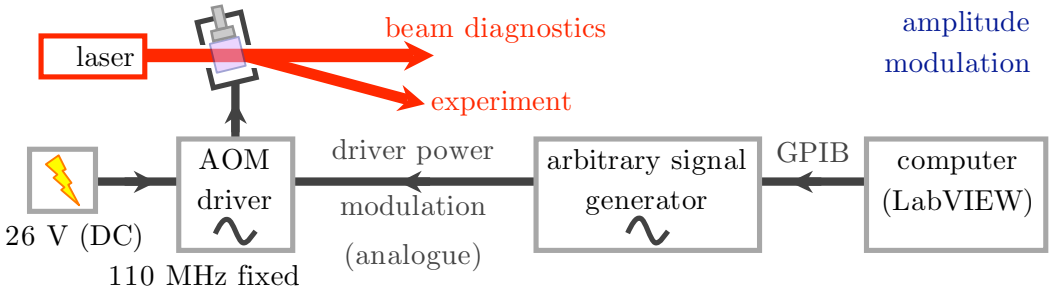

FIGURE 4.26: The amplitude modulation section of the chirped, pulse system. The undiffracted beam is taken to beam diagnostics while the diffracted beam is used for the experiment.

diffracted beam is used for the experiment and the undiffracted beam for diagnostics such as monitoring the wavelength and output mode. Using the diffracted beam means a complete shut off of the beam (with a 0 V analogue input) is possible[21] whereas this is not the case using the undiffracted beam as the AOM efficiency is far less than 100%. The 110 MHz shift can be ignored in the experiments as it is the frequency difference between the two Raman beams that matters, not their common offset from this AOM.

4.5.4 Frequency Modulation

There are two main optical components to the frequency modulation setup shown in figure 4.28. The first is an AOM which is driven at a fixed 310 MHz. Because this frequency is quite high for an AOM, the aperture is smaller (1.0×1.5 mm) and the diffraction efficiency is only $\sim 65\%$. The beam deflection is 3° and both beams are used. The diffracted beam continues on towards the vapour cell while the undiffracted beam is passed though an EOM. The alignment of the AOM is such that the beam is shifted *down* by 310 MHz (see figure 4.27).

The EOM puts both upper and lower frequency side-bands on the laser but causes no deflection, so the laser light emerging from the output aperture contains three frequency components super-imposed. If the EOM drive power is sufficiently high, it can also add on a further set of (second order) frequency sidebands. With optimal tuning of the EOM centre frequency and drive power, it is possible to obtain very close to an equal $1/3^{\text{rd}}$ split of optical power, i.e. 33% in the lower- and upper-sidebands and the carrier. Our EOM is set at a centre frequency of 2.726 GHz, driven by an RF power amplifier with a 40 dBm gain. For a fixed frequency shift, the input into this amplifier comes from

[21] A 0 V analogue modulation input to the AOM driver should mean no power to the AOM crystal, however there may still be some non-zero AOM drive (hence some diffracted beam) but in our case, this was so small as to be negligible and was ignored. The amount is AOM model and driver dependent.

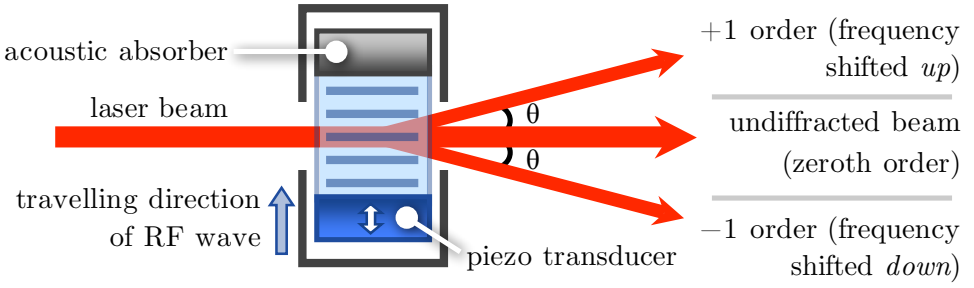

FIGURE 4.27: An AOM can shift the frequency of a laser beam up or down. When the incident light is normal to the AOM (Raman-Nath regime), both +ve and −ve diffraction orders are produced. It is possible to rotate the AOM so that only the +ve or −ve order is produced (Bragg regime).

an Agilent RF frequency generator. When a laser frequency chirp is required, an I&Q (In-phase and Quadrature) Modulator and an arbitrary signal generator is used also.

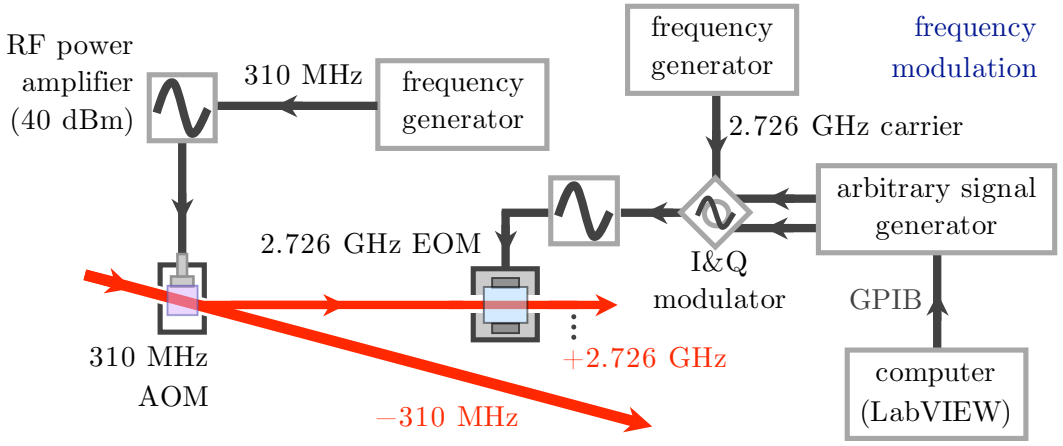

FIGURE 4.28: The frequency modulation section of the chirped, pulse system. The chirping comes from mixing the RF frequencies of the 2.726 GHz carrier and the I and & Q signals from an arbitrary signal generator, hence changing the EOM frequency and shifting the position (frequency) of the sidebands.

The I&Q modulator is an RF mixer that requires three inputs, the carrier, I and Q. The carrier comes from a fixed frequency signal generator running at 2.726 GHz while the I and Q both come from an arbitrary signal generator. From the schematic shown in figure 4.29, the modulator takes the carrier signal and splits it into two independent branches, one branch is phase shifted by 90° and mixed with Q, the other branch is mixed with I. Finally, the two branches are mixed together and this becomes the output.

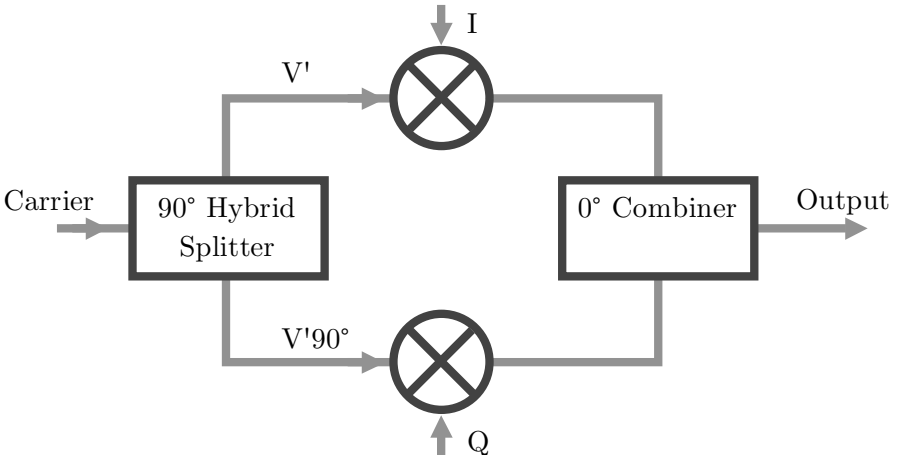

FIGURE 4.29: An electronic schematic showing how an I&Q Modulator works by taking a carrier signal, splitting it into two branches, phase shifting one by 90° and mixing it with Q and the other with I and then mixing these together again to produce the final, modulated RF output.

4.5.5 Laser Frequencies and Selecting Detuning

With the frequency shifts from the AOMs and the sidebands from the EOM, there are several laser frequencies to keep track of. This becomes important when choosing a detuning from the ^{85}Rb excited levels for the two-photon experiments as it is easily possible for an unused sideband to be resonant with a transition, this becomes even more awkward because of the presence of ^{87}Rb.

From the diagram in figure 4.30, it can be seen that the detuning does need to be carefully chosen and a value of about 1 GHz from the excited states is a good detuning to choose to avoid any one of the frequencies becoming resonant. The only other option is to detune far to the red or blue to avoid the rubidium D_2 lines altogether but the further the detuning, the greater the laser power needed to drive the two-photon process.

4.5.6 Directional Switching

The two recombined Raman beams have orthogonal polarisations and for the pulsing experiments it is important that they be the same. To achieve this the beams are passed through a $\lambda/4$ waveplate that converts the orthogonal, linear polarisations into oppositely circular polarisations, then a PBS is used to convert this back into linear polarisations. This process means that the two recombined beams now have the same polarisations at the cost of losing half the combined beam power at the PBS cube.

The two beams are then passed through a Pockels cell, which rotates the plane of polarisation by 90° when 300 V is applied. After the Pockels cell another PBS is used

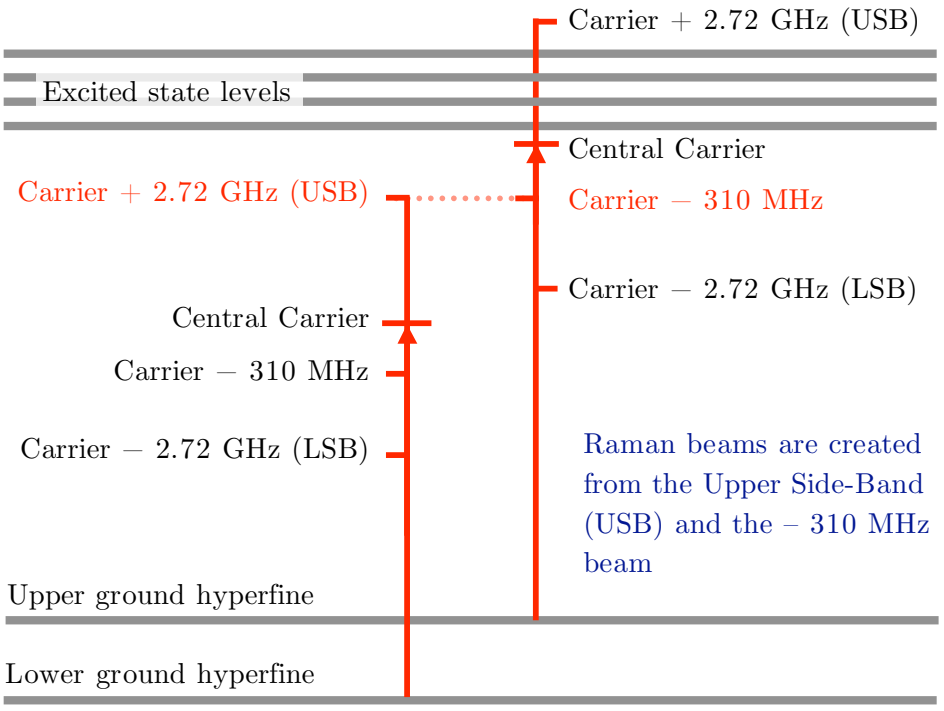

FIGURE 4.30: The several laser frequencies involved in the two-photon Raman scheme. Care must be taken to choose a detuning that does not involve one of the frequencies becoming resonant with a transition in either ^{85}Rb or ^{87}Rb.

and hence there is now directional switching: the two combined beams can either be reflected or transmitted through the PBS depending on the voltage through the Pockels cell.

4.5.7 Computer Control and Triggering

The instruments are daisy-chained together with GPIB cables and controlled through National Instruments LabVIEW. During software development, it was found that using the Perl scripting language together with LabView greatly simplified the development process, in particular for generating the wave forms that would be uploaded to the arbitrary signal generators.

LabView and Perl

LabView is able to call Perl scripts indirectly through the 'System Exec.vi' (virtual instrument). This involves building the command string and passing it to the System Exec.vi as a standard input. The string is executed as a shell command and returns the

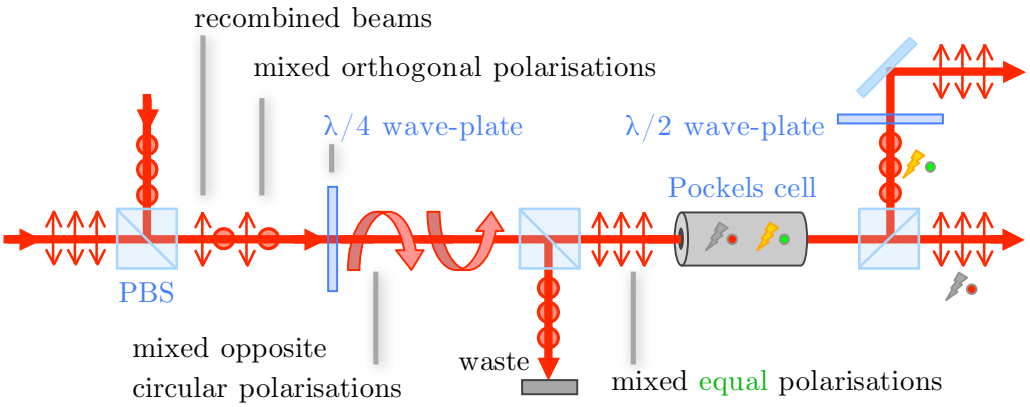

FIGURE 4.31: The layout for the Pockels cell that is used for switching the pulse direction. As the recombined beams are oppositely polarised, a $1/4\lambda$ waveplate and PBS is needed to make them equal. This results in a large waste of optical power at the second PBS.

standard output and error. In this way, LabView controls the Perl script execution, but in our implementation the case is reversed as the VIs are written such that LabView waits for Perl to send commands to it.

Perl and LabView communicate using the TCP and UDP network protocols. This is necessary as there is currently no way to 'call' LabView from Perl. UDP has little overhead[22] and allows rapid, repeated communication between Perl and LabView. TCP is a handshake and session based protocol and so has significantly more network overhead but can be used to return data sets from LabView to Perl.

Both Perl and LabView are required as Perl cannot directly control the instruments and LabView does not have the simple power of a scripting language[23]. A LabView vi is written to simply listen for data or commands on a specified UDP port, Perl is then run and sends instrument commands over the UDP port LabView is listening to. LabView then takes these commands and sends them over GPIB to the instrument specified in the Perl script.

The commands sent from Perl are required to be in SCPI format (Standard Commands for Programmable Instruments) that the instrument can understand. SCPI commands available for an instrument are documented by the manufacturer. The power of SCPI is that instruments can be programmed without having to use the manufacturer's supplied

[22]The UDP protocol is stateless and does not perform authentication, packet ordering or checks as to whether the datagram arrived or not.

[23]There exists 'GPIB::ni', which is a Perl module that provides GPIB extensions so that Perl can make direct instrument calls on the GPIB bus, however it is in a very early stage of development and the latest release was in January 2002. Exclusively using Perl would also mean that the user interfaces (or instrument front panels) would have to be written in Tcl/Tk.

programs or drivers, hence control of the instrument can be through Perl sending simple ASCII text commands to LabView. The simple and human readable syntax of SCPI makes programming easier[24]. Presently, it is not quite possible for Perl to directly communicate with the instrument because these SCPI commands have to be encapsulated in the GPIB protocol, which is the function of LabView.

Perl Scripting Arbitrary Functions

The arbitrary functions for the waveform generators were also made using Perl. The process involves several Perl scripts resulting in the full waveform built as an array of numbers (time and voltage value) from pre-defined primitives. Next, the completed array (which now contains the arbitrary signal required) is passed to another Perl script that converts it into a binary format the instrument can understand and saves the file to disk. Perl then passes the file information and location to LabView, which then prepares the instrument to receive data and uploads the binary waveform file to it.

Though the manufacturer supplies drivers and software for the waveform generators, there was no way to include it in any higher level script that could be written to perform frequency scans and take data as an automated process. The automatic control and scanning of instruments was the main driver for the use of Perl scripting and LabView.

Command Propagation Delay

There are several instruments daisy-chained together and spread across two GPIB buses, this means that the cable length to each instrument is different, meaning the time taken for a command to be sent from LabView and received by any particular instrument is also different. Adding in time-delays from computer and LabView processing means that these time delays must be taken into account in the pulsing scheme.

The microsecond timescale is fine enough to show the effect of the combined signal delay from the computer and signal propagation, particularly in the AOM switching (repump and amplitude modulation AOMs). These time delays can be measured and factored in as a variable in the Perl scripts for the function generators to compensate for this.

[24]This is still subject to the quality and correctness of the manufacturer's supplied SCPI documentation.

Chapter 5

Vacuum System and Other Experimental Apparatus

5.1 Atomic Source

The mixed-isotope rubidium atoms for the MOT are supplied by alkali metal dispensers (from SAES Getters) located inside the chamber. The material containing the rubidium is an alkali metal chromate (Rb_2CrO_4) with a zirconium-aluminium[1] reducing agent. Passing a current through this material heats it and causes a reduction reaction that releases the rubidium.

The dispensers need to be heated to ~ 400 °C before the rubidium is released. This is achieved by passing a current of at least 3.0 Amps[2] through the metal housing of the dispenser. In operation, a slow release and build-up of vapour in the chamber is preferred over a short, rapid release, which runs the risk of exhausting the supply of rubidium. The MOT chamber has five such dispensers that can be powered independently.

5.1.1 Preparation and Operation of the Alkali Metal Dispensers

The alkali metal dispensers were spot welded onto the prongs of an electrical Ultra High Vacuum (UHV) feedthrough. They are electrically connected at the ends to a single prong that serves as a common ground. The feedthrough is connected to a standard bench top power supply able to deliver up to 5 A.

[1] In a ratio of Zr 84% and Al 16%, also known as material 'St 101'.

[2] When using the metal dispensers for the first time, a short burst of high current (> 4.5 A for 15 s) is recommended to clean them of any impurities that may have adsorbed onto the surface, though most impurities should have been removed during the bake-out procedure.

The ion pump is switched off and a current of $3.5 - 4.0$ A is passed through a single dispenser (there are five dispensers in the chamber) for 30 seconds or until the fluorescence is just visible with a CCD camera with a fully open iris. This quantity of rubidium is sufficient to begin creating a cold atom cloud and there is enough to last several days before another recharge of rubidium from a dispenser is required.

5.2 Vacuum Chamber

Vacuum chambers can be specified and bought from specialist companies however, ours was machined in the Department's Mechanical Workshop from a solid block of stainless steel.

The design includes a large number of view ports for the size of the chamber. There are two, 135 mm horizontal windows for the z-axis trapping beams; four, 65 mm (vertical) windows for the trapping beams in the x-y-plane; three, 38 mm windows between these for optical access (with the fourth leading through to the arm of the vacuum system) and finally there are sixteen, 16 mm diameter ports of which thirteen are blanked, one contains a feedthrough for the rubidium dispensers and the remaining four are windows located diametrically opposite each other for the chirped, pulsed laser beams[3].

The vacuum system needs to minimally have three pairs of of orthogonal ports for the six MOT beams. Additionally, it needs a port for the vacuum pumps and a port for a UHV feedthrough containing the atomic rubidium source. Further ports for optical access are also highly recommended. For our system, an additional pair of orthogonal ports were required for the chirped pulsed laser source. The overall geometry of the vacuum system should comply to the geometry requirements for the magnetic coil spacing to produce the optimal anti-helmoltz field that has the steepest field gradient at the centre of the MOT (see Appendices E and I). Using CF style (Conflat – metal knife edge) flanges, seals and fittings with metal (copper) gaskets is essential to successfully reach the UHV vacuum level required for the MOT.

5.2.1 Cleaning the Vacuum Components

An important aspect of attaining UHV pressures inside a vacuum system is having all the UHV components meticulously cleaned and as grease- and dust-free as possible.

Once the vacuum chamber was completed in the Mechanical Workshop, it was submerged in an ultrasonic bath with household washing-up liquid for several hours. After drying,

[3]The window sizes specified are industry standard sizes for viewports.

FIGURE 5.1: The vacuum chamber (shown on its side) just completed by the Mechanical Workshop and now ready to be cleaned and assembled.

the next stage was to clean the inside and out with de-ionised water and then again using acetone and finally with methanol.

This three-stage, water-acetone-methanol cleaning process was also done for the viewports, gaskets, flanges and other components attached to the system. Powder-free latex gloves were used and any component accidentally touched with bare fingers (the gloves tend to tear at the fingertips), meant that it needed to be cleaned again.

The viewport windows are coated with a delicate anti-reflection coating for 780 nm and only the knife-edge seals can be cleaned in the manner previously described. Dust and particles settled on the glass surface may be gently blown off using dry, clean compressed air[4].

[4]Cans of dry, compressed, 'clean' air are available from specialist camera and photography shops.

It is important to remove all traces of grease inside the chamber as grease will continue to out-gas even after bake-out and limit the minimum pressure attainable with an ion pump. The knife-edge seals and gaskets must also be free of surface dirt particles to ensure a completely air-tight, metal-metal seal.

5.2.2 Assembling the Vacuum System

With the chamber and components cleaned they could be assembled together. Annealed copper[5] gaskets were used for all the viewports as it is softer than normal copper gaskets This lessens the stress from uneven torque when tightening the screws of a viewport to the chamber, reducing the chance of the glass shattering from excessive warping. Silver coated copper gaskets were used on the remaining flanges and fittings as it is less reactive with the environment and can be baked to higher temperatures.

Care must be taken in keeping the gaskets positioned correctly over the vertically orientated knife-edge seals as they are liable to move or drop. A gasket should only be used once and a one that has a kink or bend should be discarded, as should gaskets that have excessive amounts of oil or dirt on their surface.

All screws need to be lubricated with high-temperature vacuum grease (for bake-out). This prevents them from seizing and becoming jammed in the screw holes (should they need to be removed). Care is needed to ensure no grease is transferred to the knife-edge seal, gasket or inside surface.

All flanges should be screwed in a particular manner. Sequentially tightening all the screws of a flange in order would result in a potentially dangerous pressure wave running round the flange rim. Instead, screws should be gradually tightened in a star pattern, only turning a maximum of a quarter circle once the screws become tight. Care must be taken with the largest viewports and using a torque wrench with a gauge is recommended.

The arm extending from the vacuum chamber holds the sorption pump, the ion pump

[5]Annealing is the process of heating the metal to a temperature that causes re-crystallisation and can significantly soften the metal upon cooling.

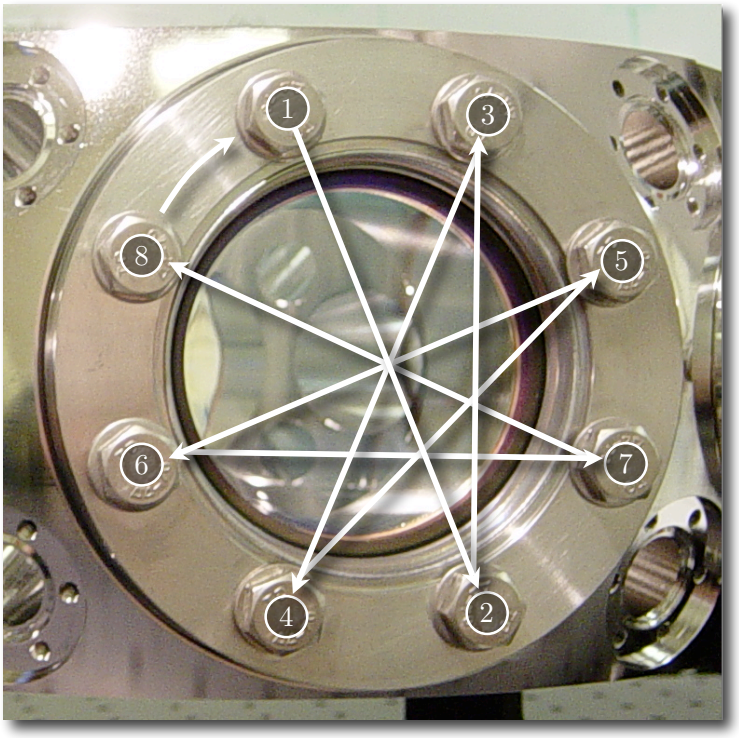

FIGURE 5.2: The alternate 'star-cross' pattern that should be used to tighten viewports to a vacuum system. This method reduces the stress and warping across the viewport reducing the risk of it shattering.

and a UHV valve at the end that is connected to a turbo[6] and scroll pump during pump-down. To keep the ion pump as uncontaminated as possible, it was only unsealed and attached to the system immediately before bake-out.

5.2.3 Initial Pump-down

An initial pump-down to test for leaks is recommended before proceeding to bake the system. When returning the chamber to atmosphere, it is better to refill with dry nitrogen[7] instead of atmospheric air to keep the inside as clean and dust-free as possible. This also reduces the amount of water vapour inside, which is difficult to pump out of

[6] A turbo pump resembles a jet engine, in that it has a stack of turbine rotor blades mounted on a common axle that forms an axis. The axle is rotated at a very high tangential velocity. The rotor blades are angled such that when a gas molecule is hit by the underside of a blade, it is given momentum in the direction of the exhaust. The gas enters through the main inlet flange of a turbo pump and is literally "batted" out towards the exhaust by the rotating turbine blades. Turbo pumps reach a steady state pumping limit when the pumping rate equals the rate of gas entering back through the pump through diffusion (without being struck by the rotors). Turbo pumps have similar pumping rates for all gas molecules since they work mechanically, though rates are typically slightly lower for the lighter gas molecules such as hydrogen.

[7] A standard nitrogen gas cylinder should be composed of 99.95% N_2 and is suitable.

a vacuum system. Although baking removes much of the water vapour, our system was flushed through with dry nitrogen before pumping down.

Referring to figure 5.3, the nitrogen was passed through an inline filter[8], past the four-way connection, through the turbo pump and onto the vacuum system. The connectors used are KF-ISO flanges and clamps as Conflat flanges with knife-edge seals are only required for the UHV sections of the system.

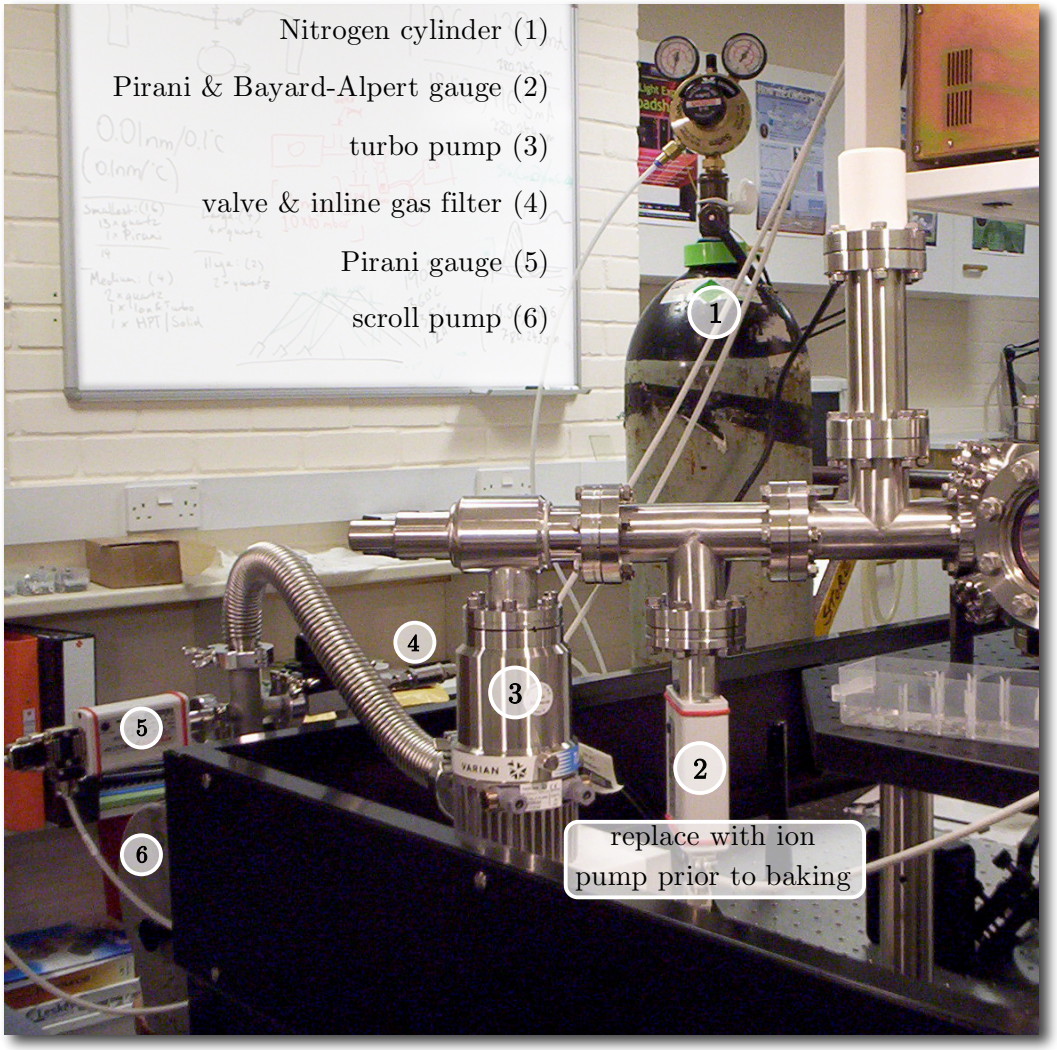

FIGURE 5.3: Apparatus used for the initial pump down and tests for leaks. When verified, the chamber can be filled with nitrogen and the UHV valve sealed, ready for transportation. The Pirani and Bayard-Alpert combination gauge (2) is replaced with the ion pump immediately before baking.

The system is flushed through with nitrogen just before the final viewport is put on. The nitrogen should be passed through so that it blows gently out of the final port hole. After a short period, the nitrogen pressure is reduced to just above one atmosphere and

[8] A 15 μm pore size, brass, inline, gas filter.

then the final viewport is added to seal the chamber. Care must be taken not to have the nitrogen pressure too high, risking a dangerous pressure build-up inside the system.

The roughing pump is started once the system is sealed. The pressure is monitored using a Pirani gauge. When the pressure drops to a few 10^{-2} mbar, the turbo pump is started, which should drop the pressure down to a few 10^{-6} mbar (measured using a Pirani and Bayard-Alpert combination gauge).

The turbo pump inlet can tolerate atmospheric pressure, however this is only advisable if the pump is actively cooled (by the affixing a water cooling kit) as a lot of heat is generated. It is likely that the pump blades will not be able to spin up to full speed in time with such a high inlet pressure and so the controller will shut the pump down.

A hissing noise during pump-down indicates a large leak or air gap that can be sealed by tightening the leaking viewport or flange further or by replacing the gasket. Smaller leaks can be tested for by running acetone around the viewports and flanges. A sudden rise in pressure, means the acetone vapour has managed to enter into the chamber. There may be smaller leaks that can only be detected using a helium leak detector, however the ion pump should be able to compensate for these very small leaks without significant loss of vacuum quality.

After several hours of pumping down, the pressure will level and no longer significantly decrease. At this stage, the out-gassing from the interior walls of the system matches the turbo pump's pumping speed. A final leak test should be performed with acetone and if no pressure change is recorded, the pumps can be turned off and the system refilled with nitrogen back to atmosphere. The system is now ready to bake.

5.3 Bake-out Procedure

In vacuum terminology, 'baking' is a procedure where a vacuum system and components are heated to a high temperature for several days to remove impurities on the interior walls and to release gases absorbed by the metal. This procedure is necessary to attain UHV levels.

There are two main methods for baking a system. The first is to wrap the system with resistive heater tape and insulating jackets and the second is to place the system inside a large 'oven' and literally 'bake' the system.

The advantage of using heater tape is there is no need to build an 'oven' (or bake-out rig) for the system, though bake-out enclosures and insulated 'tents' are available from vacuum specialists. Heater tapes are the only option for very large vacuum systems

where building a rig to contain the system is unfeasible. The temperature to which individual parts or sections can be baked at can also be better controlled by careful placement of the heater tape and control of the current flow through them.

The disadvantage is there is a risk of creating local 'hot spots', particularly around t-sections where several tapes may be close together. Hot spots cause significant stress to flanges and viewports from large temperature gradients. Ideally backup power supplies should be used when using heater tape as a power failure would cause the system to cool down quickly and non-uniformly, risking warping and shattering of viewports from the resulting large temperature gradients.

A bake-out rig has the advantage that although the entire system is enclosed and heated to the same temperature, it can be done so uniformly, without dangerous temperature gradients or 'hot-spots'. A failure of power to the heaters is not so critical as a well-insulated oven is able to keep the resulting cooling at a rate slow enough to maintain temperature gradients within safe levels.

A bake-out rig was used for the MOT system, though one did not have to be constructed because the QuOLS[9] group at Imperial College[10] already has a suitable rig. Once the chamber was leak tested, refilled with nitrogen and the UHV valve sealed, it was transported there for bakeout.

5.3.1 Preparation Work

There is some preparation work be to be done before baking. The first is to cover all viewports with aluminium foil (though the foil should *not* touch the glass). The foil stops airborne grease and dust from settling onto the glass during bake-out. The rubidium dispensers will be one of the 'cooler' parts in the chamber so evaporated gases tend to condense and be absorbed there. To prevent this, a continuous current is run through these during the bake-out. As the dispensers are activated at currents above 4.5 A, a current of 3.0 A is reasonable. The electrical wire used has to have bakeable insulation (not standard plastic as this would melt). The sorption pump also requires power to heat and clean the filaments during bakeout (this is also another 'cool' spot of the system). A continuous current of 3.0 A is run through these during bake-out[11].

Cleaning the outside of the vacuum system with acetone and methanol is optional but any grease left will colour to a golden orange during bake-out. The UHV valve is

[9] QuOLS: Quantum Optics and Laser Science.

[10] Blackett Laboratory, Imperial College, South Kensington, London, SW7 2BW.

[11] Currents required depend on the manufacturer and model of the alkali metal dispensers and sorption pump used.

connected to a bakeable metal vacuum hose that leads to the outside of the oven and connects to a turbo and scroll pump. Finally, the ion pump is attached to the vacuum arm.

Ion pumps are supplied factory sealed at high vacuum. The sealing flange has a cut-off, crimped copper tube. The method to open an ion pump and keep it as clean is to cover the crimped pipe with a nitrogen-filled balloon and use pliers to prise the pipe open, this way nitrogen is sucked into the pump body and not air (which is full of water vapour and dust particles). The scroll and turbo pumps can then be restarted and the UHV valve opened to pump out the nitrogen from the chamber.

Two thermocouples are used inside the oven, one attached to the chamber (using high temperature tape) and the other to monitor the ambient air temperature. This is required during the heating and cooling phases to ensure there is not more than a few degrees difference between the chamber and ambient air temperatures.

The highest temperature the oven can be raised to is limited by the vacuum component with the lowest bake-out temperature. Table 3.1 shows the vacuum components and their corresponding bake-out temperatures.

Torr Scientific	viewports	350 °C
	window coating	250 °C
Ion Pump (Varian)	body	400 °C
	magnet	250 °C
	flange	500 °C
Caburn	CF flanges	450 °C
	straight connector	450 °C
	vacuum hose	450 °C
	feedthrough	350 °C
SAES	sorption pump	400 °C

TABLE 5.1: Quoted bakeout temperatures for various vacuum components.

From table 3.1, the bakeout temperature is determined by the ion pump magnets and the anti-reflection coatings on the viewports. Another consideration is the heating rate, which has to be slow enough so the whole system heats uniformly and temperature gradients – particularly across the viewports – are minimised. The Torr Scientific viewports used quote a maximum heating rate of 2 °C per minute.

The heaters for the oven are connected to a variable power supply that can be varied from 0% to 100% of mains power. The correct heating rate is achieved by simply monitoring the thermocouple readouts with time and adjusting the heater power appropriately. It was decided to heat to a maximum temperature of 220 °C[12]. It should be noted that

[12]This actually corresponds to Gas Mark 7 as the equivalent

even when power to the heaters is not increased, the temperature can continue to rise for some time afterwards due to the large thermal constants of the vacuum components, this is particularly important when close to maximum temperature so as not to overshoot.

5.3.2 Baking Procedure

With the preparation finished, the procedure for the bake-out cycle is as follows:

- Open the UHV and turbo pump valves, switch on scroll to pump out the nitrogen
- When the pressure drops to $\sim 10^{-2}$ mbar, turn on the turbo pump
- When the pressure drops to $\sim 10^{-6}$ mbar, close oven door and begin heating
- Drive 3.0 A through the dispensers and sorption pump
- When at full temperature (220 °C) drive 5.0 A for 15 s through each dispenser separately to degas them
- Bake with the turbo and scroll pumps for three or four days (coincide with the weekend)

As the temperature of the oven is raised, the pressure inside the vacuum system will rise as out-gassing rates increase and contaminants are driven from the interior walls. The turbo is used to pump these out and it is not unusual to see pressures rise to 10^{-4} mbar at full bake-out temperature, over the course of a few days, this will eventually drop as the out-gassing rates decrease.

5.3.3 Cooling Down and Finish

The cooling down phase must also be carefully controlled, gently ramping down the power to the heaters to maintain the 2 °C per minute change required by the viewports. As the oven and vacuum system cools, the pressure will begin to drop. When the pressure drops below 10^{-6} mbar the system should be sealed at the turbo inlet. The pressure will continue to drop to 10^{-8} or 10^{-9} mbar by the time the system returns to room temperature.

Power to the dispensers and the sorption pump can be switched off. The UHV valve should now be tightly closed (torque wrench recommended) so the vacuum system is sealed from the outside. The ion pump can now be switched on and – provided there are no large air leaks – will be able to take the pressure down another one or two orders

of magnitude into UHV region of 10^{-10} or 10^{-11} mbar. Note that it is difficult to obtain accurate measurements in this pressure range. The ion pump current reading is only useful to give an order of magnitude indication.

5.4 Vacuum Pumps

To achieve an ultra-high vacuum (UHV) of $10^{-9} - 10^{-10}$ mbar requires a series of stages in vacuum pumping. A single pump alone does not have the range to reduce the pressure from atmosphere to UHV (see figure 5.4); instead three are required.

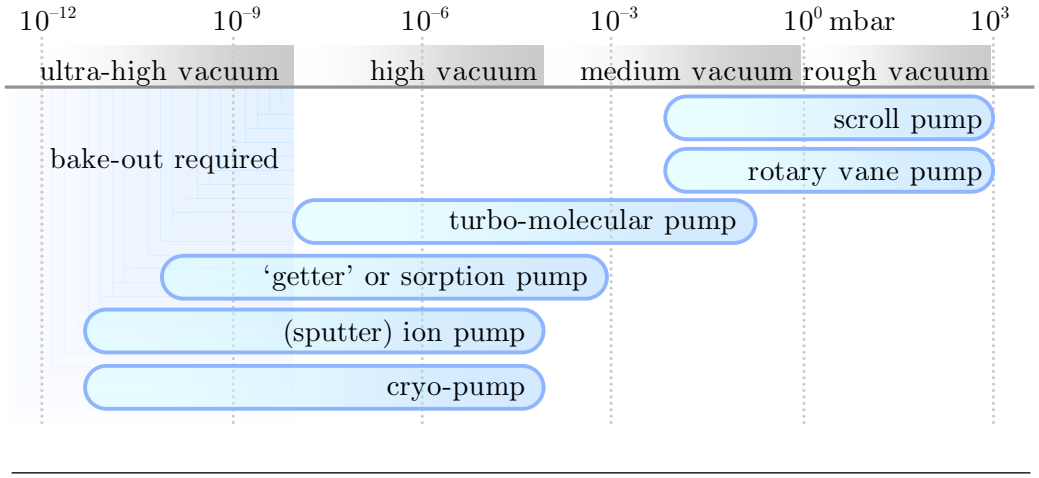

FIGURE 5.4: Vacuum pumps have to be used in combination to achieve UHV from atmosphere. This diagram shows some types of pumps available and the pressure ranges over which they work.

A dry (oil-free) scroll pump is first used to reduce the pressure from atmosphere to 10^{-2} mbar. Next, the turbo pump is activated to bring the pressure down further to $10^{-6} - 10^{-7}$ mbar. A turbo pump can tolerate atmospheric pressure at the inlet though this causes significant heating as the turbine rotation speed increases, most likely leading to the controller shutting the pump down. The turbo pump inlet is fitted to the vacuum chamber after the UHV valve (see figure 5.5 and 5.3) and its exhaust fitted to the inlet of the scroll pump (so that it supports the turbo pump). The exhaust of the scroll pump can be open to air but it is recommended to divert it to the outside.

Out-gassing from the inside surfaces of the vacuum system limits the pressure from decreasing further than $10^{-6} - 10^{-7}$ mbar. Obtaining UHV requires *baking out* the vacuum chamber and components at a high temperature for several days to evaporate and remove the contaminants adsorbed onto their surfaces. The process is described in section 5.3.

The vacuum system holds the pumps along an arm whose end has a UHV valve with the turbo and scroll pump beyond. Directly connected to the vacuum system, closest to the chamber is an ion pump, this should only be activated once the whole system is sealed (the UHV valve is closed) and the pressure is below 10^{-6} mbar.

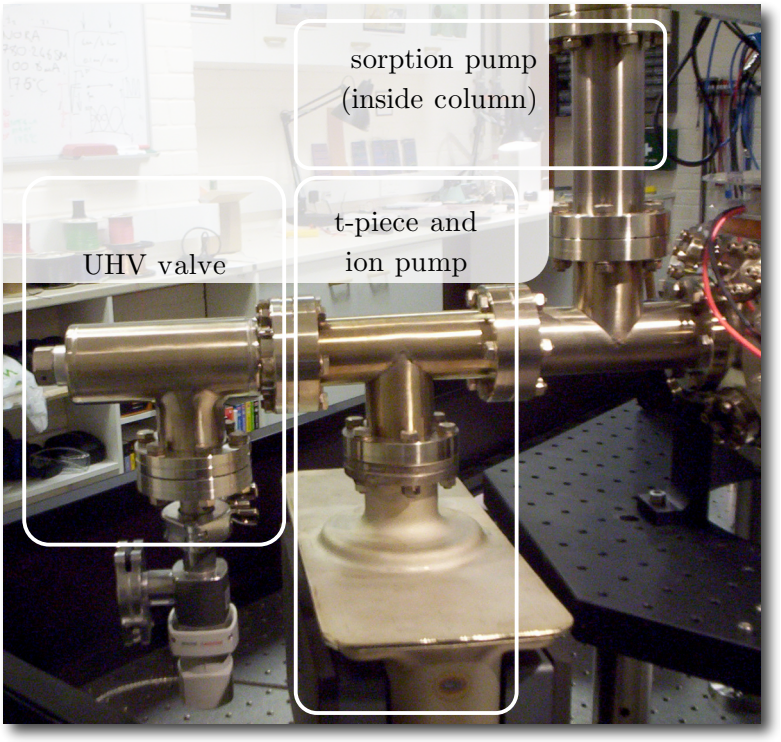

FIGURE 5.5: Vacuum pumps and connections along the arm of the vacuum system.

When the chamber has been baked, the UHV valve can be closed and the turbo and scroll pumps beyond, removed. This leaves the ion pump directly connected to the system and can now be activated. The ion pump will then take the pressure down to $10^{-9} - 10^{-10}$ mbar levels providing all windows and flanges are well sealed and the bake-out procedure was thorough enough for the remaining out-gassing to be sufficiently low for the ion pump to cope with.

An ion pump should have low, medium and high voltage levels. It is sufficient to keep a medium voltage for continuous operation (at the lowest level, the reading becomes too small for the controller to measure). From experience, the current reading can fluctuate on a daily basis, when it creeps too high (an order of magnitude from the average), the voltage can be increased for a brief period (around ten minutes) before lowering it again. This reduces the pressure and returns the reading to normal levels. It is not advisable to keep the voltage high continuously due to an increased risk of electrical discharge and shorting (uncontrolled high-potting) within the ion pump, which can damage it.

The sorption pump (also known as a Getter Pump) is used to pump out light molecules such as Carbon Dioxide, Oxygen and water vapour. It contains a porous material (a 'Getter' alloy), which these gas molecules react with and adhere to, hence removing them from the system. A Getter pump comes as a ready-built cartridge attached to a UHV flange for direct mounting onto a vacuum system.

Initially the getter alloy surface is covered with a layer of oxide from exposure to air. The pump first needs to be activated by heating it under vacuum (or inert gas) and this is done during baking by running a current through it. This removes the oxide layer and prepares the Getter alloy surface for pumping. The pumping efficiency can be increased by heating the sorption pump during operation, but this can cause out-gassing of Hydrogen and so is unsuitable for UHV systems below 10^{-9} mbar.

5.5 Vacuum Measurement

In a similar fashion to vacuum pumps, more than one vacuum gauge is required to measure the pressure from atmosphere to UHV. Figure 5.6 shows some available vacuum gauges and the ranges they work over.

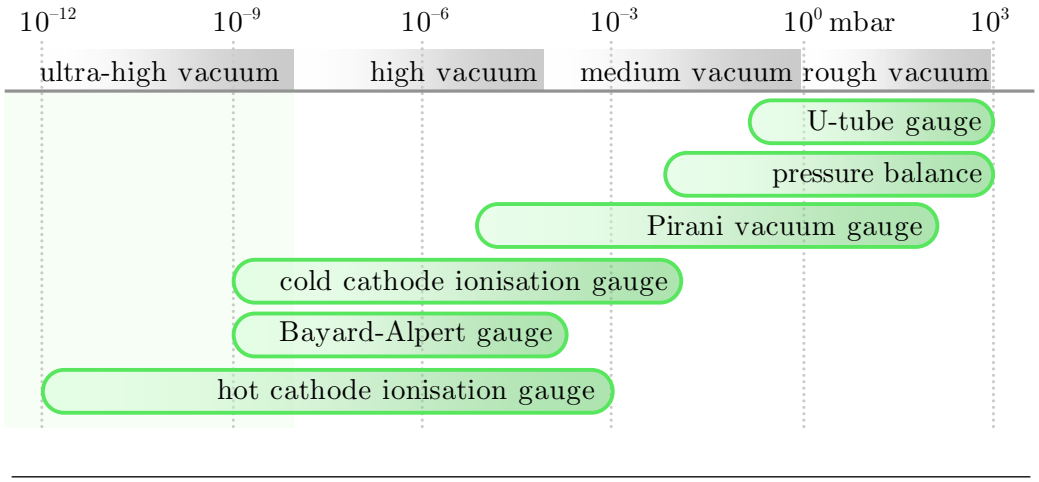

FIGURE 5.6: Some of the vacuum gauges available and the range they work over.

One of the gauges used was a Pirani gauge, which measures the resistance of a piece of wire filament placed inside the vacuum. The wire is heated by an electrical current and as the pressure is reduced, heat removal by conduction is reduced and so the wire heats up further, thereby increasing its resistance. This type of gauge can measure from atmosphere (though it is very inaccurate) down to $\sim 10^{-5}$ mbar.

The Pirani gauge was used to test for leaks when the vacuum system was first pumped down and was placed close to the scroll pump. To measure pressures in the UHV region,

a hot cathode ionisation gauge was used. This gauge has a heated cathode filament to emit electrons that travel through free space (vacuum) and are attracted to an anode by an applied potential. If an electron hits a gas molecule on the way, it can ionise it and the positive ion created is attracted to a negatively charged 'ion collector'. The current created from attracting the gas ions is measured, amplified and translated to a pressure reading.

Using a hot cathode gauge at UHV pressures has a risk of the filament breaking or out-gassing. Just before the chamber bake-out, these two gauges were removed from the system and so the only way to measure the pressure was to use the current reading from the ion pump controller. The ion pump can be viewed as an ionisation gauge though at UHV, vacuum measurement is inaccurate and only an order of magnitude pressure reading can be inferred.

5.6 Magnetic Field Coils

The inhomogeneous field required for the MOT is created by using a pair of wire coils laid horizontally and positioned above each other where the currents in both coils flow in *opposite* directions, this is known as the anti-Helmholtz arrangement[13]. While the Helmholtz condition specifies that the radius of the coils, a is equal to their separation, $2b$ for a uniform field, this is *not* the case for the anti-Helmholtz condition. Section E derives the anti-Helmholtz condition and shows that in order to produce a field that is zero at the centre and has the steepest field gradient at this point, $\sqrt{3}a = 2b$ [121].

The vacuum chamber has two large horizontal circular grooves (above and underneath) that were designed as spaces for the anti-Helmholtz field coils. This immediately constrains the coil radius and width and allows us to determine other physical parameters such as wire gauge and number of turns using the information in Appendix I.

The coils (shown in figure 5.8) were made in the Mechanical Workshop. An aluminium pre-form was made and polyester insulated copper wire wound onto this using a slow turning lathe. After each row the wire is fixed by painting on a thin layer of epoxy. It is important to wind the wire as uniformly and tightly as possible as initial kinks and bumps grow as further layers are wound over the top.

It is possible for the wire insulation to be scratched during winding and a short may be created within the coil. Testing coil resistance and current drawn and comparing to prior calculations is important to detect this.

[13]Note that reversing the direction of the current flow in both coils reproduces the same anti-Helmholtz field seen in figure 5.7, but with the field direction reversed. Both currents flowing in the *same* direction produces the Helmholtz arrangement (a large region of uniform magnetic field between the coils).

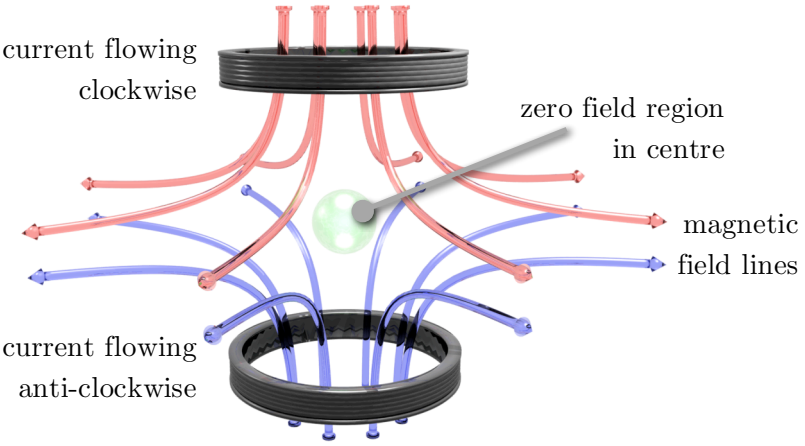

FIGURE 5.7: The magnetic field produced from an anti-Helmholtz coil pair of radius, a and separation, $2b$. The field is inhomogeneous and has a zero field region in the centre which is also the point of maximum field gradient.

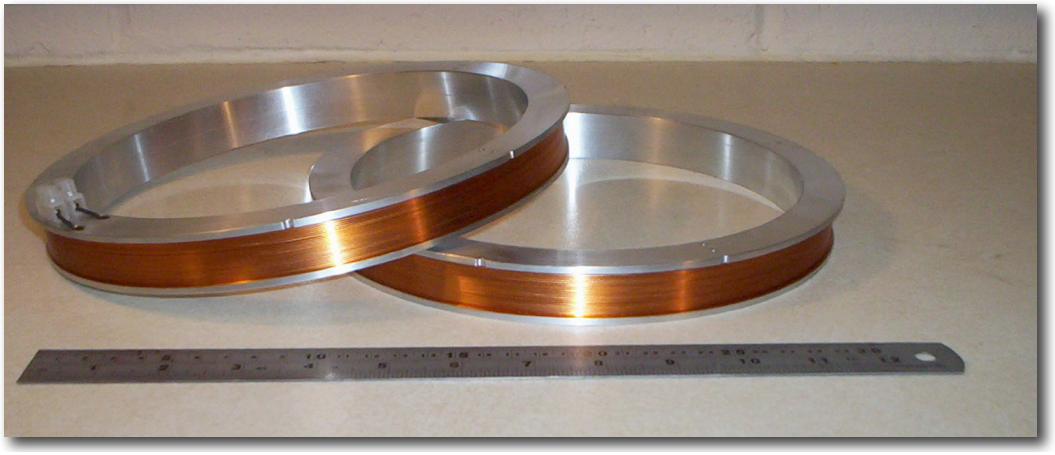

FIGURE 5.8: Magnetic field coils for the MOT; 432 turns each, wound on aluminium pre-forms (3 mm thick) with 22 SWG insulated copper wire.

The aluminium pre-forms have a thickness of 3 mm. The inner radius is constrained to $a = 103$ mm and the groove width to 15 mm. With this coil cross section, A it was decided to use $\simeq 430$ turns of 0.710 mm (Standard Wire Gauge: 22, closest American Wire Gauge: 21) copper wire.

Wire is sold by mass so a SWG 22 wire coil of 500 turns[14] gives a length, l of about, $2\pi aN \simeq 300$ metres. This corresponds to a volume, $V = l \times \pi r^2_{\text{SWG-22}} \simeq 1.3 \times 10^{-4}$ m^3. The density of Copper, $\rho_{\text{Cu}} = 8920$ kgm^{-3}, and so the mass of the coil is simply $V\rho_{\text{Cu}} \simeq 1.14$ kg. This means a 3 kg reel is sufficient for two coils.

[14]Over estimated for contingency as too long a length is better than too short.

After passing electrical continuity checks, a simple magnetic field characterisation along the central axis of the coil pair was performed using a Hall probe. The results, with the theory[15] are shown in figure 5.9.

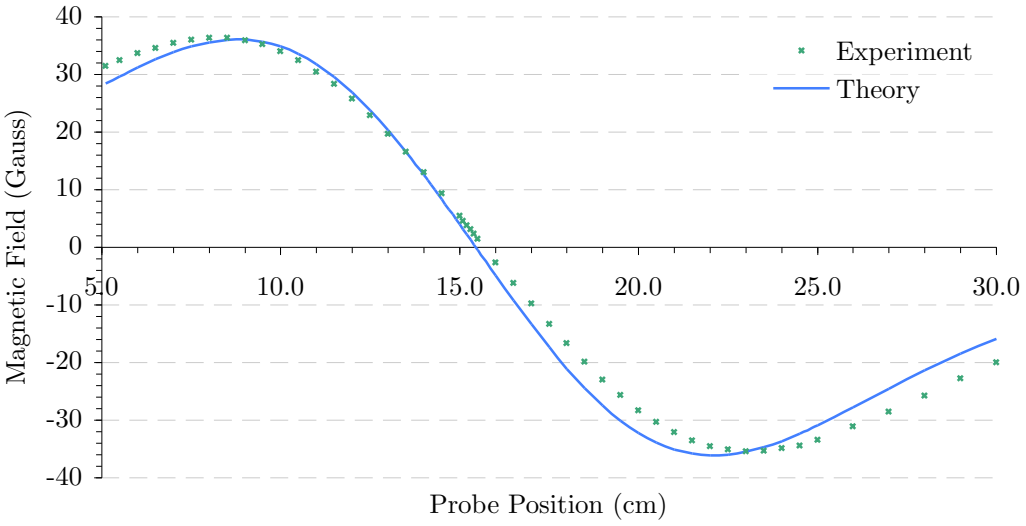

FIGURE 5.9: The axial field profile for our pair of anti-Helmholtz coils (and the theoretical prediction).

There is some discrepancy between the theoretical curve and the measured values though the overall shape is correct. The differences can be attributed to experimental error, in particular that the Hall probe was likely to have been off-centre from the coil pair centre axis.

The power supply used to run the coils must be set to 'current control' or 'current limited' mode, this is because as current flows through the coils they heat up, increasing their resistance and so requiring an increasing voltage to drive the same current. A 'voltage limited' mode means the current would slowly decrease as the coils heated and this would cause the magnetic field to decrease with it.

The coils produce a suitable field gradient of ~ 5 Gcm^{-1} when a current of 2.0 A flows through each coil. As the coils are passively air-cooled, the resistive heat produced can become a problem at higher currents. Though the vacuum chamber acts as a large heat sink, coil temperatures need to be monitored if they have been on for a long period of time (over an hour). The coils reach a steady state temperature of $\sim 70°$ for a 2.0 A current.

[15]The theory and the equation for the curve in figure 5.9 is described in Appendix D.

Chapter 6

MOT Characteristics

6.1 Introduction

Our first working MOT was achieved in early 2007. This chapter describes the characterization of the MOT in terms of the number, temperature and volume of the trapped atoms, the accumulation time and sensitivity to experimental parameters.

Initial operation of the MOT was frustrated by the transverse beam quality of the trapping laser, until it was improved by spatial filtering of the beam by focusing it through a small iris to obtain a more Gaussian-like profile[1]. Persistence with parameters such as laser alignment, detuning and waveplate orientation (see section 4.4.1) eventually produced the tiny, brightly glowing (but invisible to the naked eye) dot of cold atoms at the centre of the vacuum system, as shown in figure 6.1.

The atoms are guided towards regions where the net magneto-optical, magnetic and gravitational force is zero, and it is possible to manipulate the shape of the MOT cloud by adjusting the alignment of the lasers or the magnetic field. Passing unequal currents through the anti-Helmholtz coils tends to shunt the cold atom cloud vertically along z. The laser alignment has a more dramatic *shearing* effect on the MOT cloud because of the unequal Doppler forces created. A range of interesting shapes such as rings, figures of '8' and dumbbells can be created with careful adjustment of the laser alignment and magnetic field as shown in figure 6.2.

[1]When a laser beam is passed through a lens, the pattern produced at the focus is the 2D Fourier transform of the transverse (spatial) profile of the incoming laser beam. An iris can be used at the focus to cut out the higher frequency components and hence cut out the higher spatial modes of the beam to hopefully just leave the main, single frequency (and hence single Gaussian spatial mode) of the laser. There is a trade-off between the improvement in transverse beam quality and the power lost due to the diameter of the aperture or iris. It was later discovered that focusing through the AOMs performs a similar spatial filtering function.

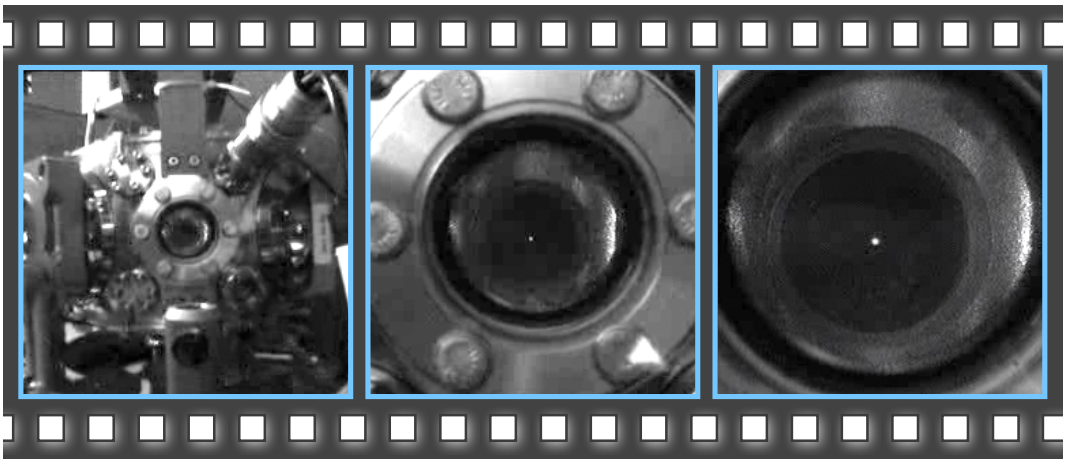

FIGURE 6.1: The first images of the cold atom cloud of the MOT. The MOT beams are just visible in the picture on the right.

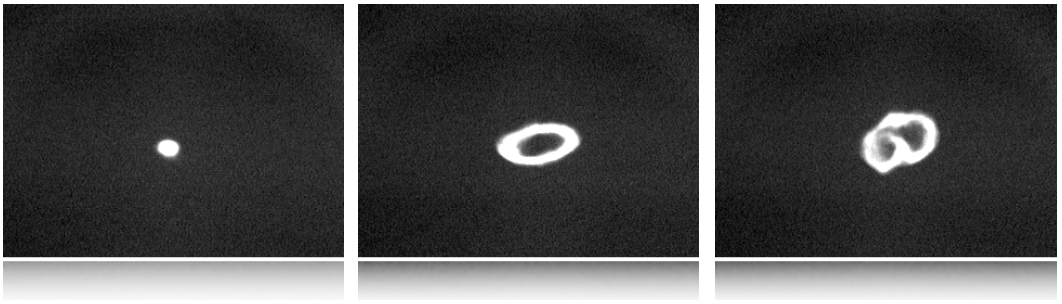

FIGURE 6.2: The ideal shape for the cold atomic cloud of a MOT is spherical (left image), however, through small adjustments of the magnetic field and mis-alignments of the trapping beams, unequal scattering (Doppler) forces shear and contort the cloud into an interesting array of shapes such as rings (middle image) and figures of '8' (right image).

The imaging system used to record videos of the MOT (from which still images are captured) is a simple zoom lens and monochrome CCD camera, similar to typical security cameras and sensitive into the near infra-red; the output from the CCD can be recorded using a computer with a video capture card. For more quantitative recording, a carefully aligned and suitably masked amplified photodiode was used.

6.2 Capture Velocity

The capture velocity, v_c, is the maximum velocity at which atoms may become caught and trapped in the MOT. An atom travelling at v_c and entering the MOT region comes to a stop by the time it reaches the far end of the region (the edge of the laser beam). The greater the capture velocity, the larger the fraction of atoms from the initial Maxwellian

speed distribution (shown in figure 6.3) that can be caught, and hence the larger the MOT cloud.

An initial estimate of the capture velocity can be obtained from

$$v_c \simeq 2\Gamma\lambda \tag{6.1}$$

where the factor, $\Gamma\lambda$ is the velocity for which the Doppler shift of the laser, as seen by the moving atom, equals the transition linewidth, Γ. The estimate in equation 6.1 assumes that atoms will absorb from the optical molasses beams up to twice the linewidth before the laser becomes no longer resonant. It also assumes very large (infinite) diameter beams. For ^{85}Rb, we thus obtain a capture velocity of, $v_c \sim 60$ ms^{-1}. This approximate value proves however to be optimistic, and more precise calculations – taking into account the finite beam diameter – produce a lower figure.

The frequency detuning of the optical molasses beams and the energy level shift from the magnetic field puts a limit on the Doppler frequency shift for which the atoms will absorb from the laser beams. Atoms travelling too quickly will have too great a Doppler shift and will therefore not absorb and not be laser cooled. Numerical simulations and experiments show v_c to depend on the saturation intensity and frequency detuning of the optical molasses. Increasing the detuning increases the capture velocity at the cost of a higher final temperature of the MOT cloud (as the Doppler temperature depends on the detuning) to the point where atoms are not sufficiently slowed to become trapped. A large detuning also runs the risk of exciting hyperfine levels other than just the cooling transition.

A better estimate of the capture velocity, v_c can be obtained by beginning with equating the atomic kinetic energy, E_K to the atomic internal energy, E_I

$$E_K = E_I \tag{6.2}$$

$$\frac{1}{2}mv_c^2 = \frac{3}{2}k_{\mathrm{B}}T$$

$$v_c = \sqrt{\frac{3k_{\mathrm{B}}T}{m}} \tag{6.3}$$

The temperature, T appears in E_I and this is the energy that must be dissipated by Doppler cooling, E_D over the extent of the MOT trapping region (the width, d of the

region where the MOT beams overlap). Hence E_K can be equated to E_D

$$\begin{aligned} E_K &= E_D \qquad (6.4) \\ \frac{3}{2}k_{\mathrm{B}}T &= Fd \\ T &= \frac{2Fd}{3k_{\mathrm{B}}} \qquad (6.5) \end{aligned}$$

Where F is the Doppler cooling force. The MOT trapping region – where the beams overlap – is approximately the beam width, $2z'$, where z' is the beam radius. The Doppler cooling force, F can be substituted from the expression given in equation 3.25 to give

$$T = \frac{2}{3k_{\mathrm{B}}} \cdot \left[\frac{\hbar k \Gamma}{2} \cdot \frac{s_0}{1 + s_0 + (2\delta/\Gamma)^2} \right] \cdot 2z' \qquad (6.6)$$

A final assumption is made that the atoms see no laser detuning, δ because the inhomogeneous field of the MOT Zeeman shifts the atomic energy levels so that the laser (with a fixed detuning) remains on resonance with the atoms as their speed slows while they are being cooled so $\delta = 0$ in equation 6.6 giving the final result of [122]

$$T_0 = \frac{2\hbar k \Gamma z' s_0}{3k_B(s_0 + 1)} \qquad (6.7)$$

where the experimental parameters are

$$\begin{aligned} \text{Total Beam Power} &= 30 \text{ mW} \\ &= 5 \pm 0.1 \text{ mW per beam} \\ \text{Beam Radius, } z' &= 0.75 \pm 0.1 \text{ cm} \\ \text{Beam Area} &= 1.8 \pm 0.3 \text{ cm}^2 \\ \text{Saturation Intensity, } I_0(\mathrm{Rb}) &= 1.6 \text{ mWcm}^{-2} \\ \text{Beam Intensity, } I &= 2.8 \pm 1.3 \text{ mWcm}^{-2} \\ \text{On resonance saturation parameter, } s_0(= I/I_0) &= 1.8 \pm 0.8 \end{aligned} \qquad (6.8)$$

where T_0 is akin to a 'temperature depth' of the MOT and z' is the radius of the trapping beams. Even with a small beam radius, z' and low saturation parameter, s_0, the resulting temperature depth, $T_0 \sim 1.2 \pm 0.5$ K. This translates to a $v_c \sim 18 \pm 9$ ms^{-1} (with the equipartition of energy theorem). The large errors in T_0 and v_c come from the uncertainty in the beam diameter. As the beam does not have a top-hat transverse profile, it is difficult to judge a suitable value for the 'diameter', $2z'$ of the

beam. The error from this value propagates through further calculations and contributes significantly to the error in each result.

The rubidium evaporating from the alkali metal dispensers creates a background vapour of atoms with a Boltzmann energy distribution from which the MOT loads. Though these atoms are at room temperature (from collisions with the chamber walls), there are enough atoms in the lower energy tail end of the distribution with a velocity at v_c or less to load a MOT cloud, however as the probability is small, this would explain why the MOT takes several seconds to load from the background vapour[2].

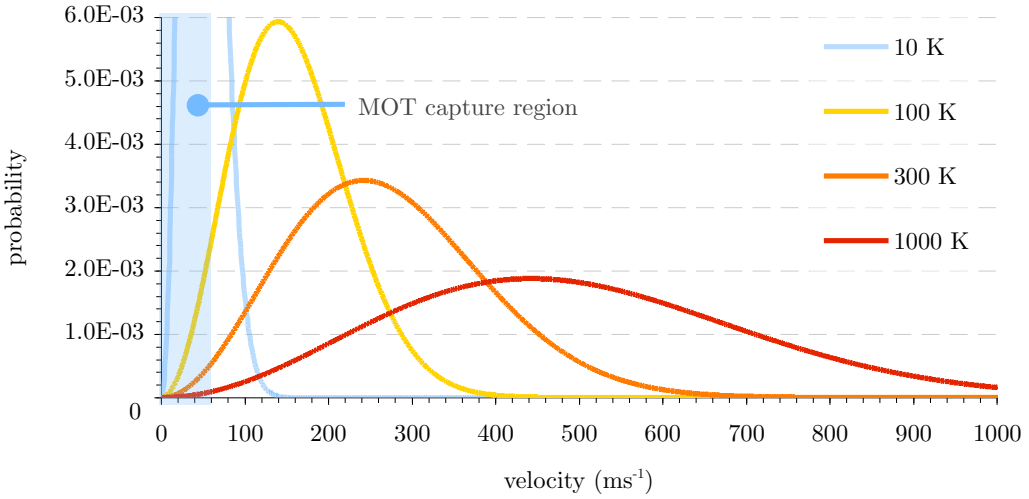

FIGURE 6.3: The Maxwell speed distribution for a range of temperatures for ^{85}Rb. The MOT capture region is small but the large number of atoms in the background vapour means the cold MOT cloud can still contain many million atoms.

The pressure of rubidium inside the vacuum chamber is $(1 \pm 0.5) \times 10^{-10}$ mBar from the ion pump current reading. This corresponds to $(2.4 \pm 1.2) \times 10^{6}$ atoms cm^{-3} (using the ideal gas law). As shown in figure 6.3, a significant number of atoms remain below v_c to allow a MOT cloud to be created containing a few million atoms from the background vapour.

6.3 MOT Loading Time and Behaviour

The MOT loading characteristics can be established by observing the growth, in size and intensity, of the MOT cloud with time when the trapping and repump beams are suddenly switched on. This requires simultaneous triggering of AOMs and oscilloscope (to record the signal) and is done using an arbitrary signal generator controlled with a

[2]Note that the capture velocity determines the fraction of atoms that can be trapped in a MOT from a background vapour, it does not relate to the final number of atoms in the MOT cloud.

computer. Loading takes several seconds and so can be easily seen in real-time with a CCD camera and is shown in figure 6.4.

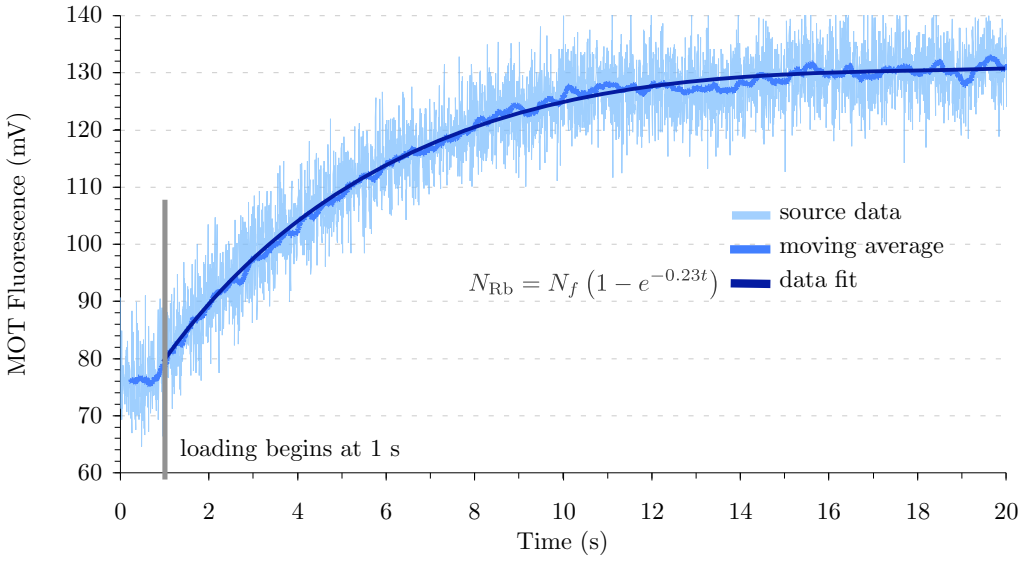

FIGURE 6.4: The MOT loading from the background vapour, made by recording the fluorescence with time. INSET: a simple equation of exponential form is used to fit the loading curve and gives a loading time constant of ~ 0.23 s.

The curve in figure 6.4 can be fitted to [84, 123]

$$N(t) = N_{max}\left(1 - e^{(-t/\tau_{MOT})}\right) \tag{6.9}$$

The MOT loading time is defined by τ_{MOT} and N_{max} is the final number of trapped atoms in the MOT cloud. A loading rate, R can be defined where [123]

$$R = \frac{N_{max}}{\tau_{MOT}} \tag{6.10}$$

So for a MOT cloud containing $\sim (4.4 \pm 0.7) \times 10^6$ atoms and a loading time constant of $\tau = 1/(0.23 \pm 0.01)$ s^{-1}, the MOT loading rate $R = (1.0 \pm 0.2) \times 10^6$ atoms s^{-1}. This can be compared with an independent, analytical expression for R [35]

$$R = 0.5\rho_{\mathrm{Rb}} V^{2/3} v_c^4 \left(\frac{m_{\mathrm{Rb}}}{2k_B T}\right)^{3/2} \tag{6.11}$$

This equation, with a notable sensitivity to the capture velocity v_c, gives the predicted loading rate in terms of the density of the background rubidium vapour, ρ_{Rb}, the trapping volume, V (dependent on the diameter of the trapping beams) and the capture

velocity, v_c. For our experimental parameters

$$\begin{aligned} T &= 300 \text{ K} \\ V &= (3.38 \pm 1.35) \times 10^{-6} \text{ m}^3 \\ P &= (1.0 \pm 0.5) \times 10^{-10} \text{ mBar } = (1.0 \pm 0.5) \times 10^{-8} \text{ Pa} \\ \rho_{\text{Rb}} &\sim (2.42 \pm 1.21) \times 10^{12} \text{ atoms m}^{-3} \\ v_c &= 17 \pm 9 \text{ ms}^{-1} \end{aligned}$$

where the trapping volume, V, is here taken to be the cube of the beam diameter (even though this is not strictly true), giving a predicted loading rate of $R = (1.8 \pm 3.9) \times 10^6$ atoms s^{-1}. The massive uncertainty is due to the quartic dependence upon the poorly known capture velocity v_c and beam diameter. Since the minimum loading rate of $(1.8 - 3.9) \times 10^6$ atoms s^{-1} does not make sense, only an upper bound of $(1.8 + 3.9) \times 10^6$ atoms s^{-1} can be stated.

6.3.1 Changing the MOT Loading Rate

In a recent paper by Klempt *et al* [123], the MOT loading rate was shown to be dramatically increased by shining UV light into the vacuum chamber. The UV light causes the rubidium coated on the inside chamber walls to be desorbed and contribute to the background vapour, which in turn increases the loading rate. The process is termed Light-Induced Atomic Desorption (LIAD)[3].

As a rough verification of this, an array of 10 UV diodes at $\lambda = 400 \pm 26$ nm (FWHM) was made and shone into the chamber and the MOT cloud was made. Usually, the magnetic field coils have to be switched on for an around an hour to heat the chamber to cause a sufficient amount of rubidium to desorb from the walls to create the MOT cloud. With the UV light, the MOT cloud could be created with no prior heating necessary. Shining the UV light in the chamber while the MOT cloud was present increased its size and brightness so significantly that the effect could clearly be seen with the CCD and monitor screen.

LIAD is a convenient process that means by using (easily replaceable) UV LEDs, the finite material in the rubidium dispensers inside the chamber does not need to be activated as frequently and consequently will last for a longer period of time before requiring replacement[4].

[3] Possible interpretations of LIAD are discussed in a paper by Hatakeyama *et al* [124].

[4] A process that requires the vacuum chamber to be brought back up to atmospheric pressure for replacement of the dispensers and the baking process to be redone afterwards.

6.4 MOT Characteristics

6.4.1 MOT Cloud Dimensions

The MOT spatial size was measured by focusing the CCD at the image plane of a lens looking at the MOT cloud. A scale was also placed at the image plane so that the MOT and scale were simultaneously in focus. The MOT-lens and lens-image plane distances were kept equal so the magnification of the MOT cloud was kept at 1:1. This arrangement – shown in figure 6.5 – allowed us to estimate the MOT cloud extent to be 0.8 ± 0.2 mm in diameter.

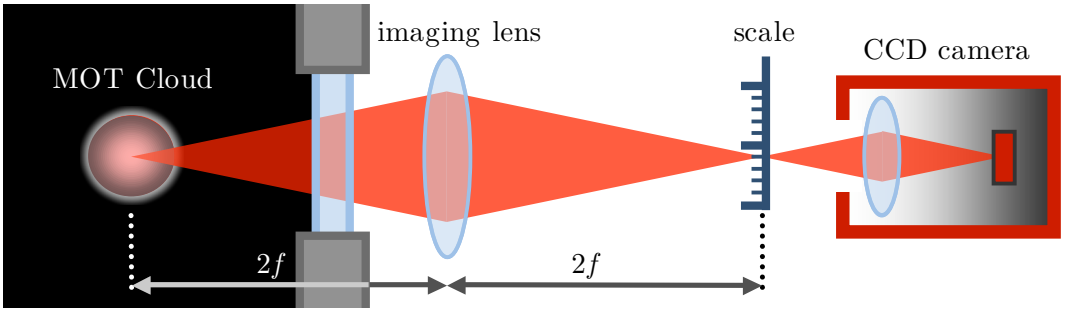

FIGURE 6.5: The method of determining the size of the MOT cloud by projecting its image onto a scale. The chamber geometry determines the focal length of the imaging lens used and the image-lens-object distances must be noted to take into account any image magnification.

6.4.2 MOT Atom Number

The number of rubidium atoms in the MOT can be derived from carefully calibrated measurements of the absolute intensity of fluorescence when the atoms are pumped by the trapping and repump lasers; the relevant equations and parameters are summarized in figure 6.6.

$$N = \frac{\xi\tau}{hf\eta_e\varrho_e} \qquad \varrho_e = \frac{1}{2}\frac{s}{s+1} \qquad s = \frac{s_0}{1+(2\delta/\Gamma)^2} \qquad \eta_e = \frac{\pi r_l^2}{4\pi d_l^2}$$

ξ	measured fluorescence
τ	excited state lifetime
hf	photon energy
η_e	geometrical detection efficiency
r_l	lens radius
d_l	MOT-lens distance
s	off-resonance sat. parameter

FIGURE 6.6: The equations needed to find the number of atoms in the MOT cloud. The fluorescence measurement, ξ has the largest uncertainty.

Most parameters can be easily determined, and the precision of the result is dominated by uncertainties in the measured fluorescence intensity, ξ (this also includes the quantum efficiency of the detector used to measure the fluorescence) and the on-resonance saturation parameter, s_0. The large uncertainty in the laser beam diameter, $2z'$ propagates through the calculation for the beam area, A and to the beam intensity, $I = P/A$ (where P is the laser beam power). As $s_0 = I/I_0$ where I_0 is the saturation intensity for rubidium, the large error in s_0 originates from the error in the laser beam diameter, $2z'$.

For our MOT system, these parameters are

$$\begin{aligned}
\xi &= 1.2 \pm 0.2 \text{ nW} \\
\tau &= 26 \text{ ns} \\
hf &= 780.24 \text{ nm } = 2.55 \times 10^{-19} \text{ J or } 1.6 \text{ eV} \\
r_l &= 1.27 \text{ cm} \\
d_l &\sim 18.0 \pm 0.1 \text{ cm} \\
s_0 &= 1.77 \pm 0.84 \\
\delta &= 2\pi \cdot 18 \text{ MHz} \\
\Gamma &= 2\pi \cdot 6 \text{ MHz}
\end{aligned}$$

We thus obtain an upper bound for the number of rubidium atoms in the MOT of $N = (4.4 + 4.9) \times 10^6$ within but at the lower end of typical values reported for similar systems elsewhere. The large uncertainty in N can be traced through the on-resonance saturation parameter, s_0 and back to the uncertainty in the beam diameter, $2z'$. Using top-hat profile beams with a well-defined diameter would greatly reduce the uncertainty in z' and this would filter through several calculations dependent upon it to give reduced uncertainties for the MOT atom number N, MOT density ρ_{MOT} and other MOT cloud characteristics.

The first measurement was made using a low-noise optical power meter and repeated using a photodiode detector. The photodiode was more difficult to align and to obtain consistent results from and also required a low noise current preamplifier. From the signal obtained and working through the equations in 6.6 a value of 5.9×10^5 was obtained. This value is low and is likely due to difficulties aligning the detector to collect all the light from the imaging lens.

6.4.3 MOT Density

From the values for the MOT size and atom number obtained above, the density of the trapped atom cloud was calculated to be $\rho_{\mathrm{MOT}} \sim (1.64 \pm 1.2) \times 10^{10}$ atoms cm^{-3}. The uncertainty is comparable with the result itself because of the uncertainty in the beam diameter, $2z'$.

6.5 Determinations of the MOT Cloud Temperature

There are various methods for measuring the temperature of a cold atomic cloud. The 'release and recapture' method allows a brief period of free flight, and determines the fraction of the trapped population that remains within the trapping region until it is re-established. Time-of-flight imaging determines the atomic velocity distribution from images of the spatial distribution after a period of free expansion. Alternatively, the velocity distribution may be measured directly by Doppler or recoil-induced resonance spectroscopy. Here, we report results using the first two approaches.

6.5.1 Release and Recapture

From the various techniques of measuring the atom cloud temperature, 'release and recapture' [125] was chosen for its simplicity. The method involves creating a MOT cloud and then switching off both the trapping and repump lasers for an interval of time in which the MOT cloud undergoes free expansion, and then flashing both lasers for a few milliseconds to determine the fraction of the atoms remaining inside the volume occupied by the original MOT cloud[5]. The time interval between extinction and probe is then varied to give a 'trap-loss' curve.

One such experiment can be seen in the diagram in figure 6.7, where the MOT trapping and repump beams – on at the start – are suddenly switched off and there is a dark period of 15 milliseconds for the hottest atoms to escape from the cloud. Then there is a brief flash of both lasers lasting two milliseconds that produces the second fluorescence spike. The height of this spike indicates the fraction of atoms remaining in the original MOT cloud volume. Since the initial fluorescence from the MOT is also recorded, the fraction remaining can be determined.

[5]Ideally the laser beams would be narrowed to cause fluorescence from just the atoms remaining in the original MOT cloud volume, experimentally this is not possible without using a fast adjustable iris to narrow the beams and unrealistically precise alignment. Instead the MOT cloud volume and the region around it is probed.

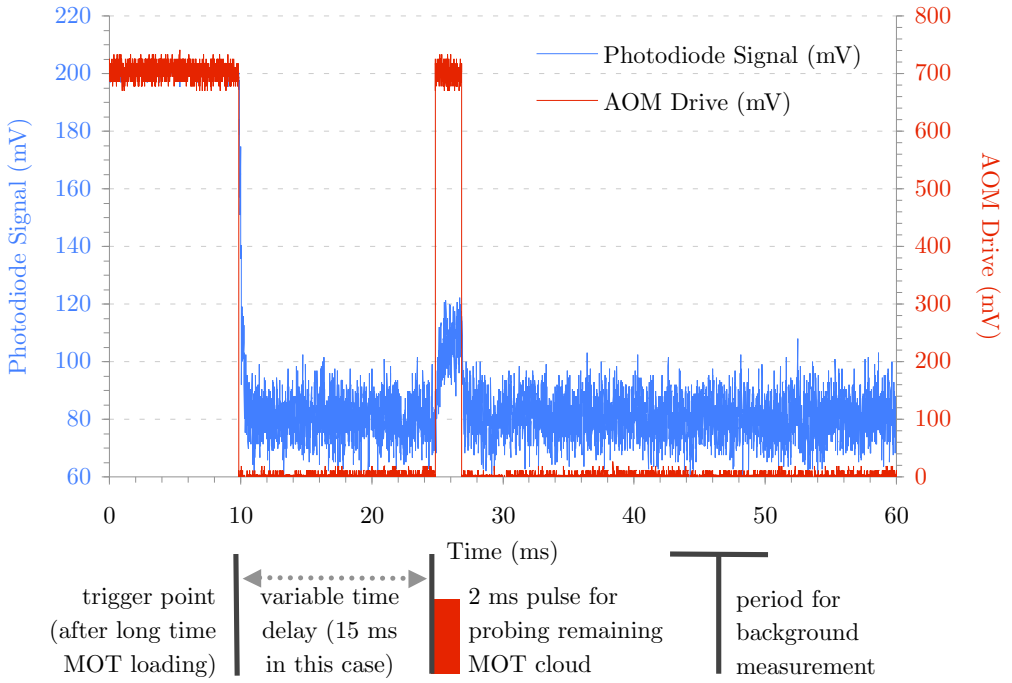

FIGURE 6.7: A single run from a 'release and recapture' experiment. The height of the photodiode peak from the flash is an indication of how much of the original MOT cloud remains after the optical molasses is switched off.

For each time interval a percentage remaining is recorded and can be plotted in a final graph of trap loss with time to give the trap loss curve. From this, it is possible to find a value for the MOT cloud temperature. Figure 6.8 shows the loss curve from two separate experiments. In one experiment, care was taken to align and optimise the MOT whereas in the other it wasn't. This shows itself in the differing loss rates, the optimised MOT falls off slower as the atoms are overall cooler and have a lower average temperature.

From the trap-loss curve a theoretical model is created in which a uniform density MOT cloud is assumed[6] and each atom is given a random velocity from the Boltzmann velocity distribution. These two are then convolved and evolved in time and the fraction remaining in the original MOT cloud area is calculated as shown in figure 6.9. This approach appears simple but runs into analytical difficulties that produce unphysical results (e.g. ring distributions) when extrapolated to three dimensions in spherical co-ordinates.

Remaining in 1-D and inputting our experimental conditions into the model parameters gives a MOT cloud temperature of $\sim 80 \pm 40$ μK. The uncertainty comes in because

[6] A thermalised, uniform density MOT cloud has been shown in [126] to be unphysical. Removing these assumptions requires a much more complicated analytical approach that is not covered here.

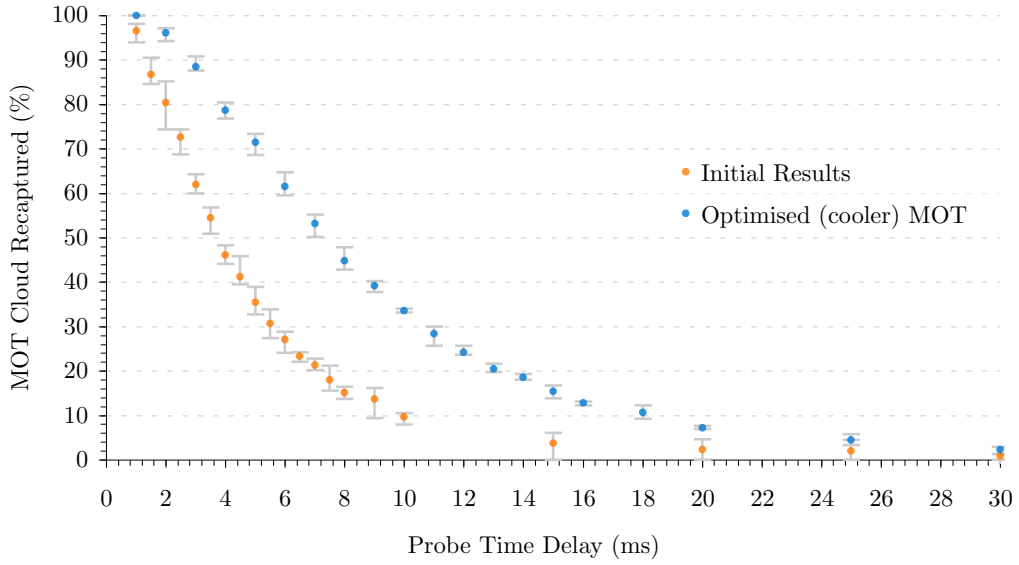

FIGURE 6.8: Trap loss rate curves using the 'release and recapture' method. The optimised MOT shows a slower decay rate because of the lower average temperature of the cloud.

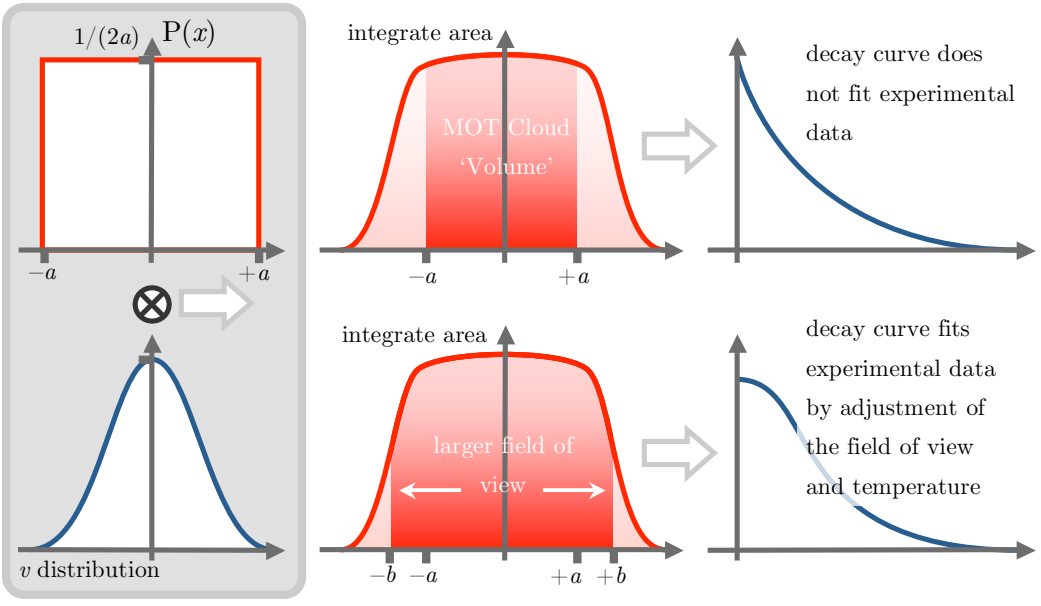

FIGURE 6.9: By analytically convolving a uniform density MOT cloud with the Boltzmann velocity distribution (left) and evolving in time, the trap loss can be reproduced by integrating the area under the resulting curve (centre). Integrating just the original MOT cloud 'volume' does not fit experimental data (top right) but requires a larger field of view (bottom right).

some parameters (such as field of view of the MOT, which relates to integrated area) had large uncertainties. Despite this, the MOT cloud temperature result appears to be lower than the Doppler temperature limit for rubidium, $T_{\mathrm{D}}(^{85}\mathrm{Rb}) = 150\ \mu\mathrm{K}$. This result indicates that there are sub-Doppler cooling processes occurring that is reducing the temperature of the MOT cloud beyond the Doppler limit, T_{D}.

A numerical computer simulation for the MOT has been developed by James Bateman[7], where the MOT cloud is modelled by giving each atom in it an initial random position in a sphere and a velocity according to the Boltzmann distribution. Each atom then isotropically releases photons in a spherical shell (from fluorescence caused by the probe beams). The photons are ray-traced and those that fall within a certain solid angle are collected by a modelled 'lens'. The refraction by the lens is calculated for each photon and those that fall onto the photodiode area are counted. This model is then evolved in time to give a trap loss curve.

By running the simulation with the measured experimental parameters and varying the cloud temperature in the model, a series of decay curves is calculated and the cloud temperature can be inferred when the experimental data are overlaid as shown in figure 6.10.

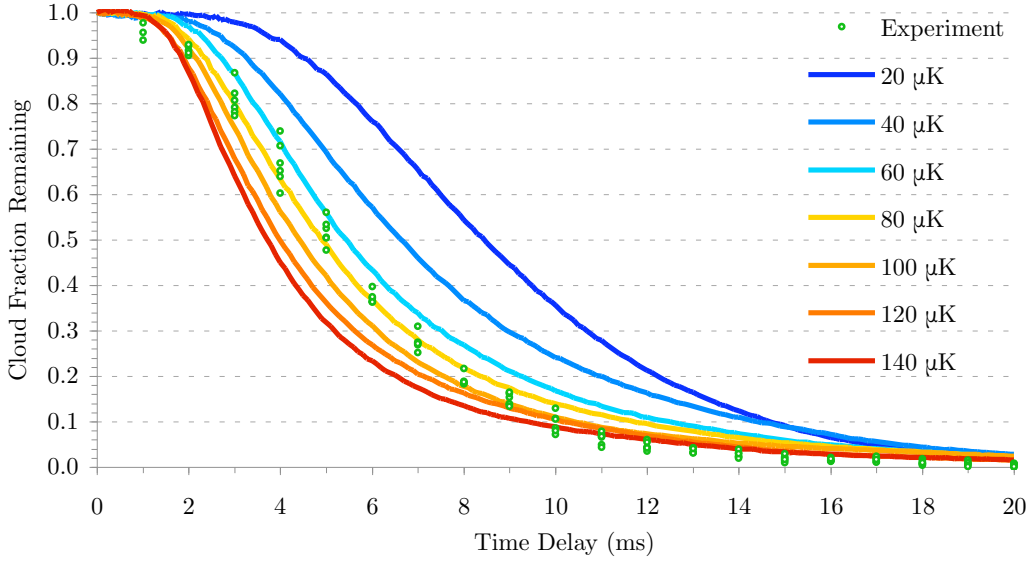

FIGURE 6.10: The experimental 'release and recapture' data overlaid onto a series of temperature curves predicted by a numerical simulation. The simulation predicts the MOT cloud to be at $70 \pm 30\ \mu\mathrm{K}$, which is well below the Doppler Limit for $^{85}\mathrm{Rb}$.

Until a discontinuity in the tail at 10 ms (from figure 6.10) – caused by the repump laser drifting out of lock and having to be reset before the experiment could continue

[7]James Bateman, Quantum Control Group, School of Physics and Astronomy, University of Southampton, Southampton, UK.

– the data fit closely to the 80 μK curve, especially in the most sensitive region when around half of the cloud remains, and almost all points lie between the curves for 60 and 100 μK. We therefore estimate the MOT cloud temperature to be 80 ± 10 μK, consistent with the more primitive 1-D analysis above.

6.6 MOT Cloud Expansion

A high frame-rate camera allows the possibility of capturing images of the MOT cloud as it undergoes ballistic expansion when the MOT beams are switched off. From these images it is possible to track the expansion rate, ascribe it a speed and convert it to a temperature to compare with the 'release and recapture' experiments in the previous section.

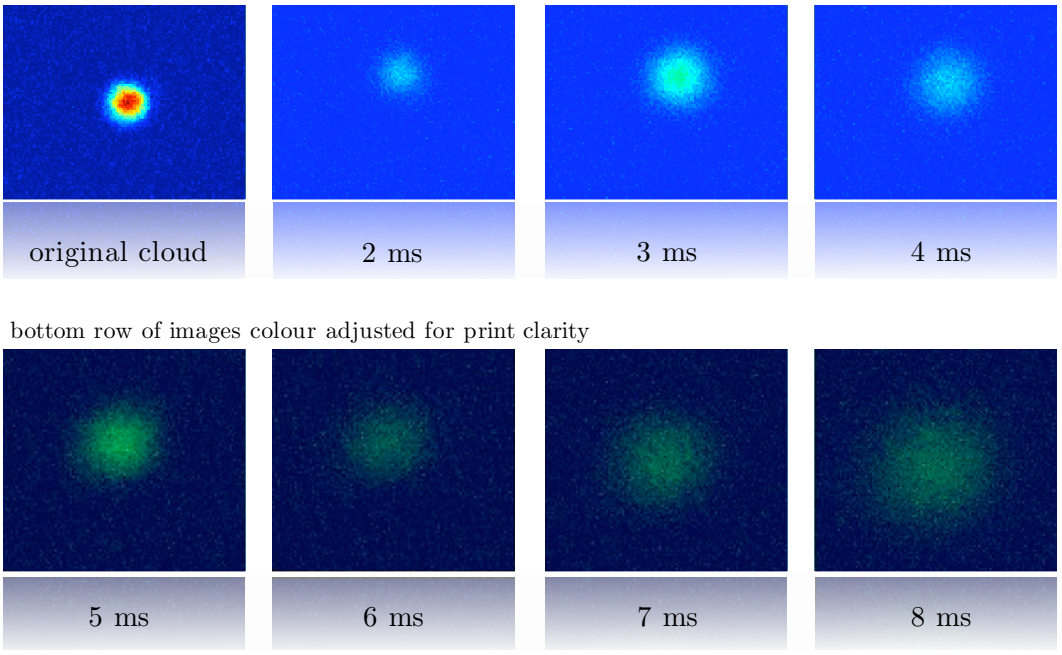

FIGURE 6.11: False-colour images taken by a fast camera running at 500fps, showing the expansion of the MOT cloud in time. The expansion rate can be measured and translated into a velocity and hence a temperature to compare with the 'release and recapture' results in the previous section.

The MOT expansion images were taken by a process similar to 'release and recapture', where after loading the MOT, the beams are switched off and then – after a variable time-delay – flashed as probe beams to record the fluorescence image. A frame rate of 500 frames per second (500 fps) was achieved through careful adjustment and optimisation of the gain, exposure and region of interest (ROI)[8].

[8]Decreasing the exposure can rapidly increase the frame rate at the cost of brightness of the image, which can severely affect cloud images at longer time delays. This can be offset by increasing the gain,

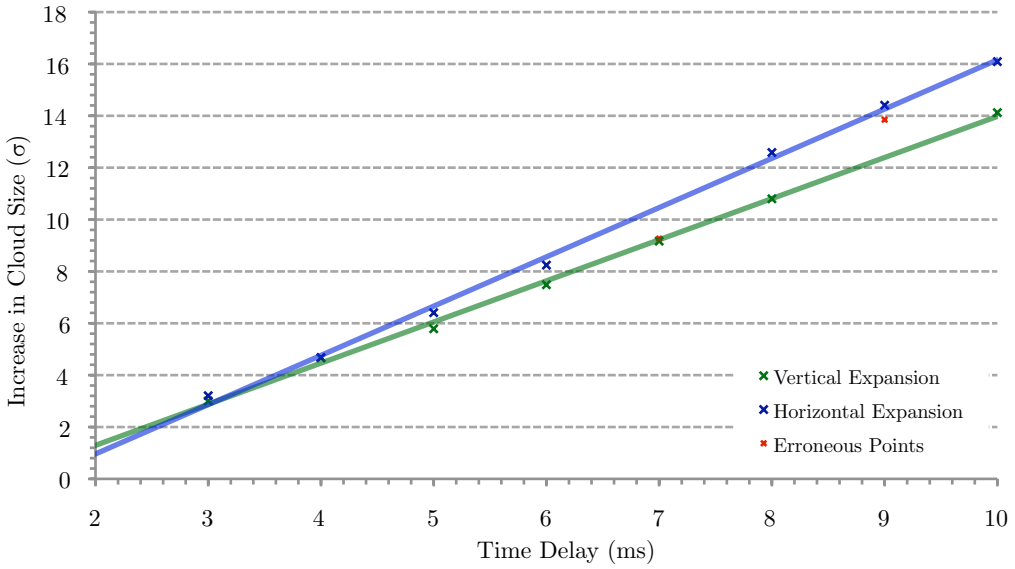

FIGURE 6.12: Tracking the difference in σ (corresponding to the MOT cloud width) in time for the x and y directions of the expanding MOT cloud. The expansion rate corresponds to a temperature of $\sim 50 \pm 35$ μK, in reasonable agreement with the 'release and recapture' measurements of the previous section.

Time delays from 3 ms to 10 ms were recorded and each time delay requires a new MOT cloud. Processing the images involves averaging the intensity in the x (horizontal) and y (vertical) pixel-line directions to create a separate single-line intensity profile for the x and y axes. This averaged intensity profile is then fitted to a Gaussian curve and reveals information about the centre position of the cloud and its extent (from the Gaussian standard deviation, σ).

For each time delay, σ along x and y is recorded for the original MOT cloud and again for the expanded cloud and the difference is plotted against the time delay. The results are shown in figure 6.12 and the gradient of the lines give the expansion rate both in the horizontal and vertical directions. As the two gradients appear linear, the MOT cloud expansion can be assumed to be at constant velocity and acceleration can be ignored, this means that the gradients give an expansion in terms of pixels per second and need to be translated into metres per second by determining the size of a single pixel in 'real-world' terms by using the measurements for the MOT cloud dimensions in section 6.4.1. The velocity can then be converted into a MOT cloud temperature by using the Equipartition of Energy theorem and the formula in equation 2.1.

The MOT cloud appears to expand slightly faster in the x (horizontal plane) direction than the y (vertical). This may be due to the fact that the anti-Helmholtz field is twice as

but at the cost of increasing noise in the image. The ROI can be reduced but care needs to be taken so that the extremes of the expanded cloud are not beyond the ROI.

strong vertically than it is horizontally, causing a retardation in the cloud expansion in y. When calculating the MOT cloud temperature, the x result was used – as it is influenced less by the anti-Helmholtz field – and the resulting temperature, $T_{\mathrm{MOT}} = 50 \pm 40$ μK, using this cloud expansion method.

6.6.1 Camera Synchronisation

The fast-frame camera needs 1 ms light integration time per frame to give a 1000 fps frame rate. The laser pulsing also occurs on the millisecond time-scale and so there is a significant chance for the lasers to switch on or off half-way through the camera integrating a frame. This is particularly true for the read-out pulse and the problem is shown in figure 6.13.

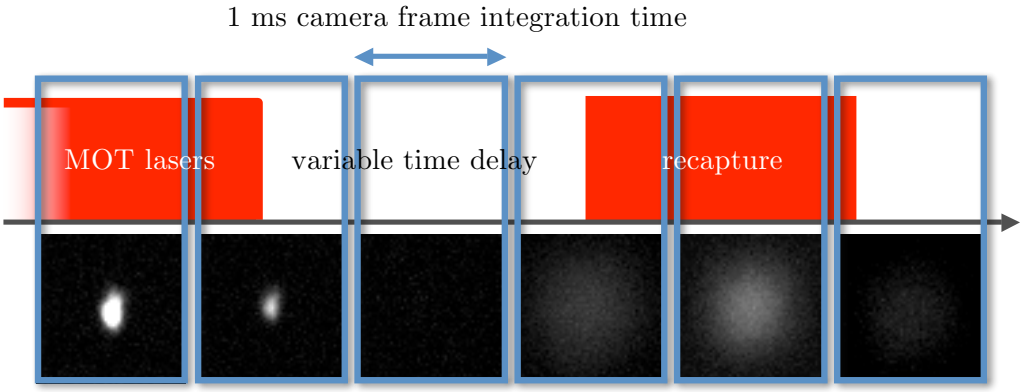

FIGURE 6.13: When the camera is not synchronised with the MOT beams, the lasers can switch on or off halfway through the camera integrating a frame and this causes a large uncertainty in the variable time delay.

To solve this problem, the trigger features of the fast frame camera were used to synchronise the camera with the laser pulses. The camera was triggered to take one frame, 1 ms before the MOT beams were turned off (the 'before' or unexpanded picture) and triggered again immediately as the MOT beams were flashed on again for the read out (expanded MOT cloud frame). With the fast camera synchronised to the MOT beams, the expansion experiment was repeated and this time, a higher temperature of 80 μK was obtained, but with a improved uncertainty of ± 30 μK.

6.7 Summary of MOT Cloud Temperature Measurements

Figure 6.14 summarises the results and uncertainties from the four determinations of the temperature of the MOT cloud.

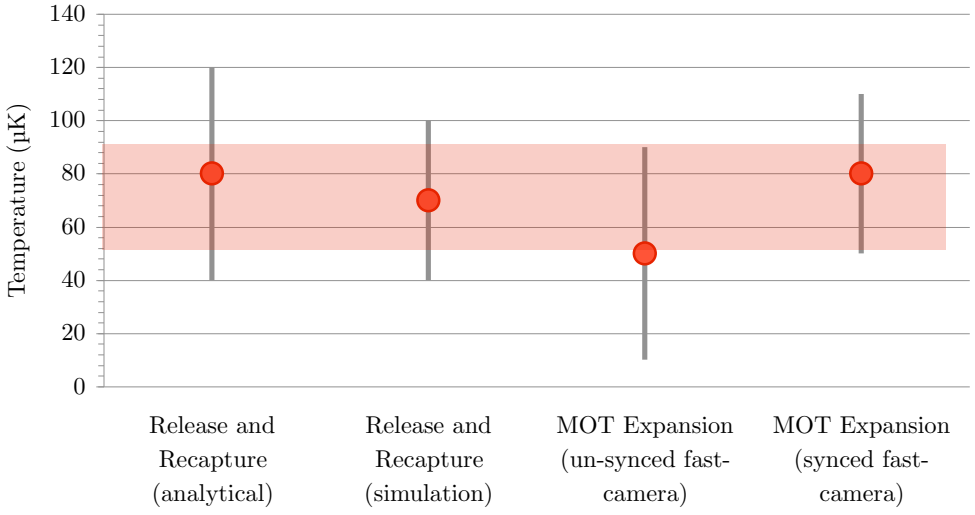

FIGURE 6.14: The results from the four methods of measuring the MOT cloud temperature. The conclusive result is that the temperature is lower than the Doppler limit of 150 μK for ^{85}Rb.

It can be concluded from the results in figure 6.14 that the temperature of the MOT cloud is lower than the Doppler Limit of 150 μK for ^{85}Rb. The 'release and recapture' method shows the largest uncertainty, mainly due to the calibration and determination of the MOT cloud fluorescence and the laser beam diameter. The 'ideal' release and recapture simulation produces a similar temperature result but with a smaller uncertainty. The MOT expansion experiment (un-synced) produces the lowest temperature result but also a large uncertainty, which comes from the uncertainty in the camera frame integration position with respect to the probe pulses. When the fast-frame camera was synchronised with the probe pulses, the error became significantly reduced, but the temperature result also increased, the difference between the un-synced and synced results may be an indication of the systematic error introduced when the camera is not synchronised with the probe pulses.

The final temperature of the MOT cloud considering the four results in figure 6.14 is 70 ± 35 μK.

6.8 Motion of the Released MOT Cloud

As it expands, the released MOT cloud falls under gravity but remains subject to the inhomogeneous anti-Helmholtz magnetic field which may affect its acceleration. By tracking the centre of mass of the cloud as it falls, the acceleration can be calculated and compared with purely gravitational acceleration to reveal the effect of the magnetic field alone.

A method similar to that used to determine the MOT expansion was used, but instead of recording the width of the fitted Gaussian, the height of its centre of mass was recorded, before release and for time delays between 3 and 10 ms. The results are fitted to the simple expression $y = (1/2)at^2$ for motion subject to a constant acceleration a.

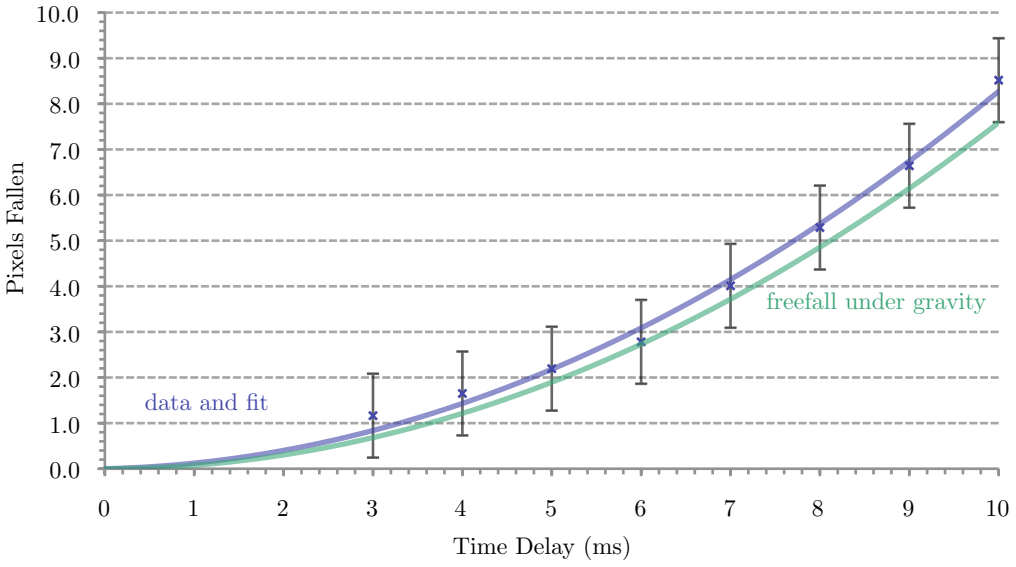

FIGURE 6.15: Variation of cloud centre height with time as the atoms fall under gravity within the anti-Helmholtz magnetic field. The curve from free-fall due to gravity alone is also plotted.

The graph in figure 6.15 tracks the position of the MOT cloud in time as it free-falls under gravity through the anti-Helmholtz magnetic field. The curve from the free-fall due to just gravity is also plotted and the two are very near each other. The polynomial fit to the data results in an acceleration of 15 ± 7 ms^{-2}, despite the closeness of the data with the gravity-only free-fall curve. The large uncertainty in the acceleration is from the pixel-to-distance conversion, improved accuracy is required before the effect of the magnetic field on the MOT cloud free-fall can be conclusively demonstrated.

6.9 Reproducibility of MOT Characteristics

In operation, the MOT appears to be a remarkably robust system. If required, the ion pump is capable of returning the vacuum chamber down to UHV pressures after the release of rubidium from the dispensers. The magnetic field appears stable and the coils do not over heat if the current is kept ~ 2.0 A. The lifetime of the MOT is only dependent on how long the lasers are able to remain locked to the wavelength required. This in turn depends in whether the lasers are in a 'happy' mode where the grating feedback and cavity modes compliment each other, or not. A well-locked laser has been known to maintain the MOT cloud throughout the day.

Although we find the MOT loading to be reproducible under similar experimental conditions, the loading rate and other parameters depend notably upon the background rubidium pressure, the size, intensity, uniformity and alignment of the trapping beams, the magnetic field gradient, etc. Recent work since that described here has used fibre beam filtering to improve the uniformity of the trapping beams, and additional magnetic field coils have been added along all three axes for the compensation of the Earth's and other stray fields and fine adjustment of the trap centre. As a result, a more uniform atomic cloud can now be produced, containing a several ten of millions of trapped atoms for it to be visible (despite the infra-red wavelength) to the naked eye.

Chapter 7

Two-Photon Experiments

7.1 Atomic Coherence in a Vapour Cell

One of the first tests of the pulsed laser system was to use just one beam of the pair to study the 'coherence time' (by which we mean the time for which the atomic level populations remained unchanged by external processes such as collisions or population migration) of the rubidium atoms in the vapour cell. Calculations of the mean free path in Appendix C predict coherence times between 40 and 60 μs.

Initially, all ^{85}Rb atoms are prepared to be in the lower ground hyperfine state ($F = 2$) by tuning the laser to the $F = 3$ level (hence emptying it). The population of the upper ground hyperfine state is probed in time by a series of short (a few μs long) probe pulses and the transmission is recorded with a photodiode. As the whole experiment lasts less than a millisecond, this process can be continuously cycled and seen on an oscilloscope. The probe pulses were kept as short as possible – as they also affect the state occupation – but had to remain longer than the photodiode response time.

The trace in figure 7.1 shows the drive sent to the amplitude modulation AOM and corresponds to the laser intensity with an initial, long preparation pulse and a series of short probe pulses. Figure 7.2 shows the trace when the laser is far off resonance. As expected, there is no change in the photodiode signal as the state preparation was ineffective since there is no absorption when the laser is far from resonance.

Comparing the AOM drive and the photodiode signals in figure 7.3 a lower limit on the photodiode response time can be inferred. From the trace it can be seen that this is about 2 μs, so the probe pulses should not be shorter than this.

With the laser tuned to the ^{85}Rb, $F = 3 \rightarrow F'$ transitions, the trace obtained is as shown in figure 7.4, from which it is apparent that it takes ~ 50 μs to empty the upper

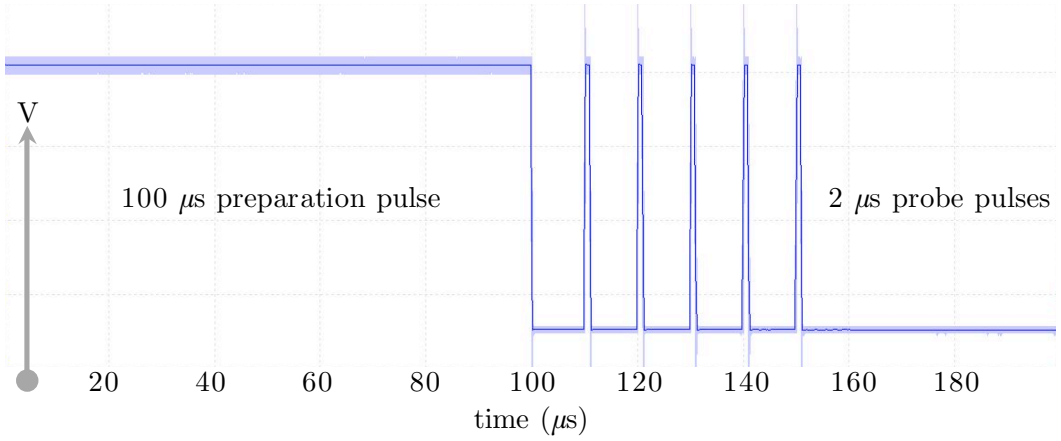

FIGURE 7.1: The signal sent to the amplitude modulation AOM for the vapour cell coherence studies.

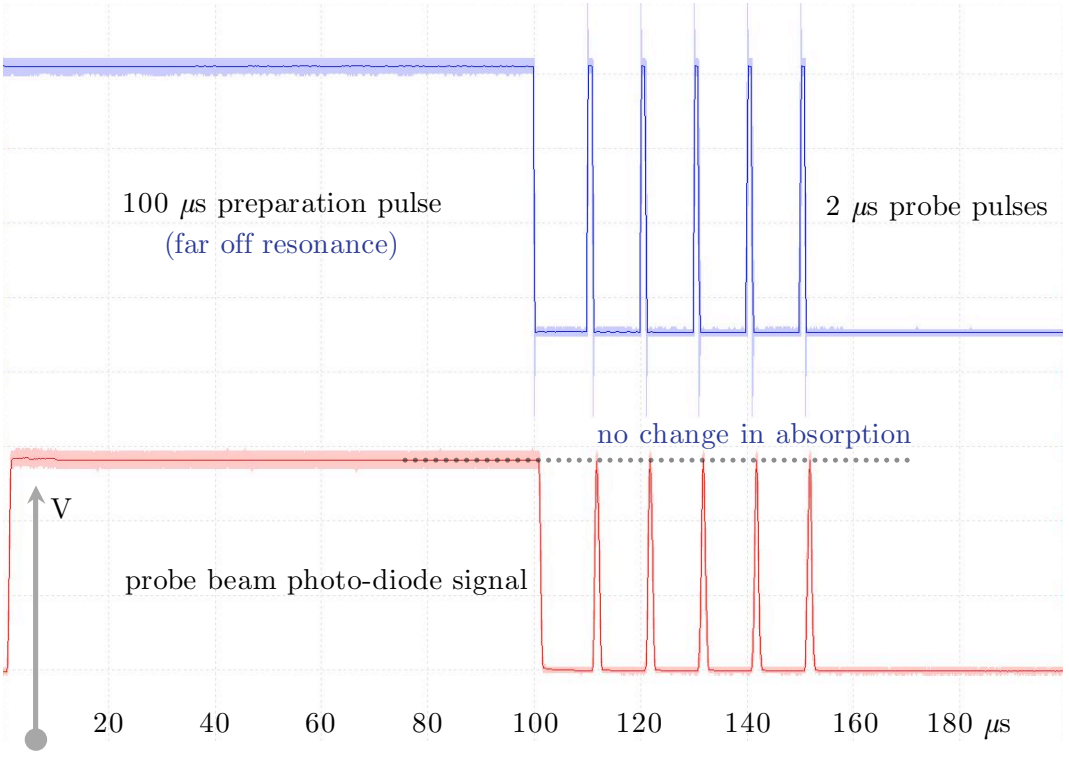

FIGURE 7.2: The photodiode response when the laser is far off-resonance. No change in absorption is expected nor seen.

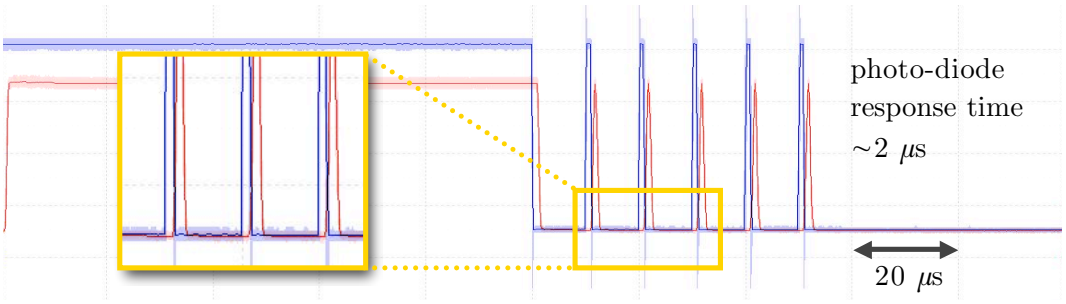

FIGURE 7.3: A zoomed section of the previous figure showing the photodiode response superimposed onto the AOM drive. It can be seen that the photodiode response time is about 2 μs. The difference in height between the AOM drive and photodiode response is not important.

ground hyperfine state. The decreasing height of the probe pulses shows that it takes $40 - 60$ μs for collisions to mix the ground hyperfine states again.

The distribution of the population between the two ground hyperfine levels can be calculated using the Boltzmann distribution

$$\frac{N_2}{N_1} = e^{\left(\frac{-(E_2-E_1)}{k_B T}\right)} \tag{7.1}$$

where N_1 and N_2 are the populations in the lower ground and upper ground hyperfine states respectively and E_1 and E_2 are the energies of the lower ground and upper ground hyperfine states respectively. Taking the ground hyperfine splitting $(E_2 - E_1)$ to be 3.036 GHz, for a rubidium vapour cell – where the temperature, $T = 298$ K – the ratio of $N_2/N_1 = 0.995$. So $N_2 \simeq N_1$ hence it can be assumed that at room temperature, the population is equally distributed between the upper and lower hyperfine ground states and achieves this by 60 μs after an initial state preparation that empties one of the ground hyperfine levels.

The calculations for the coherence time do not take into account atoms coming into the laser beam volume from the outside or state-prepared atoms leaving it. With a vapour cell diameter of 2.5 cm and beam diameter of 5 mm, a rubidium atom with a typical thermal velocity will travel ~ 2.5 mm in the 8 μs between probe pulses. This is a sizeable fraction of the beam diameter and is the major contributor to the restoration of the measured hyperfine population.

7.2 Attempted Observation of Two-Photon Absorption

The next series of tests, using both of the laser beams with a 3.036 GHz frequency difference, formed an unsuccessful attempt to see two-photon processes in the vapour

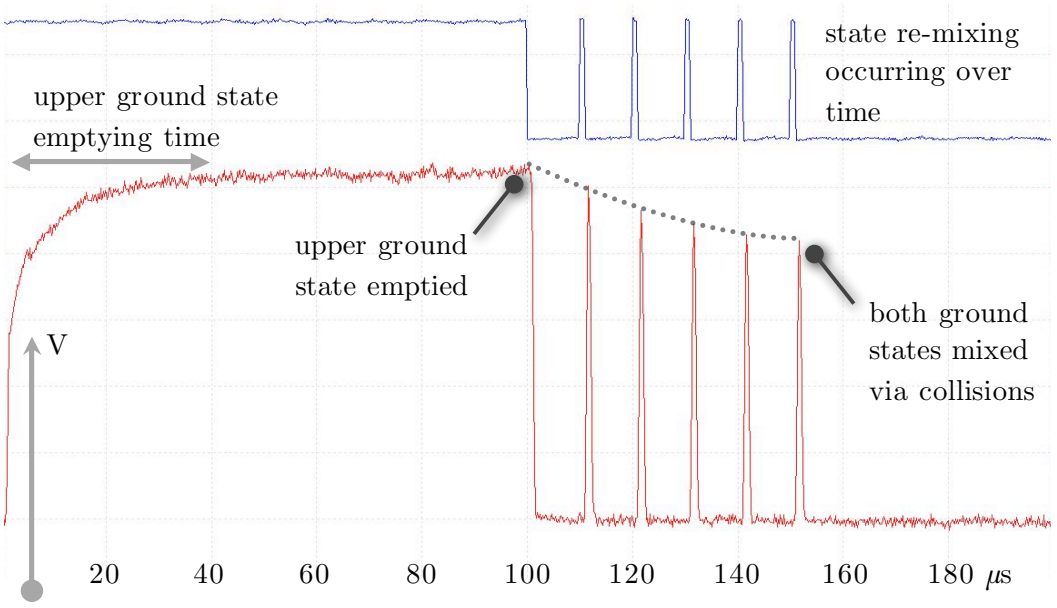

FIGURE 7.4: The state preparation being slowly destroyed over time by atomic and cell wall collisions.

cell. The method used was to have a state preparation pulse to empty the upper ground hyperfine level, followed by a pulse of the Raman beams (that would cause some of the population to transfer back to the upper ground hyperfine level via two-photon absorption). Evidence of population transfer would come from the change in absorption seen in the subsequent probe pulses. Figure 7.5 shows the pulse sequence.

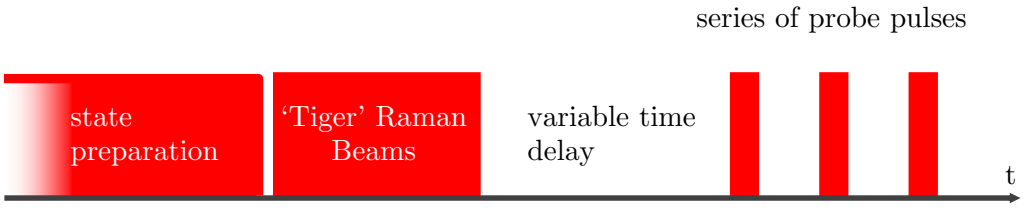

FIGURE 7.5: The pulse sequence from the state preparation and Raman beams for two-photon absorption.

Figure 7.6 shows the level diagram and the effect of the various pulses on the electronic state.

Unfortunately, the Raman pulses appeared to have no discernible effect on the electronic state population and no difference was seen from the behaviour in figure 7.4. Looking at possible causes, problems with the EOM line were eliminated by looking at the side-bands on the OSA and tracing the RF signal on a fast oscilloscope. Overall, no obvious

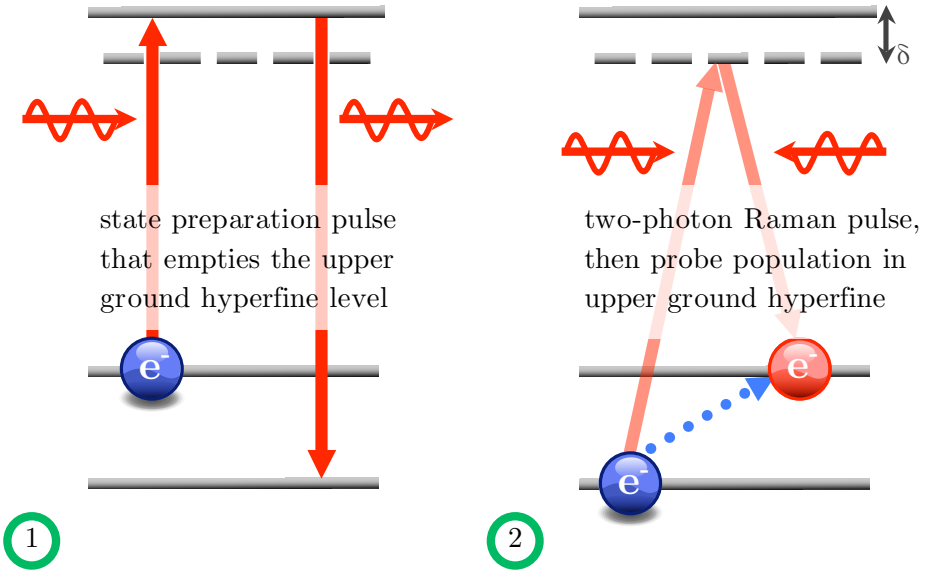

FIGURE 7.6: In (1) the state preparation pulse empties the upper-ground hyperfine state and this is followed by the Raman pulses (2) where the two-photon process transfers some of the population back to the emptied state and then this is then probed by a series of further probe pulses.

problem with the chirped pulse system could be identified. The EOM frequency was scanned to cover the region around the ground hyperfine splitting. The splitting for ^{85}Rb is 3.035 732 439±5 GHz, the AOM accounts for 310 MHz and so the EOM needs to be run at 2.725 732 439 GHz and was scanned ±20 MHz from this value at a resolution of 1 MHz. It was hoped this would be sufficient to see the two-photon effect, but it was not observed.

Further attempts involved using a telescope arrangement to increase the beam intensity to drive the two-photon transition harder but this was also unsuccessful. It is believed that due to the large Doppler profile of the room temperature rubidium atoms, a large detuning has to be used to avoid single photon processes, and hence there is insufficient beam power to drive the two-photon transition at an observable rate using large diameter beams. Unfortunately, increasing the beam power by narrowing the beam diameter means the effect of atoms entering the beam volume from outside swamped any observable effects.

7.3 Unexpected Induced Transparency

It was during the these experiments that a rather counter-intuitive 'induced transparency' type of effect was observed where the fluorescence of the rubidium vapour

cell could be controlled with a weaker probe beam. This surprising effect was easily detectable by looking at the vapour cell using the infra red camera (CCD).

7.3.1 Electromagnetically Induced Transparency

When two or more transitions in an energy level structure are coupled by resonant radiation, the intuitive picture would be that fluorescence occurs when electrons relax from the various excited state levels. However, the quantum picture is much richer because when multiple levels are coupled, coherent superpositions between the different states can occur and this leads to some novel optical phenomena because quantum interference can occur between these states.

One of the optical effects that has been observed is Electromagnetically Induced Transparency (EIT) where a medium that would otherwise absorb from a resonant laser beam is rendered transparent to the pump laser by applying a second beam, resonant with another level. A destructive interference effect occurs between the two excited states that renders the pump level 'transparent'. The effect was theoretically predicted in [127] and first observed in Strontium in [4]. Since then, EIT has been observed in a range of systems [5, 6, 128] and practical applications are being investigated [129–132].

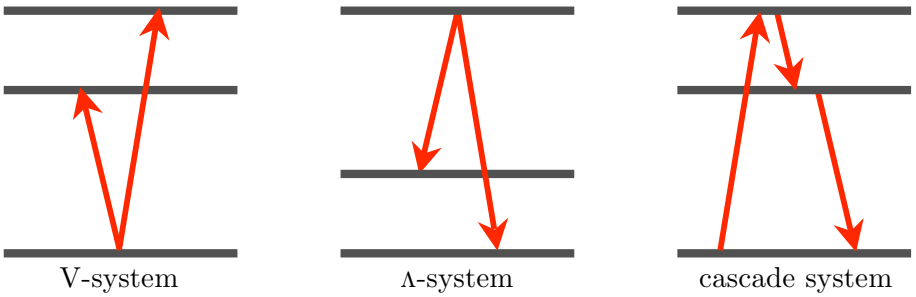

FIGURE 7.7: Interesting optical effects occur when three energy levels are coupled together in a Λ-type scheme (left) or a V-type scheme (centre).

These coherent optical effects have been studied for energy level systems with three levels where either a single ground state is coupled to two excited states (a 'V'-type system) or where two (typically hyperfine) ground states are coupled to a single excited state level (a 'Λ'-type system).

EIT can be described using either a dressed-atom picture or a "bare"-level picture. When looking at the bare-level picture, EIT arises from the interference of electronic absorption to the excited state via two different pathways. From figure 7.8 in a three-level scheme where $|3\rangle$ is the excited state, an electron beginning in the lower ground state, $|1\rangle$ is able

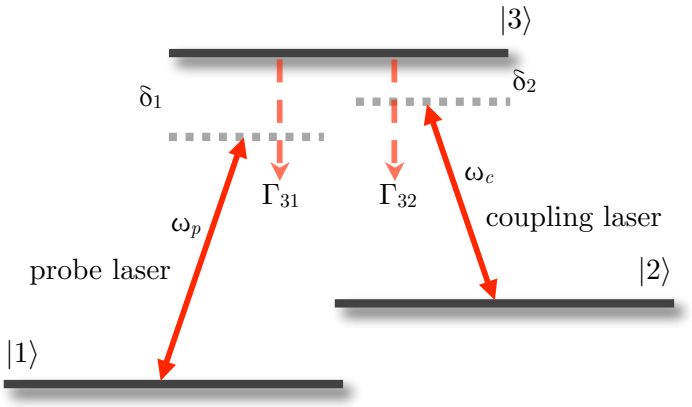

FIGURE 7.8: EIT occurs when there is interference between two routes to the same excited state. The probability amplitudes of these two routes are opposite in sign and can be made to cancel by choosing the appropriate parameters (intensity and detuning) for the probe and coupling lasers.

to reach $|3\rangle$ by directly absorbing a photon from the probe laser to go from $|1\rangle \rightarrow |3\rangle$, or indirectly through two absorptions and a decay following the path, $|1\rangle \rightarrow |3\rangle \rightarrow |2\rangle \rightarrow |3\rangle$.[1] If the coupling laser is higher in intensity than the probe laser, then the probability amplitude for an electron to follow the indirect excitation route becomes comparable to that of an electron following the direct path. The probability amplitude for the indirect route is also of opposite sign and so the detuning and amplitudes of the coupling and probe lasers can be chosen such that these two probability amplitudes become equal resulting in no amplitude for the electron to reach $|3\rangle$, hence no absorption of the laser beam hence EIT.

EIT was theoretically developed by Harris in 1989 [133] and this was followed by an experimental demonstration two years later in 1991 [134]. The experiment in his paper used a Λ-type scheme in a strontium vapour and involved pulsed lasers for the probe and coupling fields. They noted that the transmittance of the probe beam with the coupling field was many orders of magnitude greater than without the coupling field.

Another optical phenomenon is Coherent Population Trapping (CPT) where a population becomes trapped in a dark eigenstate of a three-level system when the mode spacing of the resonant/illuminating laser is made to be the same as the hyperfine splitting between the two ground state levels. CPT is based on the same underlying principals as EIT and can arguably be considered as the same process but in different regimes.

[1] Other similar higher order pathways are also possible but are not considered here.

Background to Coherent Population Trapping

CPT can be used to trap a population of atoms into a particular "dark" (non-absorbing) state. It requires a Λ-type level scheme where the two ground states are typically hyperfine ground states separated by some GHz in frequency. The theory of CPT was developed by Orriols and Arimondo in [135] when it was observed by Orriols in a Sodium vapour cell that was illuminated by a multi-mode laser in [136]. Orriols *et at* found that as the pulse frequency (mode-spacing) of the laser was brought closer to the hyperfine ground state splitting of the Sodium atoms, the fluorescence reduced until it "switched off" when the mode spacing matched the hyperfine ground state splitting frequency. The population was trapped in the lower ground state, unable to move to the upper ground state. CPT was experimentally demonstrated by two separate groups in Pisa [137] and New York [138].

This phenomenon can be described by thinking of the initial atomic state as a superposition of the two hyperfine ground state levels, $|1\rangle$ and $|2\rangle$. By applying the illuminating field at the frequency of the ground hyperfine splitting frequency, the two paths to reach the excited state, $|3\rangle$ (one path is $|1\rangle \rightarrow |3\rangle$ and the other is $|2\rangle \rightarrow |3\rangle$) interfere destructively.

By looking at the dressed-state picture and considering the two Eigenstates of the Hamiltonian of the atom-field system, the coupled and uncoupled equations for the ground hyperfine levels are,

$$|\text{coupled}\rangle = \frac{\Omega_1}{\Omega_x}|1\rangle + \frac{\Omega_2}{\Omega_x}|2\rangle \tag{7.2}$$

$$|\text{uncoupled}\rangle = \frac{\Omega_2}{\Omega_x}|1\rangle - \frac{\Omega_1}{\Omega_x}|2\rangle \tag{7.3}$$

where

$$\Omega_x = \sqrt{\Omega_1^2 + \Omega_2^2} \tag{7.4}$$

It is then possible to take these two dressed-state equations and calculate the result when they are coupled to the excited state by electric dipole transitions (photon absorption). The expression giving the coupling strength for equation 7.3 to the excited state is

$$\left\langle \frac{\Omega_2}{\Omega_x}|1\rangle - \frac{\Omega_1}{\Omega_x}|2\rangle \,\middle|\, \mu \,\middle|\, 3 \right\rangle \tag{7.5}$$

where μ is the electric dipole transition operator. By carefully selecting the intensity and detuning of the lasers (and thus, changing the values of Ω), the coupling strength (equation 7.5) can be reduced to zero, so that the state can neither decay, nor absorb

incident light. This state then becomes the "dark state" of Coherent Population trapping and is one of several optical phenomena that come under the umbrella of EIT.

7.3.2 Observations in Rb-85

The induced transparency effect was first seen in ^{85}Rb and is easily reproducible. The apparatus involves using both beams passing through the vapour cell. The EOM is *not* switched on so the frequency difference between the two beams is only −310 MHz. The frequency shifted (probe) beam is weakened to around 50 mW with a neutral density filter and the undiffracted (pump) beam is unchanged. With the laser set to around 780.244 nm, there is strong fluorescence caused by the pump beam exciting the ^{85}Rb $F = 3 \rightarrow F' = 2, 3, 4$ transition as shown in figure 7.9. The probe beam is shifted down to an even longer wavelength by the AOM and even with the Doppler profile, causes very little fluorescence since 310 MHz is a sizeable fraction of the Doppler width.

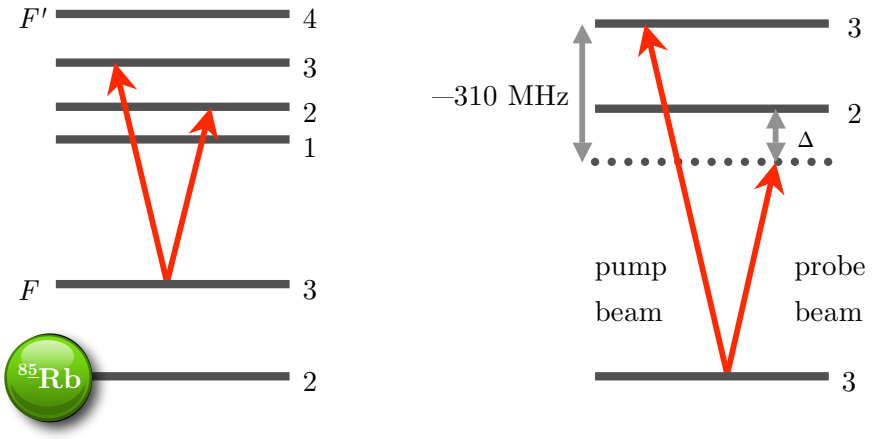

FIGURE 7.9: The V-type level diagram for the apparent induced transparency effect in ^{85}Rb.

Referring to figure 7.10, the image on the left is the fluorescence from just the probe beam. The middle image shows the strong fluorescence from the pump beam. The image on the right shows how this fluorescence is almost shut off by having both beams passing through the cell. The images are unmodified stills taken from a CCD camera set to a manual (fixed) gain and light levels that were kept constant throughout. From the images it appears that the probe beam is able to control the absorption of the pump beam, instead of adding to the fluorescence, its presence switches it off.

The wavelength meter gives a coarse idea of which isotope and ground hyperfine level is being addressed. To obtain a better picture of what was happening to the fluorescence, a spectroscopic study of this phenomenon was done.

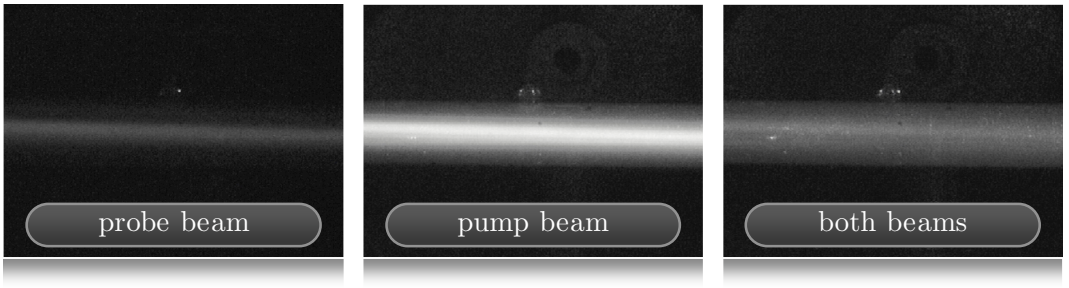

FIGURE 7.10: An interesting effect noted while testing the chirped pulse system is that a weak 'probe' beam (frequency shifted by −310 MHz is able to switch off the fluorescence from a resonant pump beam.

Using the wavelength meter the laser was scanned from 780.243−780.247 nm using a 2 V peak to peak triangular wave form sent to the piezo (controlling the tuning grating) at a 50 Hz frequency. This meant the photodiode signal could be seen using an oscilloscope. As this tuning range is large (over 2.5 GHz) the single mode output was verified by slowing the scanning frequency down so the eye could follow it on the trace from the OSA, it was then set back to 50 Hz for the experiments.

The −310 MHz shifted probe beam measured ∼ 55 mW and the pump ∼ 220 mW. The spectrum of the pump beam, with the probe beam *blocked* is shown in figure 7.11.

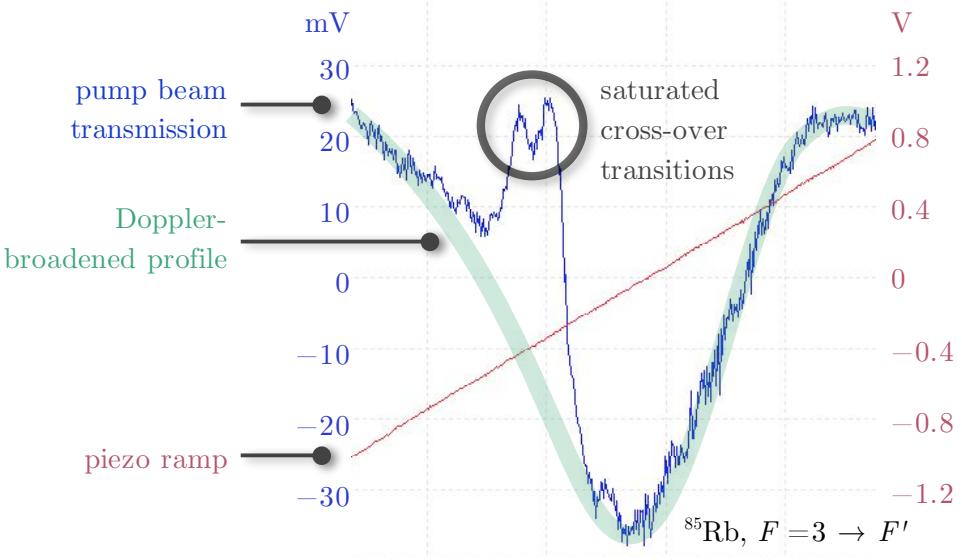

FIGURE 7.11: Transmission of the 222 mW pump beam through the vapour cell. The slight Doppler-free saturated absorption features come from the back reflection of the pump beam from the cell ends.

Two large cross-over transitions can be seen and this is due to a fraction of the pump being back-reflected from the cell ends causing pump-probe spectroscopy (see section

4.3.1). The peaks are significantly broadened because of the large pump beam intensity, which is much greater than the saturation intensity.

Now the −310 MHz shifted probe beam (at 55 mW) was unblocked and passed through the cell, overlapping the pump beam. The linear polarisations of the beams were orthogonal (the beams are combined at a PBS), with the probe beam horizontally polarized. The transmission of the pump beam was greatly affected and is shown – compared with the original Doppler spectrum – in the oscilloscope trace in figure 7.12. The displacement between the troughs of the transmission spectrum is believed to be attributable to a drift in the laser frequency.

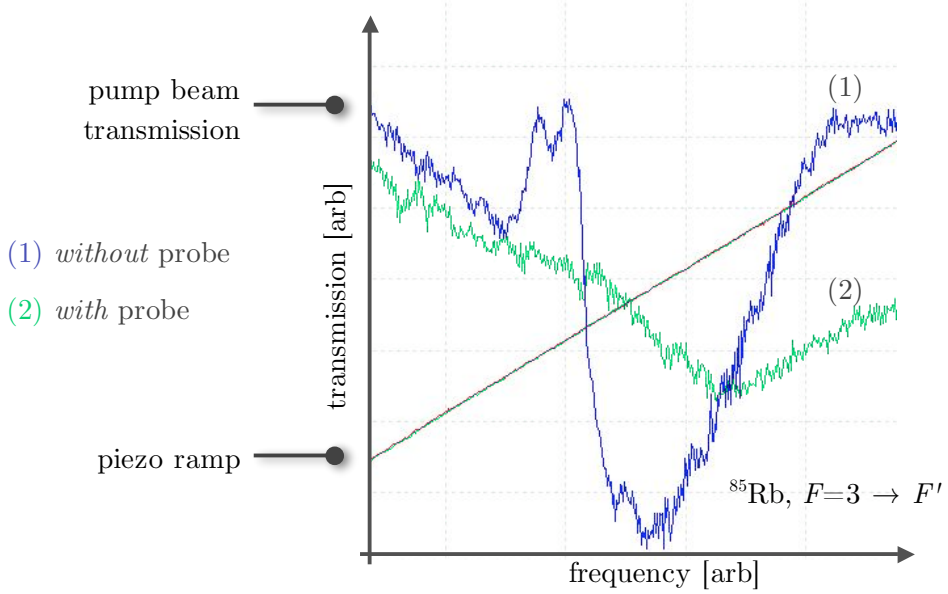

FIGURE 7.12: Transmission of the pump beam with (2) and without (1) the probe beam. The troughs of the traces are offset due to drift in the laser frequency. The AC coupling means that the photodiode voltage cannot be directly compared.

7.3.3 Observations in Rb-87

With such a strong effect seen in ^{85}Rb, the laser (pump beam) was retuned to the ^{87}Rb spectrum to see if a similar effect could be seen with it. The region investigated was around 780.243 nm, which corresponds to the ^{87}Rb upper ground to excited states ($F = 2 \rightarrow F'$) as shown in figure 7.13.

No difference in fluorescence intensity could be convincingly discerned by eye from the CCD camera images, but a small but reproducible effect was apparent upon more quantitative measurement using a photodiode, as shown in figure 7.14, the presence of the probe beam resulting in a region of reduced absorption to the blue side of the Doppler broadened peak.

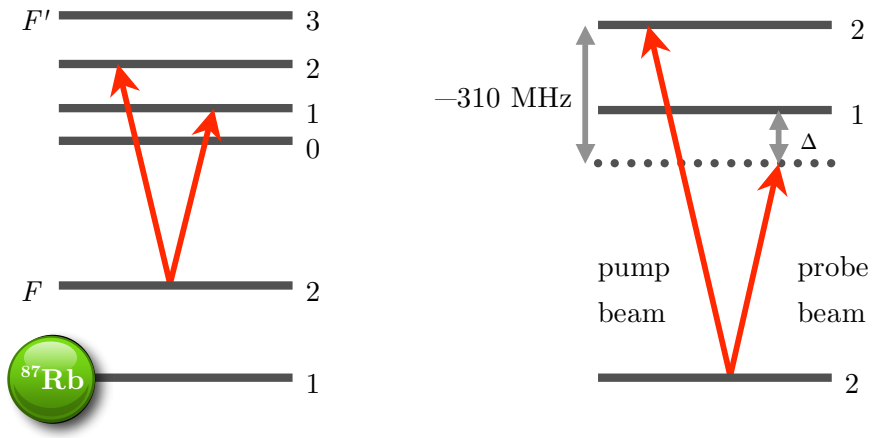

FIGURE 7.13: The V-type level diagram for the apparent induced transparency effect in ^{87}Rb.

As in the case for ^{85}Rb, there is a reduction in absorption of the pump beam in the presence of the probe beam yet it is much more subtle in ^{87}Rb as shown in figure 7.14. With just the pump present, the normal, room-temperature Doppler profile is expected and seen[2]. When the probe beam is applied, there is a slight reduction in absorption in particular along one side of the Doppler profile.

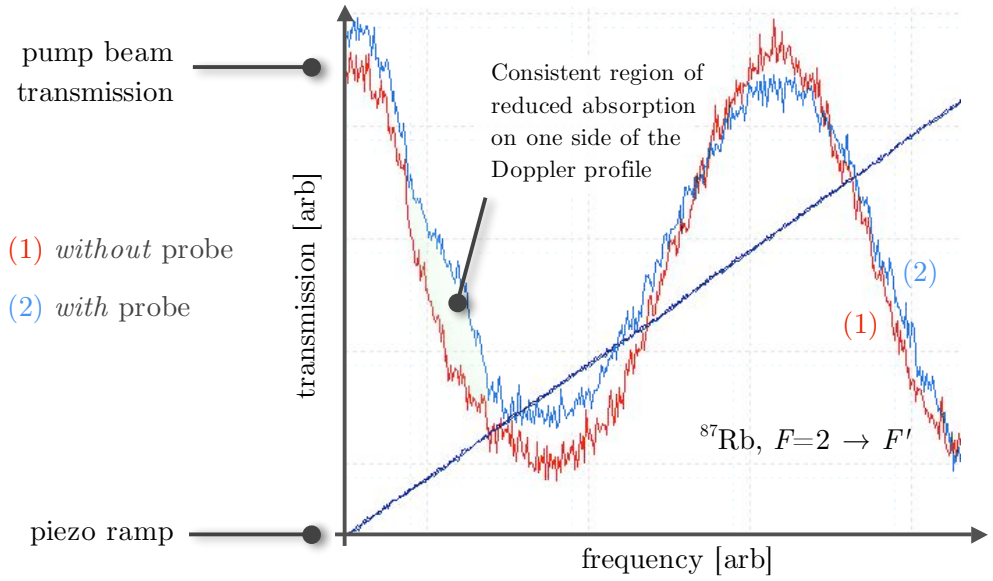

FIGURE 7.14: Overlay of two traces showing that the induced transparency type effect – while present – is far less pronounced in ^{87}Rb than it is for ^{85}Rb.

These results are very similar to those obtained by the group of Goran Pichler from the University of Zagreb, Croatia [31]. When they use a 35 mW 'coupling' laser tuned to

[2]There is a reduced amount of Saturated Absorption from the cell window reflections as the whole vapour cell was at a small angle to the beam, meaning the beam did not travel along its axis.

the ^{85}Rb, $F = 2 \rightarrow F' = 2$ transition and independently scan a 'probe' laser across the ^{85}Rb, $F = 2, 3 \rightarrow F'$ and ^{87}Rb $F = 1, 2 \rightarrow F'$ transitions, they obtain an increased transmission spectrum very similar to the results shown in figures 7.12 and 7.14.

Further, more detailed experiments were regrettably thwarted by the failure of the commercial Tiger diode laser system, which was not satisfactorily repaired until almost a year later.

7.4 Experiments with the MOT Cloud

After difficulties with observing the two-photon process in the vapour cell, it was decided to repeat the pulsing experiments using the MOT cloud. Two major improvements were made to the detection apparatus in an effort to increase sensitivity: a two-inch collection lens was used and placed closer to the MOT cloud to increase the geometrical detection efficiency and a photon counter was used as the detector.

By carefully using the arbitrary signal generators to control the molasses, repump and Tiger (Raman) lasers, it became possible to cycle the pulsing experiments such that the MOT cloud was now no longer destroyed after each pulse cycle, but rapidly re-created. This was achieved by keeping the MOT lasers on continuously apart from a short 'window' of a few milliseconds in which the Tiger was operated. The MOT cloud expansion pictures in figure 6.11 show that the cloud does not expand significantly within this time frame and can easily be recaptured for another pulsing experiment at a rate of several experiments per second. The photon counter analogue output[3] was recorded using a fast-scope, triggered by a 'sync' signal from the signal generators.

Two methods of searching for the two-photon transition were used, the first using varying pulse lengths and the second using the I&Q modulator to sweep the ground hyperfine splitting frequency. Both methods involved searching a parameter space of pulse length, polarisation, Raman detuning and hyperfine frequency.

7.4.1 Varying Pulse Length

The scheme for varying pulse length involves a state preparation pulse followed by the Raman pulses and finally a short read-out pulse. The width of the window where the MOT and repump beams are off allowed several pulse lengths and read-outs to be used.

[3]The photon counter consists of a detector head and a counting unit that integrates the detected photon pulses and converts the signal into a 'counts per unit time' value but only the raw, analogue output was of importance in this application.

Figure 7.15 shows this scheme. Within the experimental window, the repump laser is used initially to empty the lower ground hyperfine ($F = 2$) level. Next, a series of Raman pulses from the Tiger laser is fired, each with a varying length. After each individual pulse, a read out pulse from the repump laser is fired to probe any atoms that may have transferred back to the $F = 2$ via the two-photon process.

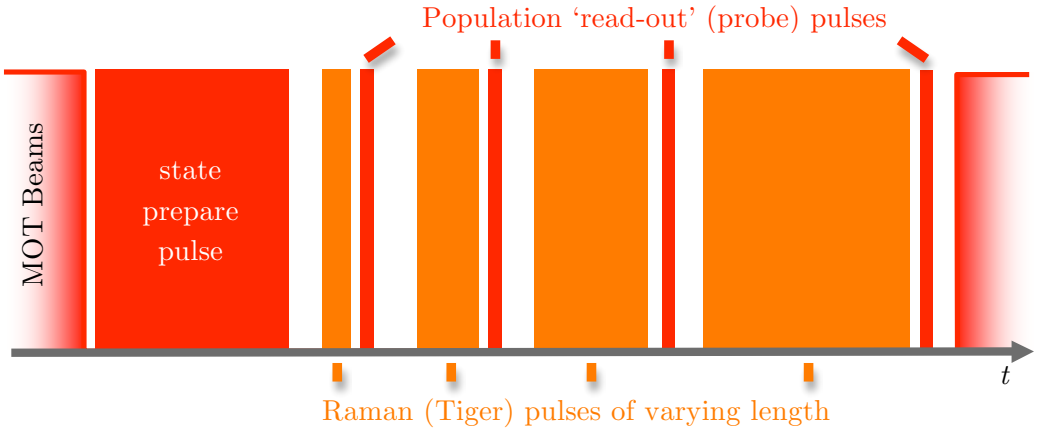

FIGURE 7.15: The varying-length Raman pulses being fired in the experimental window. Several pulse and probe experiments can be done in each window and repeated at a rate of several Hz without destroying the MOT cloud.

Unfortunately, read-out pulses indicated that the Raman pulses were having little or no effect. After much exploring the parameter space, the two-photon signal was still not seen; the reason being unclear. It was suspected that the hyperfine ground splitting frequency was incorrect for our setup. Changes to this frequency occur from being in a non-zero magnetic field region. This could be the case for the MOT system, where the molasses beams do not quite intersect at the zero-field region. The subsequent Zeeman splitting of the states can cause a shift in the hyperfine ground splitting frequency of up to several MHz for the local area around the MOT cloud.

The ion pump has a strong square horse-shoe magnet and its field was discovered using a Hall probe to extend over the vacuum system. The field strength varied from 6 Gauss on the near side closest to the Ion pump and fell to 1.5 Gauss on the far side (the Earth's field is around 1 Gauss). This field gradient distorts the anti-Helmholtz field of the trapping coils and can cause a further Zeeman shift of the energy levels and also needed to be taken into account.

7.4.2 Using the I&Q Modulator

Finding the correct ground Hyperfine splitting needs to take into account the effect of any possible Zeeman splitting arising from the magnetic fields (including that of the ion

pump). The I&Q modulator was also introduced into the Tiger/Raman system to give an adiabatic 'sweep' of this splitting frequency over a 10 MHz range either side of the centre frequency.

Within the experimental window, it was possible to have one pulse with the I&Q off and one with the I&Q on in addition to the readout pulses for comparison between the two. The only concern was that the bandwidth of the EOM was not quite large enough[4] to ensure a high efficiency across this large frequency range, meaning the sidebands at either ends of the frequency sweep were much weaker than at the centre frequency. This is a restriction of the equipment and there is no suitable way of dynamically changing the bandwidth or centre frequency in mid-experiment.

7.4.3 Results from Analysis

Despite collecting and analysing data from both methods outlined in the previous section, signs of population transfer from the two-photon process were still not evident. As we are working with the $m_F = 0$ states, there should be no Zeeman shift of these levels from stray magnetic fields and the DC field from the ion pump should only shift the position of the zero field region inside the MOT. The quality and power of the Raman beams remains a concern, future efforts will concentrate on improving both of these by improving beam alignment through optical components (by introducing precision stages) and by the use of optical fibre to give the beams a 'clean' Gaussian profile.

7.5 Latest Developments

While this thesis has been in preparation, continued improvements and refinements to the MOT and chirped pulsed system by James Bateman *et al* in the lab has resulted in the successful observation of the two-photon process with rubidium in the MOT cloud as shown in figure 7.16.

Figure 7.16 shows the fraction of the population transferred by the two-photon process as the EOM frequency is scanned, beginning at 2.725 732 440 GHz at the 0 kHz detuning point. An optimum frequency is found -4 kHz from this chosen EOM frequency. The Raman beam power available is low – on order of ~ 10 mW in a 2 mm diameter beam – and this increases the sensitivity to the hyperfine splitting frequency and any subsequent frequency drifts (from the laser or the signal generators).

[4]The EOM has a bandwidth of ~ 15 MHz.

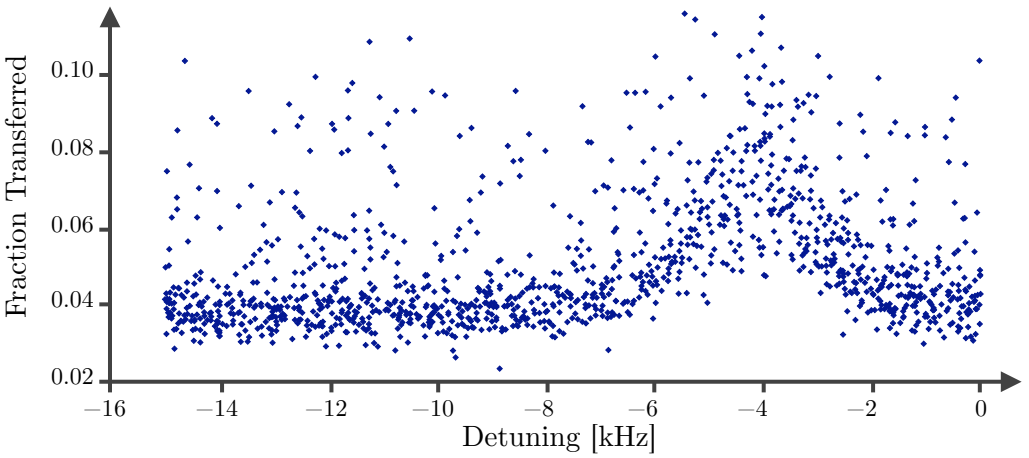

FIGURE 7.16: Evidence for a weak two-photon process occurring −4 kHz detuned (due to frequency generator drift) from a frequency of 2.725 732 440 GHz. The peak shows the fraction of the population that have been transferred back to the $F = 3$ level via the Raman beams.

The method used can be seen in figure 7.17, both trapping and repump lasers are on at the start but are suddenly switched off at time, $t = 0$. After an interval of only 5 μs, the trapping laser is switched back on for ~ 500 μs as the 'prepare pulse' and this empties the $F = 3$ ground hyperfine level. Next, a 500 μs Raman pulse is applied, which (if the experimental parameters are favourable) may transfer some of the population in the $F = 2$ level, back to the $F = 3$ level via the two-photon process.

To measure the two-photon process, the trapping beam is then turned on again for ~ 500 μs to probe the fluorescence from this state. Once this 'probe' pulse has finished both trapping and repump beams are switched back on again to resume the MOT. This experiment operates on a time scale of only a few milliseconds at most and so the MOT cloud can be quickly restored and the sequence repeated up to a rate of 100 Hz, accelerating the rate at which the parameter space – particularly the correct EOM frequency – can be explored.

A major modification was made to the magnetic field setup of the MOT apparatus; the anti-Helmholtz coils of the MOT system were also supplemented by an extra magnetic field of 1 G oscillating at 100 Hz. This additional field oscillates at the same frequency of the pulsing experiment yet is too rapid for the MOT cloud to follow in space. At the maximum amplitude of the magnetic field, the MOT cloud is in a non-zero region of sum magnetic field and so causes a Zeeman splitting of ~ 1 MHz of the rubidium m_F levels. This means that the Raman beams can only target atoms in a specific (chosen) m_F level since they are no longer degenerate. At this point, the co-propagating, equal circular polarisation Raman beams are applied and drive $\Delta m_F = 0$ transitions only. Since this extra magnetic field is oscillating, it does not affect the position of the cold rudium cloud

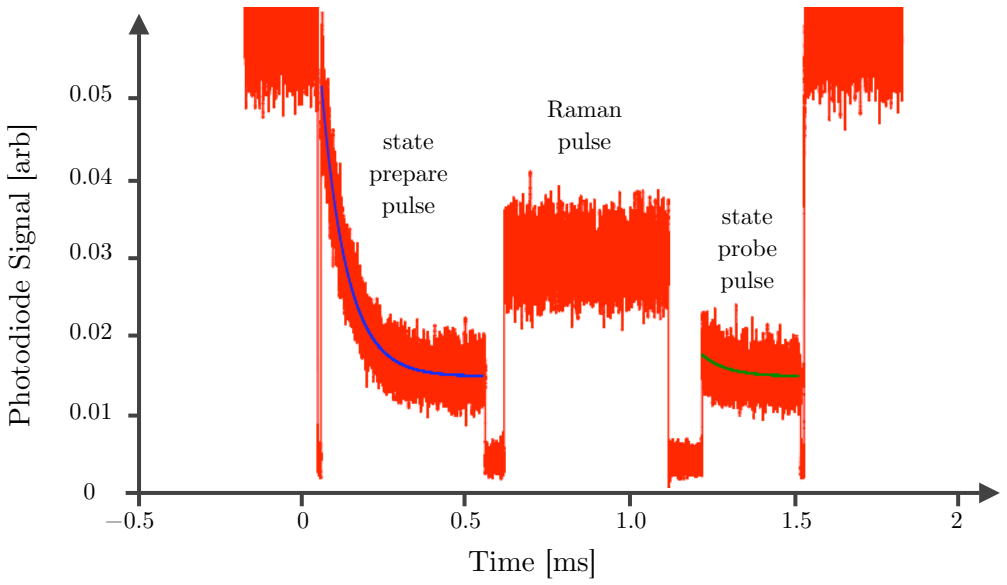

FIGURE 7.17: The fluorescence signal during a typical pulsing scheme experiment. The evidence of the two-photon effect comes from the presence of the slight exponential decay of the probe pulse fluorescence caused by atoms having been transferred back to the probe state by the Raman beams.

in the MOT. While scanning the EOM frequency, it was found that the signal generator supplying the carrier frequency (2.726 GHz) drifts by ~ 4 kHz, equivalent to ~ 1 ppm and while this is within the specification for the generator, it had a noticeable effect up on the two-photon process.

Further improvements continue to be made to increase the efficiency and rate of the two-photon process. Current efforts are focused on increasing the quality and power of the Raman beams by using fibre coupling for precision alignment through various optical components as well as introducing a semiconductor laser amplifier to significantly boost the Raman beam power.

Chapter 8

Conclusion

8.1 The MOT and Chirped Pulse System

This thesis has described the preparation and construction of a magneto-optical trap for ^{85}Rb, the assembly of its optical components, vacuum system, stabilized lasers, control and detection systems. It reports the characterization of MOT operation, including determination of the temperature, density and number of atoms for the trapped atom cloud. These experimental measurements are supported by a theoretical analysis, starting with a basic two-level atom picture and extending it to eventually encompass the electronic hyperfine structure of the alkali elements and their interaction with polarised light in the MOT environment.

The MOT system is robust, stable and overall very satisfactory. With plenty of optical access, ample rubidium supply in the five dispensers and a high quality vacuum, there is no need for any change to this system in the near future. The two-inch diameter optics used throughout the system (including mirrors, PBS cubes and waveplates) means the diameter of the trapping beams can be significantly expanded (and hence create a bigger cold atom cloud) by purchasing a higher power laser if the opportunity arises. Presently however, this is not necessary as there is still enough power in the home-built diodes currently being used and is more than adequate.

The feedback electronics for the DFFML setup work well as much time has been spent on their development and testing, especially in reducing external and 50 Hz line noise. Their rack-mount, modular design has consolidated and simplified what was previously a large collection of separate RF electronics (inline and otherwise) and signal generators that was prone to noise and ground-loops in particular. Small tweaks and adjustments continue to be made in the circuit schematics (on computer, in the circuit design and

simulation software) that may culminate in another revision of the locking electronics when the collective improvements become significant.

In addition to the MOT, a chirped pulse system has been developed for two-photon Λ (Raman) transitions between the upper and lower hyperfine ground states in ^{85}Rb. The system is a combination of AOMs and EOMs driven by arbitrary frequency generators controlled and timed by a computer with LabView and Perl. The Raman beams are separated by the ^{85}Rb ground state splitting of 3.036 GHz and is tunable. The pulses can be on the microsecond time-scale. This system will be used for coherent state manipulation experiments such as atomic interferometry and amplified Doppler cooling as described in Chapter 2.

The MOT and chirped pulse systems have been completed and demonstrated to work reliably and satisfactorily, and the two have been used together to determine the trapped atom 'coherence time', by which we mean the time for which the atomic level populations remained unchanged by external processes such as collisions or population migration, the results being consistent with a simple theoretical analysis. Two-photon transitions however, proved elusive, and have only been observed recently – beyond the period described in this thesis – following further improvements to the MOT beam quality, magnetic field control, and general experimental control and data acquisition.

As reported in the previous chapter, we have observed a curious and unexpected induced transparency effect in the vapour cell, whereby a weak frequency shifted probe beam is able to switch on and off the resonant absorption of a more powerful pump beam. We have so far been unable to ascertain the origin of this effect, although many EIT conditions have been discovered, tested experimentally and theoretically explained. The closest match comes from the group of Goran Pichler at the Institute of Physics in Zagreb, whose results are almost identical although their experimental set-up is greatly different.

8.2 Outlook

The MOT apparatus and chirped pulse system is now completely assembled, tested and demonstrated. After the initial frustrations, continual further improvements and modifications are now starting to demonstrate the desired effects such as the success of seeing evidence for Raman transitions. With further refinement, we can therefore hope to investigate in due course a range of pulsed manipulation schemes, including the atomic interferometry and amplified cooling schemes described in chapter 2.

Our experimental apparatus should be suitable for many years and with it we hope to continue developing a range of new manipulation techniques that harness the characteristics of modern lasers and modulators and which may ultimately allow the control of species – new atoms and simple molecules – currently beyond our reach.

. . . . . .

Appendix A

Rabi Oscillations

A.1 Perturbation Theory Method

Imagine a group of stationary, two-level atoms being excited by a resonant laser field. With the simple picture of absorption and fluorescence as described in section 2.1, it is intuitive to conclude that the after some time, t (where t is much greater than the spontaneous decay time, τ), most of the population would be in the excited state if there was no stimulated emission. By adding in the effect of stimulated emission, half the population will occupy the excited state and the remaining half will occupy the ground state.

Though this intuitively derived solution is correct, rich detail is revealed by looking at the time dependent evolution of this group of atoms. Beginning with the simple time dependent Schrödinger equation [82]

$$i\hbar\frac{\partial}{\partial t}|\Psi(\mathbf{r},t)\rangle = H|\Psi(\mathbf{r},t)\rangle \tag{A.1}$$

the Hamiltonian, H is split into

$$H = H_0 + H_I(t) \tag{A.2}$$

where H_0 generates the standard energy levels and wavefunctions of the atoms through the solution of the time-independent Schrödinger equation and $H_I(t)$ is the time dependent, interaction Hamiltonian that includes the effect of the laser. This is a standard method of introducing external conditions into quantum systems and is commonly known as perturbation theory [82, 139].

The standard wavefunction is written as

$$\Psi_n(\mathbf{r},t) = \psi_n(\mathbf{r})\mathrm{e}^{-iE_nt/\hbar} \tag{A.3}$$

where n is the principal quantum number of the energy level of the atom. The overall wavefunction of the atom is made from a linear combination of the eigenstates:

$$\Psi(\mathbf{r},t) = \sum_{n=1}^{\infty} c_n(t)\psi_n(\mathbf{r})\mathrm{e}^{-iE_nt/\hbar} \tag{A.4}$$

The general summation is to infinity, but for a two-level system the sum stops at $N = 2$ where $n = 1$ is the ground state and $n = 2$ is the excited state. Working through the summation produces

$$\Psi(\mathbf{r},t) = c_1(t)\psi_1\mathbf{r}\mathrm{e}^{-iE_1t/\hbar} + c_2(t)\psi_2\mathbf{r}\mathrm{e}^{-iE_2t/\hbar} \tag{A.5}$$

The c_1 and c_2 coefficients need to be normalised so that

$$|c_1|^2 + |c_2|^2 = 1 \tag{A.6}$$

A.2 Electric Field Interaction

Equation A.5 gives a wavefunction to start from; now the Hamiltonian needs to be addressed, in particular, $H_I(t)$, which contains the atomic interaction with the external field. The electric field of the exciting laser can be described by [35]

$$\mathbf{E} = \mathbf{E}_0\cos(\omega_L t) \tag{A.7}$$

This electric field will perturb the atom and can be described by the Hamiltonian

$$H_I(t) = e\mathbf{r}\cdot\mathbf{E}_0\cos(\omega_L t) \tag{A.8}$$

where $-e\mathbf{r}$ is the electric dipole moment, $\mathbf{r}$ are the co-ordinates of the electron from the nucleus[1]. Note that this very simple case is for just one electron, for a multi-electron atom the interaction would have to be expanded to sum over all electrons and becomes a much more difficult problem to solve.

[1]More accurately, $\mathbf{r}$ should be the co-ordinates of the electron with respect to the centre of mass of the atom.

The wavefunction in equation A.5 can now be substituted into the time-dependent Schrödinger equation, (equation A.1), which now includes the effect of the laser field. This leads to two coupled, differential equations: [48]

$$i\frac{\mathrm{d}}{\mathrm{d}t}c_1 = \Omega\cos(\omega_L t)\mathrm{e}^{-i\omega_0 t}c_2 \tag{A.9}$$

$$i\frac{\mathrm{d}}{\mathrm{d}t}c_2 = \Omega^*\cos(\omega_L t)\mathrm{e}^{i\omega_0 t}c_1 \tag{A.10}$$

where $\omega_0 = (E_2 - E_1)/\hbar$ (the energy difference between the ground and excited states) and Ω is defined by

$$\Omega = \frac{\langle 1|e\mathbf{r}\cdot\mathbf{E}_0|2\rangle}{\hbar} \tag{A.11}$$

$$= \frac{e}{\hbar}\int \psi_1^*(\mathbf{r})\ \mathbf{r}\cdot\mathbf{E}_0\,\psi_2(\mathbf{r})\ d^3\mathbf{r} \tag{A.12}$$

Ω is known as the *Rabi frequency*. [51] A simplification can be made in the equation for Ω by noting that the electric field of the laser beam has almost uniform amplitude over the extent of the atom. This assumption is reasonable as the wavelength of light is on order of μm while atomic scales are on the order of Å (1×10^{-10} m)[2]. This means that $|\mathbf{E}_0|$ can be taken outside the integral in equation A.12. By representing the electric field as polarised along the x-axis

$$\mathbf{E} = |E_0|\hat{\mathbf{e}}_x\cos(\omega_L t) \tag{A.13}$$

and substituting this into equation A.12 and integrating gives

$$\Omega = \frac{e\langle 1|x|2\rangle|E_0|}{\hbar} \tag{A.14}$$

This has now given an expression for the Rabi Frequency, Ω, calculated using perturbation theory.

Returning to the coupled equations, A.9 and A.10, these can be de-coupled and solved by substituting the cosine identity

$$\cos\theta = \frac{1}{2}\left(\mathrm{e}^{i\theta} + \mathrm{e}^{-i\theta}\right) \tag{A.15}$$

[2]This is known as the *dipole approximation* and is valid where the laser wavelength, λ_L is much greater than the atomic diameter, a_0.

where θ is an angle in radians, into equations A.9 and A.10, which gives

$$i\frac{d}{dt}c_1 = c_2\left[e^{i(\omega_L-\omega_0)t} + e^{-i(\omega_L+\omega_0)t}\right]\frac{\Omega}{2} \quad (A.16)$$

$$i\frac{d}{dt}c_2 = c_1\left[e^{i(\omega_L+\omega_0)t} + e^{-i(\omega_L-\omega_0)t}\right]\frac{\Omega^*}{2} \quad (A.17)$$

The magnitude of the difference, $|\omega_L-\omega_0|$ is the detuning of the laser field from resonance of the atom and is typically very small (can be on the MHz scale) whereas the sum of the two frequencies, $\omega_L + \omega_0 \simeq 2\omega_0$ and hence is very large ($\sim 10^{14}$ Hz). This means that any exponent containing the factor $(\omega_L + \omega_0)t$ can be ignored as negligible. This is known at the *rotating wave approximation* and reduces equations A.16 and A.17 to [140, 141]

$$i\frac{\mathrm{d}}{\mathrm{d}t}c_1 = c_2 e^{i(\omega_L-\omega_0)t}\frac{\Omega}{2} \quad (A.18)$$

$$i\frac{\mathrm{d}}{\mathrm{d}t}c_2 = c_1 e^{-i(\omega_L-\omega_0)t}\frac{\Omega^*}{2} \quad (A.19)$$

These two equations can be combined by first differentiating A.19 again and substituting equation A.18 to give

$$\frac{\mathrm{d}^2}{\mathrm{d}t^2}c_2 + i(\omega_L-\omega_0)\frac{\mathrm{d}}{\mathrm{d}t}c_2 + \frac{\Omega^2}{4}c_2 = 0 \quad (A.20)$$

To solve this second-order differential equation it must be recast into the characteristic roots equation: [142]

$$a\ddot{y} + b\dot{y} + cy = 0 \quad \rightarrow \quad ar^2 + br^2 + cr = 0 \quad (A.21)$$

Beginning to solve this, it can be seen that

$$b^2 - 4ac \quad \rightarrow \quad -(\omega_L-\omega_0)^2 - \Omega^2 < 0 \quad (A.22)$$

This means that the solution to the roots are complex numbers in the form $r_\pm = \alpha \pm i\beta$, so the general solution takes the form

$$y = c_1 e^{\alpha t}\cos(\beta t) + c_2 e^{\alpha t}\sin(\beta t) \quad (A.23)$$

where

$$\alpha = \frac{-b}{2a} \quad \text{and} \quad \beta = \frac{\sqrt{4ac-\beta^2}}{2a} \quad (A.24)$$

So

$$\alpha = \frac{-i(\omega_L - \omega_0)}{2} \quad \text{and} \quad \beta = \frac{\sqrt{\Omega^2 + (\omega_L - \omega_0)^2}}{2} \tag{A.25}$$

Now the expressions for α and β are substituted and an initial set of starting conditions are imposed such that at $t = 0$, all the population is in the ground state, so $c_1(0) = 1$ and $c_2(0) = 0$. This finally gives

$$|c_2(t)|^2 = \frac{\Omega^2}{W^2} \sin^2\left(\frac{Wt}{2}\right) \tag{A.26}$$

where $W^2 = \Omega^2 + (\omega_L - \omega_0)^2$. The modulus squared of the coefficients ($|c_1|^2$ and $|c_2|^2$) represent the probability of finding the atom in the ground and excited state respectively at a time t. If the laser frequency is resonant with the atom ($\omega_L - \omega_0 = 0$), then $W = \Omega$ and equation A.26 reduces to

$$|c_2(t)|^2 = \sin^2\left(\frac{\Omega t}{2}\right) \tag{A.27}$$

This gives the surprising result that the population oscillates between the ground and excited state levels with time.

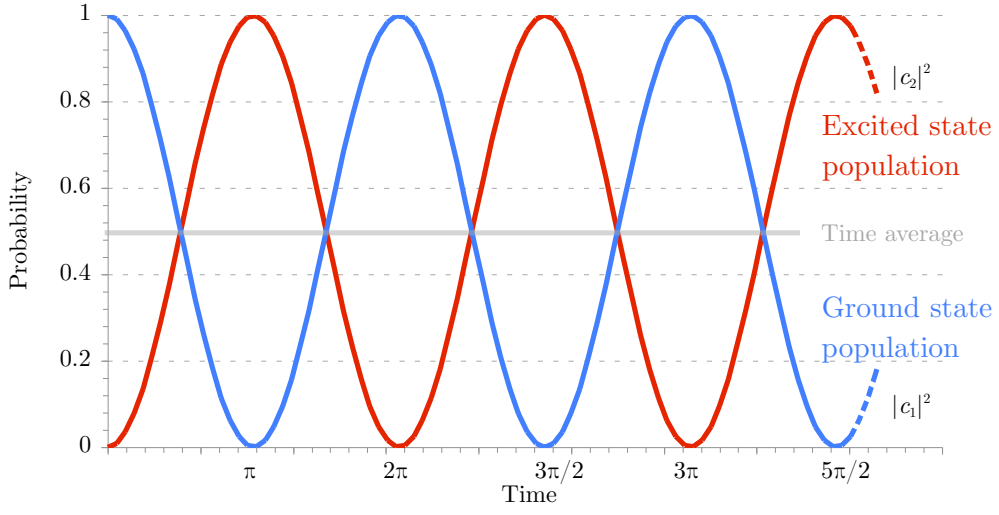

FIGURE A.1: The $|c_1|^2$ and $|c_2|^2$ coefficients oscillation in time. These correspond to the atomic population oscillating between the ground and excited states.

Though the whole population begins in the ground state at $t = 0$, when $\Omega t = \pi$, $|c_2(t)|^2 = 1$, meaning all the population has transferred to the excited state. When $\Omega t = 2\pi$, the entire population has fallen back down to the ground state again. As time progresses, the population oscillates back and forth between the ground and excited states, this is

known as *Rabi flopping* or *Rabi oscillations*. Taking the time averaged behaviour (over a complete cycle) reproduces the time-independent result that the population is equally distributed between the ground and excited states.

Figure A.2 examines the effect upon the Rabi Frequency of changing the laser detuning, δ. As δ increases, the oscillations decrease in amplitude (there is less probability of an atom being excited into the upper state) and the frequency of the Rabi oscillations increases.

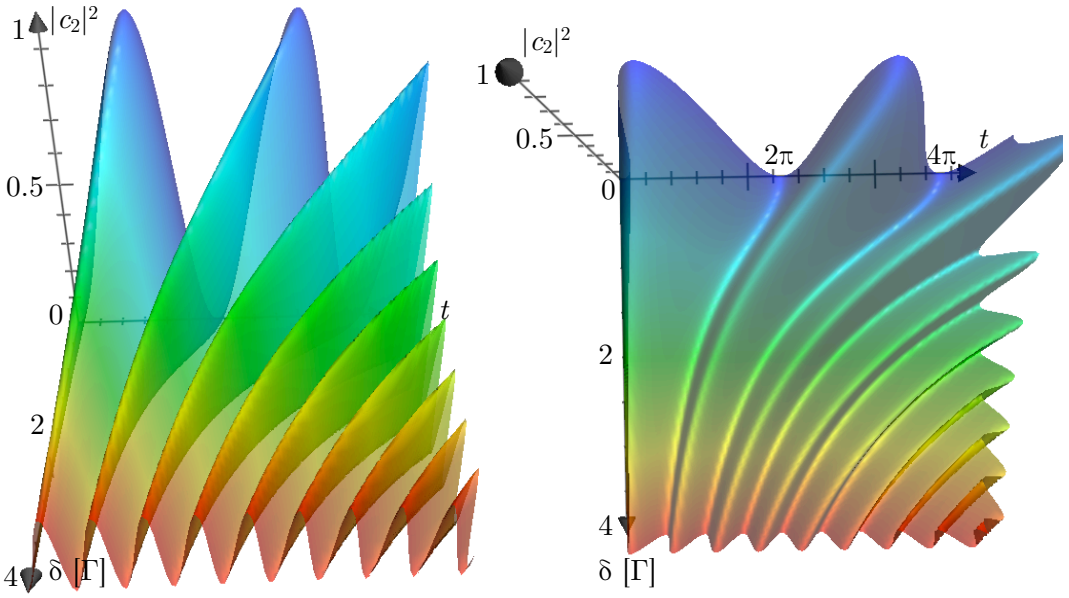

FIGURE A.2: Two views of the same 3D graph showing how the Rabi oscillations change as the laser detuning, δ is varied. The amplitude of the oscillations decreases (meaning there is less probability for excitation) and the frequency of the oscillations increases as δ increases.

Appendix B

The Bloch Sphere Representation

B.1 Forming the Bloch Sphere

The Bloch sphere is a generalisation of a unit complex number, z, where $|z|^2 = 1$ and this can be represented by a point on a unit circle in the complex plane. [143]

If $z = x + iy$ then we have:

$$\begin{aligned} |z|^2 &= z^* z \\ &= (x + iy)(x + iy) \\ &= x^2 + y^2 \end{aligned}$$

and this is the equation for a circle of radius, 1, centered at the origin.

Moving from Cartesian to Polar coordinates, $x \to r\cos\theta$ and $y \to r\sin\theta$ so

$$\begin{aligned} z &= x + iy \\ z &\to r(\cos\theta + i\sin\theta) \end{aligned} \tag{B.1}$$

However, from Euler's identity, $e^{i\theta} = \cos\theta + i\sin\theta$ and so this reduces B.1 to simply

$$z = re^{i\theta} \tag{B.2}$$

On the unit circle (because of the constraint, $|z|^2 = 1$), $r = 1$ and so this reduces equation B.2 further to

$$z = e^{i\theta} \tag{B.3}$$

The state of an electron in a two-level system can be written as

$$|\psi\rangle = \alpha\,|0\rangle + \beta\,|1\rangle \tag{B.4}$$

where the amplitude co-efficients, α and β can be complex numbers and $|0\rangle$ and $|1\rangle$ are the ground and excited states respectively. There is the constraint that the co-efficients, α and β must normalise,

$$|\alpha|^2 + |\beta|^2 = 1 \tag{B.5}$$

Equation B.4 can be transformed to Polar coordinates to give

$$|\psi| = r_\alpha e^{i\phi_\alpha}\,|0\rangle + r_\beta e^{i\phi_\beta}\,|1\rangle \tag{B.6}$$

and this has four real parameters, r_α, ϕ_α, r_β and ϕ_β.

Since the only measurable quantities are the probability amplitudes, $|\alpha|^2$ and $|\beta|^2$, it is possible to multiply through equation B.6 by a phase factor, $e^{i\gamma}$ since this should have no observable outcome, because

$$\begin{aligned}
\left|e^{i\gamma}\alpha\right|^2 &= \left(e^{i\gamma}\alpha\right)^*\left(e^{i\gamma}\alpha\right) \\
&= \left(e^{-i\gamma}\alpha^*\right)\left(e^{i\gamma}\alpha\right) \\
&= \alpha^*\alpha \\
&= |\alpha|^2
\end{aligned}$$

and this is similar for $|\beta|^2$ so it is possible to multiply by $e^{-i\phi_\alpha}$ through equation B.6 to give

$$\begin{aligned}
\left|\psi'\right\rangle &= r_\alpha\,|0\rangle + r_\beta e^{i\left(\phi_\beta-\phi_\alpha\right)}\,|1\rangle \\
&= r_\alpha\,|0\rangle + r_\beta e^{i\phi}\,|1\rangle
\end{aligned} \tag{B.7}$$

and this now has only three parameters, r_α, r_β and $\phi = \phi_\beta - \phi_\alpha$.

There is also a normalisation constraint of, $\langle\psi'|\psi'\rangle = 1$ that needs to be applied and by switching back to Cartiesian coordinates for the co-efficient of $|1\rangle$

$$\begin{aligned}
\left|\psi'\right\rangle &= r_\alpha\,|0\rangle + r_\beta e^{i\phi}\,|1\rangle \\
&= r_\alpha\,|0\rangle + (x+iy)\,|1\rangle
\end{aligned} \tag{B.8}$$

and the applying the normalisation constraint to this gives

$$\begin{aligned} |r_\alpha|^2 + |x+iy|^2 &= r_\alpha^2 + (x+iy)^* (x+iy) \\ &= r_\alpha^2 + (x-iy)(x+iy) \\ &= r_\alpha^2 + x^2 + y^2 \end{aligned} \tag{B.9}$$

Equation B.9 is the equation of a 3D unit sphere with Cartesian coordinates, (x, y, r_α). This can be converted to spherical Polar coordinates through

$$x = r\sin\theta\cos\phi \tag{B.10}$$

$$y = r\sin\theta\sin\phi \tag{B.11}$$

$$z = r\cos\theta \tag{B.12}$$

By renaming $r_\alpha \to z$ and noting that $r = 1$ (from the unit circle), equation B.8 can be rewritten as

$$\begin{aligned} \left|\psi'\right\rangle &= z\left|0\right\rangle + (x+iy)\left|1\right\rangle \\ &= \cos\theta\left|0\right\rangle + \sin\theta\left(\cos\phi + i\sin\phi\right)\left|1\right\rangle \\ \left|\psi'\right\rangle &= \cos\theta\left|0\right\rangle + e^{i\phi}\sin\theta\left|0\right\rangle \end{aligned} \tag{B.13}$$

Now equation B.13 has only two parameters that define points on the unit sphere. This is also very close to the equation for the wavefunction of an electron in a two-level system (equation B.15). It remains to look and define the range of values for θ and ϕ and by analysing orthogonal points on the Bloch sphere, it turns out that these points differ by a phase factor of -1. This means that it is only necessary to consider the upper hemisphere of the Bloch sphere where $0 \leq \theta \leq \pi/2$ since this can generate all points on the Bloch sphere. Since by convention, the limits of θ are $0 \leq \theta \leq \pi$, equation B.13 needs to be re-written as

$$\left|\psi'\right\rangle = \cos\frac{\theta}{2}\left|0\right\rangle + e^{i\phi}\sin\frac{\theta}{2}\left|0\right\rangle \tag{B.14}$$

where $0 \leq \theta \leq \pi$ and $0 \leq \phi \leq 2\pi$ and these are now the coordinates of the unit vector on the Bloch sphere.

B.2 Definition of the Bloch Sphere

The wavefunction for an electron that can be in either a ground or excited state can be written as

$$|\psi\rangle = e^{i\gamma}\left(\cos\frac{\theta}{2}|0\rangle + e^{i\phi}\sin\frac{\theta}{2}|1\rangle\right) \tag{B.15}$$

where $|0\rangle$ and $|1\rangle$ represent the ground and excited states respectively. This is also known as an arbitrary single qubit state. The θ, ϕ and γ are real numbers, θ has the range, $0 \leq \theta \leq \pi$ and ϕ has the range, $0 \leq \phi \leq 2\pi$. Additionally, since the factor, $e^{i\gamma}$ has no observable effects, it can be dropped to give simply,

$$|\psi\rangle = \cos\frac{\theta}{2}|0\rangle + e^{i\phi}\sin\frac{\theta}{2}|1\rangle \tag{B.16}$$

This represents a point on the unit Bloch sphere and it has been shown that for a two-level atom, transitions between the ground and excited states caused by an external electric (laser) field – which can be on or off resonance – can be represented by the Bloch-sphere picture with four vectors [144, 145]. The vector representing the ground state points upwards in the $+z$ direction and the vector representing the excited state points downwards in the $-z$ direction. The remaining two vectors are the state vector ψ, which represents the population occupation and the effective electric field vector ε, which represents the laser field as shown in figure B.1.

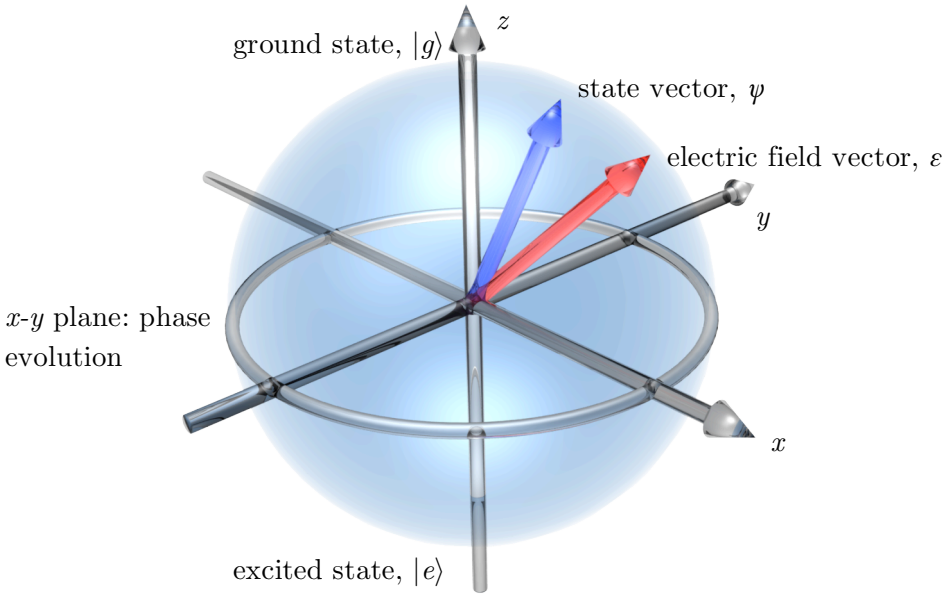

FIGURE B.1: The Bloch sphere representation of an atom interacting with a laser field. The state vector rotates about the effective field, always maintaining a constant angle. Detuning from resonance adds a zenith angle to the effective field vector.

The x, y plane represents the atomic phase and so rotations of the state vector about z are atomic phase evolutions in time. The effective field vector points in any direction along the equator if the field is directly on resonance with the atomic transition. Introducing a detuning, δ makes the effective field vector increase in zenith angle.

B.3 Rabi Oscillations on the Bloch Sphere

In the application of a resonant π-pulse, the effective field vector lies in the x, y plane, the state vector is initially pointing up (meaning all atoms are in the ground state) and rotates about this effective field vector. The rotation maintains a constant angle between it and the effective field vector (in this case 90°). The length of the π-pulse is such that the pulse ends just as the state vector reaches the excited state (pointing down). A longer pulse means that the state vector continues rotating past the excited state and back up towards the ground state. This is the simple Rabi oscillation picture and is shown in figure B.2.

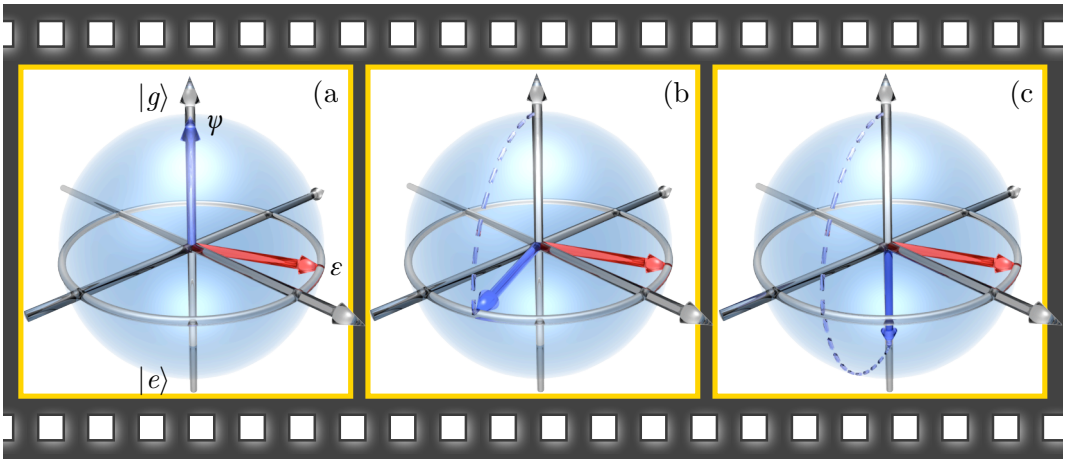

FIGURE B.2: Film strip picture of the operation of a π-pulse on the state vector in the Bloch sphere representation.

If the pulse is detuned by a small amount, δ the effective field vector no longer lies in the x, y plane but has a small zenith angle. This means the angle between it and the state vector in the ground state is no longer 90° and is maintained as the state vector rotates about the effective field, so the state vector does not quite reach the excited state and – if allowed to sweep back to the top – traces a cone as shown in figure B.3.

If the detuning, δ is great (figure B.3, (b)), the zenith angle becomes large and the state vector traces small oscillations off the pole.

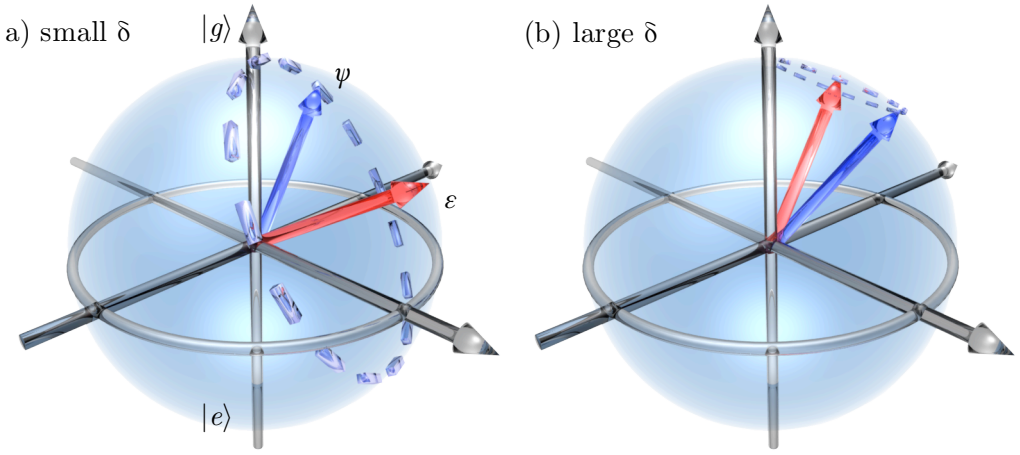

FIGURE B.3: State vector, ψ precession around the effective field vector, ε maintaining a constant solid angle. For a small detuning (a), the effective field has a small zenith angle, which increases for a large detuning from resonance (b).

Appendix C

Vapour Cell Calculations

C.1 Mean Free Path

A difficulty when performing chirped, pulsed experiments in a rubidium Vapour cell is that the coherence time for the atoms is short. A single collision with another atom or the cell wall can cause a transition between hyperfine ground states and hence loss of coherence. For atoms at room temperature travelling at hundreds of metres per second, confined in a small glass cell, the time between collisions is short.

A characteristic 'mean free time' can be calculated, which is a measure of how long an atom prepared to be in a certain state will remain there before a collision disrupts it.

To begin calculating this, the scattering cross-section, A_{Rb} of a single ^{85}Rb atom of diameter, d is required:

$$A_{\mathrm{Rb}} = \pi d^2 \tag{C.1}$$

Note this is not the same as the cross section of the atom[1]. The effective collision area is greater as both atoms in a collision have a finite area as shown in figure C.1.

An estimate for the mean free path, λ is then taken as the distance travelled, $\bar{v}t$ divided by the interaction volume, $A_{\mathrm{Rb}}\bar{v}t$ times the number of atoms per unit volume, n_V:

$$\lambda = \frac{\bar{v}t}{\pi d^2 \bar{v} t n_V} = \frac{1}{\pi d^2 n_V} \tag{C.2}$$

The $\bar{v}$ used is the average velocity of one atom while assuming all other atoms are at rest. This is not physically true and so $\bar{v}$ needs to be modified to take into account

[1]The scattering cross-section would be the same as the atomic cross section if one of the two particles involved in the collision was considered to be point-like.

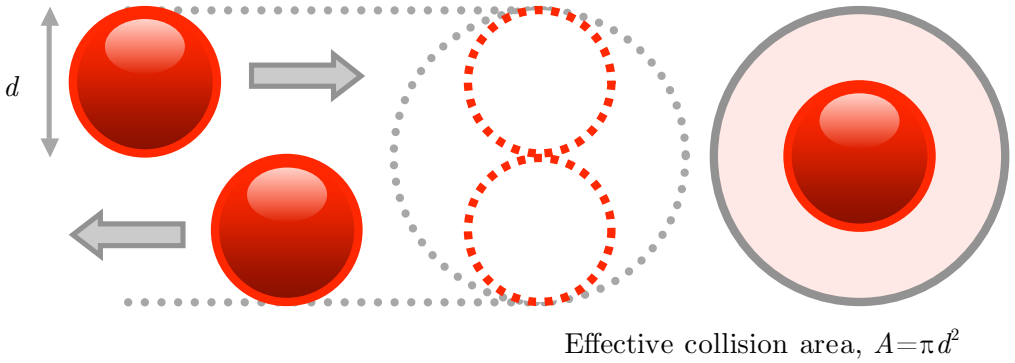

FIGURE C.1: The effective collision area is not simply the area of a single particle, but extends to $A_{\mathrm{Rb}} = \pi d^2$, where d is the atomic diameter.

the fact that all the atoms are moving. Calculating the average *relative velocity*, $\bar{v}_{\mathrm{rel}}$ between the atoms and the other randomly moving 'targets' modifies $\bar{v}$ to be

$$\bar{v}_{\mathrm{rel}} = \sqrt{2}\bar{v} \tag{C.3}$$

This modifies λ in equation C.2 to

$$\lambda = \frac{\bar{v}t}{\sqrt{2}\pi d^2 \bar{v} t n_V} = \frac{1}{\sqrt{2}\pi d^2 n_V} \tag{C.4}$$

Note that the numerator does not have the $\sqrt{2}$ factor as it is the distance of the atom travelled only, while the denominator includes the atom and targets hence uses $\bar{v}_{\mathrm{rel}}$.

The number of atoms per unit volume, n_V can be expressed using Avogadro's number, N_A with the Ideal Gas law: [146]

$$PV = nRT \qquad \text{Ideal Gas law} \tag{C.5}$$

$$n_V = \frac{nN_A}{V} = \frac{nN_A}{nRT/P}$$

$$n_V = \frac{N_A P}{RT} \tag{C.6}$$

Substituting this into the revised mean free path (equation C.4) gives

$$\lambda = \frac{RT}{\sqrt{2}\pi d^2 N_A P} \tag{C.7}$$

Intuitively, the mean free path depends linearly on the temperature, T and inversely to the pressure, P. Taking room temperature to be 298 K and the atomic velocity, $v \simeq 300$ ms^{-1} (from equation 2.2), the vapour pressure of rubidium at room temperature to be 1 Pa gives the mean free path to be, $\lambda \simeq 0.0168$ m (1.68 cm). The mean free time, τ can be calculated by dividing the mean free path by the atomic velocity giving

$$\tau = \lambda/v \tag{C.8}$$

$$\simeq 60\ \mu\text{s} \tag{C.9}$$

Rubidium atoms remain coherent on average for around $\tau \simeq 60\ \mu$s in a room temperature vapour cell. The cell is a finite length cylinder of 50 mm and 25 mm diameter (d) so if an atom begins at the on-axis centre, the time, t_{vc} taken for it to move radially outward to the cell wall is

$$t_{\text{vc}} = d/v \tag{C.10}$$

$$= 0.0125/300$$

$$t_{\text{vc}} \simeq 40\ \mu\text{s} \tag{C.11}$$

These two calculated times, τ and t_{vc} are similar such that the atom is almost as likely to loose coherence from a collision with another atoms as it is from a collision with the cell wall. The pulsing experiments and state manipulation need to be done within t_{vc} to retain as much of the coherence of the system as possible before collisions mix the state-prepared populations.

Appendix D

Magnetic Field Equations

The Magneto-Optical Trap requires the combination of Optical Molasses together with a position dependent cooling force provided by an anti-Helmholtz magnetic field. This non-uniform magnetic field is created by a pair of wire coils with the currents flowing in opposite directions. The field can be calculated by initially beginning with the Biot-Savart law:

$$\mathrm{d}\mathbf{B} = \frac{\mu_0}{4\pi} I \frac{\mathrm{d}\mathbf{l} \times \hat{\mathbf{r}}}{r^2} \tag{D.1}$$

The following sections use this equation to derive the magnetic field at the centre of a wire loop, which is then extended to the on-axis field and finally a coil pair.

D.1 Field From a Wire Loop

Referring to the diagram in figure D.1, the field at the centre of a current carrying circular loop or radius, a can be calculated by

$$\mathrm{d}\mathbf{B} = \frac{\mu_0}{4\pi} I \frac{\mathrm{d}\mathbf{l} \times \hat{\mathbf{r}}}{r^2} \quad \rightarrow \quad \frac{\mu_0}{4\pi} I \frac{\mathrm{d}l \sin\theta}{a^2} \tag{D.2}$$

This is a special case because $\sin\theta$ is always 1 because θ is always at 90° (tangential) for all points on the current loop and the distance, $R(=a)$ is the radius of the loop hence is also constant. Integrating to find the expression for B gives

$$B = \oint_0^{2\pi} \frac{\mu_0}{4\pi} \frac{I}{a^2} \mathrm{d}l \quad \rightarrow \quad \frac{\mu_0}{4\pi} \frac{I}{a^2} \oint_0^{2\pi} \mathrm{d}l \tag{D.3}$$

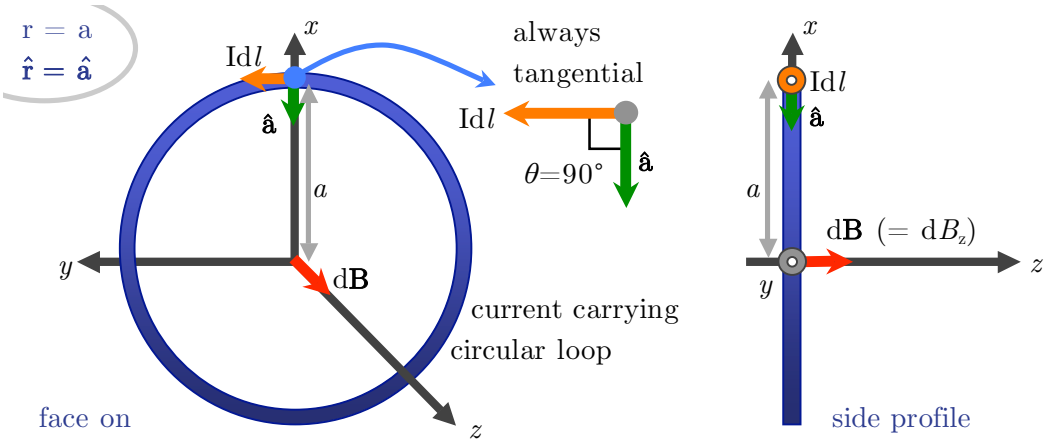

FIGURE D.1: The geometry for calculating the magnetic field at the centre of a current carrying circular loop of radius a.

Integrating round the current loop (full 2π circle) gives

$$B = \frac{\mu_0 I}{2a} \tag{D.4}$$

as the magnitude of the magnetic field at the centre of the current loop.

D.2 On Axis Field

The simple picture in the previous section can be extended to give an expression for the value of the field anywhere along the axis that passes through the centre of the current loop. The geometry (shown in figure D.2) is helpful in simplifying the cross product term of the Biot-Savart Law (equation D.1).

$\mathrm{d}\mathbf{l} \times \hat{\mathbf{r}} = \mathrm{d}l$ as $\mathrm{d}\mathbf{l}$ and $\hat{\mathbf{r}}$ are always perpendicular, so

$$|\mathrm{d}\mathbf{B}| = \frac{\mu_0 I}{4\pi}\frac{|\mathrm{d}\mathbf{l} \times \hat{\mathbf{r}}|}{r^2} \quad \rightarrow \quad \frac{\mu_0 I}{4\pi}\frac{\mathrm{d}l}{(a^2+z^2)} \tag{D.5}$$

$\mathrm{d}B_x = 0$ from the symmetry arguments of summing up the field contributions around the z-axis (where $x = 0$).
$\mathrm{d}B_y = 0$ as there is no component parallel to $\mathrm{d}\mathbf{l}$ along the line of $\mathrm{d}\mathbf{l}$
So the only non-zero, on-axis component remaining is $\mathrm{d}B_z$:

$$\mathrm{d}B_z = \mathrm{d}\mathbf{B}\sin\theta \tag{D.6}$$

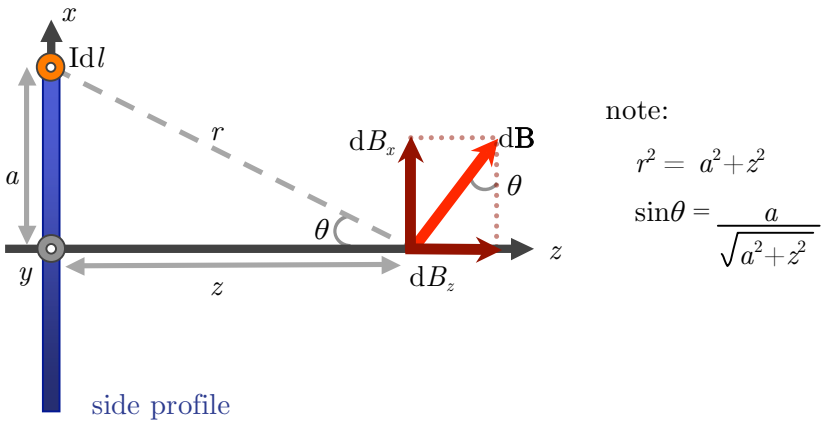

FIGURE D.2: The geometry for calculating the magnetic field along the central axis of a current carrying circular loop of radius a.

From the geometry in figure D.2, $\sin\theta = a/\left[(a^2+z^2)^{1/2}\right]$, substituting this back into equation D.6 and integrating dl around 2π gives

$$B_z = \frac{\mu_0 I}{2}\frac{a^2}{(a^2+z^2)^{3/2}} \tag{D.7}$$

which is the expression for the magnetic field along the axis of a current loop.

D.3 Extension to a Coil Pair

Finally, equation D.7 is modified by placing the current loop at a position b along the z-axis, this done by applying a simple transform of $z \rightarrow z-b$. For an anti-Helmholtz model, there also needs to be a second coil at position, $-b$ along the z-axis (to form the coil pair). This adds a second term, identical to equation D.7 but with the z co-ordinate transformed to $z+b$ and a negative sign to represent the current flowing in the opposite sense to the first coil. The final field is obtained by adding these two terms together to obtain

$$B_z = \frac{\mu_0 I}{2}\left[\frac{a^2}{(a^2+(z-b)^2)^{3/2}} - \frac{a^2}{(a^2+(z+b)^2)^{3/2}}\right] \tag{D.8}$$

This gives the equation for the on-axis magnetic field from a pair of current loops (coils) of radius a, separated by a distance $2b$. It does not take into account the finite width of the coil, nor its depth (thickness), these can be factored in by calculating the field from the extremities of the coil (transforming a and b appropriately and obtaining four terms per coil) and adding or subtracting to take an average. This degree of accuracy is unnecessary for our purposes and is not covered here.

Appendix E

The Anti-Helmholtz Condition

Appendix D derives the basic equations for the on-axis field produced by a circular, current carrying loop from the Biot-Savart law. Though they are suitable in most cases for Helmholtz and anti-Helmholtz coils, they are too simple to outline a subtle difference between the Helmholtz and anti-Helmholtz conditions.

The Helmholtz condition states that in order obtain the optimum, uniform field between the coil pair, the coil radius, a must be equal to the distance between coils, $2b$. This comes from differentiating the equation for the magnetic field produced by a Helmholtz coil pair and finding the expression for a and b by setting the derivative, $\mathrm{d}B/\mathrm{d}z$ along the axis to zero (i.e. field gradient is zero – which is equivalent to a uniform, constant field).

In contrast, the anti-Helmholtz condition is where the field gradient, $\mathrm{d}B/\mathrm{d}z$ along the axis is at a maximum and the Helmholtz condition, $a = 2b$, is incorrect in this case. The correct expression can be found by looking at the exact equation for the on-axis magnetic field from a circular current loop, the derivation of which is beyond the scope of this thesis [121]:

$$B_z = \frac{\mu I}{2\pi} \frac{1}{\sqrt{(a+\rho)^2 + (z-b)^2}} \left[K(k^2) + \frac{a^2 - \rho^2 - (z-b)^2}{(a-\rho)^2 + (z-b)^2} E(k^2) \right] \tag{E.1}$$

where $K(k^2)$ and $E(k^2)$ are the complete elliptic integrals of the first and second kind respectively and

$$k^2 = \frac{4a\rho}{(a+\rho)^2 + (z-b)^2} \tag{E.2}$$

This is for a circular current loop of radius, a carrying a current, I and displaced from the origin along the z-axis by a distance, b. Introducing a second coil displaced by a

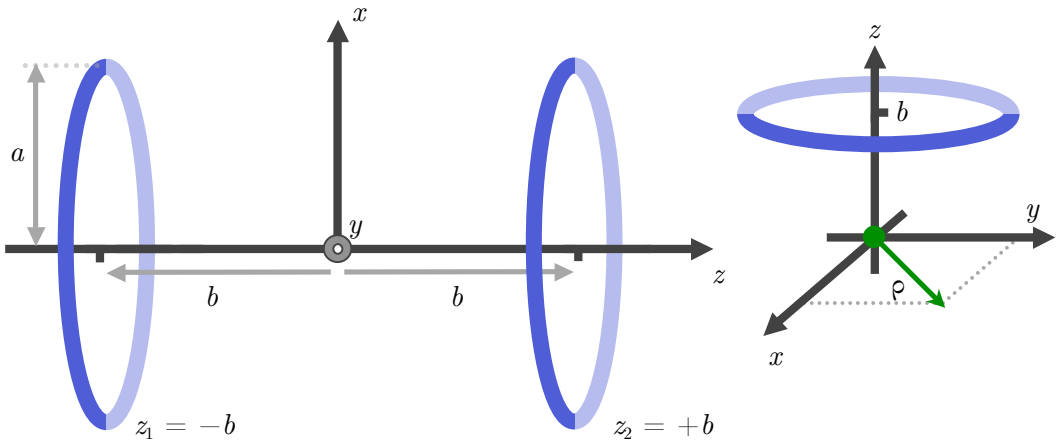

FIGURE E.1: The geometry for calculating the magnetic field for an anti-Helmholtz coil pair and for deriving the expression for a and b for which the magnetic field gradient at the on-axis centre is greatest.

distance, $-b$ along the z-axis reproduces the coil pair as shown in figure E.1 and equation E.1 needs to have a second B_z factor for this coil added to it[1].

The region of interest for the anti-Helmholtz condition is at the on-axis mid-point between the two coils. This is the region around the origin, where $z, \rho = 0$. The expression for B_z in equation E.1 needs to be expanded as a power series to third order to obtain

$$\begin{aligned} B_z &= \mu_0 I \frac{1}{2}\frac{a^2}{(b^2+a^2)^{3/2}} + \overbrace{\mu_0 I \frac{3}{2}\frac{a^2 b}{(b^2+a^2)^{5/2}}}^{\text{axial field gradient}} z + \overbrace{\mu_0 I \frac{3}{4}\frac{a^2(4b^2-a^2)}{(b^2+a^2)^{7/2}}}^{\text{axial curvature}}(z^2 - \rho^2/2) \\ &\quad + \mu_0 I \frac{5}{4}\frac{a^2(4b^2-3a^2)}{(b^2+a^2)^{9/2}}(4z^3 - 6\rho^2 z) + \ldots \end{aligned} \tag{E.3}$$

For an anti-Helmholtz coil pair, this equation reduces to

$$B_z = 3\mu_0 I \frac{a^2 b}{(b^2+a^2)^{5/2}} z + \mu_0 I \frac{15}{24}\frac{a^2(4b^2-3a^2)}{(b^2+a^2)^{9/2}}(4z^2 - 6\rho^2 z) + \ldots \tag{E.4}$$

Note that the first term in equation E.4 is the axial field gradient, which is the result obtained by differentiating the equation for the magnetic field of a current loop (equation D.7 in Appendix D) with respect to z (ie. $\mathrm{d}B/\mathrm{d}z$).

Equation E.4 gives the magnetic field of an anti-Helmholtz coil pair to third order. To find the optimum constraint for a and b, which will produce the steepest field gradient (maximum $\mathrm{d}B/\mathrm{d}z$) the double differential, $\mathrm{d}^2B/\mathrm{d}z^2$ is calculated and set equal to zero,

[1] Remembering to reverse the signs for b because of its position on the z axis.

this gives

$$\frac{\mathrm{d}B_z^2}{\mathrm{d}z^2} = 0 \tag{E.5}$$

$$15\mu I \frac{a^2(4b^2 - 3a^2)}{(a^2 + b^2)^{9/2}} z = 0 \tag{E.6}$$

Cancelling down gives

$$\sqrt{3}a = 2b \tag{E.7}$$

Whereas before, in the Helmholtz condition, $a = 2b$, for the anti-Helmholtz condition, the geometry of the coils needed to produce the steepest field gradient is when $a = (2/\sqrt{3})b$.

Appendix I describes how the anti-Helmholtz condition together with the vacuum system geometry and field gradient requirements were used to calculate the physical parameters for the field coils such as wire gauge, number of turns and coil dimensions.

Appendix F

Linear Doppler Damping Force

F.1 Damping Parameter Expression

From the results of calculating the Doppler force in Optical Molasses (in section 3.2.2), it was noted that close to the origin, around $u = 0$, the Doppler force becomes linear and analogous to a velocity dependent damping force, F_{OM} of the form

$$F_{\mathrm{OM}} = \beta \dot{x} \tag{F.1}$$

where β is the damping constant. The original expression for the Doppler force (from equation 3.32) can be expanded around the region where $u = 0$, so $ku \ll \Gamma, \delta$ to give

$$F_{\mathrm{OM}} = \frac{\hbar k \Gamma s_0}{2} \left[\frac{1}{1 + s_0 + \left(\frac{2(\delta - ku)}{\Gamma}\right)^2} - \frac{1}{1 + s_0 + \left(\frac{2(\delta + ku)}{\Gamma}\right)^2} \right] \tag{F.2}$$

$$F_{\mathrm{OM}} = -4\hbar k^2 \cdot u \cdot \frac{2 s_0 (\delta/\Gamma)}{\left(1 + s_0 + (2\delta/\Gamma)^2\right)^2} \tag{F.3}$$

$$= -\beta u \tag{F.4}$$

In the expanded equation F.3, when the detuning is to the red ($\delta < 0$) then $\beta > 0$. The expression also contains the saturated scattering force, $\hbar k \Gamma/2$ (from equation 3.30) and is a function of the velocity, u. This is analogous to a particle moving through a viscous fluid experiencing the velocity dependent damping force – hence the name 'Optical molasses' given to Doppler laser cooling.

Equation F.3 can be reduced and simplified to give the expression for β to be

$$\beta = -\hbar k^2 \frac{4s_0(\delta/\Gamma)}{(1+s_0+(2\delta/\Gamma)^2)^2} \tag{F.5}$$

It can be seen that β is not constant, but is a function of the detuning, δ and the saturation parameter, s_0. This can be plotted as a 3D graph, shown in figure F.1 and the conditions found for δ and s_0 that give the maximum value of β.

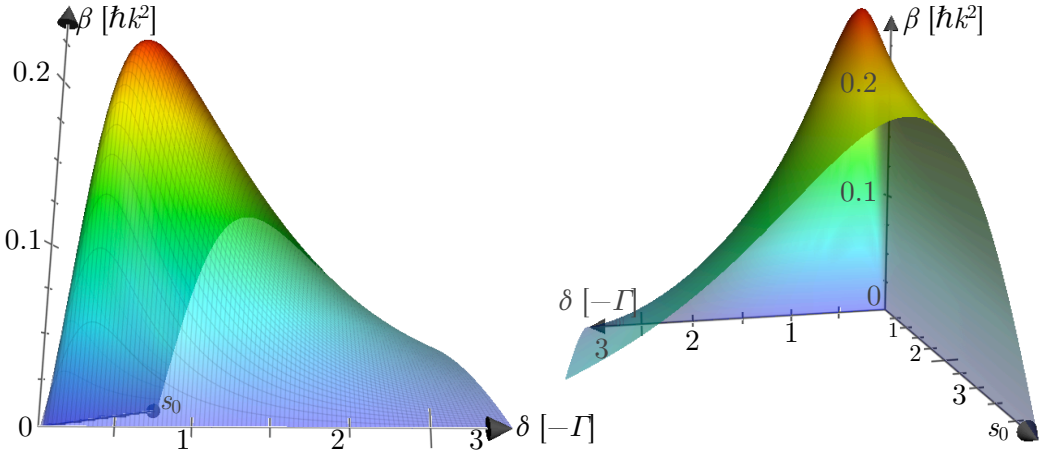

FIGURE F.1: Two views of the same 3D graph showing how the damping parameter, β (from the linear region around $u = 0$ for the Doppler force) varies with detuning, δ and the saturation parameter, s_0. The conditions for these two parameters can be found that give the maximum value of β.

F.2 Optimising the Damping Parameter

Optimising δ and s_0 by differentiating the expression for β in equation F.5 gives

$$\frac{\partial\beta}{\partial\delta} = -\frac{2\hbar k^2 s_0(1+s_0-12\delta^2)}{(1+s_0+4\delta^2)^3} = 0 \tag{F.6}$$

$$\frac{\partial\beta}{\partial s_0} = \frac{2\hbar k^2 \delta(-1+s_0-4\delta^2)}{(1+s_0+4\delta^2)^3} = 0 \tag{F.7}$$

Solving for s_0 and δ gives

$$s_0 = 1+(2\delta/\Gamma)^2 \tag{F.8}$$

$$\delta = \pm\frac{\Gamma\sqrt{1+s_0}}{2\sqrt{3}} \tag{F.9}$$

Substituting the expression for δ (equation F.9) into s_0 (equation F.8), the two conditions that give the maximum value of β are

$$s_0 = 2 \tag{F.10}$$

$$\delta = \pm\Gamma/2 \tag{F.11}$$

Equation F.11 for δ has two solutions, this is because $-\delta$ represents red-detuning while $+\delta$ is blue-detuning. The point at which $\delta = -\Gamma/2$ is also the same condition for obtaining the lowest Doppler temperature. Substituting these into equation F.5 gives

$$\beta_{\max} = \hbar k^2/4 \tag{F.12}$$

For ^{85}Rb, this gives a damping constant, $\beta \simeq 1.7 \times 10^{-21}$ kgs^{-1}. Though this seems very small, compared to the mass of a rubidium atom ($\simeq 1.4 \times 10^{-25}$ kg), a damping force of this magnitude is sufficient to significantly slow rubidium atoms from thermal velocities in much less than a second.

F.3 Effect of the Magnetic Field

Aside from the viscous damping force of Optical Molasses, there is an additional force, which appears when looking at the MOT system. With the addition of the magnetic field, the full expression for δ in equation 3.29 needs to be used and substituting this into the Doppler Force equation (equation 3.25) gives

$$\begin{aligned}
\delta &\rightarrow \delta_{\sigma^\pm} \mp k.\mathbf{u} \pm \mu_B g_J B(z)/\hbar \\
B(z) &= Az \qquad \text{(linear around z=0, the trap centre)} \\
F_{\text{MOT}} &= \frac{\hbar k \Gamma s_0}{2}\left[\frac{1}{1+s_0+\left(\frac{2(\delta-k.\mathbf{u}+\mu_B g_J Az/\hbar)}{\Gamma}\right)^2}\right. \\
&\qquad \left. -\frac{1}{1+s_0+\left(\frac{2(\delta+k.\mathbf{u}-\mu_B g_J Az/\hbar)}{\Gamma}\right)^2}\right]
\end{aligned} \tag{F.13}$$

This is now the equation for the force on an atom in a magneto-optical trap. When both the Doppler and Zeeman shifts are smaller than the detuning, δ, the denominator of F_{MOT} can be expanded in a similar manner to equation F.3 to obtain

$$F = -\beta u - \kappa z \tag{F.14}$$

This is now the damped harmonic oscillator equation, β is the same velocity dependent damping constant as in equation F.5 and κ is a spring constant (position dependent force) and the two are related through

$$\kappa = \frac{\mu_B g_J A}{\hbar k}\beta \tag{F.15}$$

The full MOT force of equation F.13 can be plotted, as it is a function of both the velocity and magnetic field, figure F.2 shows the force as a 3D graph.

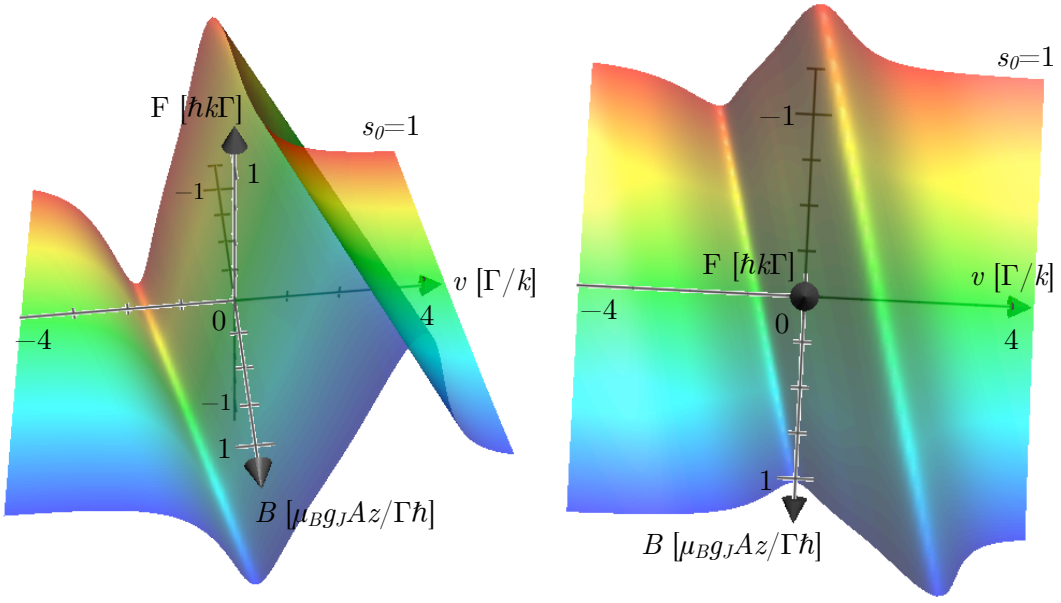

FIGURE F.2: Two views of the same 3D graph showing how the MOT force of equation F.13 is shunted by the magnetic field with the sign depending on the field direction.

Appendix G

Sisyphus Cooling

G.1 The Polarisation Gradient

The first theoretical explanations – put forward by Jean Dalibard and Claude Cohen-Tannoudji to explain the sub-Doppler temperatures reached by the first atom cooling experiments in a MOT – considered a 1-D optical molasses where the polarisations of the laser beams were linear but orthogonal to each other[1] i.e. beams travelling in the opposing z directions with one polarised along the x axis and the other along the y-axis [86]. The total electric field in this case is given by

$$E(z,t) = E(z)\mathrm{e}^{-i\omega_L t} + E^*(z)\mathrm{e}^{i\omega_L t} \tag{G.1}$$

where the electric field vector, $E(z)$ is given by

$$\begin{aligned} E(z) &= E_0\left(\hat{\mathbf{e}}_x \mathrm{e}^{iqz} + \hat{\mathbf{e}}_y \mathrm{e}^{-iqz}\right) \\ &= E_0 \mathrm{e}^{iqz}\left(\hat{\mathbf{e}}_x + \hat{\mathbf{e}}_y^{-2iqz}\right) \\ &= \sqrt{2}E_0\ \mathrm{e}^{iqz}\hat{\mathbf{e}}(z) \end{aligned} \tag{G.2}$$

From the expression of the electric field vector, the sum polarisation, $\hat{\mathbf{e}}(z)$ of the light field varies in space. The values for z in terms of fractions of the wavelength, λ can be substituted to see how the polarisation changes and the results are shown in table G.1.

The intensities of the two polarisation components varies as $[1 \mp \sin(2qz)]/2$. Figure G.1 shows how the polarisation varies in space over the distance of half a wavelength.

[1] A two-dimensional, theoretical treatment of this setup can be found in [147].

z	$\hat{\mathbf{e}}(z)$	Polarisation
0	$(\hat{\mathbf{e}}_x + \hat{\mathbf{e}}_y)/\sqrt{2}$	linear at 45° from the x-axis
$\lambda/8$	$(\hat{\mathbf{e}}_x - i\hat{\mathbf{e}}_y)/\sqrt{2}$	circular handed, σ^-
$\lambda/4$	$(\hat{\mathbf{e}}_x - \hat{\mathbf{e}}_y)/\sqrt{2}$	linear at −45° from the x-axis
$3\lambda/8$	$(\hat{\mathbf{e}}_x + i\hat{\mathbf{e}}_y)/\sqrt{2}$	circular handed, σ^+
$\lambda/2$	$(\hat{\mathbf{e}}_x + \hat{\mathbf{e}}_y)/\sqrt{2}$	linear at 45° from the x-axis

TABLE G.1: The variation of the sum polarisation of two linear, orthogonally polarised beams. The polarisation cycles in a period of only half the wavelength producing a sharp polarisation gradient.

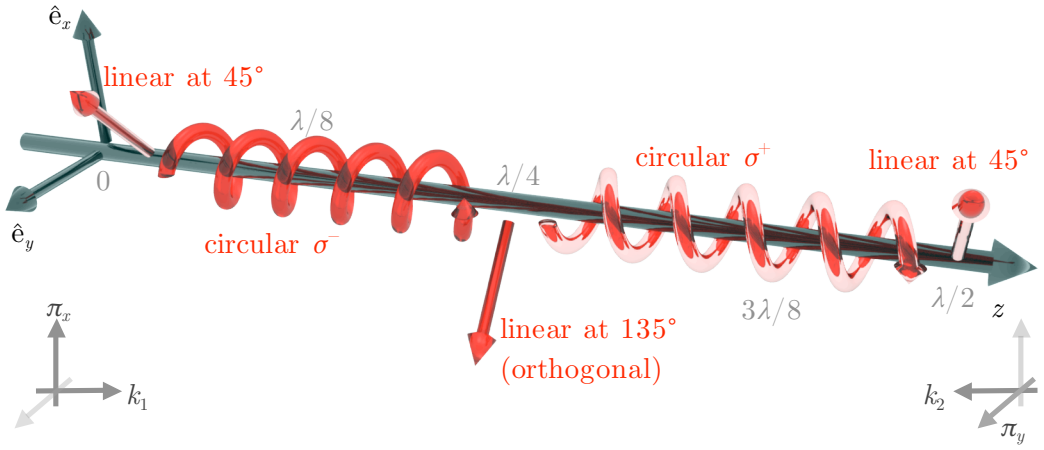

FIGURE G.1: The sum polarisation seen by an atom in a 1-D optical molasses with linear, orthogonally polarised beams.

The 'combined' polarisation switches from linear to circularly polarised, to linear (but orthogonal to the original direction) to circularly polarised in the opposite sense and back to linear again. These polarisation changes happen over a distance just half the wavelength of light and so the polarisation gradients are very steep and cause the m_J sub-states of the fine-structure levels in the rubidium atom to shift up or down in energy depending on the state of polarisation. This is called the *light shift* and is due to the AC Stark effect from the electric field of the laser light.

G.2 Transitions and Clebsch-Gordan Coefficients

Taking the example of ^{85}Rb, the $5S_{1/2}$ ground state has $J_g = 1/2$ and so has sub-states $m_J = +1/2$ and $-1/2$. The $5P_{3/2}$ excited state has $J_g = 3/2$ and so has $m_J = +3/2, +1/2, -1/2, -3/2$. With no laser field present, these m_J states are degenerate in energy, as shown in figure G.2.

The numbers on the transitions shown are the square of the *Clebsch-Gordan* coefficients, C_{ge}^2 and are an indication of the coupling strength of the atom to the light field or the

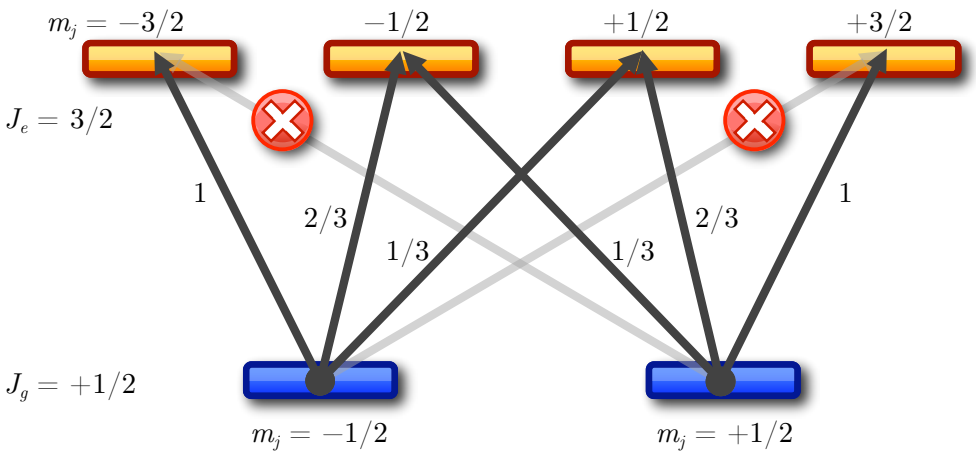

FIGURE G.2: Degenerate m_J fine-structure for an atom (with $J_g = 1/2$ and $J_e = 3/2$) with no laser field present.

transition probability (e.g. transitions with coefficient $C_{ge}^2 = 1$ are three times more likely than those that have $C_{ge}^2 = 1/3$.

The selection rules for the transitions in this scheme are based on angular momentum conservation. Circular polarised, σ^+ light carries one unit of angular momentum so is only capable of $\Delta m_J = +1$ transitions, alternatively, σ^- light is only capable of $\Delta m_J = -1$ transitions and linear polarisation cannot change the m_J number as it has no associated angular momentum. These rules are reflected in figure G.2 by the fact that the transitions, $|1/2, -1/2\rangle \rightarrow |3/2, +3/2\rangle$ and $|1/2, +1/2\rangle \rightarrow |3/2, -3/2\rangle$ are forbidden.[2]

The effect of polarised light is to lift the degeneracy of the m_J sub-states and cause them to shift in energy. The shift originates from the Stark shift from the electric field of the light and can be calculated using

$$\Delta E_g = \frac{\hbar \delta s_0 C_{ge}^2}{1 + (2\delta/\Gamma)^2} \tag{G.3}$$

where ΔE_g is the energy level shift and C_{ge} is the Clebsch-Gordan coefficient. The C_{ge} coefficients differ according to the particular transition involved (magnetic sub-level quantum numbers, polarisation, angular momentum etc...).

In addition, the polarisation is not static, but cycles over a period of half the wavelength of light. This strong polarisation gradient means that the energy level shift becomes

[2]This is using the notation of $|J_{g/e}, m_J\rangle$ where $J_g = 1/2$ and $J_e = 3/2$.

position dependent for the affected atom and can be plotted by

$$V^{\pm}(z) = V_0(-2 \pm \sin(2qz)) \tag{G.4}$$

which is a measure of the Stark shift.

Immediately it can be seen that for the ground state, J_g, the $m_J = +1/2$ and $m_J = -1/2$ are opposite in sign. Figure G.3 plots how the m_J sub-states vary in energy with the polarisation in space.

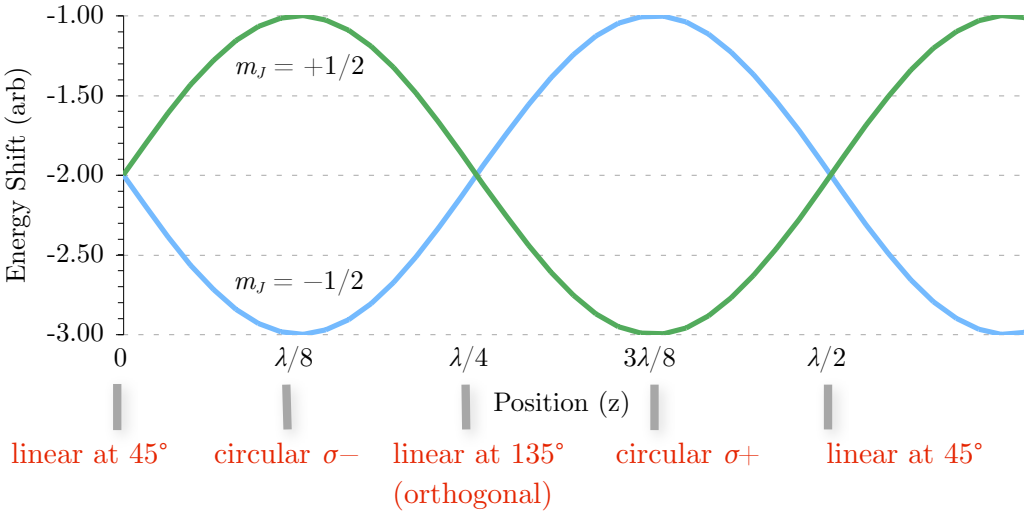

FIGURE G.3: The energy level shift of the ground state m_J sub-states caused by the different coupling strengths of linear, σ^+ and σ^- polarisations of light.

G.3 Optical Pumping

For an atom in the ground state at a position in space where the polarisation of the light field is σ^+, the allowed transitions are, $|1/2, -1/2\rangle \rightarrow |3/2, +1/2\rangle$ and $|1/2, +1/2\rangle \rightarrow |3/2, +3/2\rangle$. For the latter transition, the only option for spontaneous emission is to drop back down into the $|1/2, +1/2\rangle$ level as no other transitions are allowed. For the former, the atom has the option of dropping into either of the ground $|1/2, \pm 1/2\rangle$ states. However, referring to the Clebsch-Gordan coefficients for these transitions, it is more likely that the atom will decay into the $|1/2, +1/2\rangle$ state, which has a C_{ge} coefficient of $2/3$ than the $|1/2, -1/2\rangle$ state, which has a C_{ge} coefficient of $1/3$.

Over many absorption and spontaneous emission cycles for a group of atoms, the weighted probability from the Clebsch-Gordan coefficients mean that the population transfers to the $|1/2, +1/2\rangle$ ground state for σ^+ polarised light. The opposite is true

if the light is σ^- polarised, the atoms are driven into the $|1/2, -1/2\rangle$ ground state. This process of transferring populations between different ground state levels using the polarisation of light is called *optical pumping* [148].

G.4 Sisyphus Cooling

The situation described above is simply absorption and emission with probabilities given by the Clebsch-Gordan coefficients. The cooling aspect comes in when looking at the combination of the light-shift and optical pumping. Returning to the atom in the σ^- field and referring to figures G.3 and G.4, the $|1/2, -1/2\rangle$ is at the lower energy and the atom is optically pumped into this state. As the atom travels in space, it also travels through the polarisation gradient field and as the polarisation becomes linear, the $|1/2, -1/2\rangle$ level increases in energy meaning the atom has to climb the potential hill. When it reaches the top, the light has become σ^+ polarised and the Clebsch-Gordan coefficients pump the atoms into the $|1/2, +1/2\rangle$ ground state, this is at the bottom of the hill (since the polarisation is now σ^+, the $|1/2, +1/2\rangle$ state is light shifted to lower energy). As the atom travels further this state now increases in energy as the polarisation begins to change again and when the atom reaches the top, the light is σ^- polarised and the atom is dropped to the bottom of the potential again.

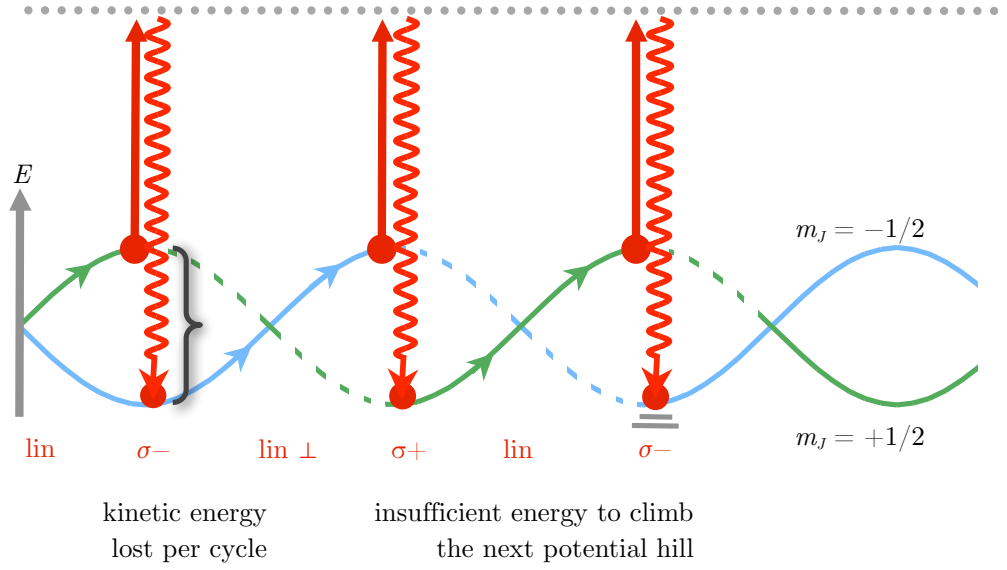

FIGURE G.4: In *Sisyphus Cooling*, the atom is always made to climb a potential hill (and hence loose energy) from the combination of the light-shifts and Clebsch-Gordan coefficients.

The atom climbs the potential hill to the top only to be dropped back down to the bottom, so it has to climb again. This is commonly known as *Sisyphus cooling* (from Greek mythology). The kinetic energy (hence motion) of the atom is used to climb the hill and the atom continues until it does not have enough kinetic energy to climb to the top of the next potential. Each optical pumping event, where the atom switches J_g state results in the absorption of a photon which is at a lower energy than the spontaneous emission down to the bottom of the potential hill, the energy lost per cycle corresponds to the energy difference (or light-shift) between the $m = -1/2$ and $m = +1/2$ ground state levels.

Appendix H

Waveplates and Polarisation

H.1 Light Polarisation

The simple picture of light as a travelling electromagnetic wave is complicated by the fact that the electric field has an orientation ie. can have different components along the x (E_x) and y axes (E_y) if the wave is travelling along z. This means that the magnitude of the field, E_0 has an orientation characterised by $\hat{\mathbf{e}}$, called the polarisation vector and points in the direction of the sum field.

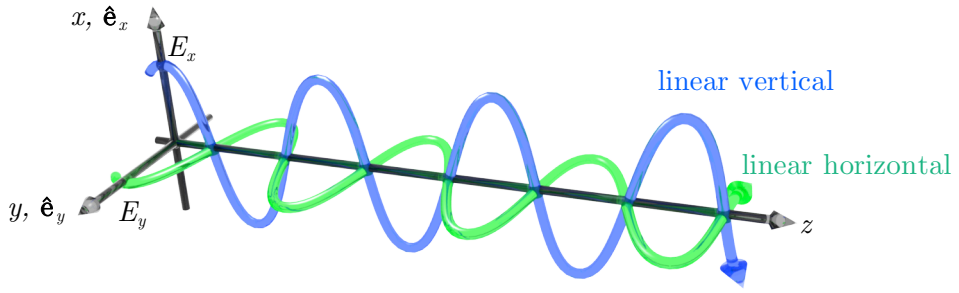

FIGURE H.1: Linear vertical polarisation (blue) with the full electric field magnitude, E_0 along x and so the polarisation vector, $\hat{\mathbf{e}} = \hat{\mathbf{e}}_x$. Linear horizontal polarisation (green) with the full magnitude, E_0 along y and so $\hat{\mathbf{e}} = \hat{\mathbf{e}}_y$. The wave is travelling in the $+z$ direction.

There are four special cases of light polarisation, linear horizontal and linear vertical, and left- and right-circular. Left circular polarisation is also labelled as σ^- polarisation and right-circular as σ^+ by convention.

Intuitively, linear horizontal polarisation contains only the E_y (horizontal) component and so $\hat{\mathbf{e}}$ points along $\hat{\mathbf{y}}$. Similarly, linear vertical contains just E_x and $\hat{\mathbf{e}}$ points along $\hat{\mathbf{x}}$.

Both linear polarisations carry no unit of photon angular momentum and are referred to as 'π polarisation'.

H.2 Circular Polarisation

Circular polarisation contains one unit of angular momentum per photon and contains both E_y and E_x components that are phase shifted relative to each other, hence $\hat{\mathbf{e}}$ rotates in time. There can be ambiguities in determining whether circular polarised light is left- or right-circular. A popular convention (and one used in this thesis) is to point the thumb of the right hand in the travelling direction of the wave and if the rotation of $\hat{\mathbf{e}}$ is in the same direction that the fingers naturally curl in, then this is right-circular (σ^+) polarisation. Alternatively, if you use the left hand and point the thumb in the wave direction and $\hat{\mathbf{e}}$ follows the natural curl of the fingers, then this is called left-circular (σ^-) polarisation.

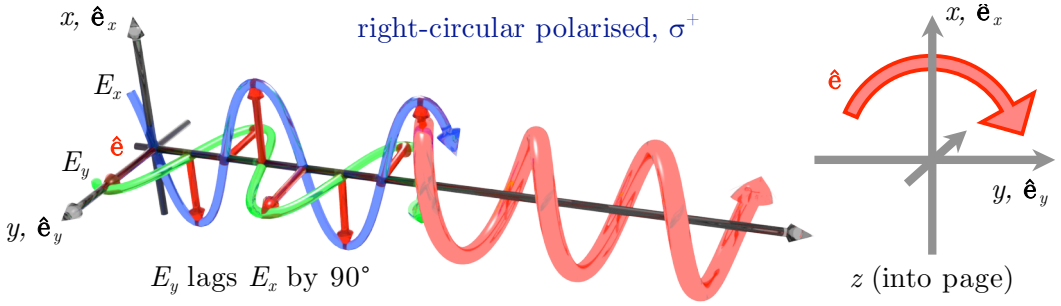

FIGURE H.2: Right circular (or σ^+ polarisation). This is caused by E_y lagging behind E_x by $\pi/2$ (90°) making $\hat{\mathbf{e}}$ corkscrew, for this case, $\hat{\mathbf{e}} = (\hat{\mathbf{e}}_x + i\hat{\mathbf{e}}_y)/\sqrt{2}$.

If E_y lags behind E_x by $\pi/2$ (90°), this causes $\hat{\mathbf{e}}$ to corkscrew towards the *right* as seen from the *source* (use the right hand) and this produces right-circular or σ^+ polarised light. Alternatively, if E_x lags behind E_y by $\pi/2$ (90°), this causes $\hat{\mathbf{e}}$ to corkscrew towards the *left* as seen from the *source* (use the left hand) and this produces left-circular or σ^- polarised light.

H.3 Waveplates

Waveplates are made from a birefringent crystal that has a fast and slow axis that are orthogonal to each other. The crystal is cut so that these axes are perpendicular to the incident light and have no component along z. The fast axis allows the component of E_0 parallel to it to travel through the crystal at a quicker speed than the component of

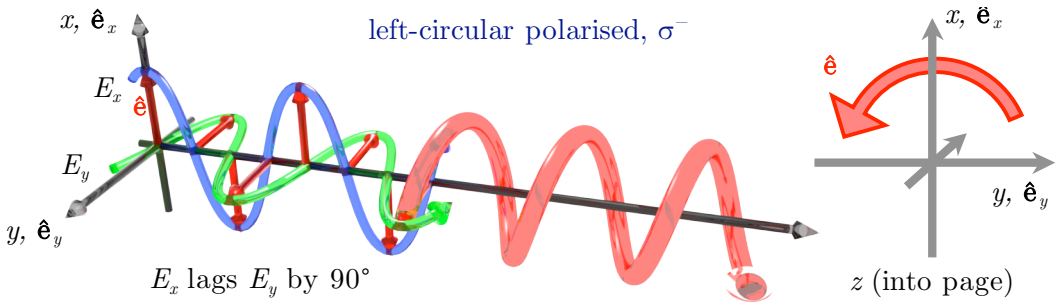

FIGURE H.3: Left circular (or σ^- polarisation). This is caused by E_x lagging behind E_y by $\pi/2$ (90°) making $\hat{\mathbf{e}}$ corkscrew, for this case, $\hat{\mathbf{e}} = (\hat{\mathbf{e}}_x - i\hat{\mathbf{e}}_y)/\sqrt{2}$.

E_0 parallel to the slow axis[1]. Hence the slow axis causes a retardation of the component of E_0 that travels along it, hence waveplates are also referred to as *retardation plates*.

Two types of waveplate exist, the $\lambda/2$- or half-waveplate and the $\lambda/4$- or quarter-waveplate. As the names suggest, the former causes a retardation of $\lambda/2$ for the component of E_0 along the slow axis and the latter causes a $\lambda/4$ retardation. This is equivalent to the $\lambda/2$ plate causing a phase shift of π between the component of E_0 travelling along the fast and slow axes and the $\lambda/4$ causing a $\pi/2$ phase shift. These two waveplates have a special effect upon the polarisation cases discussed in the previous section.

H.3.1 The Half WavePlate

Taking vertically polarised light ($E_0 = E_x$) and using a $\lambda/2$ waveplate whose fast and slow axes are at $+45°$ and $-45°$ from $\hat{\mathbf{x}}$ respectively, it can be seen that equal halves of E_x now travel along the fast and slow axes. The slow axis for a half-waveplate causes a $\lambda/2$ retardation along it and by drawing the results, it can be seen that the linear vertical polarisation has been turned into linear *horizontal* polarisation. This is a very useful property of the half-waveplate.

Circular polarised light similarly affected, the slow axis of the waveplate causes one of the E_0 components to become lagged by 180° and this is equivalent to reversing the lag in the E_x and E_y components and so left- becomes right- and right- becomes left- for circular polarised light passing through a half-waveplate.

[1]The refractive index, n now depends upon the orientation of the electric field of light through the crystal. The fast axis has a lower refractive index than the slow axis.

H.3.2 The Quarter WavePlate

The quarter waveplate has orthogonal fast and slow axes, however, the retardation along the slow axis is now 1/4 λ and is somewhat more involved to visualise. If vertically or horizontally polarised light ($E_0 = E_x$ or $E_0 = E_y$) encounters a quarter waveplate with the axes at $\pm 45°$ to the vertical, the light becomes circularly polarised.

The handedness of the polarisation depends upon the whether the slow axis is to the left or right of the incoming polarised light. If the slow axis is to the left, the light becomes left circular polarised (σ^-) and if the slow axis is to the right, it becomes right circular polarised (σ^+). Conversely, circular polarised light will revert back to linear polarisation upon passing through a circular waveplate.

H.4 Jones Matrices

When several polarising components and waveplates are in a beam line it is tedious and difficult to continually draw the effect of these optics on the electric field components and work out the resulting polarisation. A much quicker method is to use *Jones Matrices*. In Jones calculus, polarised light is represented by a Jones vector and each optical component by a Jones matrix corresponding to the effect that optic has on the polarisation. To find the output polarisation, the Jones matrix of the optic operates upon the input Jones vector. For a series of optical components, corresponding to a series of Jones matrices, the matrices operate on the input Jones vector in *reverse order* to the optics encountered by the beam in real-life.

Numerous resources exist that show the Jones matrix associated with a particular optical component or polarisation of light. There is also a *rotation matrix* that takes into account the orientation of any component[2]. For example, a linear polariser could be at 45° to the vertical and so a rotation matrix is needed to account for this.

The following table H.1 shows some common Jones matrices.

Generic definition	$\begin{pmatrix} E_x(t) \\ E_y(t) \end{pmatrix}$

[2]Many optical components have an axis or axes (eg. the polarisation axis of a linear polariser) but the Jones matrix describes the component when it is in a specific orientation (eg. axis horizontal). The rotation matrix is needed to account for any 'real-world' rotation of the component by an angle, θ.

Linear polarised light (in x)	$\begin{pmatrix} 1 \\ 0 \end{pmatrix}$
Linear polarised light (in y)	$\begin{pmatrix} 0 \\ 1 \end{pmatrix}$
Linear polarised light (45° from x)	$\frac{1}{\sqrt{2}} \begin{pmatrix} 1 \\ 1 \end{pmatrix}$
Right circular polarised light	$\frac{1}{\sqrt{2}} \begin{pmatrix} 1 \\ -i \end{pmatrix}$
Left circular polarised light	$\frac{1}{\sqrt{2}} \begin{pmatrix} 1 \\ i \end{pmatrix}$
Linear horizontal polariser	$\begin{pmatrix} 1 & 0 \\ 0 & 0 \end{pmatrix}$
Linear vertical polariser	$\begin{pmatrix} 0 & 0 \\ 0 & 1 \end{pmatrix}$
Linear polariser at angle θ	$\begin{pmatrix} \cos^2\theta & \cos\theta\sin\theta \\ \sin\theta\cos\theta & \sin^2\theta \end{pmatrix}$
Left circular polariser	$\frac{1}{2} \begin{pmatrix} 1 & -i \\ i & 1 \end{pmatrix}$
Right circular polariser	$\frac{1}{2} \begin{pmatrix} 1 & i \\ -i & 1 \end{pmatrix}$
Half-wave plate with (fast axis in the horizontal)	$\begin{pmatrix} i & 0 \\ 0 & i \end{pmatrix}$
Quarter-wave plate with (fast axis in the horizontal)	$e^{i\pi/4} \begin{pmatrix} 1 & 0 \\ 0 & i \end{pmatrix}$
Rotation Matrix, $R(\theta)$	$\begin{pmatrix} \cos\theta & \sin\theta \\ -\sin\theta & \cos\theta \end{pmatrix}$

TABLE H.1: Jones matrices for various polarisations of light and optical components

The Jones matrix for any optical element, M arbitrarily rotated through an angle, θ can be calculated using the Rotation matrix, $R(\theta)$ in the following manner:

$$M(\theta) = R(-\theta)MR(\theta) \tag{H.1}$$

H.5 Quarter waveplate Orientation for the MOT

In the MOT system, just outside every chamber window into which the optical molasses beams enter is a quarter waveplate, these set up the σ^+, σ^- polarisations for polarisation gradient cooling[3]. Though the manufacturers mark the fast axis of the plates – usually with a notch – it is advisable to perform a small experiment to determine the orientation of the axes. It is not possible to determine which is the slow or fast axis of a quarter waveplate (and hence whether the light is σ^+ or σ^- polarised) with conventional polarising optics without using a Babinet-Soleil or Berek compensator. In a MOT using three retro-reflected beams (as is the case in this thesis), only the first quarter waveplate for each incoming beam needs to be correctly aligned, the second can be at any orientation[4]. In the case where six individual lasers are used, all the quarter waveplates must be aligned.

Unfortunately, the handedness of the polarisation needs to be correct for the position dependent cooling to work. The external magnetic field causes the magnetic sub-states of the atom to split and shift according to the field strength and *direction*. The correct handedness required to drive atoms towards the trap centre is reproduced in figure H.4, sub-diagram (a). The level shift together with the correct polarisation causes preferential absorption such that the subsequent recoil is in the direction of the trap centre. If the polarisation handedness were reversed, the opposite would be true and the preferential absorption and recoil would act to drive the atoms away from the trap centre as shown in sub-diagram (b) of figure H.4.

In addition, the handedness also needs to be correct for σ^+, σ^- polarisation gradient cooling (see section 3.4.2). If the circular handedness were reversed, the sum polarisation vector $\hat{\mathbf{e}}$ of the two beams would spatially rotate in the opposite sense and the consequent optical pumping would cause preferential absorption from the incorrect beam and so the momentum recoil would act to drive the atom away from the trap centre instead of towards it.

Without the Babinet-Soleil or Berek compensators, the only way to tell whether the handedness of the beams is correct is by trial and error. If the cold atomic cloud cannot be created inside the MOT, it is likely that the axis alignment of at least one of the quarter waveplates is incorrect and needs to be reversed[5] and the possible combinations

[3] See section 3.4.

[4] This is because after passing through the first quarter waveplate, the light is circularly polarised and so the orientation of the second waveplate's axes do not matter due to circular symmetry. The light passes through this second quarter waveplate, is retro-reflected by a mirror and passes through the waveplate a second time thereby reversing the handedness of the circular polarisation of the incoming beam.

[5] This is simply done by rotating the quarter waveplate by 90°.

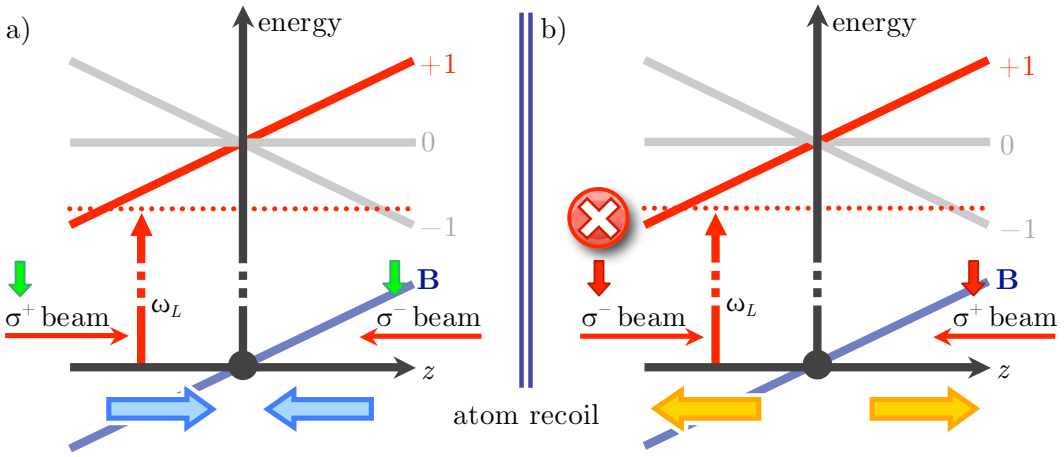

FIGURE H.4: The circular polarisation handedness matters for the position dependent cooling with the external magnetic field. The correct handedness is shown in (a). The incorrect handedness causes preferential absorption from the wrong beam and the momentum recoil acts to drive the atoms out from the trap centre as shown in (b).

for the three directions in a retro-reflecting beam MOT needs to be worked though (of which the most is, $2^3 = 8$ possible combinations[6]).

Figure H.5 shows the correct circular polarisations required for the MOT depending on the direction of the anti-Helmholtz field. Unfortunately, because of the $\sigma^+ - \sigma^-$ naming convention, the picture can become very confusing and counter intuitive.

The main point to note is that the circular polarisation in the horizontal plane must be the same due to cylindrical symmetry and in turn this must be opposite to the polarisation in the vertical (along the axis) as in this direction, the **B** field is in the opposite direction.

H.6 Setting Waveplate Orientation

The quarter waveplates for a retro-reflecting beam MOT can be aligned by following the simple experiment and steps outlined below and shown in figure H.6.

The first polarising beam splitter cube (PBS 1) ensures that only vertically polarised light is used. It is important to keep the correct orientation of the quarter waveplates once marked, both rotationally and to note which side of the waveplate 'faced' the oncoming laser beam. This is crucial as the plate can become easily flipped when being placed into the MOT optics and so the waveplate no longer follows the setup described in figure H.5.

[6]This would increase to, $2^6 = 64$ combinations if the six-beam MOT configuration was being used.

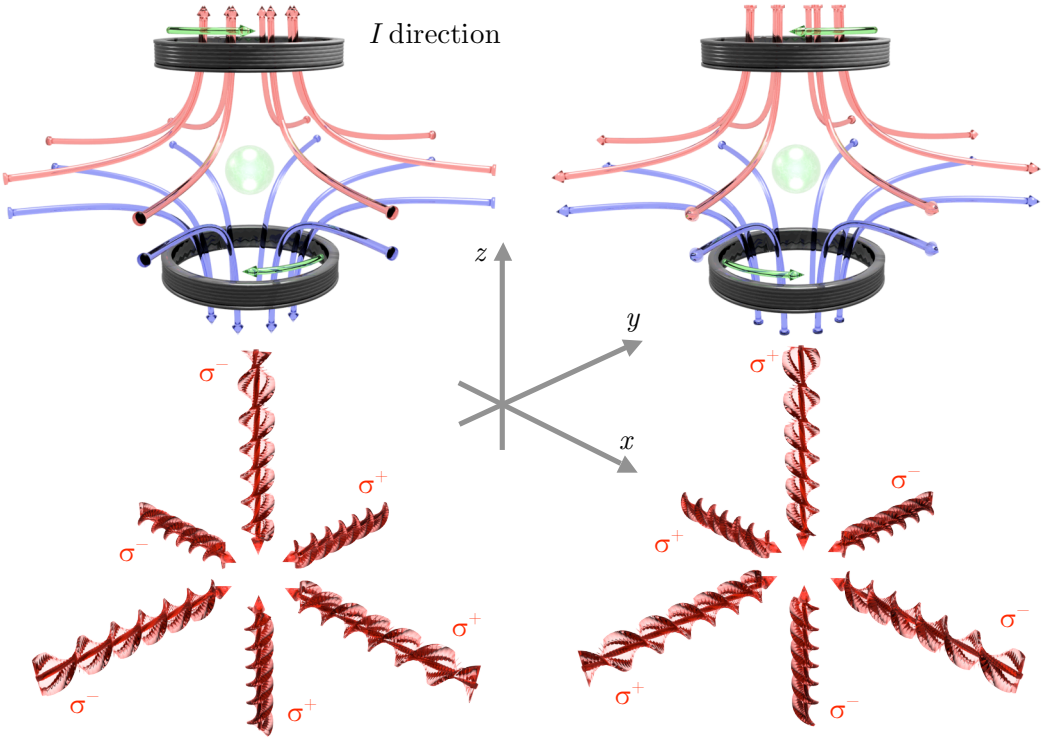

FIGURE H.5: The correct circular polarisations required for the MOT depending on the direction of the magnetic field. In both cases of the magnetic field, the circular polarisation of the horizontal planar propagating ($+x$, $+y$) beams must be equal, and these in turn must be of opposite handedness to the propagating ($+z$) beam.

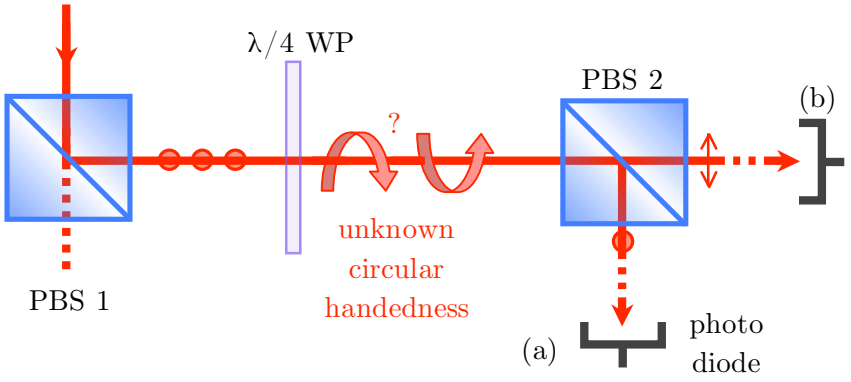

FIGURE H.6: A simple method for aligning quarter waveplates for a three-beam retro-reflecting MOT. It is not trivial to tell whether the light after the waveplate is left- or right-circular polarised.

For alignment, simply place the photo detector at position (a) and maximise the photo detector reading by slowly rotating the quarter waveplate. At the point where the value is maximised, one of the quarter waveplate axes is aligned to the incoming vertically polarised light but it is not possible to tell if it is the fast or slow axis without further experimentation. Now rotate the waveplate by 45° so the vertically polarised light is coming in at 45° to both the fast and slow axes and thus the waveplate is producing circular polarised light, though its handedness cannot be easily determined. As a check, place the photo detector at position (b) and the value should be maximised when the waveplate is producing circularly polarised light.

Lock and mark the rotation of the quarter waveplate, note its laser facing side and repeat for two more quarter waveplates. These three waveplates can now be placed as the first waveplate for each of the three incoming MOT beams for the x, y and z directions and the rest of the waveplates can be inserted with any axis orientation.

Finally, since the orientation of the fast and slow axes for the quarter waveplates was not determined, the handedness of the circular polarisations inside the MOT is unknown and some trial and error is required in attempting to create a MOT cloud and changing the rotation of the aligned waveplates (by 90° each time to reverse the orientation of the fast and slow axes) before the correct circular polarisation is achieved for each MOT beam and the cold atom cloud is successfully produced inside the MOT.

Appendix I

MOT Coil Parameters

The theory for an anti-Helmholtz coil pair calculated in Appendix E needs to be translated into physical parameters for the coils themselves (e.g. wire gauge, number of turns, coil dimensions etc.). Frequently quoted magnetic field gradients for MOT coils range between 1 and 10 Gcm^{-1} (or 0.01 to 0.1 Tm^{-1}).

I.1 Drive Current and Power Dissipation

From the equation for the on-axis field of a coil (equation D.7 in Appendix D), the anti-Helmholtz condition ($2b = \sqrt{3}a$) can be substituted to give

$$\frac{\partial B}{\partial z} = \frac{3\sqrt{3}}{2(7/4)^{5/2}} \frac{\mu_0 I}{a^2} \tag{I.1}$$

where the field gradient $\partial B/\partial z$ is 0.01 to 0.1. Rearranging for I gives

$$I = [0.01 - 0.1] \times \frac{2(7/4)^{5/2}}{3\sqrt{3}} \frac{\mu_0}{a^2} \simeq 125 \text{ A} - 1250 \text{ A} \tag{I.2}$$

If the coil radius, a is taken to be about 10 cm then equation I.2 calculates the current needed to flow round a coil to maintain a 0.01–0.1 Tm^{-1} field gradient. If this current flows round a coil of total cross sectional area A (with a circumference, $2\pi a$) and the coil is made from a material with resistivity ρ, then its resistance is

$$R = \frac{\rho l}{A} \tag{I.3}$$

$$= \frac{2\pi a \rho}{A} \tag{I.4}$$

The power dissipated in the coil is given by

$$P = VI = I^2R \tag{I.5}$$
$$= I^2\frac{2\pi a\rho}{A} \tag{I.6}$$

Copper is used for the field coils and it has a resistivity[1] of $\rho = 16.8 \times 10^{-9}$ Ωm. Using the current values in equation I.2 and taking the coil cross-section A to be ~ 1 cm^2 one finds

$$P = [125 - 1250]^2\frac{0.1 \times 2\pi.16.8 \times 10^{-9}}{1 \times 10^{-4}} \tag{I.7}$$
$$\simeq 1 \text{ W} - 150 \text{ W} \tag{I.8}$$

These results are just as valid for a coil with N turns whose total cross-sectional area is A as it is for a solid ring of copper whose cross-section is also A. For a coil of N turns, each loop has a cross-section of A/N and carries a current I/N. The voltage needed to drive the coil is calculated by

$$V = IR \tag{I.9}$$
$$= \frac{2\pi a\rho N}{A}I \tag{I.10}$$

The coil radius, a is fixed by the geometry of the vacuum chamber. The current required is up to 1250 A for a field gradient of 10 Gcm^{-1}. There is some flexibility in the cross-sectional area, A but this is limited to ~ 1 cm^2 again, from the geometry of the vacuum chamber. As is it not feasible to create a single, thick coil to carry a current of 1250 A, these parameters can be used to calculate the number of turns the coils should contain and the current and voltage required to drive them to produce the field gradient required.

I.2 Selecting a Suitable Wire Gauge

Copper wire is available in several wire gauges of which there are two standards, the 'American Wire Gauge', (AWG) and the Imperial (British standard), 'Standard Wire Gauge' (SWG). The two standards do not have the same wire diameters. Since wire is sold in this way, the best method is to work from the wire gauge and calculate the number of turns required. Table I.1 shows the wire gauges and corresponding MOT coil parameters.

[1]The resistivity of copper is actually a function of temperature, increasing in value as the temperature increases.

SWG Number	Diameter (mm)	Turns (N)	Resistance (Ω)	Current (A)	Voltage (V)
16	1.626	49	0.25	22.4	5.58
18	1.219	86	0.78	12.7	9.86
20	0.914	153	2.50	7.13	17.6
22	0.711	252	6.70	4.32	29.0
24	0.559	408	17.6	2.67	46.8
26	0.457	610	39.3	1.78	70.1
28	0.376	910	85.7	1.21	104
30	0.315	1,284	174	0.85	147
32	0.274	1,696	304	0.64	195
34	0.234	2,326	571	0.47	267
36	0.193	3,419	1,230	0.32	393
38	0.152	5,511	3,210	0.20	633
40	0.122	8,555	7,720	0.13	983
42	0.102	12,238	15,800	0.09	1,400

TABLE I.1: A table of available SWG wire diameters and the parameters (such as number of turns and the current and voltage) needed to drive the MOT coils to produce the required field gradient of ~ 10 Gcm^{-1}.

From table I.1, as the wire diameter decreases (SWG increases) the number of turns, and coil resistance increases, but the current required to produce the field decreases. When considering which SWG to use, it is important to take into consideration the power supply that will be used to drive the coils (e.g. power supplies that deliver 22 A are not widely available). Using a large number of turns (thousands) makes the manufacture of the coils difficult and also increases heating both from resistive heating and coil/wire insulation.

Appendix J

An In-House Built Diode Laser

Commercial, tunable diode lasers based on the Littrow configuration are available, however for the trapping laser it was decided to 'home-build' our own using the design described in the paper by Malcolm Boshier *et al* [92] from the University of Sussex. This is based on a standard, one inch, commercial optical mount that is modified to hold the diode package, collimating lens and diffraction grating with a piezo for micro-metre precision tuning.

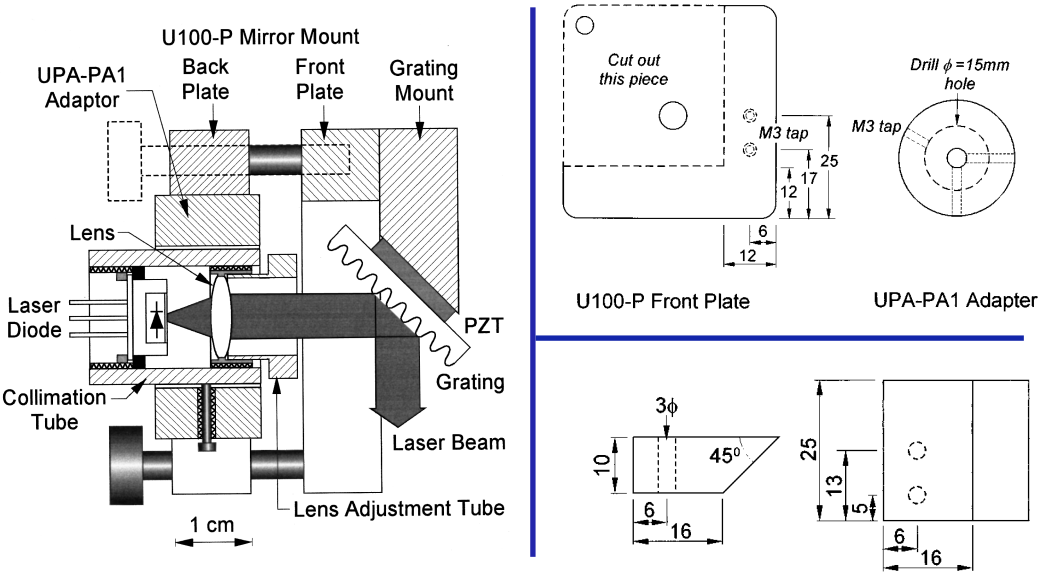

FIGURE J.1: Technical drawings of the ECDL design from Sussex University, reproduced from the paper by Boshier *et al* [92].

A prototype following this design was built and characterised and performed well. The output was tunable and single mode with a linewidth of less than 10 MHz (as measured by the OSA – instrument limited). However, the 'modified optic mount' route was not

the most elegant solution, as the heat sink was held on with string and the temperature sensor with Blu-Tak. We proceeded to design an integrated mount that has the same form as the Boshier design though there are fewer pieces to assemble, which improves mechanical stability. Wire connections are made with industry standard Lemo connectors to reduce electrical noise and a better designed heat sink and larger contact area for the Peltier cooler improves the thermal stability and the temperature range over which the diode can be operated.

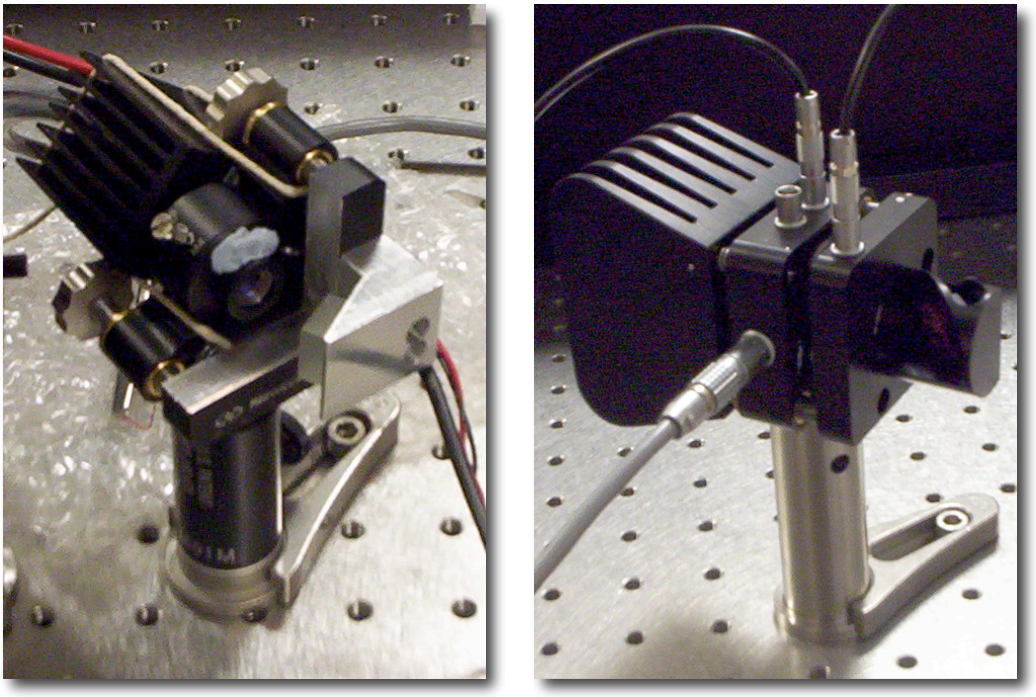

Enid: (Boshier design) Beryl: (refined design)

FIGURE J.2: *Enid*: an external cavity diode laser based on the Boshier design of the modified commercial optical mount. *Beryl*: our refined design, based on Enid but further modified to be more compact and integrated with better wire connectors to improve thermal and mechanical stability and reduce electrical noise.

Several working diode lasers were produced with this new design though the process of assembling these diode lasers is more involved and is done in several stages. First the Lemo connectors are attached; one for the temperature sensor and Peltier cooler, one for the laser diode power and one for the piezo electric stack. The diode can then be mounted, wired and fixed in the main block.

J.1 Diode Assembly and Collimation

The first task is to collimate the beam by adjusting the position of the aspheric lens in front of the diode by screwing the lens in and out using a spanner wrench (from

Thorlabs). The beam was sent back and forth along the full length of the optical table (four metres) four times and the lens carefully adjusted so that the beam remained as collimated as possible without passing through a focus.

The output is now collimated but the shape of the beam will still be elliptical. The next task is to rotate the diode itself so that the long axis of the ellipse is horizontal. This means that the output beam is linearly, vertically polarised.

The temperature sensor – an AD590 chip – is attached to the front of the main block and the heat sink can be attached to the back making sure the Peltier cooler sits within the shallow inset machined into the back of heat sink to hold it in place.

Finally the diffraction grating can be mounted onto the front. Some care is needed to make sure the piezo is in direct contact with the actuator on the main block. The separate parts of the diode laser can be seen in the photo in figure J.3.

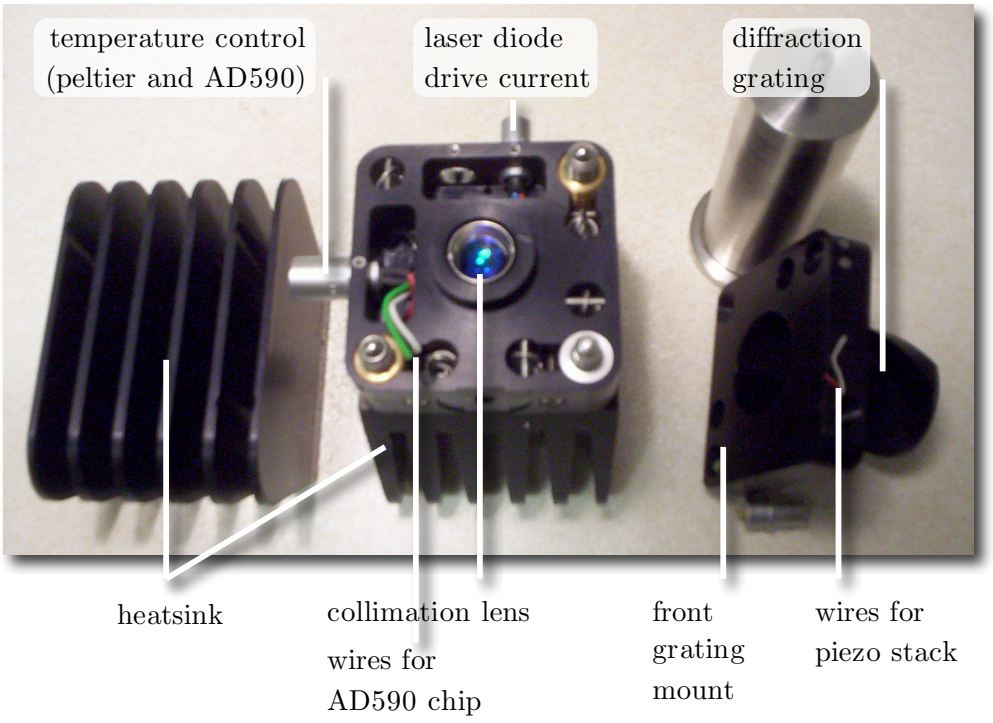

FIGURE J.3: The component parts of the new diode laser.

J.2 Grating Alignment

When the diode laser is fully assembled and collimated, the external cavity needs to be aligned so that the first order diffracted beam is being fed back into the laser diode.

This is done by passing the diode output through a lens and looking at the image at the focus with a CCD camera. If the grating is close to alignment, two dots should be apparent, one is the main laser output and the second is the reflected first order beam. If this is not initially the case, the grating is far from alignment and a scanning with the actuators is required.

The grating is aligned when the two dots are superimposed. A sudden increase in brightness is noticeable when the two dots overlap as the first order feedback begins to work and enhance the stimulated emission.

Further fine-tuning of the grating is required and is done by reducing the diode drive current to just above threshold and then aligning the dots, again looking for the sudden increase in brightness that occurs when the first order and main output beams overlap. Continue, reducing the drive current and fine tuning until no further improvement is seen. An optical power meter can also be used and the grating should be aligned to give the maximum power reading on the meter.

Vertical alignment of the grating is critical, horizontal alignment is less so. Once the feedback is aligned, the next task is to use a wavelength meter to tune horizontally the diffraction grating until the desired wavelength is reached. The diodes were required to output in the region of 780.24 nm and this can be achieved by not only tuning the grating, but also the temperature and the drive current. Fine tuning with the piezo is used to obtain the third decimal place on the wavelength meter.

Careful tuning with the grating, drive current and temperature is important to make sure the feedback is making the laser output on an allowed cavity mode. If the cavity and external feedback modes do not overlap, the laser is likely to have a multi-mode output and be unstable. Single mode output at the wavelength desired is possible by scanning these variables.

Bibliography

[1] Peter J. Mohr and Barry N. Taylor. CODATA recommended values of the fundamental physical constants: 2002. *Reviews of Modern Physics*, 77(1):1, March 2005. doi: 10.1103/RevModPhys.77.1. URL http://link.aps.org/abstract/RMP/v77/p1.

[2] Zachary Dutton, Naomi Ginsberg, Christopher Slowe, and Lene Vestergaard Hau. The art of taming light: Ultra-slow and stopped light. *Europhysics News*, March/April(2):33–38, 2004. URL http://www.europhysicsnews.com/full/26/article1/article1.html.

[3] Lene Vestergaard Hau, S. E. Harris, Zachary Dutton, and Cyrus H. Behroozi. Light speed reduction to 17 metres per second in an ultracold atomic gas. *Nature*, 397 (6720):594–598, February 1999. doi: 10.1038/17561. URL http://www.nature.com/nature/journal/v397/n6720/full/397594a0.html.

[4] K.-J. Boller, A. Imamoğlu, and S. E. Harris. Observation of electromagnetically induced transparency. *Physical Review Letters*, 66(20):2593–2596, May 1991. doi: 10.1103/PhysRevLett.66.2593. URL http://link.aps.org/abstract/PRL/v66/p2593.

[5] Michael Fleischhauer. Electromagnetically induced transparency and coherent-state preparation in optically thick media. *Optics Express*, 4(2):107–112, January 1999. URL http://www.opticsinfobase.org/abstract.cfm?URI=oe-4-2-107.

[6] A. M. Akulshin, S. Barreiro, and A. Lezama. Electromagnetically induced absorption and transparency due to resonant two-field excitation of quasi-degenerate levels in Rb vapor. *Physical Review A*, 57(4):2996–3002, April 1998. doi: 10.1103/PhysRevA.57.2996. URL http://link.aps.org/abstract/PRA/v57/p2996.

[7] Erik Gustafsson. *Design Study of a Magneto-Optical Trap for Laser Cooling of Rubidium Atoms.* PhD thesis, Lund Reports on Atomic Physics, LRAP-325, June 2004. URL http://www.atto.fysik.lth.se/publications/master/gustafsson_LRAP325_2004.pdf.

[8] Angela S. Mellish and Andrew C. Wilson. A simple laser cooling and trapping apparatus for undergraduate laboratories. *American Journal of Physics*, 70(9): 965–971, September 2002. doi: 10.1119/1.1477435. URL `http://link.aip.org/link/?AJP/70/965/1`.

[9] E. Arimondo, M. Inguscio, and P. Violino. Experimental determinations of the hyperfine structure in the alkali atoms. *Reviews of Modern Physics*, 49(1):31–75, January 1977. doi: 10.1103/RevModPhys.49.31. URL `http://link.aps.org/abstract/RMP/v49/p31`.

[10] Achim Peters, Keng Yeow Chung, and Steven Chu. Measurement of gravitational acceleration by dropping atoms. *Nature*, 400:849–852, August 1999. doi: doi:10.1038/23655. URL `http://www.nature.com/nature/journal/v400/n6747/abs/400849a0_fs.html`.

[11] D. S. Weiss, B. C. Young, and S. Chu. Precision measurement of $\hbar/m_{\mathrm{cs}}$ based on photon recoil using laser-cooled atoms and atomic interferometry. *Applied Physics B: Lasers and Optics*, 59(3):217–256, September 1994. doi: 10.1007/BF01081393. URL `http://www.springerlink.com/content/w2703mp20t144426/`.

[12] Cheng Chin, Véronique Leiber, Vladan Vuletić, Andrew J. Kerman, and Steven Chu. Measurement of an electron's electric dipole moment using Cs atoms trapped in optical lattices. *Physical Review A*, 63(3):033401, February 2001. doi: 10.1103/PhysRevA.63.033401. URL `http://link.aps.org/abstract/PRA/v63/e033401`.

[13] A. Steane. Quantum computing. *Reports on Progress in Physics*, 61(2):117–173, February 1998. doi: 10.1088/0034-4885/61/2/002. URL `http://stacks.iop.org/0034-4885/61/117`.

[14] J. J. García-Ripoll, P. Zoller, and J. I. Cirac. Quantum information processing with cold atoms and trapped ions. *Journal of Physics B: Atomic, Molecular and Optical Physics*, 38(9):S567–S578, April 2005. doi: 10.1088/0953-4075/38/9/008. URL `http://stacks.iop.org/0953-4075/38/S567`.

[15] Martin Weitz. Towards controlling larger quantum systems: From laser cooling to quantum computing. *IEEE Journal of Quantum Electronics*, 36(12):1346–1357, December 2000. doi: 10.1109/3.892553. URL `http://ieeexplore.ieee.org/search/wrapper.jsp?arnumber=892553`.

[16] D. B. Sullivan, J. J. Bollinger, W. D. Lee, D. Meekhof, T. E. Parker, J. C. Bergquist, F. L. Walls, J. C. Bergquist, and D. J. Wineland. Primary atomic frequency standards at NIST. *Journal of Research of The National Institute of*

Standards and Technology, 106(1):47–63, January 2001. URL `http://nvl.nist.gov/pub/nistpubs/jres/106/1/j61sul.pdf`.

[17] S. Bize, Y. Sortais, M. S. Santos, C. Mandache, A. Clairon, and C. Salomon. High-accuracy measurement of the ^{87}Rb ground-state hyperfine splitting in an atomic fountain. *Europhysics Letters*, 45(5):558–564, March 1999. doi: 10.1209/epl/i1999-00203-9. URL `http://publish.edpsciences.com/abstract/epl/v45/p558`.

[18] C. S. Edwards, G. P. Barwood, H. S. Margolis, P. Gill, and W. R. C. Rowley. Development and absolute frequency measurment of a pair of 778 nm two-photon rubidium standards. *Metrologia*, 42(5):464–467, October 2005. doi: 10.1088/0026-1394/42/5/018. URL `http://stacks.iop.org/0026-1394/42/464`.

[19] L. Hollberg, C. W. Oates, G. Wilpers, C. W. Hoyt, Z. W. Barber, S. A. Diddams, W. H. Oskay, and J. C. Bergquist. Optical frequency/wavelength references. *Journal of Physics B: Atomic, Molecular and Optical Physics*, 38(9):S469–S495, April 2005. doi: 10.1088/0953-4075/38/9/003. URL `http://stacks.iop.org/0953-4075/38/S469`.

[20] C. Gabbanini, A. Fioretti, A. Lucchesini, S. Gozzini, and M. Mazzoni. Cold rubidium molecules formed in a magneto-optical trap. *Physical Review Letters*, 84(13):2814–2817, March 2000. doi: 10.1103/PhysRevLett.84.2814. URL `http://link.aps.org/abstract/PRL/v84/p2814`.

[21] S. Inouye, M. R. Andrews, J. Stenger, H.-J. Miesner, D. M. Stamper-Kurn, and W. Ketterle. Observation of feshbach resonances in a Bose-Einstein condensate. *Nature*, 392(6672):151–154, March 1998. doi: doi:10.1038/32354. URL `http://www.nature.com/nature/journal/v392/n6672/abs/392151a0_fs.html`.

[22] Cindy A. Regal, Christopher Ticknor, John L. Bohn, and Deborah S. Jin. Creation of ultracold molecules from a fermi gas of atoms. *Nature*, 424(6944):47–50, July 2003. doi: 10.1038/nature01738. URL `http://www.nature.com/nature/journal/v424/n6944/abs/nature01738.html`.

[23] Ph. Courteille, R. S. Freeland, D. J. Heinzen, F. A. van Abeelen, and B. J. Verhaar. Observation of a feshbach resonance in cold atom scattering. *Physical Review Letters*, 81(1):69–72, July 1998. doi: 10.1103/PhysRevLett.81.69. URL `http://link.aps.org/abstract/PRL/v81/p69`.

[24] Matt Mackie, Andrew Carmichael, Marijan Koštrun, Rory J. Perkins, Chen Xu, Yi Zhen, Kalle-Antti Suominen, and Juha Javanainen. Rapid adiabatic passage

from an atomic to a molecular condensate. arXiv:physics/0210131 v2, May 2003. URL `http://arxiv.org/abs/physics/0210131`.

[25] Peter Horak, Bruce G. Klappauf, Albrecht Hasse, Ron Folman, Jörg Schmiedmayer, Peter Domokos, and E. A. Hinds. Possibility of single-atom detection on a chip. *Physical Review A*, 67(4):043806, 2003. doi: 10.1103/PhysRevA.67.043806. URL `http://link.aps.org/abstract/PRA/v67/e043806`.

[26] Shengwang Du. *Atom-Chip Bose-Einstein Condensation in a Portable Vacuum Cell*. PhD thesis, University of Colorado at Boulder, Colorado, United States, May 2005. URL `http://jilawww.colorado.edu/pubs/thesis/du/`.

[27] Peter D. D. Schwindt. *Magnetic Traps and Guides for Bose-Einstein Condensates on an Atom Chip: Progress toward a Coherent Atom Waveguide Beamsplitter*. PhD thesis, The Evergreen State College, Colorado, United States, 2003. URL `http://jilawww.colorado.edu/pubs/thesis/schwindt/schwindt_thesis.pdf`.

[28] Raymond T. Newell. A portable magneto-optical trap. Master's thesis, University of Wisconsin-Madison, Wisconsin, United States, 1998. URL `http://www-atoms.physics.wisc.edu/portatrap/Raysthesis.pdf`.

[29] Martin Weitz, Brenton C. Young, and Steven Chu. Atomic interferometer based on adiabatic population transfer. *Physical Review Letters*, 73(19):2563–2566, November 1994. doi: 10.1103/PhysRevLett.73.2563. URL `http://link.aps.org/abstract/PRL/v73/p2563`.

[30] Mark Kasevich and Steven Chu. Atomic interferometry using stimulated Raman transitions. *Physical Review Letters*, 67(2):181–184, July 1991. doi: 10.1103/PhysRevLett.67.181. URL `http://link.aps.org/abstract/PRL/v67/p181`.

[31] Silvije Vdović, Ticijana Ban, Damir Aumiler, and Goran Pichler. EIT at $5^2S_{1/2} \rightarrow 6^2P_{3/2}$ transition in a mismatched V-type Rubidium system. *Optics Communications*, 272(2):407–413, April 2007. doi: doi:10.1016/j.optcom.2006.12.001. URL `http://dx.doi.org/10.1016/j.optcom.2006.12.001`.

[32] E. F. Nichols and G. F. Hull. The pressure due to radiation (second paper). *Physical Review (Series I)*, 17(1):26–50, July 1903. doi: 10.1103/PhysRevSeriesI.17.26. URL `http://link.aps.org/abstract/PRI/v17/p26`.

[33] Hugh D. Young, Roger A. Freedman, T. R. Sandin, and A. Lewis Ford. *Sears and Zemansky's University Physics*. Addison Wesley, January 2000. ISBN 0201603365.

[34] Claude Cohen-Tannoudji. *Atom Photon Interactions: Basic Processes and Applications*. Wiley Science Paperback Series. John Wiley International, April 1998. ISBN 0471293369.

[35] Harold J. Metcalf and Peter van der Straten. *Laser Cooling and Trapping*. Springer, November 1999. ISBN 0387987479.

[36] Adam Micolich. Thermal physics, 3: Temperature. University Lecture Course PHYS2060, University of New South Wales, Sydney, Australia, 2006. URL `http://www.phys.unsw.edu.au/PHYS2060/pdf/PHYS2060%20Thermal%20Physics%20Lecture%203.pdf`.

[37] Adam Micolich. Thermal physics, 5: Equipartition of energy. University Lecture Course PHYS2060, University of New South Wales, Sydney, Australia, 2006. URL `http://www.phys.unsw.edu.au/PHYS2060/pdf/PHYS2060%20Thermal%20Physics%20Lecture%205.pdf`.

[38] Steven Chu. Laser manipulation of atoms and particles. *Science*, 253(5022): 861–866, August 1991. doi: 10.1126/science.253.5022.861. URL `http://www.sciencemag.org/cgi/content/abstract/253/5022/861`.

[39] R. N. Watts and C. E. Wieman. Manipulating atomic velocities using diode lasers. *Optics Letters*, 11(5):291–293, May 1986. URL `http://www.opticsinfobase.org/abstract.cfm?URI=ol-11-5-291`.

[40] William D. Phillips and Harold J. Metcalf. Laser deceleration of an atomic beam. *Physical Review Letters*, 48(9):596–599, Mar 1982. doi: 10.1103/PhysRevLett.48.596. URL `http://link.aps.org/abstract/PRL/v48/p596`.

[41] William D. Phillips, John V. Prodan, and Harold J. Metcalf. Laser cooling and electromagnetic trapping of neutral atoms. *Journal of the Optical Society of America B*, 2(11):1751–1767, November 1985. URL `http://www.opticsinfobase.org/abstract.cfm?URI=josab-2-11-1751`.

[42] John Prodan, Alan Migdall, William D. Phillips, Ivan So, Harold Metcalf, and Jean Dalibard. Stopping atoms with laser light. *Physical Review Letters*, 54(10): 992–995, March 1985. doi: 10.1103/PhysRevLett.54.992. URL `http://link.aps.org/abstract/PRL/v54/p992`.

[43] P. D. Lett, W. D. Phillips, S. L. Rolston, C. E. Tanner, R. N. Watts, and C. I. Westbrook. Optical molasses. *Journal of the Optical Society of America B*, 6(11): 2084–2107, November 1989. URL `http://www.opticsinfobase.org/abstract.cfm?URI=josab-6-11-2084`.

[44] David S. Weiss, Erling Riis, Yaakov Shevy, P. Jeffrey Ungar, and Steven Chu. Optical molasses on multilevel atoms: Experiment. *Journal of the Optical Society of America B*, 6(11):2072–2083, November 1989. URL `http://www.opticsinfobase.org/abstract.cfm?URI=josab-6-11-2072`.

[45] P. Jeffrey Ungar, David S. Weiss, Erling Riis, and Steven Chu. Optical molasses on multilevel atoms: Theory. *Journal of the Optical Society of America B*, 6(11): 2058–2071, November 1989. URL `http://www.opticsinfobase.org/abstract.cfm?URI=josab-6-11-2058`.

[46] W. D. Phillips, P. D. Lett, S. L. Rolston, C. E. Tanner, R. N. Watts, C. I. Westbrook, C. Salomon, J. Dalibard, A. Clairon, and S. Guellati. Optical molasses: The coldest atoms ever. *Physica Scripta*, 1991(T34):20–22, August 1991. doi: 10.1088/0031-8949/1991/T34/003. URL `http://stacks.iop.org/1402-4896/T34/20`.

[47] Steven Chu, L. Hollberg, J. E. Bjorkholm, Alex Cable, and A. Ashkin. Three-dimensional viscous confinement and cooling of atoms by resonance radiation pressure. *Physical Review Letters*, 55(1):48–51, July 1985. doi: 10.1103/PhysRevLett.55.48. URL `http://link.aps.org/abstract/PRL/v55/p48`.

[48] Marcus Kylén. A magneto-optic trap for ^{87}Rb. Master's thesis, Stockholms Universitet, Sweden, 2002.

[49] C. S. Adams and E. Riis. Laser cooling and trapping of neutral atoms. *Progress in Quantum Electronics*, 21(1):79, 1997. doi: 10.1016/S0079-6727(96)00006-7. URL `http://dx.doi.org/10.1016/S0079-6727(96)00006-7`.

[50] E. L. Raab, M. Prentiss, Alex Cable, Steven Chu, and D. E. Pritchard. Trapping of neutral sodium atoms with radiation pressure. *Physical Review Letters*, 59 (23):2631–2634, December 1987. doi: 10.1103/PhysRevLett.59.2631. URL `http://link.aps.org/abstract/PRL/v59/p2631`.

[51] Christopher J. Foot. *Atomic Physics*. Oxford Master Series in Physics. Oxford University Press, November 2004. ISBN 0198506961.

[52] L. D Landau and E. M. Lifshitz. *Quantum Mechanics*, volume 3 of *Course of Theoretical Physics*. Butterworth-Heinemann Ltd, 3 edition, December 1981. ISBN 0080291406.

[53] Norman F. Ramsey. A molecular beam resonance method with separated oscillating fields. *Physical Review*, 78(6):695–699, June 1950. doi: 10.1103/PhysRev.78.695. URL `http://link.aps.org/abstract/PR/v78/p695`.

[54] Norman F. Ramsey. Resonance experiments in successive oscillatory fields. *Review of Scientific Instruments*, 28(1):57–58, January 1957. doi: 10.1063/1.1715708. URL http://link.aip.org/link/?RSI/28/57/1.

[55] Adriano A. Batista and D. S. Citrin. Rabi flopping in a two-level system with a time-dependent energy renormalization: Intersubband transitions in quantum wells. *Physical Review Letters*, 92(12):127404, March 2004. doi: 10.1103/PhysRevLett.92.127404. URL http://link.aps.org/abstract/PRL/v92/e127404.

[56] T. G. M. Freegarde, J. Walz, and T. W. Hänsch. Confinement and manipulation of atoms using short laser pulses. *Optics Communications*, 117(3–4):262–267, June 1995. doi: 10.1016/0030-4018(95)00172-5. URL http://dx.doi.org/10.1016/0030-4018(95)00172-5.

[57] A. Goepfert, I. Bloch, D. Haubrich, F. Lison, R. Schütze, R. Wynands, and D. Meschede. Stimulated focusing and deflection of an atomic beam using picosecond laser pulses. *Physical Review A*, 56(5):R3354–R3357, November 1997. doi: 10.1103/PhysRevA.56.R3354. URL http://link.aps.org/abstract/PRA/v56/pR3354.

[58] B. Nölle, H. Nölle, J. Schmand, and H. J. Andrä. Atomic-beam deflection by double-π-pulse laser technique. *Europhysics Letters*, 33(4):261–266, February 1996. doi: 10.1209/epl/i1996-00330-9. URL http://publish.edpsciences.com/abstract/epl/v33/p261.

[59] B. W. Shore, K. Bergmann, A. Kuhn, S. Schiemann, J. Oreg, and J. H. Eberly. Laser-induced population transfer in multistate systems: A comparative study. *Physical Review A*, 45(7):5297–5300, April 1992. doi: 10.1103/PhysRevA.45.5297. URL http://link.aps.org/abstract/PRA/v45/p5297.

[60] V. S. Malinovsky and J. L. Krause. General theory of population transfer by adiabatic rapid passage with intense, chirped laser pulses. *European Physical Journal D*, 14:147–155, 2001. URL http://publish.edpsciences.com/abstract/epjd/v14/p147.

[61] J. F. Xia, J. H. Sanderson, W.-K. Liu, and D. Strickland. Experimental observation of Raman chirped adiabatic rapid passage. *Journal of Physics B: Atomic, Molecular and Optical Physics*, 36(21):L409–L414, November 2003. doi: 10.1088/0953-4075/36/21/L06. URL http://stacks.iop.org/0953-4075/36/L409.

[62] F. Bloch. Nuclear induction. *Physical Review*, 70(7–8):460–474, October 1946. doi: 10.1103/PhysRev.70.460. URL http://link.aps.org/abstract/PR/v70/p460.

[63] John C. Edwards. Principles of NMR. Technical report, Process NMR Associates, 2005. URL http://www.process-nmr.com/pdfs/NMR%20Overview.pdf.

[64] Lieven M. K. Vandersyper and Isaac L. Chuang. NMR techniques for quantum control and computation. arXiv:quant-ph/0404064 v2, June 2004. URL http://arxiv.org/abs/quant-ph/0404064.

[65] J. A. Jones, R. H. Hansen, and M. Mosca. Quantum logic gates and nuclear magnetic resonance pulse sequences. *Journal Of Magnetic Resonance*, 135(2):353–360, December 1998. doi: 10.1006/jmre.1998.1606. URL http://dx.doi.org/10.1006/jmre.1998.1606.

[66] Warren S. Warren. Effects of arbitrary laser or NMR pulse shapes on population inversion and coherence. *Journal of Chemical Physics*, 81(12):5437–5448, December 1984. doi: 10.1063/1.447644. URL http://link.aip.org/link/?JCP/81/5437/1.

[67] Debabrata Goswami and Warren S. Warren. Effects of pulses with simple phase and frequency modulations. *Physical Review A*, 50(6):5190–5196, December 1994. doi: 10.1103/PhysRevA.50.5190. URL http://link.aps.org/abstract/PRA/v50/p5190.

[68] G. P. Djotyan, J. S. Bakos, G. Demeter, and Zs. Sörlei. Population transfer in three-level λ atoms with Doppler-broadened transition lines by a single frequency-chirped short laser pulse. *Journal of the Optical Society of America B*, 17(1):107–113, January 2000. URL http://www.opticsinfobase.org/abstract.cfm?URI=josab-17-1-107.

[69] Debabrata Goswami. Optical pulse shaping approaches to quantum control. *Physics Reports*, 374(6):385–481, September 2002. doi: 10.1016/S0370-1573(02)00480-5. URL http://dx.doi.org/10.1016/S0370-1573(02)00480-5.

[70] Bruce W. Shore. Definition of virtual levels. *American Journal of Physics*, 47(3):262–263, March 1978. doi: 10.1119/1.11854. URL http://link.aip.org/link/?AJP/47/262/1.

[71] M. Weitz and T. W. Hänsch. Frequency-independent laser cooling based on interferometry. *Europhysics Letters*, 49(3):302–308, February 2000. doi: 10.1209/epl/i2000-00149-4. URL http://publish.edpsciences.com/abstract/epl/v49/p302.

[72] T. Heupel, M. Mei, M. Niering, B. Gross, M. Weitz, T. W. Hänsch, and Ch. J. Bordé. Hydrogen atom interferometer with short light pulses. *Europhysics Letters*,

57(2):158–163, January 2002. doi: 10.1209/epl/i2002-00556-5. URL http://publish.edpsciences.com/abstract/epl/v57/p158.

[73] Martin Weitz, Brenton C. Young, and Steven Chu. Atomic manipulation based on delayed laser pulses in three- and four-level systems: Light shifts and transfer efficiencies. *Physical Review A*, 50(3):2438–2444, September 1994. doi: 10.1103/PhysRevA.50.2438. URL http://link.aps.org/abstract/PRA/v50/p2438.

[74] Mark Kasevich, David S. Weiss, Erling Riis, Kathryn Moler, Steven Kasapi, and Steven Chu. Atomic velocity selection using stimulated Raman transitions. *Physical Review Letters*, 66(18):2297–2300, May 1991. doi: 10.1103/PhysRevLett.66.2297. URL http://link.aps.org/abstract/PRL/v66/p2297.

[75] Tim Freegarde, Geoff Daniel, and Danny Segal. Coherent amplification in laser cooling and trapping. *Physical Review A*, 73(3):033409, March 2006. doi: 10.1103/PhysRevA.73.033409. URL http://link.aps.org/abstract/PRA/v73/e033409.

[76] J. S. Bakos, G. P. Djotyan, G. Demeter, and Zs. Sörlei. Transient laser cooling of two-level quantum systems with narrow natural linewidths. *Physical Review A*, 53(4):2885–2888, April 1996. doi: 10.1103/PhysRevA.53.2885. URL http://link.aps.org/abstract/PRA/v53/p2885.

[77] G. P. Djotyan, J. S. Bakos, G. Demeter, and Zs. Sörlei. Manipulation of two-level quantum systems with narrow transition lines by short, linearly polarized frequency-chirped laser pulses. *Journal of the Optical Society of America B*, 13 (8):1697–1705, August 1996. URL http://www.opticsinfobase.org/abstract.cfm?URI=josab-13-8-1697.

[78] G. K. Woodgate. *Elementary Atomic Structure*. Oxford Science Publications. Oxford University Press, 2 edition, August 1983. ISBN 0198511566.

[79] U. D. Rapol, A. Krishna, and V. Natarajan. Precise measurement of hyperfine structure in the $5P_{3/2}$ state of ^{85}Rb. *European Physical Journal D*, 23: 185–188, April 2003. doi: 10.1140/epjd/e2003-00069-9. URL http://publish.edpsciences.com/abstract/epjd/v23/p185.

[80] Daniel A. Steck. Rubidium 87 D-line data. Online, Theoretical Division, Los Alamos National Laboratory, October 2003. URL http://george.ph.utexas.edu/~dsteck/alkalidata/rubidium87numbers.pdf.

[81] Ayan Banerjee and Vasant Natarajan. Saturated absorption spectroscopy: Eliminating crossover resonances by use of co-propagating beams. *Optics Letters*, 28(20): 1912–1914, October 2003. URL http://www.opticsinfobase.org/abstract.cfm?URI=ol-28-20-1912.

[82] Claude Cohen-Tannoudji. *Quantum Mechanics*, volume 1 and 2. Wiley-VCH (InterScience), 1977. ISBN 047116433X, 0471164356.

[83] Wolfgang Korsch. Technical note on electron paramagnetic resonance. Technical Note E94-010, TN 11, Thomas Jefferson Lab National Accelerator Facility, 1998. URL `http://www.jlab.org/e94010/tech_note_11.ps.gz`.

[84] Lennart C. Karssen. Building a rubidium MOT using polarisation spectroscopy stabilised diode lasers. Master's thesis, Universiteit Utrecht, Nederland, June 2002. URL `http://www.fys.ruu.nl/~karssen/verslagen/rubidium_thesis.pdf`.

[85] Paul D. Lett, Richard N. Watts, Christoph I. Westbrook, William D. Phillips, Phillip L. Gould, and Harold J. Metcalf. Observation of atoms laser cooled below the doppler limit. *Physical Review Letters*, 61(2):169–172, July 1988. doi: 10.1103/PhysRevLett.61.169. URL `http://link.aps.org/abstract/PRL/v61/p169`.

[86] Jean Dalibard and Claude Cohen-Tannoudji. Laser cooling below the Doppler limit by polarization gradients: Simple theoretical models. *Journal of the Optical Society of America B*, 6(11):2023–2045, November 1989. URL `http://www.opticsinfobase.org/abstract.cfm?URI=josab-6-11-2023`.

[87] J. Dalibard, S. Reynaud, and C. Cohen-Tannoudji. Potentialities of a new $\sigma^+ - \sigma^-$ laser configuration for radiative cooling and trapping. *Journal of Physics B: Atomic, Molecular and Optical Physics*, 17(22):4577–4594, November 1984. doi: 10.1088/0022-3700/17/22/018. URL `http://stacks.iop.org/0022-3700/17/4577`.

[88] Carl E. Wieman and Leo Hollberg. Using diode lasers for atomic physics. *Review of Scientific Instruments*, 62(1):1–20, January 1991. doi: 10.1063/1.1142305. URL `http://link.aip.org/link/?RSI/62/1/1`.

[89] R. A. Boyd, J. L. Bliss, and K. G. Libbrecht. Teaching physics with 670 nm diode lasers: Experiments with Fabry-Perot cavities. *American Journal of Physics*, 64 (9):1109–1116, September 1996. doi: 10.1119/1.18330. URL `http://link.aip.org/link/?AJP/64/1109/1`.

[90] Carl Wieman, Gwenn Flowers, and Sarah Gilbert. Inexpensive laser cooling and trapping experiment for undergraduate laboratories. *American Journal of Physics*, 63(4):317–330, April 1995. doi: 10.1119/1.18072. URL `http://link.aip.org/link/?AJP/63/317/1`.

[91] Sharp Microelectronics. *Sharp Diode GH0781JA2C High Power Laser Laser Diode for Max.×32 Speed CD-R Drive.* Sharp, August 2001. URL `http://www.sharpsma.com/Page.aspx/americas/en/part/GH0781JA2C/`.

[92] A. S. Arnold, J. S. Wilson, and M. G. Boshier. A simple extended-cavity diode laser. *Review of Scientific Instruments*, 69(3):1236–1239, March 1998. doi: 10.1063/1.1148756. URL http://link.aip.org/link/?RSI/69/1236/1.

[93] Anthony E. Siegman. *Lasers*. University Science Books, 2nd edition, October 1990. ISBN 0935702113.

[94] Advanced Physics Laboratory. Diode laser chracteristics. Online, California Institute of Technology, . URL http://www.its.caltech.edu/~ph76a/laserprimer.pdf.

[95] M. de Labachelerie, C. Latrasse, P. Kemssu, and P. Cerez. The frequency control of laser diodes. *Journal of Physics III - France*, 2:1557–1589, September 1992. doi: 10.1051/jp3:1992200. URL http://publish.edpsciences.com/abstract/jp3/v2/p1557.

[96] G. Genty, A. Gröhn, H. Talvitie, M. Kaivola, and H. Ludvigsen. Analysis of the linewidth of a grating-feedback GaAlAs laser. *IEEE Journal of Quantum Electronics*, 36(10):1193–1198, October 2000. doi: 10.1109/3.880660. URL http://ieeexplore.ieee.org/search/wrapper.jsp?arnumber=880660.

[97] Karen Liu and Michael G. Littman. Novel geometry for single-mode scanning of tunable lasers. *Optics Letters*, 6(3):117–118, March 1981. URL http://www.opticsinfobase.org/abstract.cfm?URI=ol-6-3-117.

[98] Sang Eon Park, Taeg Yong Kwon, Eun joo Shin, and Ho Seong Lee. A compact extended-cavity diode laser with a Littman configuration. *IEEE Transactions on Instrumentation and Measurement*, 52(2):280–283, April 2003. ISSN 0018-9456. doi: 10.1109/TIM.2003.809912. URL http://ieeexplore.ieee.org/search/wrapper.jsp?arnumber=1202029.

[99] C. J. Hawthorn, K. P. Weber, and R. E. Scholten. Littrow configuration tunable external cavity diode laser with fixed direction output beam. *Review of Scientific Instruments*, 72(12):4477–4479, December 2001. doi: 10.1063/1.1419217. URL http://link.aip.org/link/?RSI/72/4477/1.

[100] R. S. Conroy, A. Carleton, and K. Dholakia. A compact high performance extended cavity diode laser at 635 nm. *Journal of Modern Optics*, 46(12):1787–1791, October 1999. doi: 10.1080/095003499148828. URL http://www.journalsonline.tandf.co.uk/openurl.asp?genre=article&id=doi:10.1080/095003499148828.

[101] Johan Hult, Iain S. Burns, and Clemens F. Kaminski. Wide-bandwidth mode-hop-free tuning of extended-cavity GaN diode lasers. *Applied Optics*, 44(18):3675–3685, June 2005. URL http://ao.osa.org/abstract.cfm?id=84278.

[102] R. W. P. Drever, J. L. Hall, F. V. Kowalski, J. Hough, G. M. Ford, A. J. Munley, and H. Ward. Laser phase and frequency stabilization using an optical resonator. *Applied Physics B: Lasers and Optics*, 31(2):97–105, July 1983. doi: 10.1007/BF00702605. URL `http://www.springerlink.com/content/rgg2823656435593`.

[103] Eric D. Black. An introduction to the pound-drever-hall laser frequency stabilization. *American Journal of Physics*, 69(1):79–87, January 2001. doi: 10.1119/1.1286663. URL `http://link.aip.org/link/?AJP/69/79/1`.

[104] Eric D. Black. Notes on the pound-drever-hall technique. Technical Report LIGO-T98845-00-D, California Institute of Technology, 1998. URL `http://www.ligo.caltech.edu/docs/T/T980045-00.pdf`.

[105] Oded Mor and Ady Arie. Performance analysis of drever-hall laser frequency stabilization using a proportional and integral servo. *IEEE Journal of Quantum Electronics*, 33(4):532–540, April 1997. doi: 10.1109/3.563380. URL `http://ieeexplore.ieee.org/search/wrapper.jsp?arnumber=563380`.

[106] Kristan L. Corwin, Zheng-Tian Lu, Carter F. Hand, Ryan J. Epstein, and Carl E. Wieman. Frequency-stabilized diode laser with the Zeeman shift in an atomic vapor. *Applied Optics*, 37(15):3295–3298, May 1998. URL `http://www.opticsinfobase.org/abstract.cfm?URI=ao-37-15-3295`.

[107] Jan Max Walter Krüger. A novel technique for frequency stabilising laser diodes. Master's thesis, University of Otago, New Zealand, 1998. URL `http://jmwkrueger.googlepages.com/DipSci_JMWKrueger_1998.pdf`.

[108] J. Peter Campbell. Saturated absorption and DAVLL-observed Zeeman shifts at 780 nm in ^{85,87}Rb. Technical report, Davidson College, Charlotte, North Carolina, United States, March 2003. URL `http://www.phy.davidson.edu/StuHome/pecampbell/Zeeman%20Spectra%20Lab2.doc`.

[109] Lennart C. Karssen. Building a rubidium MOT using polarisation spectroscopy stabilised diode lasers: Erratum. Master's thesis, Universiteit Utrecht, Nederland, November 2003. URL `http://www.phys.uu.nl/~karssen/verslagen/erratum.pdf`.

[110] C. E. N. M. Rosenbaum. The rubidium MOT revisited. Master's thesis, Universiteit Utrecht, Nederland, 2004. URL `http://www.phys.uu.nl/~karssen/verslagen/verslagRosenbm0402.pdf`.

[111] B. J. Wolfring and W. G. Kaenders. Injection-locked diode laser system delivering up to 200 mw tunable single-mode output at 685 nm. In *Quantum Electronics and Laser Science Conference, 1999. Technical Digest. Summaries of Papers Presented at the*, pages 63–64. IEEE, May 1999. ISBN 155752576X. URL http://ieeexplore.ieee.org/iel5/6552/17494/00807301.pdf.

[112] M. Gertsvolf and M. Rosenbluh. Injection locking of a diode laser locked to a Zeeman frequency stabilized laser oscillator. *Optics Communications*, 170(4–6): 269–274, November 1999. doi: 10.1016/S0030-4018(99)00470-8. URL http://dx.doi.org/10.1016/S0030-4018(99)00470-8.

[113] R. A. Valenzuela, L. J. Cimini, R. W. Wilson, K. C. Reichmann, and A. Grot. Frequency stabilisation of AlGaAs lasers to absorption spectrum of rubidium using Zeeman effect. *Electronics Letters*, 24(12):725–726, June 1988. URL http://ieeexplore.ieee.org/xpl/freeabs_all.jsp?tp=&arnumber=5780&isnumber=286.

[114] Stanislav Baluschev, Nir Friedman, Lev Khaykovich, Dina Carasso, Ben Johns, and Nir Davidson. Tunable and frequency-stabilized diode laser with a Doppler-free two-photon Zeeman lock. *Applied Optics*, 39(27):4970–4974, September 2000. URL http://www.opticsinfobase.org/abstract.cfm?URI=ao-39-27-4970.

[115] Saturated absorption spectroscopy. Online, August 2003. URL http://www.phys.ufl.edu/courses/phy4803L/group_III/sat_absorbtion/SatAbs.pdf.

[116] David A. Smith and Ifan G. Hughes. The role of hyperfine pumping in multilevel systems exhibiting saturated absorption. *American Journal of Physics*, 72(5):631–637, January 2004. doi: 10.1119/1.1652039. URL http://link.aip.org/link/?AJP/72/631/1.

[117] Lisa M. Larrimore. Doppler-free saturated absorption laser spectroscopy. Online. URL http://www.sccs.swarthmore.edu/users/02/lisal/physics/labs/dop_free.pdf.

[118] Advanced Optics Laboratory. Doppler-free saturated absorption spectroscopy: Laser spectroscopy. Online, California Institute of Technology, . URL http://www.its.caltech.edu/~ph76a/satabs.pdf.

[119] Thomas Rieger and Thomas Volz. Doppler-free saturation spectroscopy. Max-Planck-Institut für Quantenoptik, Garching. URL http://www.mpq.mpg.de/qdynamics/teaching/praktikum/saturation_spectroscopy.pdf.

[120] Doppler-free spectroscopy. Online, MIT Department of Physics, February 2005. URL http://ocw.mit.edu/NR/rdonlyres/Physics/

8-13-14Fall-2004-Spring-2005/EBFEFA08-5537-4447-8FDC-64B2006EEEEE/0/jlexp48.pdf.

[121] Todd P. Meyrath. Electromagnet design basics for cold atom experiments. Technical report, Atom Optics Laboratory, University of Texas at Austin, 2004. URL http://george.ph.utexas.edu/~meyrath/informal/electromagnets.pdf.

[122] Harold J. Metcalf. Magneto-optical trapping and its application to Helium metastables. *Journal of the Optical Society of America B*, 6(11):2206–2210, November 1989. URL http://www.opticsinfobase.org/abstract.cfm?URI=josab-6-11-2206.

[123] C. Klempt, T. van Zoest, T. Henninger, O. Topic, E. Rasel, W. Ertmer, and J. Arlt. Ultraviolet light-induced atom desorption for large rubidium and potasium magneto-optical traps. *Physical Review A*, 73(1):013410, January 2006. doi: 10.1103/PhysRevA.73.013410. URL http://link.aps.org/abstract/PRA/v73/e013410.

[124] Atsushi Hatakeyama, Markus Wilde, and Katsuyuki Fukutani. Classification of light-induced desorption of alkali atoms in glass cells used in atomics physics experiments. *e-Journal of Surface Science and Nanotechnology*, 4:63–68, January 2006. doi: 10.1380/ejssnt.2006.63. URL http://www.jstage.jst.go.jp/article/ejssnt/4/0/4_63/.

[125] William D. Phillips. Laser cooling and trapping on neutral atoms (nobel lecture). *Reviews of Modern Physics*, 70(3):721–741, July 1998. doi: 10.1103/RevModPhys.70.721. URL http://link.aps.org/abstract/RMP/v70/p721.

[126] A. S. Arnold and P. J. Manson. Atomic density and temperature distributions in magneto-optical traps. *Journal of the Optical Society of America B*, 17(4):497–506, April 2000. URL http://www.opticsinfobase.org/abstract.cfm?URI=josab-17-4-497.

[127] A. Imamoğlu and S. E. Harris. Lasers without inversion: Interference of dressed lifetime-broadened states. *Optics Letters*, 14(24):1344–, 1989. URL http://www.opticsinfobase.org/abstract.cfm?URI=ol-14-24-1344.

[128] Vincent Wong, Ryan S. Bennink, Alberto M. Marino, Robert W. Boyd, Jr. C. R. Stroud, and F. A. Narducci. Influence of coherent Raman scattering on coherent population trapping in atomic sodium vapor. *Physical Review A*, 70(5):053811, November 2004. doi: 10.1103/PhysRevA.70.053811. URL http://link.aps.org/abstract/PRA/v70/e053811.

[129] A. Nazarkin, R. Netz, and R. Sauerbrey. Interference-induced transparency and coherent control of quantum systems by frequency-chirped pulses. *Physical Review A*, 67(4):041401, April 2003. doi: 10.1103/PhysRevA.67.041401. URL `http://link.aps.org/abstract/PRA/v67/e041401`.

[130] J. Eschner, G. Morigi, C. Keitel, C. Roos, D. Leibfried, A. Mundt, F. Schmidt-Kaler, and R. Blatt. Ground-state laser cooling of trapped atoms using electromagnetically induced transparency. In Steven Chu, Vladan Vuletić, Andrew J. Kerman, and Cheng Chin, editors, *Laser Spectroscopy - Proceedings of the XV International Conference*, Snowbird, Utah, United States, June 2001. World Scientific Publishing. ISBN 981-02-4781-8. URL `http://heart-c704.uibk.ac.at/publications/papers/icols01_eit_eschner.pdf`.

[131] F. Schmidt-Kaler, J. Eschner, G. Morigi, C. F. Roos, D. Leibfried, A. Mundt, and R. Blatt. Laser cooling with electromagnetically induced transparency: Application to trapped samples of ions or neutral atoms. *Applied Optics*, 73(8):807–814, November 2001. doi: 10.1007/s003400100721. URL `http://www.springerlink.com/content/k8rwnyvgk02jg6ug/`.

[132] A. André, M. D. Eisaman, R. L. Walsworth, A. S. Zibrov, and M. D. Lukin. Quantum control of light using electromagnetically induced trasparency. *Journal of Physics B: Atomic, Molecular and Optical Physics*, 38(9):S589–S604, May 2005. doi: 10.1088/0953-4075/38/9/010. URL `http://stacks.iop.org/0953-4075/38/S589`.

[133] S. E. Harris. Lasers without inversion: Interference of lifetime-broadened resonances. *Physical Review Letters*, 62(9):1033–1036, February 1989. doi: 10.1103/PhysRevLett.62.1033. URL `http://link.aps.org/abstract/PRL/v62/p1033`.

[134] K.-J. Boller, A. Imamoğlu, and S. E. Harris. Observation of electromagnetically induced transparency. *Physical Review Letters*, 66(20):2593–2596, May 1991. doi: 10.1103/PhysRevLett.66.2593. URL `http://link.aps.org/abstract/PRL/v66/p2593`.

[135] Ennio Arimondo and Gaspar Orriols. Nonabsorbing atomic coherences by coherent two-photon transitions in a three-level optical pumping. *Lettere al Nuovo Cimento*, 17(10):333–338, November 1976. doi: 10.1007/BF02746514. URL `http://www.springerlink.com/content/j74w5q037jn3n140`.

[136] G. Alzetta, A. Gozzini, L. Moi, and G. Orriols. An experimental method for the observation of R.F. transitions and laser beat resonances in oriented Na vapour. *Il Nuovo Cimento B*, 36(1):5–20, November 1976. doi: 10.1007/BF02749417. URL `http://www.springerlink.com/content/nj0pj454g8862571`.

[137] G. Alzetta, L. Moi, and G. Orriols. Nonabsorption hyperfine resonances in a sodium vapour irradiated by a multimode dye-laser. *Il Nuovo Cimento B*, 52(2):209–218, August 1979. doi: 10.1007/BF02739035. URL `http://www.springerlink.com/content/j6053713g1823k71`.

[138] H. R. Gray, R. M. Whitley, and Jr. C. R. Stroud. Coherent trapping of atomic populations. *Optics Letters*, 3(6):218–220, December 1978. doi: 10.1364/OL.3.000218. URL `http://ol.osa.org/abstract.cfm?URI=ol-3-6-218`.

[139] J. Wong, J. C. Garrison, and T. H. Einwohner. Multiple-time-scale pertubation theory applied to laser excitation of atoms and molecules. *Physical Review A*, 13 (2):674–687, February 1976. doi: 10.1103/PhysRevA.13.674. URL `http://link.aps.org/abstract/PRA/v13/p674`.

[140] Marco Frasca. Two-level dynamics: Rabi flopping in the strong coupling regime. *Journal of Optics B: Quantum and Semiclassical Optics*, 3(1):S15–S17, February 2001. doi: 10.1088/1464-4266/3/1/353. URL `http://stacks.iop.org/1464-4266/3/S15`.

[141] Jani-Petri Martikainen. Two level atom interacting with laser light, Doppler cooling and MOTs. University Lecture Course 3, Department of Physics, University of Helsinki, Finland, 2006. URL `http://theory.physics.helsinki.fi/%7Equantumgas/Lecture3.pdf`.

[142] Mary L. Boas. *Mathematical Methods for the Physical Sciences*. John Wiley International, 3 edition, June 2004. ISBN 0471365807.

[143] Ian Glendinning. The bloch sphere. Conference talk, Universität Wien, Austria, February 2005. URL `http://www.vcpc.univie.ac.at/~ian/hotlist/qc/talks/bloch-sphere.pdf`.

[144] T. Lu, X. Miao, and H. Metcalf. Bloch theorem on the Bloch sphere. *Physical Review A*, 71(6):061405, June 2005. doi: 10.1103/PhysRevA.71.061405. URL `http://link.aps.org/abstract/PRA/v71/e061405`.

[145] Richard P. Feynman, Jr. Frank L. Vernon, and Robert W. Hellwarth. Geometrical representation of the Schrödinger equation for solving maser problems. *Journal of Applied Physics*, 28(1):49–52, January 1957. doi: 10.1063/1.1722572. URL `http://link.aip.org/link/?JAP/28/49/1`.

[146] Richard A. L. Jones. Lecture 4: Thermal properties of matter. University Lecture Course PHY101, University of Sheffield, Sheffield, UK, 2006. URL `http://www.shef.ac.uk/physics/people/rjones/PDFs/PHY101/PHY101_RALJ_Lect4.pdf`.

[147] Yvan Castin, Kirstine Berg-Sorensen, Jean Dalibard, and Klaus Molmer. Two-dimensional Sisyphus cooling. *Physical Review A*, 50(6):5092–5115, December 1994. doi: 10.1103/PhysRevA.50.5092. URL `http://link.aps.org/abstract/PRA/v50/p5092`.

[148] C. Cohen-Tannoudji and W. D. Phillips. Standing waves, atoms, and very low temperatures. *Journal of Optics (Paris)*, 22(6):281–290, November 1991. doi: 10.1088/0150-536X/22/6/004. URL `http://stacks.iop.org/0150-536X/22/281`.